POLY(ACRYLAMIDE-CO-ACRYLIC ACID) GEL POLYMER ELECTROLYTES FOR QUANTUM DOT-SENSITIZED SOLAR CELLS

LEE YAP CHEN

FACULTY OF SCIENCE
UNIVERSITI MALAYA
KUALA LUMPUR

2022

POLY(ACRYLAMIDE-CO-ACRYLIC ACID) GEL POLYMER ELECTROLYTES FOR QUANTUM DOT-SENSITIZED SOLAR CELLS

LEE YAP CHEN

THESIS SUBMITTED IN FULFILMENT OF THE REQUIREMENTS FOR THE DEGREE OF DOCTOR OF PHILOSOPHY

DEPARTMENT OF PHYSICS
FACULTY OF SCIENCE
UNIVERSITI MALAYA
KUALA LUMPUR

2022

UNIVERSITY OF MALAYA

ORIGINAL LITERARY WORK DECLARATION

Name of Candidate: **LEE YAP CHEN**

Matric No: **17006729/1**

Name of Degree: **DOCTOR OF PHILOSOPHY**

Title of Project Paper/Research Report/Dissertation/Thesis ("this Work"):

POLY(ACRYLAMIDE-CO-ACRYLIC ACID) GEL POLYMER ELECTROLYTES FOR QUANTUM DOT-SENSITIZED SOLAR CELLS

Field of Study:

PHYSICS

I do solemnly and sincerely declare that:

(1) I am the sole author/writer of this Work;
(2) This Work is original;
(3) Any use of any work in which copyright exists was done by way of fair dealing and for permitted purposes and any excerpt or extract from, or reference to or reproduction of any copyright work has been disclosed expressly and sufficiently and the title of the Work and its authorship have been acknowledged in this Work;
(4) I do not have any actual knowledge nor do I ought reasonably to know that the making of this work constitutes an infringement of any copyright work;
(5) I hereby assign all and every rights in the copyright to this Work to the University of Malaya ("UM"), who henceforth shall be owner of the copyright in this Work and that any reproduction or use in any form or by any means whatsoever is prohibited without the written consent of UM having been first had and obtained;
(6) I am fully aware that if in the course of making this Work I have infringed any copyright whether intentionally or otherwise, I may be subject to legal action or any other action as may be determined by UM.

Candidate's Signature Date: 27/10/2022

Subscribed and solemnly declared before,

Witness's Signature Date: 27/10/2022

Name:

Designation:

POLY(ACRYLAMIDE-CO-ACRYLIC ACID) GEL POLYMER ELECTROLYTES FOR QUANTUM DOT-SENSITIZED SOLAR CELLS

ABSTRACT

Sodium based gel polymer electrolytes (GPEs) have been developed and used in quantum dot sensitized solar cells (QDSSCs). Poly(acrylamide-co-acrylic acid) (PAAm-PAA) which contains lone pairs of electrons, such as oxygen and nitrogen atoms was used as the polymer host. The GPE with PAAm-PAA : sodium sulfide (Na_2S) aqueous solution : sulfur (S) : ethylene carbonate (EC) : potassium chloride (KCl) in wt.% ratio of 24.7 : 72.5 : 1.8 : 0.4 : 0.6 exhibits the highest ionic conductivity of 70.75 $mS \cdot cm^{-1}$. The chemical bonds between solvent, polymer, salt and additive were identified by Fourier transform infrared (FTIR) spectroscopy. Different methods of electrode deposition for titanium dioxide (TiO_2) layers have been applied for QDSSCs. Cadmium sulfide (CdS) and zinc sulfide (ZnS) sensitized photoanode were synthesized by successive ionic layer adsorption and reaction (SILAR) method. The TiO_2 with different particle sizes (~14 and 21 nm) was deposited by spin coating and doctor blade methods. The spin coating and doctor blade methods give the thickness of 0.70 µm and 10.51 µm, respectively. The most efficient charge transfer process was observed when the TiO_2 electrode was made from the combination of spin-coated 14 nm-TiO_2 and doctor-blade 21 nm-TiO_2 layers. The best efficiency and charge transfer resistance at the photoanode/ electrolyte interface are 1.80% and 35.33 Ω, respectively.

Keywords: Gel polymer electrolyte, quantum dot-sensitized solar cell, poly(acrylamide-co-acrylic acid), ionic conductivity, charge transfer.

ELEKTROLIT GEL POLIMER POLI(ASID AKRILAMID-KO-ASID AKRILIK) UNTUK SEL SURIA TERPEKA BINTIK KUANTUM

ABSTRAK

Elektrolit gel polimer (GPE) berasaskan natrium telah dibangunkan dan digunakan dalam sel suria terpeka bintik kuantum (QDSSCs). Poli(asid akrilamid-ko-asid akrilik) (PAAm-PAA) yang mengandungi pasangan elektron tunggal, seperti atom oksigen dan nitrogen, telah digunakan sebagai tuan rumah polimer. GPE dengan PAAm-PAA : larutan berair natrium sulfida (Na_2S) : sulfur (S) : etilena karbonat (EC) : kalium klorida (KCl) dalam nisbah berat 24.7 : 72.5 : 1.8 : 0.4 : 0.6 menunjukkan kekonduksian ionik tertinggi iaitu 70.75 $mS \cdot cm^{-1}$. Ikatan kimia antara pelarut, polimer, garam dan bahan tambahan boleh dikenal pasti melalui spektroskopi inframerah fourier transformasi (FTIR). Kaedah pengendapan elektrod yang berbeza bagi lapisan titanium dioksida (TiO_2) telah digunakan untuk QDSSCs. Fotoanod terpeka kadmium sulfida (CdS) dan zink sulfida (ZnS) telah disintesis melalui kaedah penjerapan dan tindak balas lapisan ionik berturutan (SILAR). TiO_2 dengan saiz zarah yang berbeza (~14 and 21 nm) telah dimendapkan dengan kaedah salutan putaran dan kaedah bilah doktor. Lapisan TiO_2 yang dimendapkan dengan kaedah salutan putaran dan kaedah bilah doktor memberikan ketebalan masing-masing 0.70 µm dan 10.51 µm. Proses pemindahan cas yang paling cekap dapat dilihat apabila elektrod TiO_2 yang dibuat daripada gabungan lapisan 14 nm-TiO_2 dan lapisan 21 nm-TiO_2 yang masing-masing disediakan melalui kaedah salutan putaran dan bilah doctor. Kecekapan terbaik dan rintangan pemindahan cas pada antara muka fotoanod/elektrolit masing-masing adalah 1.80% dan 35.33 Ω.

Kata kunci: Elektrolit gel polimer, sel suria terpeka bintik kuantum, poli(asid akrilamid-ko-asid akrilik), kekonduksian ionik, pemindahan cas

ACKNOWLEDGEMENTS

I would like to express my heartfelt gratitude to my research supervisors, Dr. Mohd Hamdi bin Ali @ Buraidah and Dr. Woo Haw Jiunn, for their acceptance, knowledge sharing and guiding me from time to time to complete this research. I am very grateful for everything they have provided me and would like to teach me step by step. I am honored to have both of them as my mentors. My sincere appreciation to their families for their tolerance and patience during the research discussion and thesis preparation I had with my supervisors, especially during the pandemic.

I sincerely thank Professor Abdul Kariem bin Haji Mohd Arof, the founder of Centre for Ionics University of Malaya (C.I.U.M.), for providing me the learning opportunities regardless of my research or life. His ideas, vision, passion and dedication to research inspired me deeply. I would not be able to complete this research without the support of my seniors, Dr. Zieauddin, Dr. Teo, Dr. Li Na, Dr. Farhana, Dr. Wendy and my lab mates, Dr. Ammar Ming, Shah, Najla, Dr. Kim, Richard, Nada, Sharifah (to name a few), and others. I am sorry I can't mention them all.

Thanks to my family and friends for their endless support. Mom, you have been standing behind me, caring and sacrified, educating and preparing me for my future. My achievements and doctorate are because you believed in me. I am very much thankful to my siblings for their love, prayers and continuing support to complete this research work. Deepest thanks to YJ, who has always supported my adventure and kept reminding me of my ultimate goal. Thank you very much KK for encouraging me during difficult times. His support, understanding and prayers are of great significance to me. My heartfelt thanks to my country for vaccinating me, my family and friends so that we can fight the Coronavirus. I hope everyone will be safe and sound until we meet again after the pandemic. Amen.

TABLE OF CONTENTS

LIST OF FIGURES

LIST OF TABLES

LIST OF SYMBOLS AND ABBREVIATIONS

E_A	:	Activation energy
R_b	:	Bulk resistance
n	:	Charge carrier density
R^2	:	Coefficient of determination
CPE	:	Constant phase element
ε'	:	Dielectric constant
η	:	Efficiency
FF	:	Fill factor
D	:	Free ions diffusion coefficient
$-\mathrm{Z''}$	:	Imaginary impedance
σ	:	Ionic conductivity
μ	:	Ionic mobility
V_{oc}	:	Open circuit voltage
Z'	:	Real impedance
J_{sc}	:	Short circuit current density
Wt.%	:	Weight percentage
CB	:	Conduction band
CBD	:	Chemical bath deposition
CdS	:	Cadmium sulfide
CE	:	Counter electrode
Cl^-	:	Chloride
EC	:	Ethylene carbonate
EDX	:	Energy dispersive x-ray
EIS	:	Electrochemical impedance spectroscopy

FESEM	:	Field emission scanning electron microscopy
FTIR	:	Fourier transform infrared spectroscopy
FTO	:	Fluorine tin oxide
GPE	:	Gel polymer electrolyte
H_2O	:	Water
IR	:	Infrared
J-V	:	Photocurrent density-voltage
K^+	:	Potassium
KCl	:	Potassium chloride
LE	:	Liquid electrolyte
Na^+	:	Sodium
Na_2S	:	Sodium sulfide
PAAm-PAA	:	Poly(acrylamide-co-acrylic acid)
Pt	:	Platinum
QD	:	Quantum dot
QDSSC	:	Quantum dot sensitized solar cell
S	:	Sulfur
S^{2-}/S_n^{2-}	:	Sulfide/polysulfide
SILAR	:	Successive ionic layer adsorption and reaction
SPE	:	Solid polymer electrolyte
T	:	Temperature
TiO_2	:	Titanium dioxide
VB	:	Valence band
XRD	:	X-ray diffraction
ZnS	:	Zinc sulfide

CHAPTER 1: INTRODUCTION

1.1 Introduction

The impetuous increase of the earth's population and economic has created a huge energy demand. The sustainability of energy is essential as it may cause a crucial impact to economy development as the global population increases and technology getting more advance day by day. The consumption of fossil fuels has increased over the decades to meet the ever-increasing energy demand. This has led to high carbon dioxide emissions and the greenhouse effect. Scientists are having a harsh time to deal with the shortage of existing fossil fuel reserves and its consequences of greenhouse effect to the ozone. Thus, alternate sustainable energy/renewable energy is essential and required (Kannan & Vakeesan, 2016; Kouhnavard et al., 2014; Mekhilef et al., 2012; Rühle et al., 2010). Solar energy is a type of renewable energy that uses sunlight to generate electricity and does not create secondary pollution to the environment. Sunlight in nature is abundant and can be obtained freely from the natural environment. Therefore, rural areas can also use solar energy and operate day and night (Cook et al., 2010; John & Tony, 2017; Su'ait et al., 2015).

Solar cells are divided into three generations. The first generation (conventional cells) are mono- and poly-crystalline silicon (Si) wafers, while the second generation is thin film cells based on amorphous Si or cadmium telluride (CdTe) (Babar et al., 2020). Their working principle is based on single p-n junction formed between p-type and n-type semiconductors (Kong et al., 2019). In 2018, first- and second-generation solar cells accounted for 95% and 5% of the photovoltaic market, respectively (Green, 2019; Luceño-Sánchez et al., 2019). However, they suffer high manufacturing cost, limited Si supply (first generation) and low efficiency (second generation), respectively. Third generation (photoelectrochemical cells), such as quantum dot-sensitized solar cells (QDSSCs), dye-sensitized solar cells (DSSCs), organic solar cells and perovskite

sensitized solar cells (PSSC), which generally give high efficiency at lower manufacturing cost are emerging as new solar cell alternatives (Akinoglu et al., 2021).

Quantum dot sensitized solar cells (QDSSCs) have been widely studied in recent research credits to the unique photoelectric property of QD sensitizer. QD is an artificial atom made through quantum confinement, which can produce nano-sized particles and discrete energy levels. This is the source of the unique photoelectric properties of QD sensitizer, such as tunable band gap, large intrinsic dipole moments, high molar extinction coefficient, alterable absorption edge from infrared to ultraviolet region and multiple exciton generations (MEG) (Chebrolu & Kim, 2019; Chung et al., 2021; Sahu et al., 2020; Singh et al., 2022) In particular, according to the literature review, the power conversion efficiency (PCE) of QDSSCs may exceed the Shockley and Queisser limits of traditional silicon-based solar cells (first generation solar cell), that is, more than 32% (Rühle et al., 2010; Shockley & Queisser, 1961). This makes QDSSCs an excellent alternative to high-capacity silicon-based solar cells in the commercial solar cell industry in the future.

QDSSC has a photovoltaic structure made by sandwiching an electrolyte between two electrodes. Each component plays a role in obtaining high-performance QDSSC. Most QDSSCs use liquid electrolytes to ensure smooth charge transfer, but there will inevitably be problems with leakage and volatilization, not to mention that electrons are most likely to recombine at the QD-liquid electrolyte interface. In addition, the manufacturing cost of QDSSC with liquid electrolyte is relatively high due to the sealing cost. For example, solar cells with liquid electrolytes require double-layer sealed packaging to prevent leakage and evaporation of electrolyte solvents, and to protect the liquid electrolyte from external moisture and high temperatures to ensure the thermal stability of solar cells (Matsui et al., 2009). In this fashion, alternatives such as gel polymer electrolyte (GPE) in QDSSC has aroused great interest to eliminate problems such as leakage, volatilization,

high electron recombination rate, and high manufacturing costs. GPE guarantees long-term durability and thermal stability (Nogueira et al., 2001; Zhang et al., 2006), hinders the rate of electronic recombination (Arof et al., 2013), and increases short-circuit current density (J_{sc}) (Buraidah et al., 2017) and open-circuit voltage (V_{oc}) (Kim et al., 2016b) to obtain high-performance QDSSC.

In QDSSC, the commonly used salt for liquid electrolytes is water-soluble sodium sulfide (Na_2S), which contains sulfide/polysulfide (S^{2-}/S_n^{2-}) redox couples (Jun et al., 2013a). Finding polymers with good gelatinization properties and excellent compatibility with water-soluble Na_2S is very important for the development of GPE. Poly(acrylamide-co-acrylic acid) (PAAm-PAA) is a highly transparent, good gelatinization agent, water-soluble and hydrophilic polymer (Lee et al., 2020). In this work, GPE based on PAAm-PAA will be developed to study the compatibility between Na_2S (salt), PAAm-PAA (polymer host) and water (solvent). According to literature review, the performance of GPE can be improved by addition of additives. Therefore, two GPE systems containing various weight percentages of single and dual additives will be prepared. When the best performance GPE is prepared, the photovoltaic performance of titanium dioxide/cadmium sulfide/zinc sulfide sensitized solar cells (TiO_2/CdS/ZnS-SSCs) will be found. In addition, the charge transfer mechanism in QDSSC will be explored.

1.2 Objectives

1. To prepare poly(acrylamide-co-acrylic acid) based GPEs containing water-soluble sodium sulfide salt.
2. To determine the effect of ethylene carbonate and potassium chloride incorporating to the GPEs.
3. To study the photovoltaic performance of quantum dot-sensitized solar cells using the as-prepared GPEs.

1.3 Scope of Thesis

There are seven chapters in this thesis. The first chapter introduces the background, purpose and scope of the thesis. Chapter 2 briefly introduces the various components in GPE and roles of GPE in QDSSC, as well as the role of other components in QDSSC. Chapter 3 discusses the chemicals, preparation steps, and characterization techniques of the four GPE systems. These systems are based on various weight percentages of polymer host (PAAm-PAA), salt (Na_2S and sulfur, S) and additives (ethylene carbonate, EC, and potassium chloride, KCl). Additives are added to improve the transport properties of GPE. In addition, this chapter also introduces the fabrication of other components and assembly of QDSSC, and the characterization techniques. Characterization techniques involve Fourier transform infrared (FTIR) spectroscopy, electrochemical impedance spectroscopy (EIS), field emission scanning electron microscope (FESEM), energy dispersive X-ray spectrometer (EDX), X-ray diffraction (XRD) and photocurrent density-voltage (*J-V*) characteristic. Chapter 4 presents the FTIR results of GPE systems to study the molecular interactions between all components of the GPE. The interactions will be revealed by observing the changes in the shape, intensity and peak position of each infrared spectrum. Chapter 5 presents the EIS results of GPE systems to study their electrical, dielectric and temperature dependence conductivity properties. Chapter 6 analyzes the surface morphology, elemental analysis and structure of the photoanode through FESEM, EDX and XRD analysis. Chapter 6 also presents the photovoltaic performance and impedance plots of two quasi-solid-state QDSSC systems to study their efficiency and charge transfer mechanism. These systems are based on different GPE compositions and different titanium dioxide (TiO_2) layers. In a nutshell, the results and discussion of each characterization will be summarized at the end of each chapter. Last but not least, Chapter 7 clarifies the conclusions and suggestions for future work.

CHAPTER 2: LITERATURE REVIEW

2.1 Gel Polymer Electrolyte

GPE is a polymer electrolyte that exists in a quasi-solid form regardless of its viscosity level. It is simply formed by expanding the network by cross-linking polymer chains in a salt solution (Meyer, 1998). This is also called solidification of liquid electrolyte (LE) by polymer, and there is a redox system similar to LE in GPE (Song et al., 2018). Simple GPE consists of solvent, salt, and polymer. The polymer acts as a backbone supporting the rigidity of the GPE, providing mechanical properties but not conductivity. The salt will produce charge carriers in GPE, thereby exhibiting electrical conductivity and ion migration in GPE (Jun et al., 2013a). The solvent can dissolve and diffuse ions in the provided environment (Wu et al., 2008). Since there is no polymer matrix in LE and solvent in solid polymer electrolyte (SPE), in general, GPE is not as conductive as LE, but more conductive than SPE (Brennan et al., 2017). Table 2.1 lists several GPEs applicable to QDSSC and the photovoltaic performance of QDSSC using different GPEs.

Table 2.1: Photovoltaic performance of QDSSC using different GPEs.

Electrolytes			QDSSC Performance	References
Polymer	**Solvent**	**Redox couple**		
Sodium polyacrylate	Water	S^{2-}/S_n^{2-}	J_{sc} = 20.57 mA·cm^{-2} V_{oc} = 0.66 V FF = 0.63 η = 8.54%	(Feng et al., 2016a)
Graphene implanted polyacrylamide	Water	S^{2-}/S_n^{2-}	J_{sc} = 9.63 mA·cm^{-2} V_{oc} = 0.59 V FF = 0.40 η = 2.24%	(Duan et al., 2015a)
Poly(ethylene glycol) dimethyl-ether + fumed silica	Methanol + water + potassium chloride	S^{2-}/S_n^{2-}	J_{sc} = 17.84 mA·cm^{-2} V_{oc} = 0.72 V FF = 0.42 η = 5.45%	(Kim et al., 2014)

Table 2.1, continued.

Electrolytes			QDSSC Performance	References
Polymer	**Solvent**	**Redox couple**		
Methylcellulose	Water	S^{2-}/S_n^{2-}	J_{sc} = 9.61 mA·cm^{-2} V_{oc} = 0.60 V FF = 0.50 η = 2.90%	(Mingsukang et al., 2017b)
Sodium carboxymethyl cellulose	Water	S^{2-}/S_n^{2-}	J_{sc} = 21.89 mA·cm^{-2} V_{oc} = 0.67 V FF = 0.63 η = 9.21%	(Feng et al., 2016b)
Agar + glycerol + formaldehyde	Water	S^{2-}/S_n^{2-}	J_{sc} = 13.51 mA·cm^{-2} V_{oc} = 0.58 V FF = 0.38 η = 2.98%	(Raphael et al., 2017)
Sodium carboxymethyl starch	Water	S^{2-}/S_n^{2-}	J_{sc} = 15.63 mA·cm^{-2} V_{oc} = 0.62 V FF = 0.66 η = 6.32%	(Wang et al., 2018b)
Polyacrylamide/ polypyrrole	Water	S^{2-}/S_n^{2-}	J_{sc} = 13.90 mA·cm^{-2} V_{oc} = 0.47 V FF = 0.27 η = 1.80%	(Yang et al., 2018)
Polyacrylamide/ polyaniline	Water	S^{2-}/S_n^{2-}	J_{sc} = 13.60 mA·cm^{-2} V_{oc} = 0.52 V FF = 0.33 η = 2.33%	(Yang et al., 2018)
Polyacrylamide/ polythiophene	Water	S^{2-}/S_n^{2-}	J_{sc} = 13.32 mA·cm^{-2} V_{oc} = 0.50 V FF = 0.34 η = 2.25%	(Yang et al., 2018)
Dextran	Water + potassium chloride	S^{2-}/S_n^{2-}	J_{sc} = 15.86 mA·cm^{-2} V_{oc} = 0.47 V FF = 0.44 η = 3.23%	(Chen et al., 2013b)
12-hydroxystearic acid	Water + sodium hydroxide	S^{2-}/S_n^{2-}	J_{sc} = 12.18 mA·cm^{-2} V_{oc} = 0.47 V FF = 0.42 η = 2.40%	(Huo et al., 2015)

Table 2.1, continued.

Electrolytes			QDSSC Performance	References
Polymer	**Solvent**	**Redox couple**		
Acrylamide/bis-acrylamide + ammonium persulfate	Water	S^{2-}/S_n^{2-}	J_{sc} = 12.40 mA·cm^{-2} V_{oc} = 0.53 V FF = 0.60 η = 4.00%	(Yu et al., 2010)
Poly(propylene glycol)bis(2-aminopropyl ether) + 3-isocyanatopropyl triethoxysilane	Methanol	S^{2-}/S_n^{2-}	J_{sc} = 16.30 mA·cm^{-2} V_{oc} = 0.68 V FF = 0.41 η = 4.50%	(Karageorgopoulos et al., 2012)
Konjac glucomannan	Water	S^{2-}/S_n^{2-}	J_{sc} = 12.76 mA·cm^{-2} V_{oc} = 0.50 V FF = 0.63 η = 4.06%	(Wang et al., 2013)

2.1.1 Role of Electrolyte

Electrolyte serves as a pathway for hole transport and QD regeneration in QDSSC. These effects are accomplished through redox couple in the electrolyte. An ideal electrolyte requires a few characteristics, such as high ionic conductivity, high redox potential, high solubility, high ionic mobility and long-term stability (Bang & Kamat, 2010; Evangelista et al., 2016; Li et al., 2006). Electrolytes with high ionic conductivity can ensure fast electron circulation. An electrolyte containing a redox couple has a redox potential. In QDSSCs, electrons are transferred from oxidized QDs to metal oxide (MO) semiconductors, and the oxidized QDs are rapidly reduced to the ground state (Nogueira et al., 2004; Wu et al., 2008). The ideal position for the electrolyte redox potential is between the conduction band (CB) and valence band (VB) of the QD to ensure smooth electron transfer between the photoanode and counter electrode (CE). If the redox potential of the electrolyte is lower than the VB of the QD, faster electrons recombination with oxidizing species in the electrolyte are expected (Tubtimtae et al., 2011). In addition, the electrolyte should also have long-term stability to ensure the persistence of device

(Su'ait et al., 2015). Finally, the electrolyte should be transparent in the visible spectrum. Opaque electrolyte will reduce the absorption of visible light by QD, and the excited electrons may react with the ions in the electrolyte to form a dark current (Li et al., 2006; Smestad et al., 2003; Wu et al., 2008).

The electrolyte also plays a role at the electrode/electrolyte interface of QDSSC. It is known that photovoltaic performance of QDSSC can be studied through characterization of photocurrent density-voltage (*J-V*) curve. Through the *J-V* curve, we can obtain short-circuit current density (J_{sc}), open-circuit voltage (V_{oc}), fill factor (FF) and efficiency (η). These parameters become the main force of QDSSC photovoltaic performance (Song et al., 2018). Basically, the transfer speed of redox couples in the electrolyte contributes to J_{sc}, where the ability of redox couples to be catalyzed by CE contributes to FF (Du et al., 2016c; Jiao et al., 2017; Sun et al., 2017). Meanwhile, the energy difference between the Fermi level of the MO semiconductor and the redox potential of the electrolyte contributes to V_{oc} (Bang & Kamat, 2010; Evangelista et al., 2016). The composition of the electrolyte may affect V_{oc}. Similarly, the non-electroactive substances in the electrolyte, i.e., small cations (protons), are also a factor of V_{oc} in QDSSC. These substances are intercalated into the MO semiconductor, thereby transferring the CB of the MO semiconductor to a lower energy level. As a result, when V_{oc} decreases, the interface charge injection efficiency and J_{sc} of QDSSC will increase (Kebede & Lindquist, 1998; Kelly et al., 1999; Liu et al., 1998).

2.1.2 Polymer Host

Polymer host is the main feature of GPE. It supports the rigidity of GPE, provides mechanical properties, reduces the volatility of the solar devices, and has thermal stability at high temperatures (Aziz et al., 2018; Feng et al., 2016a; Sequeira & Santos, 2010; Su'ait et al., 2015). The first criterion required for a polymer material that can be used as

a promising candidate for the polymer host in GPE is the fast segmentation kinetics with polar functional groups and polymer chains (Cheng et al., 2018). In fact, the polar functional group in the polymer acts as an electron donor, ensuring that the polymer has a long pair of electrons, forming bonds with the cation of the salt, thereby promoting the dissolution of the salt (Natesan et al., 2006). The ion transport process is actually assisted and controlled by the segmentation kinetics of the polymer chain (Chen et al., 2019). In addition, ions move faster in the amorphous phase, and when in a fluidity state, there are more voids to move. Therefore, when the viscosity of the GPE decreases and becomes more amorphous, the ionic conductivity of the GPE increases (Ngai et al., 2016). Instead, the ionic conductivity is related to the micro-Brownian motion of polymer segments above the glass transition temperature (T_g). At a temperature higher than T_g, the free volume of the polymer (i.e. pores occupied between polymer chains (Swapna et al., 2020)) will increase, so the polymer chain has greater mobility. In this case, low T_g is also the criterion for polymer candidates in GPE (Golodnitsky et al., 2015). Other criteria for good polymer host should include high degradation temperature and high molecular weight (Cheng et al., 2018). Table 2.2 lists the commonly used polymer hosts in GPE. The relevant chemical and physical properties are collected from the Sigma Aldrich database.

Table 2.2: Commonly used polymers and their chemical and physical properties.

Polymer	Chemical structure	Glass transition temperature (℃)	Melting point (℃)
Polyacrylamide	-$(CH_2CHCONH_2)_n$-	163	246-250
Poly(acrylic acid)	-$(CH_2CHCOOH)_n$-	106	116
Poly(ethylene oxide)	-$(CH_2CH_2O)_n$-	-64	65-75
Poly(acrylonitrile)	-$(CH_2CHCN)_n$-	120-125	317-326
Poly(vinyl alcohol)	-$(CH_2CHOH)_n$-	85	≈200

Among all polymers, polyacrylamide (PAM) is the most studied GPE polymer host in QDSSC due to its high absorption capacity of LE (Yu et al., 2010), three-dimensional

(3D) polymer matrix (Duan et al., 2015a; Yu et al., 2010) and homogeneous microporous structure (Yang et al., 2018). It is believed that the super absorbent capacity of PAM is attributed to its acrylamide functional group (NH), because the NH group is likely to form hydrogen bonds with water, so water will be trapped in the polymer matrix of PAM, explains the hydrophilicity and water solubility of PAM in water. Therefore, PAM is compatible with polysulfide (S_n^{2-}) electrolytes that usually prepared by dissolving sodium sulfide (Na_2S) and sulfur (S) in an aqueous solution. The homogeneous microporous structure of PAM allows a large amount of LE loading and results in high ion mobility. Therefore, the PAM matrix absorbs the polysulfide electrolyte, so that GPE has the same migration kinetics as LE (Duan et al., 2015a; Yang et al., 2018; Yu et al., 2010).

Another commonly used polymer host in GPE is poly(acrylic acid) (PAA), due to its super absorbent capacity, good gelatinization, 3D polymer matrix and hydrophilicity (Li et al., 2018; Tan et al., 2012; Tang et al., 2012). These properties are attributed to the carboxylic acid group (COOH) in PAA. In addition, the COOH groups will interact aggressively with metal ions, exhibiting high ionic conductivity and excellent surface contact with QD films (Feng et al., 2016a). Therefore, PAA swells rapidly in salt-containing solutions to form GPE, and shows the same conductivity as the LE (Iwakura et al., 2002; Li et al., 2018; Zhang et al., 2014b) and produces high-performance QDSSC (Feng et al., 2016a). However, its mechanical strength is poor after the introduction of alkaline salts unless reinforced with adhesives (Guo et al., 2016; Li et al., 2018; Zhong et al., 2015).

Both PAM and PAA contain functional groups that can interact with the cations in the Na_2S salt to form a polymer-salt complex, exhibit ionic conduction and excellent contact with the surface of the QD film. Acrylamide and carboxylic acid groups have good water solubility, good gelatinization, high absorption and easy coordination with alkali metal

cations (Ileperuma, 2013; Su'ait et al., 2015; Tan et al., 2012; Tang et al., 2012). Therefore, it is interesting to have both acrylamide group and carboxylic acid group in the copolymer. The copolymer has the advantages of electrolyte retention, gelatinization performance, high absorption, and easy cation coordination with Na_2S salt. The copolymer is poly(acrylamide-co-acrylic acid) (PAAm-PAA) composed of PAM and PAA (Hassan & Yusof, 2014; Kumaran et al., 2018). The strength of PAAm-PAA is better than PAA because the mechanical strength of PAA is enhanced by PAM (Hassan & Yusof, 2014; Kumaran et al., 2018).

2.1.3 Redox Couple

The performance of QDSSC depends on the speed at which the oxidized QD is reduced to the ground state. Under sunlight, light excitation occurs in the QD and forms electron-hole pairs. Electrons will be injected from the CB of the QD to the CB of the MO semiconductor, where holes remain in the VB of the QD. The QD after electron injection is called oxidized QD, which can be restored by receiving electrons from the redox couple in the electrolyte. All processes, including electron transfer in the MO semiconductor layer, reduction at the oxidized state of QD, electron transfer at counter electrode (CE), and dark current reaction, are all affected by redox couple (Oskam et al., 2001). An ideal redox couple should efficiently regenerate the oxidized QD and non-corrosive to QDSSC components (Sharma et al., 2018). Table 2.3 lists several redox couples suitable for QDSSC and the resulting photovoltaic performance. The redox couples are sulfide/polysulfide (S^{2-}/S_n^{2-}), iodide/triiodide (I^-/I_3^-), cobalt (II/III) (Co^{2+}/Co^{3+}) and manganese (II/III) (Mn^{2+}/Mn^{3+}). Examples of Co^{2+}/Co^{3+} redox electrolytes are $[Co(bpy)_3]^{2+/3+}$ and $[Co(phen)_3]^{2+/3+}$. $[Co(bpy)_3]^{2+/3+}$ contains 2,2′-bipyridine ligands in the electrolyte, while $[Co(phen)_3]^{2+/3+}$ contains 1,10-phenanthroline ligand in the electrolyte.

Table 2.3: Photovoltaic performance of QDSSC using different redox couples.

Redox couple	Salt	QDSSC Performance	References
S^{2-}/S_n^{2-}	Sodium sulfide	J_{sc} = 6.16 mA·cm^{-2} V_{oc} = 0.47 V FF = 0.40 η = 1.15%	(Lee & Chang, 2008)
S^{2-}/S_n^{2-}	Sodium sulfide	J_{sc} = 6.80 mA·cm^{-2} V_{oc} = 0.47 V FF = 0.44 η = 1.41%	(Jun et al., 2013a)
S^{2-}/S_n^{2-}	Sodium sulfide	J_{sc} = 7.51 mA·cm^{-2} V_{oc} = 0.71 V FF = 0.50 η = 2.70%	(Diguna et al., 2007)
S^{2-}/S_n^{2-}	Sodium sulfide	J_{sc} = 11.66 mA·cm^{-2} V_{oc} = 0.50 V FF = 0.49 η = 2.90%	(Lee et al., 2008b)
I^-/I_3^-	Lithium iodide	J_{sc} = 4.30 mA·cm^{-2} V_{oc} = 0.68 V FF = 0.63 η = 1.84%	(Lee & Chang, 2008)
I^-/I_3^-	Lithium iodide	J_{sc} = 2.61 mA·cm^{-2} V_{oc} = 0.72 V FF = 0.66 η = 1.24%	(Shalom et al., 2009a)
$[Co(phen)_3]^{2+/3+}$	Tris(1,10-phenanthroline)cobalt (II)di(bis(trifluoro methane)sulfonimide)	J_{sc} = 2.64 mA·cm^{-2} V_{oc} = 0.41 V FF = 0.57 η = 0.62%	(Lee et al., 2009)
$[Co(phen)_3]^{2+/3+}$	Tris(1,10-phenanthroline)cobalt (II)di(bis(trifluoro methane)sulfonimide)	J_{sc} = 3.15 mA·cm^{-2} V_{oc} = 0.61 V FF = 0.61 η = 1.17%	(Lee et al., 2008a)
$[Co(bpy)_3]^{2+/3+}$	Cobalt(II) chloride hexahydrate	J_{sc} = 2.80 mA·cm^{-2} V_{oc} = 0.46 V FF = 0.45 η = 0.58%	(Chae et al., 2014)

Table 2.3, continued.

Redox couple	Salt	QDSSC Performance	References
$[Co(bpy)_3]^{2+/3+}$	Cobalt(II) chloride tetrahydrate	J_{sc} = 0.77 mA·cm^{-2} V_{oc} = 0.49 V FF = 0.46 η = 0.84%	(Kessinger et al., 2018)
Mn^{2+}/Mn^{3+}	Manganese(II) chloride tetrahydrate	J_{sc} = 0.65 mA·cm^{-2} V_{oc} = 0.94 V FF = 0.56 η = 1.68%	(Kessinger et al., 2018)

The most suitable electrolyte for QDSSCs is S^{2-}/S_n^{2-} redox electrolyte (Jun et al., 2013a). The electrochemical redox potential and kinetic properties of S^{2-}/S_n^{2-} are suitable for the regeneration of several light-excited QDs, for example, cadmium selenide (CdSe) and cadmium sulfide (CdS) (Lee & Chang, 2008; Liao et al., 2015). Lee and Chang claimed that QDSSC equipped with S^{2-}/S_n^{2-} redox electrolyte results in low V_{oc} and FF, so the efficiency of QDSSC equipped with S^{2-}/S_n^{2-} redox electrolyte is lower than that of QDSSC equipped with I^-/I_3^- redox electrolyte. However, I^-/I_3^- is corrosive to most metals and semiconductor materials, which have been widely used as sensitizers in QDSSC. When QD starts to decay in the I^-/I_3^- redox electrolyte, the photocurrent decreases rapidly. It is not recommended to use I^-/I_3^- redox electrolyte for QDSSC because it fails the stability challenge of cadmium chalcogenide QDs (Lee & Chang, 2008). Eventually, Co^{2+}/Co^{3+} redox systems have emerged, such as $[Co(phen)_3]^{2+/3+}$ (Lee et al., 2009; Lee et al., 2008a) and $[Co(bpy)_3]^{2+/3+}$ (Chae et al., 2014; Kessinger et al., 2018) will be used in QDSSC to look for opportunities to replace S^{2-}/S_n^{2-} and I^-/I_3^-. Compared with I^-/I_3^-, the Co^{2+}/Co^{3+} redox electrolyte is non-corrosive, the standard rate constant is faster (Tachibana et al., 2008), and its redox potential (0.43 – 0.85 V) is lower than that of S^{2-}/S_n^{2-} (Chae et al., 2014). However, QDSSC equipped with Co^{2+}/Co^{3+} redox electrolyte can only achieve a total conversion efficiency of no more than 2% (Lee et al., 2009). This

is due to the slow diffusion rate of Co^{2+}/Co^{3+} complexes and the rapid reverse recombination of positive Co^{3+} species with negatively charged electrons in titanium dioxide (TiO_2) (Chae et al., 2014).

Compared with current redox couples, Mn^{2+}/Mn^{3+} redox electrolytes, such as bis[hydrotris(pyrazolyl)]borate manganese(II/III) ($MnTp_2$), display higher positive reduction potential and slower recombination rate, which is considered a feasible redox couple in QDSSC. The spin crossover of the $MnTp_2$ complex caused by charge transfer reduces the back electron transfer kinetics and increases its V_{oc}, while prolonging the lifetime of injected electrons, thereby improving the performance of QDSSC (Kessinger et al., 2018). However, the Mn^{2+}/Mn^{3+} complex promoted low solubility, thereby slowing down its diffusion performance, while limiting mass transfer, and ultimately failed to maintain high photocurrent (Haring et al., 2014; Kessinger et al., 2018).

After all, in terms of the overall performance of QDSSC, the S^{2-}/S_n^{2-} redox couple is still higher than other redox couples. The S^{2-}/S_n^{2-} redox electrolyte composed of Na_2S and S is still the most suitable electrolyte for QDSSC. The S^{2-}/S_n^{2-} redox couple prevents the degradation of QD chalcogenides and produces high ionic conductivity for QDSSC due to its better ion transport (Jun et al., 2013a; Lee & Chang, 2008; Li et al., 2011; Sekhar et al., 2014).

2.1.4 Additives

Incorporating additives into the electrolyte will modify electrochemical structure of the electrolyte (Sun et al., 2018). This method is simple and effective, which has aroused great interest of researchers, who are looking for compatible additives used in conjunction with polysulfide electrolytes. Additive, such as inorganic nanofiller, plasticizer or ionic liquid, is added to GPE to enhance the (i) ionic conductivity, (ii) ion transport properties, (iii) mechanical strength, and (iv) thermal stability (Kurc, 2014; Malhotra & Varshney,

2015). The poor coordination between polymer and liquid electrolyte can be overcome. Ethylene carbonate (EC) with a high boiling point of 244 ℃, a high dielectric constant of 90, and a low viscosity of 1.9 $mPa^{-1} \cdot s^{-1}$ (Kinoshita et al., 2008) has always been used as a polymer chain lubricant or additive in preparation of polymer electrolytes (Buraidah et al., 2009; Kinoshita et al., 2008; Woo et al., 2013). It helps to disorder the original polymer crystal structure by increasing inter- and intra-chain separations, thereby reducing crystallinity to increase ionic mobility in GPE system (Woo et al., 2013).

There are few reports on the effect of additives in electrolyte on QDSSC photovoltaic performance (Du et al., 2015; Jiang et al., 2016; Sun et al., 2018; Yu et al., 2017). Table 2.4 lists several additives suitable for polysulfide electrolytes and the resulting photovoltaic performance of QDSSC.

Table 2.4: Photovoltaic performance of QDSSC with different additives.

Additive	Electrolyte	QDSSC Performance	References
Potassium chloride	Liquid	J_{sc} = 6.16 mA·cm^{-2} V_{oc} = 0.47 V FF = 0.40 η = 1.15%	(Lee & Chang, 2008)
Potassium chloride	Liquid	J_{sc} = 11.66 mA·cm^{-2} V_{oc} = 0.50 V FF = 0.49 η = 2.90%	(Lee et al., 2008b)
Potassium chloride	Liquid	J_{sc} = 16.65 mA·cm^{-2} V_{oc} = 0.57 V FF = 0.49 η = 4.70%	(Ren et al., 2015)
Potassium chloride	Gel polymer	J_{sc} = 15.86 mA·cm^{-2} V_{oc} = 0.47 V FF = 0.44 η = 3.23%	(Chen et al., 2013b)
Potassium chloride + fumed silica	Gel polymer	J_{sc} = 17.84 mA·cm^{-2} V_{oc} = 0.72 V FF = 0.42 η = 5.45%	(Kim et al., 2014)

Table 2.4, continued.

Additive	Electrolyte	QDSSC Performance	References
Sodium hydroxide	Hydrogel	J_{sc} = 12.18 mA·cm^{-2} V_{oc} = 0.47 V FF = 0.42 η = 2.40%	(Huo et al., 2015)
Sodium hydroxide	Liquid	J_{sc} = 14.71 mA·cm^{-2} V_{oc} = 0.53 V FF = 0.50 η = 3.90%	(Ren et al., 2015)
Potassium chloride + 1,2-dimethyl-3-propylimidazolium iodide	Liquid	J_{sc} = 19.36 mA·cm^{-2} V_{oc} = 0.59 V FF = 0.45 η = 5.14%	(Ren et al., 2015)
Potassium chloride + poly(vinyl pyrrolidone)	Liquid	J_{sc} = 20.49 mA·cm^{-2} V_{oc} = 0.72 V FF = 0.66 η = 9.77%	(Jiang et al., 2016)
Potassium chloride + tetraethyl orthosilicate	Liquid	J_{sc} = 26.91 mA·cm^{-2} V_{oc} = 0.63 V FF = 0.61 η = 10.27%	(Yu et al., 2017)
Potassium chloride + poly-ethylene glycol	Liquid	J_{sc} = 15.80 mA·cm^{-2} V_{oc} = 0.69 V FF = 0.70 η = 7.60%	(Sun et al., 2018)
Poly-ethylene glycol	Liquid	J_{sc} = 15.66 mA·cm^{-2} V_{oc} = 0.65 V FF = 0.67 η = 6.74%	(Du et al., 2015)
Guanidine thiocyanate	Liquid	J_{sc} = 6.80 mA·cm^{-2} V_{oc} = 0.47 V FF = 0.44 η = 1.41%	(Jun et al., 2013a)

In the literature review, different types of additives can bring different advantages to the role of electrolyte in QDSSC. First, certain molecular additives can tune the redox

potential of the electrolyte and change the CB of MO semiconductors and QDs through their tiny size (Barea et al., 2010; Raga et al., 2012; Shalom et al., 2009b; Sun et al., 2018). Polymer additives have strong water absorption, making them a good gelling agent in electrolytes, thereby improving the stability of QDSSC in all aspects (Chen et al., 2013b; Feng et al., 2016a; Feng et al., 2016b; Kim et al., 2017; Kim et al., 2014; Sekhar et al., 2014; Yu et al., 2010). The organic polymer additives in the electrolyte are easily adsorbed on the surface of the photoanode, so a high-energy barrier film is formed on the interface, which hinders the recombination of electrons, resulting in a higher V_{oc} of QDSSC (Du et al., 2015; Jiang et al., 2016; Wei et al., 2016; Yu et al., 2017).

Among additives, potassium chloride (KCl) is the most studied additive in polysulfide electrolytes in liquid or gel form. This is because the KCl is compatible with aqueous solutions, polymer mixtures and alcohol solutions. The addition of KCl to the polysulfide electrolyte not only has better ionic conductivity and polymer cohesive performance, but also significantly improves the overall performance of QDSSCs by suppressing recombination processes (Jiang et al., 2016; Ren et al., 2015; Sun et al., 2018; Yu et al., 2017).

2.2 Quantum Dot Sensitized Solar Cell

QDSSC is a photochemical system composed of three functional components: QD photoanode, redox electrolyte and CE, as illustrated in Figure 2.1. Generally, the QD photoanode is composed of a MO semiconductor and a sensitizer. A common example of them is TiO_2 and CdS. In addition to the photoanode, CE or cathode also plays a vital role in QDSSC. Both electrodes use fluorine-doped tin oxide (FTO) glass substrate. The assembly of QDSSC is to sandwich S^{2-}/S_n^{2-} redox GPE between TiO_2/CdS photoanode and CE.

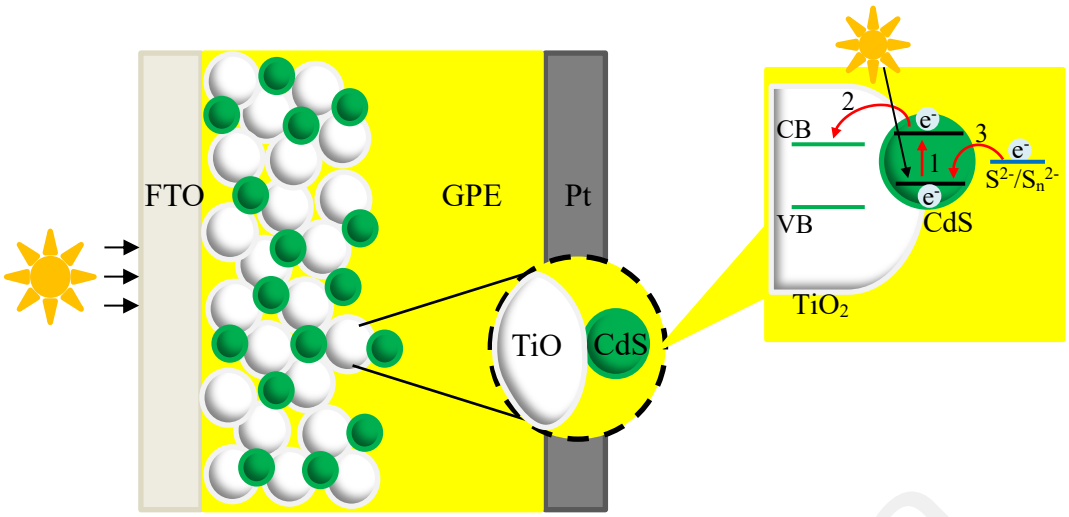

Figure 2.1: Structure and working mechanism of QDSSC.

In the working mechanism of QDSSC, electrons (e^-) transfer in TiO_2 and CdS, as shown in Figure 2.1. The gap between CB and VB is called an energy band gap. When sunlight strikes on the QDSSC, the CdS sensitizer will be excited where electrons jump from VB to the CB of the CdS in reaction 1, electron-hole pairs are generated. The excited CdS QD injects electrons into the CB of TiO_2 in reaction 2. The electrons then enter the external circuit to generate electric current. On the other hand, holes in the VB of QD will accept electrons from the S^{2-} ions in GPE (reaction 3 and equation 2.1).

$$S^{2-} - 2e^- + {S_{n-1}}^{2-} \rightarrow {S_n}^{2-} + 2{h_{QD}}^+ \qquad (n = 2-5) \tag{2.1}$$

The polysulfide, S_n^{2-} ions are produced by the reduction of QD and the oxidation of sulfide, S^{2-} ions. At the CE, electrons from the external circuit are collected to restore the S^{2-} ions in the GPE as shown in equation 2.2 (Duan et al., 2015b; Jun et al., 2013a; Mora-Sero et al., 2009).

$${S_n}^{2-} + 2{e_{CE}}^- \rightarrow S^{2-} + {S_{n-1}}^{2-} \qquad (n = 2-5) \tag{2.2}$$

It can be deduced that in reaction 3, the S^{2-} ion in GPE donates an electron to the oxidized CdS QD, and then accepts the electron from CE. These favorable processes are

circulating to ensure smooth current generation in QDSSC. The power conversion efficiency, η of QDSSC reflects the smoothness of electron transfer in QDSSC. However, some QDSSCs give very low η because they were counteracting by the recombination of the electrons. The major electron recombination found in QDSSC is radiative recombination, i.e., in reaction 2, the electrons in CB are transferred back to VB instead of injected into the CB of TiO_2. In addition, in TiO_2, the electrons in CB may also be transferred back to CdS, instead of going to an external circuit to generate current. In addition to radiative recombination, electrons may also recombine with the oxidizing species in GPE (Kamat, 2012). These behaviours are reflected in the reduction of electron separation and collection efficiency, which leads to the reduction of J_{sc}, V_{oc}, FF and η (Hodes, 2008; Ye et al., 2017). From the literature review, the recombination of electrons is preventable by imposed few steps such as introducing double layers of TiO_2 coating (Aziz et al., 2015; Baharun et al., 2020; Bandara et al., 2013; Choi et al., 2012; Lee et al., 2006; Teo et al., 2018), double layers of different QD sensitizers (Sato et al., 2016), two different sizes of same QD sensitizer (Chen et al., 2011), adopting preprepared high quality QD sensitizers (Zhao et al., 2016), incorporating dopant ions into QD sensitizers (Gopi et al., 2016; Muthalif et al., 2019), introducing passivation layer (Du et al., 2016b; Pan et al., 2014; Sogabe et al., 2016), etc. These help to enhance the mechanism of charge separation and transfer in the QDSSC, which is one of the key factors to η of QDSSC.

2.2.1 Photoanode

The photovoltaic performance of QDSSC mainly depends on the photoanode. The design of the photoanode should allow a massive loading of QD and become a smooth electron transmission channel from the QD to the external circuit. In this fashion, the photoanode has a higher electron collection efficiency and a fast electron transfer rate. A simple way to make a good photoanode is to coat the conductive surface of FTO glass with TiO_2 and CdS (Baharun et al., 2020; Mingsukang et al., 2017a). In this work, FTO

glass is preferable owing to its low and temperature stable resistivity (Sima et al., 2010). This resistivity is interrelated to the η of QDSSC.

2.2.1.1 Titanium Dioxide Layer

TiO_2 is a wide band gap MO semiconductor particularly used on the photoanode before the deposition of QD sensitizers in QDSSCs, due to its high chemical and photo-stability under visible light illumination (Bai et al., 2014; Jia et al., 2018). It is used as MO layer on the photoanode. This MO layer is essential for the photoanode to (i) allow light to pass through to the QD; (ii) act as a blocking layer between the FTO glass and the electrolyte (Choi et al., 2012; Seo et al., 2011); and (iii) act as a base for the attachment of QDs (Bandara et al., 2013). TiO_2 film can be divided into compact and mesoporous layers, according to its nanoscale particles size. For example, P90 TiO_2 is used as the compact layer of the photoanode, while P25 TiO_2 is the mesoporous layer of the photoanode (Aziz et al., 2015; Baharun et al., 2020; Bandara et al., 2013; Choi et al., 2012; Lee et al., 2006; Teo et al., 2018). The compact layer effectively blocks the close contact between the FTO glass and the electrolyte. This is to prevent the electron recombination between the FTO glass and the oxidizing species in the electrolyte during the electron separation and transfer mechanism of QDSSC (Seo et al., 2011). According to the literature review, if the photoanode is equipped with a compact layer, the η of QDSSCs will be 20% to 30% higher than that of a photoanode without the compact layer (Choi et al., 2012; Seo et al., 2011; Wu et al., 2014).

The mesoporous layer prepared by P25 TiO_2 serves as a loading bay for QDs and the pores on its surface behave as extra parking lots. The characteristics of high surface area, large pore size and volume in P25 TiO_2 created extra reactive sites at surfaces to ease photocatalytic reactions in QDSSC (Khan et al., 2010; Krašovec et al., 2009; Li et al., 2014). From literature review, it can be understood that with the presence of mesoporous

layer on the photoanode, the η of QDSSCs are improved due to enhancement in the absorption of incident light (Arof et al., 2014b; Bandara et al., 2013; Khan et al., 2010). Therefore, it is believed that the capability of photoanode to perform a good interfacial electron transfer between FTO glass and QDs is also prior criterion leading to an efficient QDSSC.

According to literature review, the thickness of compact and mesoporous layers on the photoanode affects the η of QDSSC (Ayele et al., 2013; Choi et al., 2012; Jun et al., 2013b). The η of QDSSC decreases whenever the coating layer of TiO_2 exceeded the optimum thickness. This is because the thicker layer exhibits more trap states that could effectively block the pathway of electrons from TiO_2 layer to FTO glass, and also lower the optical transmittance (Choi et al., 2012). Therefore, the deposition method that used to coat TiO_2 layer must be able to control thickness of layer. Spin coating (Dissanayake et al., 2018) and doctor blading (Mahalingam et al., 2022) are two simple techniques to coat the TiO_2 layer. Spin coating is a method to produce thin film without energy intensive or high temperature required. Instead, it controls the thickness of coated TiO_2 layer by adjusting the spinning speed and duration (Patil et al., 2003). While for the doctor blade technique, it enables a uniform film thickness formation. Doctor blade procedure is efficient and highly reproducible with high precision of catalyst loading where the volume of catalyst slurry added dropwise can be regulated using micropipette and the driven speed is manually controlled by operator. This method is claimed to be more precise compared to the rolling, spraying and hand painting techniques (Park et al., 2010).

2.2.1.2 Cadmium Sulfide Sensitizer

A QD sensitizer is used to harvest incident light in its absorption range to excite electrons to flow through external circuit for current generation in QDSSC (Ye et al., 2017). The QD sensitizers are semiconductor nanocrystals with zero dimensional

structure (Han et al., 2020), have a narrow and tunable band gap, high absorption coefficient, and multiple exciton generations (MEG). The process to tune their band gap is called quantum confinement, that is, to reduce the particle size of semiconductors into nanometer scale to quantize their energy level into discrete energy level. The quantized energy level allows QD semiconductors adjust their band gap to match the solar spectral distribution so that they can emit various color light, in absorption edge from infrared to ultraviolet (Bagher, 2016). In addition, another process namely MEG is where a single photon produces two or more electron-hole pairs in QD semiconductors (Califano et al., 2004; Ellingson et al., 2005; Schaller et al., 2005; Schaller & Klimov, 2004). This situation occurs with high-energy absorption photons, i.e., the energy carried by the absorbed photons is larger than the band gap of the QD. These favorable processes only occur in semiconductor nanocrystals, which usually have a particle size of 2 to 10 nm. They are more likely to belong to the periodic group of II-VI, III-V or IV-VI materials (Jasim, 2015).

CdS is a type II-VI QD semiconductor. The band gap of CdS is 2.4 eV, which lies within the visible solar spectrum (Duan et al., 2015b). The CB edge of CdS is higher than the CB edge of TiO_2, so CdS can easily inject excited electrons into the CB of TiO_2 and enter the external circuit to generate current. This offers the high electron injection efficiency of CdS for the photovoltaic performance of QDSSC (ChuláKim et al., 2006; Veerathangam et al., 2018). For example, CdSe has lower electron injection efficiency than CdS because the CB edge of CdSe is lower than TiO_2, although CdSe has higher absorption wavelength (720 nm) than CdS (550 nm) which enable CdSe to absorb more incident photons than CdS (Lee & Lo, 2009). Therefore, CdS has been widely used as QD sensitizer in QDSSC (Baharun et al., 2020; Lee & Chang, 2008; Li et al., 2011; Mingsukang et al., 2017a).

Besides, the synthesis of CdS QD is facile and low in cost. According to the literature review, the synthesis of CdS QD can be easily done by undergo a direct growth on the surface of TiO_2 electrode. This process is called in situ fabrication, e.g., chemical bath deposition (CBD) and successive ionic layer adsorption and reaction (SILAR) (Kouhnavard et al., 2014; Rühle et al., 2010). Table 2.5 lists the photovoltaic performance of QDSSC deposited by CBD and SILAR. Both methods are simple and low cost.

Table 2.5: Photovoltaic performance of QDSSC by CBD and SILAR.

Chemical Synthesis	QD Sensitizer	QDSSC Performance	References
CBD	CdS	J_{sc} = 4.30 mA·cm^{-2} V_{oc} = 0.68 V FF = 0.63 η = 1.84%	(Chang & Lee, 2007)
CBD	CdSe/ZnS	J_{sc} = 12.20 mA·cm^{-2} V_{oc} = 0.53 V FF = 0.31 η = 2.02%	(Shen et al., 2008)
CBD	CdS/CdSe/ZnS	J_{sc} = 16.80 mA·cm^{-2} V_{oc} = 0.51 V FF = 0.49 η = 4.22%	(Lee & Lo, 2009)
CBD	CdS/CdSe	J_{sc} = 2.05 mA·cm^{-2} V_{oc} = 0.54 V FF = 0.30 η = 0.34%	(Shalom et al., 2011)
CBD	CdS/CdSe/ZnS	J_{sc} = 13.68 mA·cm^{-2} V_{oc} = 0.58 V FF = 0.63 η = 4.92%	(Zhang et al., 2011)
SILAR	Ni-doped CdS	J_{sc} = 8.91 mA·cm^{-2} V_{oc} = 0.64 V FF = 0.54 η = 3.11%	(Gopi et al., 2016)
SILAR	CdS	J_{sc} = 10.39 mA·cm^{-2} V_{oc} = 0.57 V FF = 0.55 η = 3.23%	(Rosiles-Perez et al., 2018)

Table 2.5, continued.

Chemical Synthesis	QD Sensitizer	QDSSC Performance	References
SILAR	CdS	J_{sc} = 7.80 mA·cm^{-2} V_{oc} = 0.46 V FF = 0.68 η = 2.44%	(Tyagi et al., 2020)
SILAR	CdS	J_{sc} = 10.14 mA·cm^{-2} V_{oc} = 0.63 V FF = 0.61 η = 3.92%	(Khodam et al., 2019)
SILAR	CdSe/ZnS	J_{sc} = 13.90 mA·cm^{-2} V_{oc} = 0.54 V FF = 0.51 η = 3.84%	(González-Pedro et al., 2010)
SILAR	CdS/CdSe/ZnS	J_{sc} = 18.40 mA·cm^{-2} V_{oc} = 0.52 V FF = 0.46 η = 4.40%	(Radich et al., 2011)
SILAR	CdS/CdSe/ZnSe	J_{sc} = 20.11 mA·cm^{-2} V_{oc} = 0.58 V FF = 0.55 η = 6.39%	(Huang et al., 2016)

CBD is the most common method to synthesize the CdS QD on top of TiO_2 electrode by immerse the TiO_2 electrode into aqueous solution of reactants (Chang & Lee, 2007). It is simple, low cost and convenient. The immersion duration for CBD may takes several hours (Bulakhe et al., 2013; M.H. & Al-Jawad, 2017). SILAR is a facile and cost-effective technique. It can control the crystallite size of CdS QD and their loading amounts on top of TiO_2 electrode through immersion cycles and immersion time (Jun et al., 2014; Veerathangam et al., 2018). It is also a fast process which can be done by 10 minutes for the synthesis of CdS QD on the top of the TiO_2 electrode (Mingsukang et al., 2017a). Among the two methods, SILAR is preferable as it takes shorter duration and easy to control the desired volume and particle size of synthesized CdS QD. For example, in the comparison studies between SILAR and CBD for the synthesis of CdS QD, SILAR

appears to create better stoichiometry in CdS film than CBD. The S/Cd ratio from SILAR is increased from 0.83 to 1.04 by tuning the concentration of solution while CBD only achieved ~ 0.80 regardless the concentration of solution 1. This is because SILAR and CBD share different growth pattern and mechanism. CdS usually growth homogeneously in CBD because the reactants for Cd and S are kept together in same bath. While in SILAR, the cationic and anionic solutions are kept in two different baths, therefore the CdS can grows homogeneously or heterogeneously, depend on the concentration of each solution and immersion time.

2.2.1.3 Zinc Sulfide Passivation Layer

The surface passivation of the QD sensitizer is to inhibit electron recombination. During charge recombination, electrons will travel in a reverse way instead of entering an external circuit to generate current. Therefore, the separation and collection of electrons at the photoanode and counter electrode will be reduced. In short, when the charge recombination rate is high, the efficiency of charge separation and collection decreases. It is reported that the zinc-copper-indium-selenide (Zn-Cu-In-Se) QDSSC with zinc sulfide/silicon dioxide (ZnS/SiO_2) surface passivation achieves an impressive PCE of 11.6% (Du et al., 2016a). The ZnS passivation layer helps reduce the trapping or recombination of carriers and prevents electrons from being transferred from TiO_2 back to the electrolyte, thereby improving the charge injection efficiency and electron collection. In addition, it stabilizes QDSSC by avoiding photo-corrosion of QD in the electrolyte (Sogabe et al., 2016). A thicker shell protection layer can help QD minimize trap state defects and increase its photoluminescence quantum yield (Veamatahau et al., 2015).

Table 2.6: Photovoltaic performance of QDSSC by passivation layers.

QD Sensitizer	Passivation Layer	QDSSC Performance	References
PbS	ZnS	J_{sc} = 8.40 mA·cm^{-2} V_{oc} = 0.36 V FF = 0.45 η = 1.40%	(Chang et al., 2015)
PbS	CdS	J_{sc} = 12.90 mA·cm^{-2} V_{oc} = 0.46 V FF = 0.41 η = 2.45%	(Sato et al., 2016)
$CuInS_2$	ZnS	J_{sc} = 20.65 mA·cm^{-2} V_{oc} = 0.59 V FF = 0.58 η = 7.04%	(Pan et al., 2014)
$CuInSe_2$	ZnS	J_{sc} = 26.93 mA·cm^{-2} V_{oc} = 0.53 V FF = 0.57 η = 8.10%	(Kim et al., 2015)
Zn-Cu-In-Se	ZnS/SiO_2	J_{sc} = 25.25 mA·cm^{-2} V_{oc} = 0.74 V FF = 0.62 η = 11.61%	(Du et al., 2016b)

2.2.2 Counter Electrode

CE acts as an electron's collector in QDSSC. It should be designed in a way that allow a massive loading of electrons from the external circuit and reduce S_n^{2-} ions to S^{2-} ions at the electrolyte/CE interface, as previously mentioned in equation 2.2. This is called catalytic activity and directly affects the photovoltaic performance, fabrication cost and long-term stability of QDSSCs. CE with better catalytic activity reflects higher FF value and increased η of QDSSC (Duan et al., 2015b; Duan et al., 2014; Wu et al., 2015). CE is made by coating catalyst material on FTO glass (Sun et al., 2017). The catalyst material can be categorized into four types: noble metals, e.g. Pt (Wu et al., 2015); carbon derivatives, e.g. N-doped carbon/Cu (Zhao et al., 2018); polymers, e.g. PEDOT (Wu et al., 2015); and metallic compounds, e.g. Cu_2S (Feng et al., 2016a). These materials should

catalytically be active towards redox electrolyte for the reduction of polysulfide ions, low electrical resistance and chemically stable in the polysulfide electrolyte (Duan et al., 2015b; Duan et al., 2014; Wu et al., 2015). A simple way to make the counter electrode is to coat Pt on the conductive surface of FTO glass (Baharun et al., 2020; Jun et al., 2013a; Mingsukang et al., 2017a).

CHAPTER 3: RESEARCH METHODOLOGY

3.1 Chemicals

Table 3.1 lists the chemicals used in this work and the corresponding detailed information. These chemicals were used in their original form.

Table 3.1: Chemicals and their corresponding detailed information.

Chemicals	Chemical formula	Remarks
Poly(acrylamide-co-acrylic acid) partial sodium salt	$C_6H_8NNaO_3$	Sigma-Aldrich
Sodium sulfide hydrate	$Na_2S{\cdot}nH_2O$	Sigma-Aldrich
Sulfur	S	Sigma-Aldrich
Ethylene carbonate	$C_3H_4O_3$	Sigma-Aldrich
Potassium chloride	KCl	Systerm
P90 titanium dioxide	TiO_2	Evonik Degussa GmbH (14 nm of particle size)
P25 titanium dioxide	TiO_2	Evonik Degussa GmbH (21 nm of particle size)
Cadmium nitrate	$Cd(NO_3)_2$	Sigma-Aldrich
Zinc acetate	$Zn(CH_3COO)_2$	HmbG Chemicals
Plastisol T/SP	Pt	Solaronix
Nitric acid	HNO_3	MERCK Chemicals
Methanol	CH_3OH	Elite Advanced Materials
Ethanol	CH_3CH_2OH	Elite Advanced Materials
Triton x-100	$C_{16}H_{26}O_2$	Sigma-Aldrich
Polyethylene glycol	$(C_2H_4O)_n{\cdot}H_2O$	Merck Schuchardt oHG

3.2 Preparation of Gel Polymer Electrolytes

In this work, PAAm-PAA is the polymer host, Na_2S:S is the salt, and EC and KCl are additives. The four systems of GPE were prepared as follows:

1. W system - GPE with various wt.% of polymer host
2. X system - GPE with various molarity of salt
3. Y system - GPE with single additive
4. Z system - GPE with double additives

3.2.1 W System – Gel Polymer Electrolytes with Various Wt.% of Polymer Host

GPE was prepared by mixing PAAm-PAA with liquid electrolyte, as illustrated in Figure 3.1. The optimized liquid electrolyte was composed of Na_2S:S in an aqueous solution in a ratio of 4:1 following the literature (Baharun et al., 2020). The amount of distilled water, Na_2S and S was fixed at 2.0 g, 0.624 g and 0.064 g, respectively. An appropriate amount of PAAm-PAA was added to the liquid electrolyte, as listed in Table 3.2. The mixture was stirred using magnetic bar until a homogeneous gel at room temperature. The stirring speed was adjusted to minimum level to avoid bubbles formation in GPE.

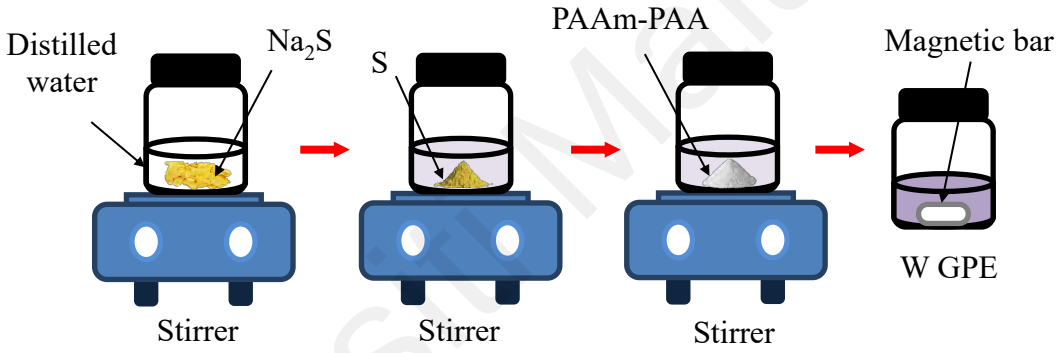

Figure 3.1: Preparation of GPE with various wt.% of PAAm-PAA.

Table 3.2: Composition of GPE with various wt.% of PAAm-PAA.

GPE	Distilled water (g)	Na_2S (g)	S (g)	PAAm-PAA (g)	Wt.%
W0	2.0	0.624	0.064	0.000	0
W1	2.0	0.624	0.064	0.142	5
W2	2.0	0.624	0.064	0.299	10
W3	2.0	0.624	0.064	0.475	15
W4	2.0	0.624	0.064	0.672	20
W5	2.0	0.624	0.064	0.896	25
W6	2.0	0.624	0.064	1.152	30
W7	2.0	0.624	0.064	1.448	35

3.2.2 X System – Gel Polymer Electrolytes with Various Molarity of Salt

GPE was prepared by dissolving fixed amount of PAAm-PAA in the different molarity of polysulfide liquid electrolyte, as shown in Figure 3.2. First, the masses of distilled

water and PAAm-PAA were fixed at 2.0 g and 0.896 g, respectively. Then, appropriate masses of Na_2S and S were added to the GPE according to Table 3.3. The masses of Na_2S and S were varied, but the optimized ratio of Na_2S:S was maintained at 4:1 following the literature (Baharun et al., 2020; Karageorgopoulos et al., 2012). The mixture was stirred using magnetic bar until a homogeneous solution.

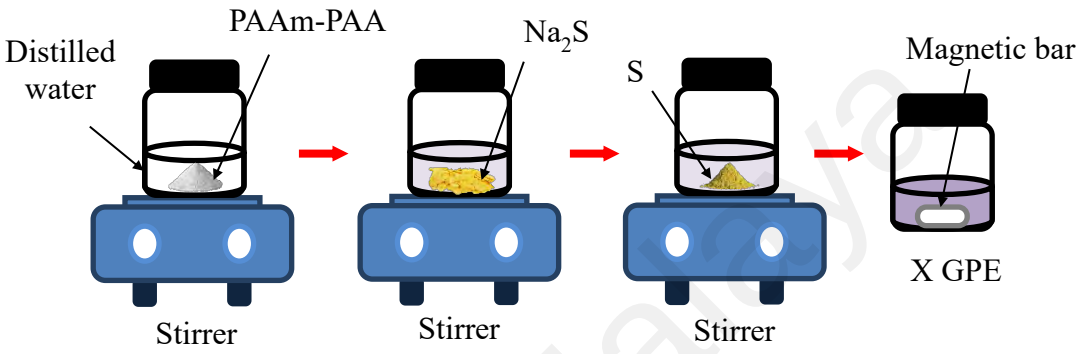

Figure 3.2: Preparation of GPE with various molarity of polysulfide electrolyte.

Table 3.3: Composition of GPE with various molarity of Na_2S:S at a fixed ratio of 4:1.

GPE	Distilled water (g)	PAAm-PAA (g)	Mass (g)		Molarity (M)	
			Na_2S	S	Na_2S	S
X1	2.0	0.896	0.312	0.032	2	0.50
X2	2.0	0.896	0.468	0.048	3	0.75
X3/W5	2.0	0.896	0.624	0.064	4	1.00
X4	2.0	0.896	0.780	0.080	5	1.25
X5	2.0	0.896	0.937	0.096	6	1.50

3.2.3 Y System – Gel Polymer Electrolytes with Single Additive

GPE with single additive was prepared by dissolving EC in the most conducting GPE from X system, X3 (also designated as W5), as illustrated in Figure 3.3. The amount of distilled water, PAAm-PAA, Na_2S and S was fixed at 2.0 g, 0.896 g, 0.624 g and 0.064 g, respectively. EC was then added to the GPE according to Table 3.4. The mixture was stirred using magnetic bar until a homogeneous solution.

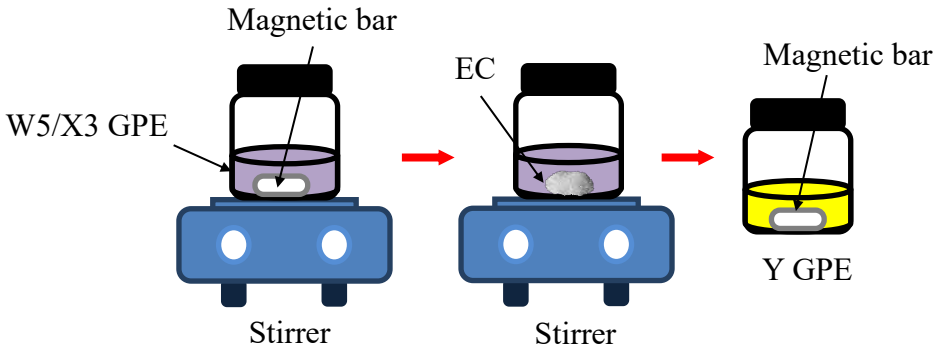

Figure 3.3: Preparation of GPE with various wt.% of EC.

Table 3.4: Composition of GPE with various wt.% of EC.

GPE	Distilled water (g)	PAAm-PAA (g)	Na_2S (g)	S (g)	EC (g)	Wt.%
X3/W5	2.0	0.896	0.624	0.064	0.000	0.0
Y1	2.0	0.896	0.624	0.064	0.007	0.2
Y2	2.0	0.896	0.624	0.064	0.014	0.4
Y3	2.0	0.896	0.624	0.064	0.022	0.6
Y4	2.0	0.896	0.624	0.064	0.029	0.8

3.2.4 Z System – Gel Polymer Electrolytes with Double Additives

GPE with double additive was prepared by dissolving KCl in the most conducting GPE from Y system, Y2, as illustrated in Figure 3.4. The amount of distilled water, PAAm-PAA, Na_2S, S and EC was fixed at 2.0 g, 0.896 g, 0.624 g, 0.064 g and 0.014 g, respectively. Appropriate mass of KCl was added to the GPE according to Table 3.5. The mass of KCl, M_{KCl} was calculated using Equation 3.1:

$$wt.\%\ of\ KCl = \frac{M_{KCl}}{(M_{KCl}+M_{water}+M_{PAAm-PAA}+M_{Na_2S}+M_S+M_{EC})}\ x\ 100\% \qquad (3.1)$$

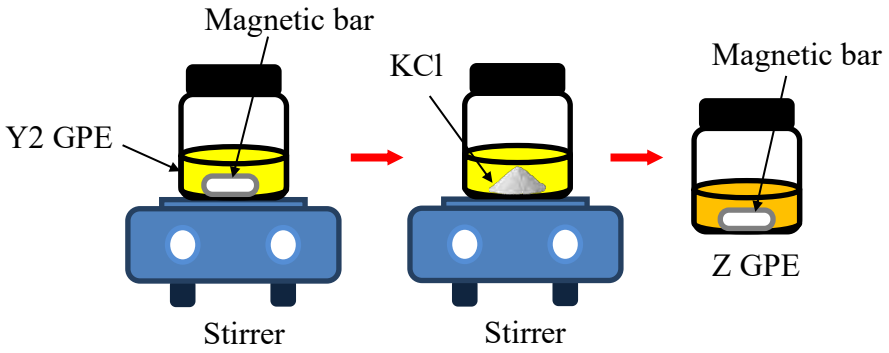

Figure 3.4: Preparation of GPE with various wt.% of KCl.

Table 3.5: Composition of GPE with various wt.% of KCl.

GPE	Distilled water (g)	PAAm-PAA (g)	Na_2S (g)	S (g)	EC (g)	KCl (g)	Wt.%
Y2	2.0	0.896	0.624	0.064	0.014	0.000	0.0
Z1	2.0	0.896	0.624	0.064	0.014	0.007	0.2
Z2	2.0	0.896	0.624	0.064	0.014	0.014	0.4
Z3	2.0	0.896	0.624	0.064	0.014	0.022	0.6
Z4	2.0	0.896	0.624	0.064	0.014	0.029	0.8

3.3 Characterization of Gel Polymer Electrolytes

The prepared GPEs will undergo characterization of Fourier transform infrared spectroscopy (FTIR) and electrochemical impedance spectroscopy (EIS).

3.3.1 Fourier Transform Infrared Spectroscopy

The Perkin Elmer Spectrum 100 FT-IR spectrometer was used to measure the structural studies of all GPE systems. The sample preparation was as described by section 3.2. The FTIR spectrum was acquired in absorbance mode with a resolution of 4 cm^{-1} in the wavenumber range from 550 to 4000 cm^{-1} (mid-infrared spectrum), as illustrated in Figure 3.5. Four regions were observed in the mid-infrared spectrum: (i) fingerprint (550 cm^{-1} to 1500 cm^{-1}), (ii) double bond (1500 cm^{-1} to 2000 cm^{-1}), (iii) triple bond (2000 cm^{-1} to 2500 cm^{-1}), and (iv) single bond (2500 cm^{-1} to 4000 cm^{-1}). Before running the samples at a FTIR scan number of 32, a background spectrum was recorded. FTIR deconvolution

method was done using Origin Pro 9.1 software with second-order derivatives to determine the hidden peaks and peak intensities. A Gaussian model was used in which maximum error associated with the simulated fits was within ±1%.

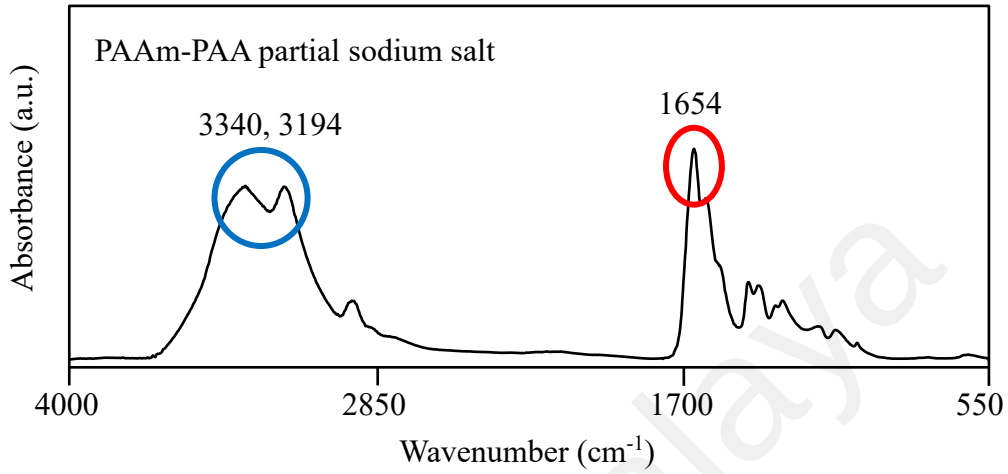

Figure 3.5: Infrared spectra of PAAm-PAA partial sodium salt.

Figure 3.5 depicts a schematic infrared spectrum of the polymer (PAAm-PAA partial sodium salt). From the infrared spectrum, we can identify functional groups and bonding between atoms by observing the peak positions (wavenumbers of the reference peaks). For example, we can observe characteristic peaks such as 3340 cm^{-1}, 3194 cm^{-1} and 1654 cm^{-1} in Figure 3.5. Depending on the wavenumber region, double peaks around 2500 cm^{-1} to 4000 cm^{-1} would indicate the possible presence of a N-H, a O-H or a C-H single bond, while the peak around 1500 cm^{-1} to 2000 cm^{-1} would indicate the possible presence of a C-O, a C-C or a C-N double bond. According to the literature, PAAm-PAA partial sodium salt has an amide functional group ($CONH_2$), which has both the N-H bond and C=O bond. Therefore, we can assign the peaks at 3340 cm^{-1}, 3194 cm^{-1} and 1654 cm^{-1} to asymmetric N-H bond, symmetric N-H bond and C=O bond, respectively. Peak shifts may occur after introduction of salt into polymer due to interactions between ions and functional groups. The peak shift can be redshift (towards lower frequency transition or shift to lower wavenumber) or blueshift (an increase in frequency or shift to higher

wavenumber). A peak shift in a small range like 20 cm^{-1} is acceptable. In addition, many peaks can be seen around 550 cm^{-1} to 1500 cm^{-1} (fingerprint region). Fingerprint region is a complex region showing many peaks and often overlapping each other. Another thing to observe from the infrared spectrum is the peak intensity. The higher the peak intensity, the stronger the functional groups associated with molecular bonds.

3.3.2 Electrochemical Impedance Spectroscopy

The HIOKI 3532 Z LCR Hi-tester was used to characterize all GPE systems for impedance studies and analysis. The sample preparation of EIS was shown in Figure 3.6. First, a coin cell was used to seal the GPE to prevent leakage. The stainless-steel blocking electrode was then used as a holder for the coin cell to run the EIS test. The coin cell was sandwiched between two electrodes separated by Teflon.

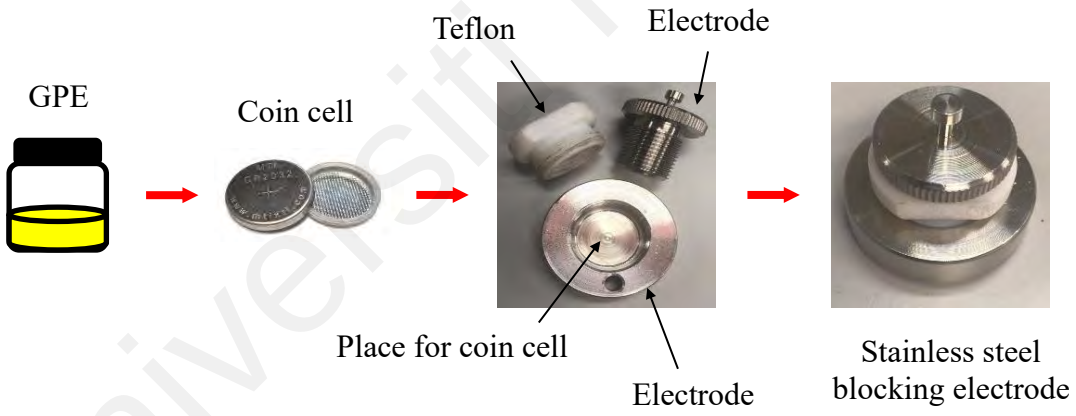

Figure 3.6: Sample preparation for impedance measurement.

The stainless-steel blocking electrode was connected to the HIOKI 3532 Z LCR Hi-tester for EIS measurement, as illustrated in Figure 3.7 (a). The impedance was measured in the range of 50 Hz to 5 MHz and generated a Nyquist plot. The Nyquist plot is a graph of negative imaginary impedance (-Z'') versus the real impedance (Z'), as shown in Figure 3.7 (b). Impedance parameters, such as bulk resistance (R_b) and ionic conductivity (σ), can be determined by the Nyquist plot. R_b is the value of Z' when -Z'' is zero, i.e., when

the Nyquist plot intersects the x-axis (see Figure 3.7 (a)), then σ can be calculated by Equation 3.2:

$$\sigma = \frac{t}{R_b A} \tag{3.2}$$

where t is the thickness of coin cell, and A is the surface area of coin cell which in contact to the stainless-steel electrode.

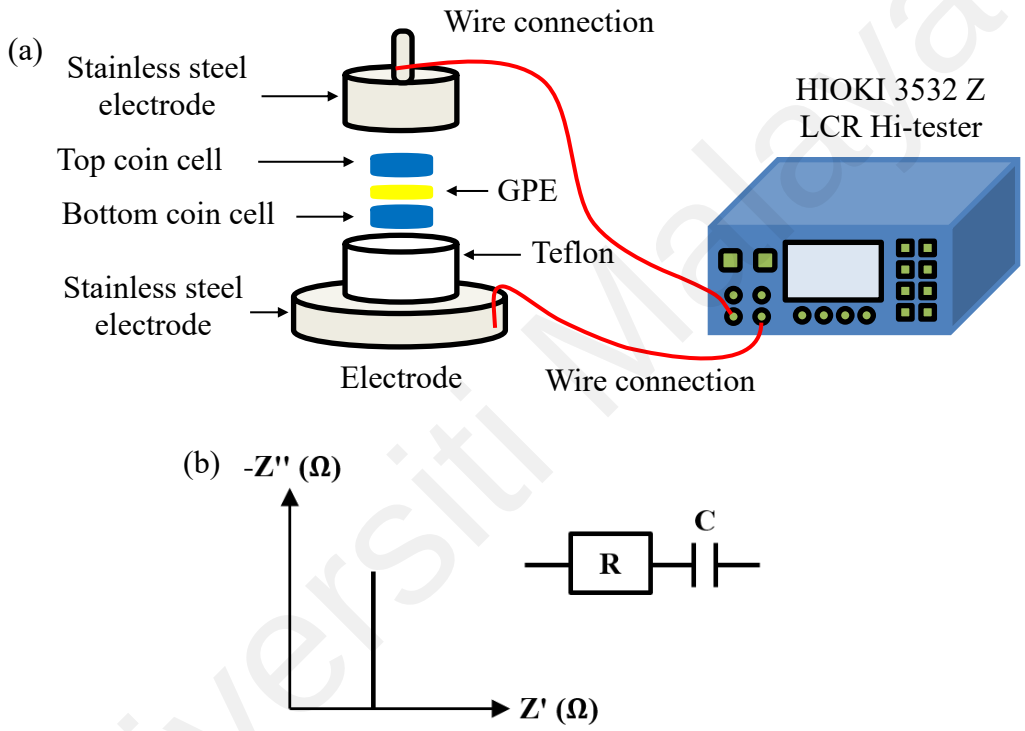

Figure 3.7: (a) Impedance measurement and (b) Nyquist plot and its equivalent circuit (R is resistor and C is capacitor).

3.4 Preparation of Electrodes

Figure 3.8 shows the images of (a) TiO_2/CdS/ZnS photoanode and (b) Pt CE. Photoanode is composed of TiO_2 compact layer (P90 TiO_2), TiO_2 mesoporous layer (P25 TiO_2), CdS QD sensitizer and ZnS passivation layer while CE is composed of platinum catalyst material.

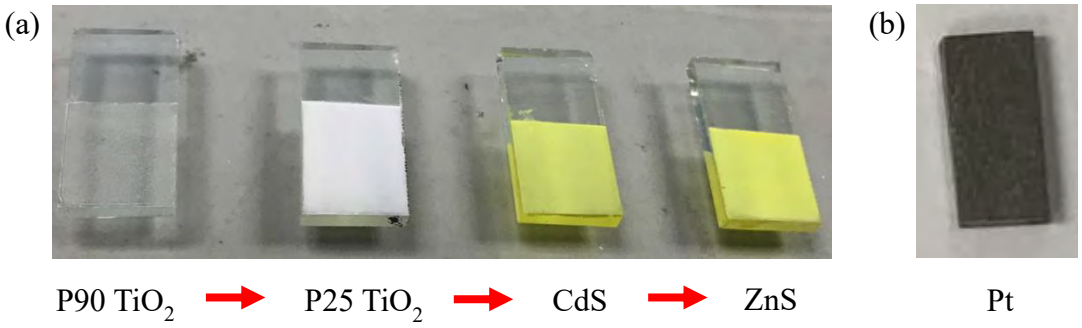

Figure 3.8: Images of (a) TiO_2/CdS/ZnS photoanode and (b) Pt counter electrode.

3.4.1 Titanium Dioxide Compact Layer

P90 TiO_2 has been used as the compact layer of the photoanode. First, 0.5 g of P90 TiO_2 was ground in an agate mortar for 30 mins and ground into a fine powder. P90 paste was prepared by mixing the fine powder in 2 mL HNO_3 (pH at 1) and continue to grind until a homogenous solution is formed, as illustrated in Figure 3.9. P90 paste was used to coat the first layer of the conductive surface of FTO glass.

Figure 3.9: Preparation of P90 TiO_2 paste.

Two deposition methods, spin coating and doctor blade, were used to coat P90 paste on FTO glass, as shown in Figure 3.10. After deposition, the samples were sintered in a furnace at 450 °C for 30 mins. The sintered samples were kept in the furnace until the furnace cooled down. Table 3.6 lists the designation of the electrodes for each deposition method used to prepare the P90 TiO_2 compact layer of the photoanode.

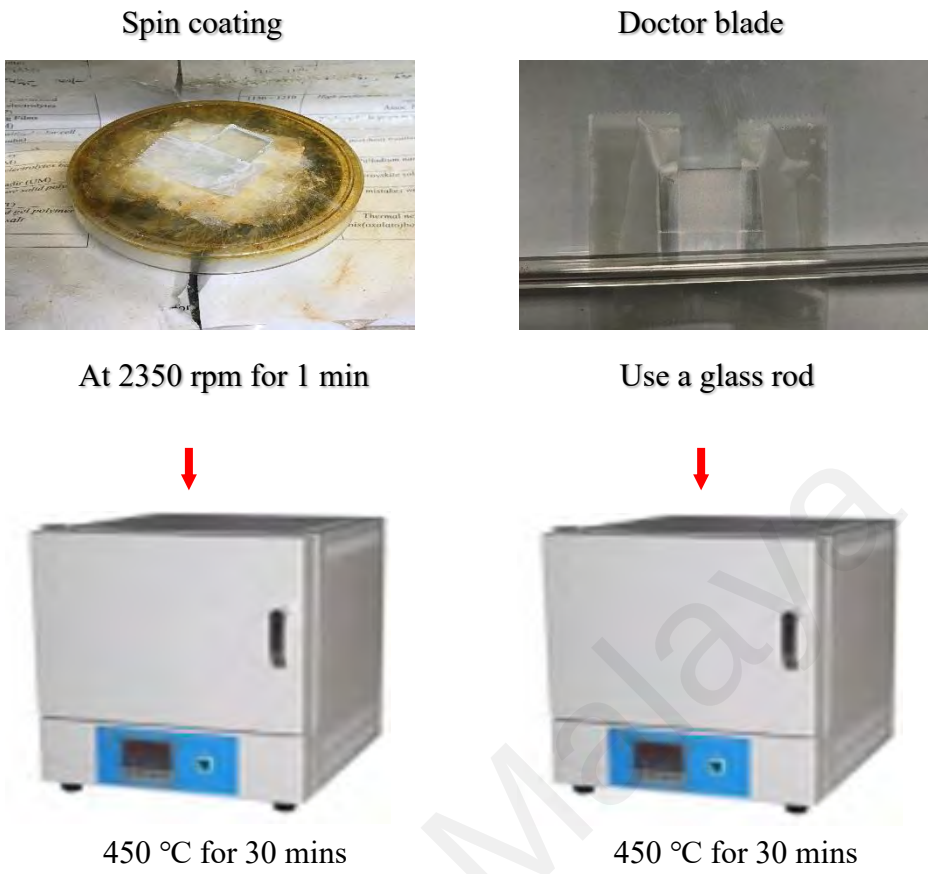

Figure 3.10: Deposition methods of P90 TiO_2 paste on the surface of FTO glass.

Table 3.6: Preparation of electrodes with TiO_2 compact layer.

Electrode	TiO_2 powder	Deposition method	Remarks
A1	P90	Spin coating	2350 rpm for 1 min
A2	P90	Doctor blade	A glass rod

3.4.2 Titanium Dioxide Mesoporous Layer

P25 TiO_2 has been used as the mesoporous layer of the photoanode. P25 paste was prepared by grinding 0.5 g of P25 TiO_2 into a fine powder and mixing it in 2 mL of HNO_3 (pH at 1). Then, 0.25 g of PEG and 2 drops of Triton X-100 were added to the mixture in sequence. The P25 paste was continuously ground into a homogenous solution, as illustrated in Figure 3.11. P25 paste was used to coat the second layer of the conductive surface of FTO glass.

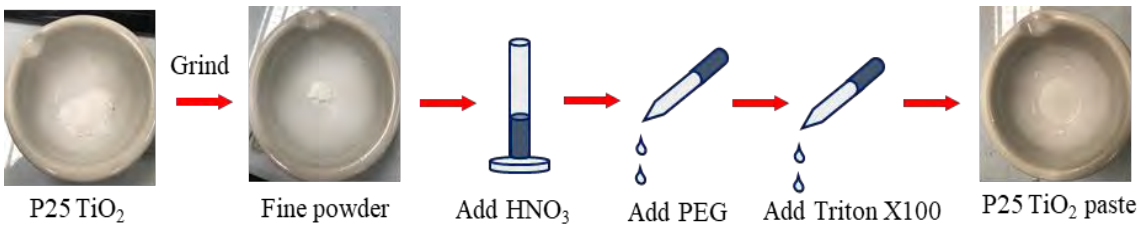

Figure 3.11: Preparation of P25 TiO_2 paste.

Doctor blade was used to coat P25 paste on FTO glass, as shown in Figure 3.12. The coated sample was sintered in a furnace at 450 ℃ for 30 mins and kept in the furnace until the furnace temperature was reduced to room temperature. Table 3.7 lists the designation of the electrodes coated with a P25 TiO_2 mesoporous layer (with or without a TiO_2 compact layer) on the electrode surface.

Figure 3.12: Deposition method of P25 TiO_2 paste on the surface of FTO glass.

Table 3.7: Preparation of electrodes with TiO_2 mesoporous layer.

Electrode	TiO_2 powder	Deposition methods
B1	P25	Doctor blade
B2	P90 + P25	Doctor blade + Doctor blade
B3	P90 + P25	Spin coating + Doctor blade

3.4.3 Cadmium Sulfide Quantum Dot Sensitizer

CdS was used as a QD sensitizer for TiO_2 electrode. The sensitization of CdS QD was done by the SILAR method. In SILAR, cationic and anionic precursors were prepared as dipping solutions. 0.1 M $Cd(NO_3)_2$ was dissolved in ethanol/water solution as the cationic

precursor, while the anionic precursor was prepared by dissolving 0.1 M Na_2S in methanol/water solution. The alcohol/water solution was prepared in a volume ratio of 7:3. First, the TiO_2 electrode was immersed in the cationic precursor (Cd^{2+}) for 1 min, rinsed and dried. Then, the TiO_2 electrode was immersed in the anionic precursor (S^{2-}) for 1 min, rinsed and dried. As shown in Figure 3.13, when the TiO_2 electrode has completed immersion in the two solutions, the SILAR process was considered complete. It was called the SILAR cycle. Five SILAR cycles were carried out for the sensitization of CdS QD on the TiO_2 electrode.

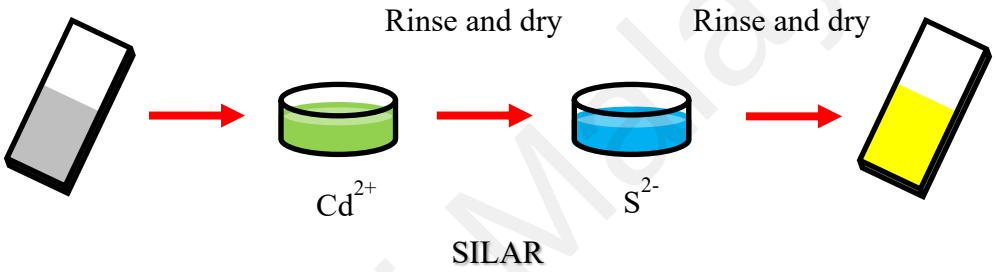

Figure 3.13: Chemical synthesis of CdS QD via SILAR.

3.4.4 Zinc Sulfide Passivation Layer

ZnS was used as the passivation layer of the TiO_2/CdS photoanode, and the passivation was done by the SILAR method. The cationic precursor was prepared by dissolving 0.1 M $Zn(CH_3COO)_2$ in ethanol/water solution, and the anionic precursor was prepared by dissolving 0.1 M Na_2S in methanol/water solution. The volume ratio of alcohol/water solution was 7:3. As shown in Figure 3.14, the TiO_2/CdS photoanode was immersed in the cationic precursor (Zn^{2+}) for 1 min, rinsed and dried, and then immersed in the anionic precursor (S^{2-}) for 1 min, rinsed and dried. Two SILAR cycles were carried out for the passivation of ZnS QD on the TiO_2/CdS photoanode.

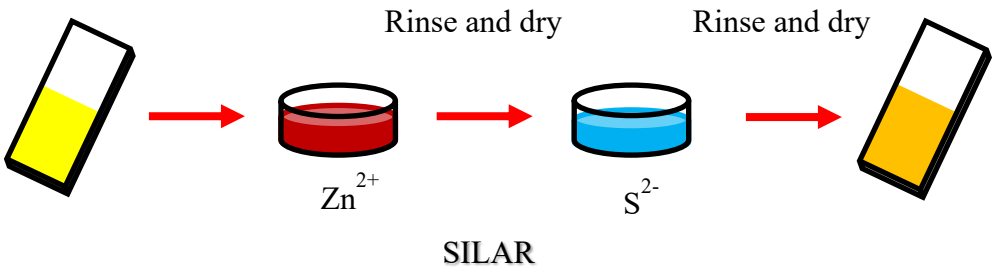

Figure 3.14: Chemical synthesis of ZnS QD via SILAR.

3.4.5 Platinum Counter Electrode

Pt was used as the catalyst material for CE. Pt CE was prepared by brush painting method, as illustrated in Figure 3.15. A dropper was used to drop the Plastisol solution onto the FTO glass on a 150 ℃ hot plate, and then brush the Plastisol solution to make the Plastisol solution evenly distributed on the FTO glass. The sample was sintered in a furnace at 450 ℃ for 30 mins.

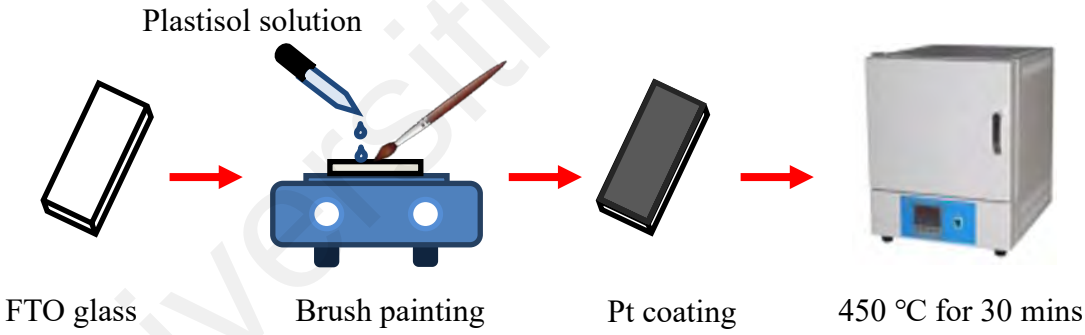

Figure 3.15: Brush painting of Plastisol solution on the surface of FTO glass.

3.5 Fabrication of QDSSC

The QDSSC was assembled by sandwiched GPE in between TiO_2/CdS/ZnS photoanode and Pt CE, as demonstrated in Figure 3.16.

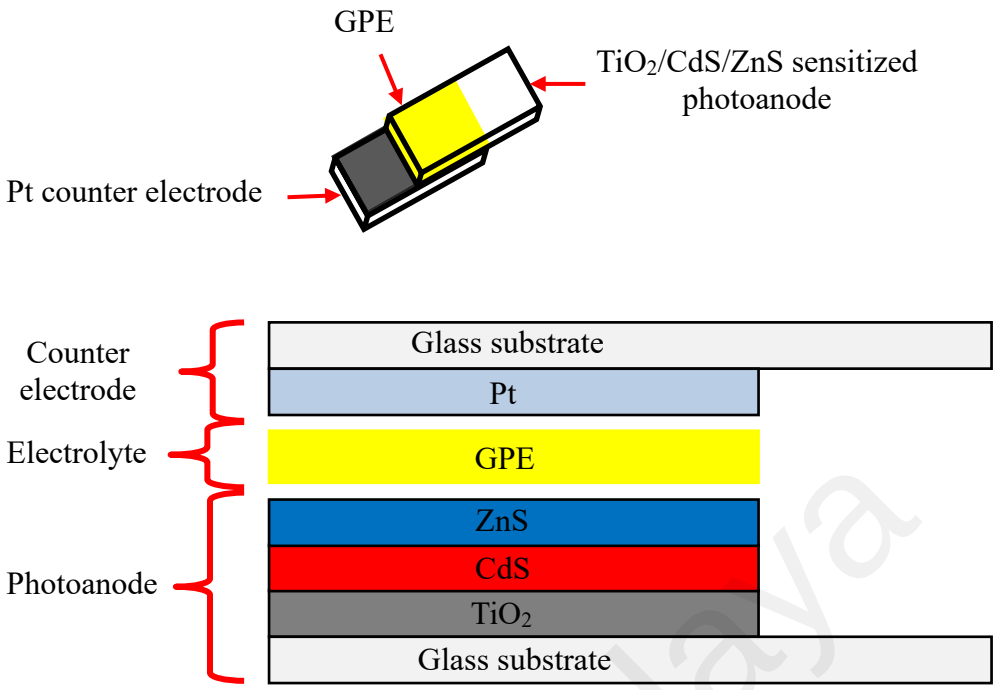

Figure 3.16: Assembly of QDSSC.

3.6 Characterization of QDSSC

The prepared TiO_2 electrode and TiO_2/CdS/ZnS photoanode will undergo characterization of field-emission scanning electron microscopy (FESEM), energy dispersive X-ray spectroscope (EDX) and X-ray diffractometer (XRD); while the prepared QDSSC undergo characterization of photocurrent density-voltage (*J-V*) and electrochemical impedance spectroscopy (EIS).

3.6.1 Field-Emission Scanning Electron Microscopy

Carl Zeiss AURIGA FESEM was used to examine the surface morphology and thickness measurement of TiO_2 compact layer. The sample preparation has been described in section 3.4.1 and 3.4.2.

For TiO_2/CdS/ZnS photoanode, the surface morphology was examined by FEI Quanta 450 FEG FESEM. The sample was prepared in four steps, as follows.

1. Spin coat the P90 paste on FTO glass at a spinning speed of 2350 rpm for 1 min, and then sinter it in a furnace at 450 ℃ for 30 mins (as described in section 3.4.1).
2. Doctor blade the P25 paste on the as-prepared P90 TiO_2 compact layer and sinter it in a furnace at 450 ℃ for 30 mins (as described in section 3.4.2).
3. Sensitize CdS QD on the as-prepared P90 TiO_2/P25 TiO_2 electrode via five SILAR cycles, with the precursors prepared as described in section 3.4.3.
4. Sensitize ZnS QD on the as-prepared TiO_2/CdS photoanode via two SILAR cycles, with the precursors prepared as described in section 3.4.4.

3.6.2 Energy Dispersive X-Ray Spectroscope

The elemental analysis of TiO_2/CdS/ZnS photoanode was examined by FEI Quanta 450 FEG EDX. The sample preparation has been described in section 3.6.1.

3.6.3 X-Ray Diffractometer

The crystalline structure of TiO_2/CdS/ZnS photoanode was examined by PANalytical Empyrean XRD. The radiation of Cu Kα was used and applied at acceleration currency of 40 mA and accelerating voltage of 40 kV. The degree of scan was ranged from 5° to 120°. The sample preparation has been described in section 3.6.1.

3.6.4 Photocurrent Density-Voltage

The potentiostat-galvanostat device (models PGSTAT128N, FRA32M, Metrohm Autolab Malaysia) was used to examine the photocurrent density-voltage (*J-V*) performance of QDSSC. *J-V* was characterized under light with an intensity of 100 $mW \cdot cm^{-2}$, which was generated by the Oriel solar simulator LCS-100 (Irvine, California), as shown in Figure 3.17. The sample preparation was as demonstrated in section 3.5.

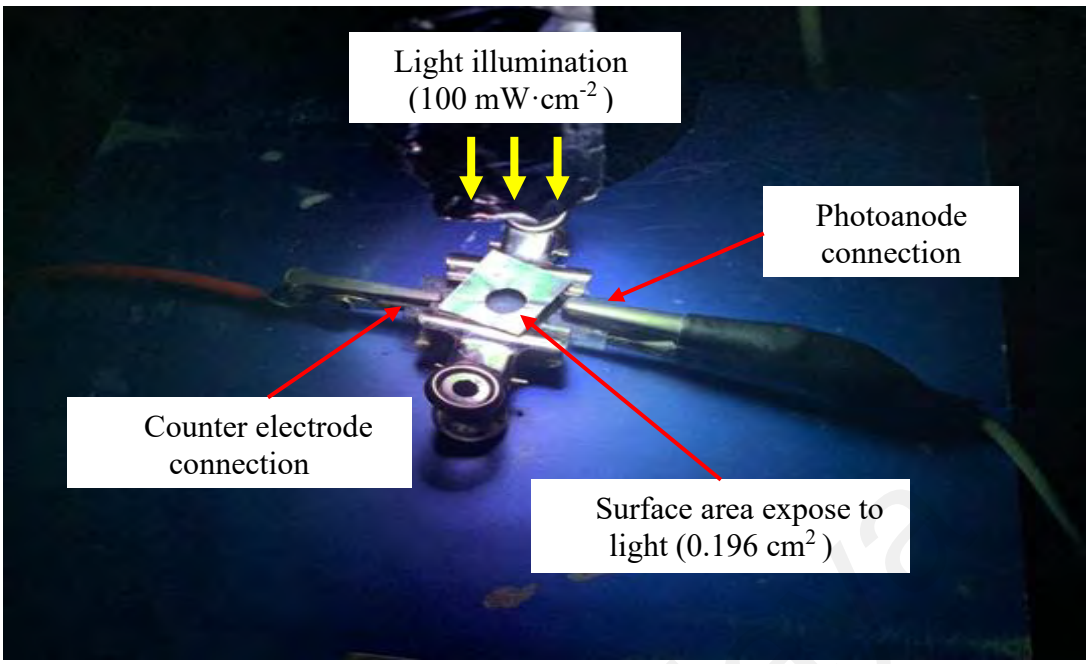

Figure 3.17: Photocurrent density-voltage (*J-V*) characterization of QDSSC.

The *J-V* curve of QDSSC was recorded to determine the open-circuit voltage (V_{oc}), short-circuit current density (J_{sc}), fill factor (FF) and power conversion efficiency (PCE), as shown in Figure 3.18. Both V_{oc} and J_{sc} were obtained from the *J-V* curve while FF and PCE were calculated using Equation 3.3 and 3.4, respectively.

$$FF = \frac{J_{max} \times V_{max}}{J_{sc} \times V_{oc}} \tag{3.3}$$

$$\text{PCE} = \frac{J_{sc} \times V_{oc} \times FF}{P_{in}} \tag{3.4}$$

where J_{max} is maximum power output of current density, V_{max} is maximum power output of voltage, and P_{in} is input of power density.

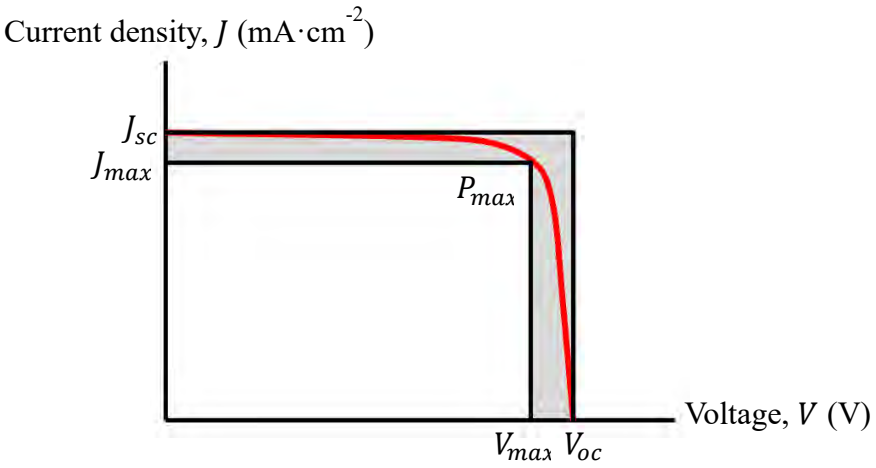

Figure 3.18: Photocurrent density-voltage (*J-V*) curve of QDSSC.

3.6.5 Electrochemical Impedance Spectroscopy

The electrochemical impedance measurement of QDSSC was examined by AUT 85988 advanced electrochemical system of Metrohm Autolab device. The sample preparation was as demonstrated in section 3.5. The impedance plot of QDSSC was measured under light with a frequency of 10 mHz to 100 kHz.

CHAPTER 4: STRUCTURAL PROPERTIES OF GEL POLYMER ELECTROLYTE

4.1 Introduction

Infrared (IR) characterization was performed to identify the interaction between solvent (distilled water), salt (Na_2S/S), polymer host (PAAm-PAA), and additives (EC and KCl) in the GPE system. In this chapter, the interaction between (i) Na_2S and distilled water, (ii) Na_2S aqueous solution and PAAm-PAA, (iii) PAAm-PAA-Na_2S GPE and EC, (iv) PAAm-PAA-Na_2S-EC GPE and KCl will be revealed by observing the changes of shape, intensity and peak position of each infrared spectrum. The functional amide (-$CONH_2$) and carboxylate (COO^-) groups in PAAm-PAA, the alcohol OH group in distilled water, and the carbonyl C=O group in EC are studied to determine whether the complexation has occurred between the polymer host, solvent and additives. In addition, they can also be complexed with Na_2S salts. The competition between PAAm-PAA, distilled water and EC to form a complex with Na_2S salt will be explored.

4.2 W System – Gel Polymer Electrolytes with Various Wt.% of Polymer Host

4.2.1 Structural Properties of Polysulfide Electrolyte

Figure 4.1 depicts the infrared spectrum of (a) distilled water, (b) $Na_2S{\cdot}nH_2O$, (c) S and (d) W0 (polysulfide electrolyte) in the region between 550 to 4000 cm^{-1}. The polysulfide electrolyte is a solution composed of S^{2-}/S_n^{2-} redox couple. A simple way to prepare S^{2-}/S_n^{2-} redox electrolyte is to add Na_2S and S to distilled water (Baharun et al., 2020; Lee et al., 2020; Lee & Chang, 2008; Mingsukang et al., 2017a). The chemical structures of distilled water, $Na_2S{\cdot}nH_2O$ and S are given as inset in Figure 4.1. In this thesis, the W0 was prepared by adding 4 M Na_2S and 1 M S to distilled water. The alcohol (OH) bands of distilled water are observed at 3383 cm^{-1} (O-H stretching) and 1644 cm^{-1} (O-H bending). According to the chemical structure of Na_2S and S, vibration bands should not be detected because they only contain S-S stretching that occurs in the region

between 502 and 528 cm^{-1} (Nyquist, 2001). Unexpectedly, the alcohol (OH) band and sulfate (SO_4^{2-}) group are observed in the spectrum, such as the O-H stretching at 3142 cm^{-1}, S=O stretching at 1430 cm^{-1}, tertiary asymmetric stretching mode (v_3) of SO_4^{2-} at 1273 cm^{-1}, v_3 SO_4^{2-} at 1135 cm^{-1}, primary symmetric stretching mode (v_1) of SO_4^{2-} at 970 cm^{-1} and asymmetric bending mode (v_4) of SO_4^{2-} at 612 cm^{-1} (Ben Mabrouk et al., 2013; Chasan & Norwitz, 1969; Doyen & Frech, 1996; Lane, 2007; Luo et al., 2002).

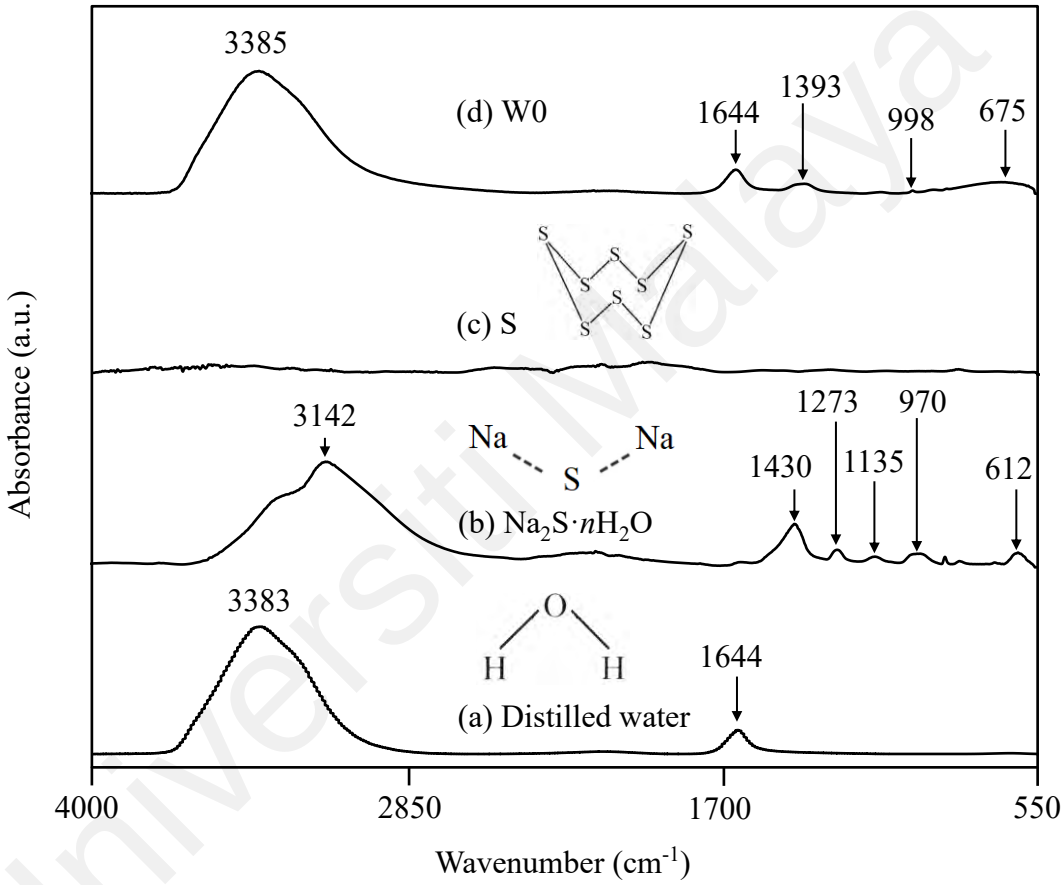

Figure 4.1: Infrared spectra of (a) distilled water, (b) $Na_2S{\cdot}nH_2O$, (c) S and (d) W0 (polysulfide electrolyte) in the region between 550 and 4000 cm^{-1}.

The Na_2S sample discussed here is the hydrated form of yellow flake, sodium sulfide hydrate, $Na_2S{\cdot}nH_2O$ where n = 1-9. Therefore, the O-H group has been detected. From the literature review, Na_2S has high hygroscopicity and chemical instability. When Na_2S was exposed to humid air, it will absorb moisture, and its hydrate will release hydrogen

sulfide, the oxygen atoms from the atmosphere will react with Na_2S to form sodium sulfate (Na_2SO_4) and water as shown follows,

$$2\ Na_2S\ (aq) + 3\ O_2\ (g) \rightarrow 2\ Na_2O\ (s) + 2\ SO_2\ (g) \quad (4.1)$$

$$2\ SO_2\ (g) + O_2\ (g) + 2\ H_2O\ (l) \rightarrow 2\ H_2SO_4\ (aq) \quad (4.2)$$

$$H_2SO_4\ (aq) + Na_2O\ (s) \rightarrow Na_2SO_4\ (aq) + H_2O\ (l) \quad (4.3)$$

$$\text{Overall reaction: } 2\ Na_2S{\cdot}nH_2O\ (aq) + 4\ O_2(g) \rightarrow 2\ Na_2SO_4\ (aq) + 2n\ H_2O\ (l) \quad (4.4)$$

We propose that the sodium cations would be initially dissociated when $Na_2S{\cdot}nH_2O$ reacts with oxygen to produce sodium oxide, Na_2O and sulfur dioxide, SO_2. The produced SO_2 reacts with the water (which is dissociated from $Na_2S{\cdot}nH_2O$) and oxygen gas to generate sulfuric acid, H_2SO_4. The H_2SO_4 would further react with Na_2O to produce sodium sulfate, Na_2SO_4 and water. In other words, the oxygen atoms in the hydrate of $Na_2S{\cdot}nH_2O$ can also react with the sulfur atoms in $Na_2S{\cdot}nH_2O$, hence it can be deduced that despite the S^{2-} anion, SO_4^{2-} is also the anion in $Na_2S{\cdot}nH_2O$. This explains why S=O and SO_4^{2-} IR bands have been observed in the spectrum of $Na_2S{\cdot}nH_2O$ (Nash, 1988; Roelands et al., 2015; Siriwardane & Woodruff, 1997).

Table 4.1 lists the peaks and assignments belonging to distilled water, $Na_2S{\cdot}nH_2O$ and W0 obtained from Figure 4.1. The O-H bands of W0 are observed at 3385 cm^{-1} which is denoted as O-H stretching and 1644 cm^{-1} which is assigned as O-H bending. The O-H stretching in the electrolyte demonstrates an upward shifting from 3383 cm^{-1} whereas the O-H bending remains unchanged. Besides, the S=O stretching of W0 is observed at 1393 cm^{-1}, red shift from 1430 cm^{-1} of $Na_2S{\cdot}nH_2O$ with a reduction of 28.5% in the peak intensity, as shown in Figure 4.2. The histogram in Figure 4.2 inset shows the percentage area for S=O stretching of $Na_2S{\cdot}nH_2O$ and polysulfide electrolyte from the FTIR

deconvolution method. In addition, the SO_4^{2-} bands of W0 are observed at 998 cm^{-1} (symmetric stretching, v_1) and 675 cm^{-1} (asymmetric bending, v_4), blue shift from 970 cm^{-1} and 612 cm^{-1}, respectively. The reduction in peak intensity and bands' shifting reveal that the Na^+ cations are bonded to the alcohol O-H band of water and form an O-Na^+ complex (Kumar et al., 2022). This shows that an interaction has occurred between distilled water (solvent) and Na_2S (salt).

Table 4.1: Assignment of IR spectra for distilled water, $Na_2S \cdot nH_2O$ and W0.

Wavenumber (cm^{-1})			Assignment	Reference
H_2O	**$Na_2S \cdot nH_2O$**	**W0**		
3383	3142	3385	O-H stretching	(Mojet et al., 2010; Ping et al., 2001)
1644	-	1644	O-H bending	(Mojet et al., 2010; Ping et al., 2001)
-	1430	1393	S=O stretching	(Luo et al., 2002)
-	1273	-	Asymmetric SO_4^{2-} stretching	(Lane, 2007)
-	1135	-	Asymmetric SO_4^{2-} stretching	(Lane, 2007)
-	970	998	Symmetric SO_4^{2-} stretching	(Ben Mabrouk et al., 2013; Chasan & Norwitz, 1969; Doyen & Frech, 1996; Lane, 2007)
-	612	675	Asymmetric SO_4^{2-} bending	(Lane, 2007)

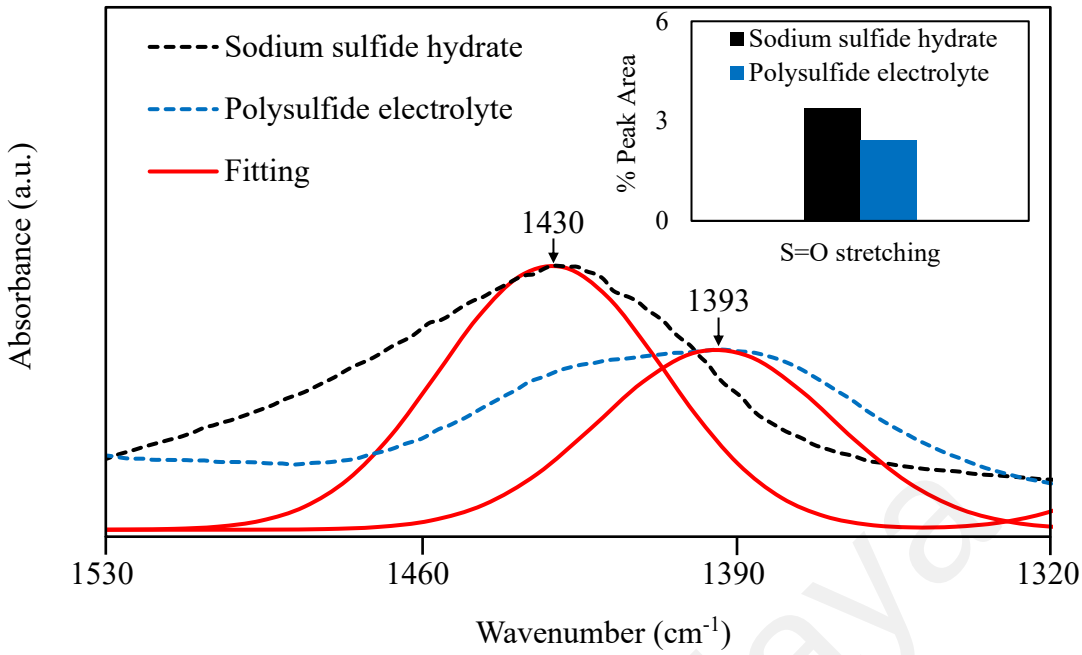

Figure 4.2: Deconvolution of FTIR region of 1320 to 1530 cm^{-1}. The inset shows the relative FTIR band percentage area of S=O stretching of $Na_2S \cdot nH_2O$ and polysulfide electrolyte.

4.2.2 Structural Properties of PAAm-PAA Partial Sodium Salt and System W

In system W, by adding 5 to 35 wt.% of PAAm-PAA to the polysulfide electrolyte (W0), the molecular interactions between Na_2S and PAAm-PAA, and between distilled water and PAAm-PAA are studied. PAAm-PAA is a copolymer composed of acrylamide and acrylic acid, which contain amide ($-CONH_2$) and carboxylic acid (COOH) functional groups. The PAAm-PAA sample discussed here is PAAm-PAA partial sodium salt, as shown in Figure 4.3. Therefore, carboxylate (COO^-) group has been detected instead of COOH group. The chemical structure of PAAm-PAA partial sodium salt is given as inset in Figure 4.3. Based on the chemical structure, PAAm-PAA partial sodium salt contains possible stretching modes, such as NH_2, N-H, C-N, COO^-, C=O, CH_2, C-H and C-C.

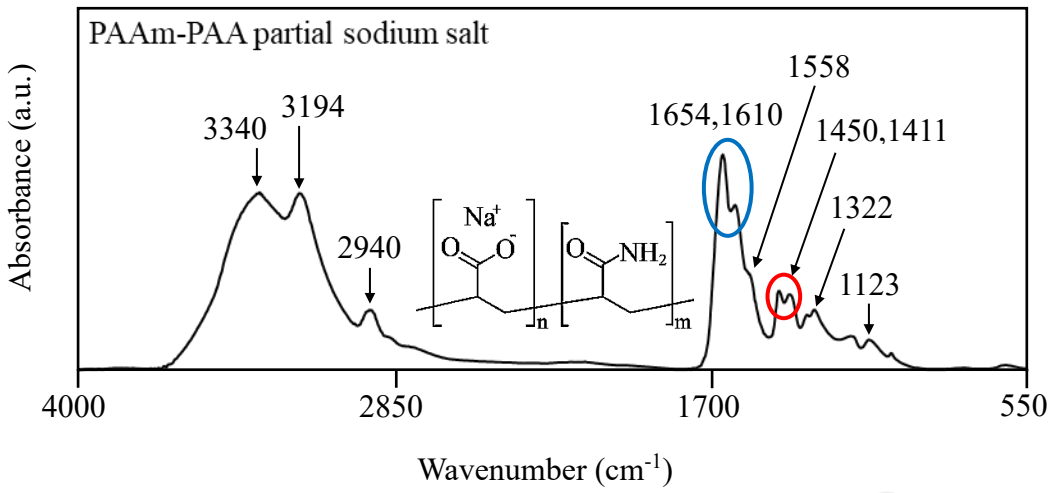

Figure 4.3: Infrared spectra of PAAm-PAA partial sodium salt in the region between 550 and 4000 cm^{-1}.

Table 4.2 lists the peaks and assignments belonging to PAAm-PAA partial sodium salt obtained from Figure 4.3. The NH_2 bands of PAAm-PAA partial sodium salt are observed at 3340 cm^{-1} (asymmetric NH_2 stretching), 3194 cm^{-1} (symmetric NH_2 stretching), 1610 cm^{-1} (N-H bending), 1411 cm^{-1} (C-N stretching) and 1123 cm^{-1} (N-H rocking) (Bashir et al., 2017; Deng et al., 2006; Estrada et al., 2020; Jing et al., 2019; Lu & Mi, 2005; Magalhães et al., 2012; Nesrinne & Djamel, 2017). Other than NH_2 bands, C=O stretching of amide group (-$CONH_2$) is observed at 1654 cm^{-1} (Chiem et al., 2006; Deng et al., 2006; Estrada et al., 2020; Lu & Mi, 2005; Magalhães et al., 2012). Meanwhile, the COO^- bands of PAAm-PAA partial sodium salt are observed at 1558 cm^{-1} (asymmetric COO^- stretching) and 1411 cm^{-1} (symmetric COO^- stretching) (Jones & McLaren, 1954; Magalhães et al., 2012). The CH_2 bands of PAAm-PAA partial sodium salt are observed at 2940 cm^{-1} (CH_2 stretching), 1450 cm^{-1} (CH_2 bending) and 1322 cm^{-1} (C-H bending) (Deng et al., 2006; Estrada et al., 2020; Jones & McLaren, 1954; Lu & Mi, 2005; Magalhães et al., 2012). As reported (Chiem et al., 2006; Deng et al., 2006; Estrada et al., 2020; Jones & McLaren, 1954; Lu & Mi, 2005; Magalhães et al., 2012), the vibrational bands of $CONH_2$ and COO^- may overlap as PAAm-PAA partial sodium salt contains amide (-$CONH_2$) and carboxylate (COO^-) functional groups. The overlap of symmetric

COO^- stretching and C-N stretching is in the region of 1400 to 1425 cm^{-1}, as shown in Figure 4.4. The hidden peaks in the 1371 to 1485 cm^{-1} region are deconvoluted, and the peaks at 1452 cm^{-1}, 1421 cm^{-1} and 1400 cm^{-1} are attributed to CH_2 bending, C-N stretching and symmetric COO^- stretching, respectively. Therefore, it can be concluded that in this work, the symmetric COO^- stretching is superimposed with the C-N stretching at 1411 cm^{-1}.

Table 4.2: Assignment of IR spectra for PAAm-PAA.

Wavenumber (cm^{-1})	Assignment	Reference
3340	Asymmetric NH_2 stretching	(Deng et al., 2006; Lu & Mi, 2005; Magalhães et al., 2012)
3194	Symmetric NH_2 stretching	(Deng et al., 2006; Lu & Mi, 2005; Magalhães et al., 2012)
2940	CH_2 stretching	(Deng et al., 2006; Jones & McLaren, 1954; Lu & Mi, 2005; Magalhães et al., 2012; Rudolph et al., 2014)
1654	$CONH_2$ stretching	(Chiem et al., 2006; Deng et al., 2006; Lu & Mi, 2005; Magalhães et al., 2012)
1610	NH_2 bending	(Chiem et al., 2006; Deng et al., 2006; Lu & Mi, 2005)
1558	Asymmetric COO^- stretching	(Jones & McLaren, 1954; Magalhães et al., 2012)
1450	CH_2 bending	(Deng et al., 2006; Jones & McLaren, 1954; Lu & Mi, 2005)
1411	Symmetric COO^- stretching/ C-N stretching	(Chiem et al., 2006; Deng et al., 2006; Jones & McLaren, 1954; Lu & Mi, 2005; Magalhães et al., 2012)
1322	C-H bending	(Deng et al., 2006; Lu & Mi, 2005)
1123	N-H rocking	(Deng et al., 2006; Lu & Mi, 2005)

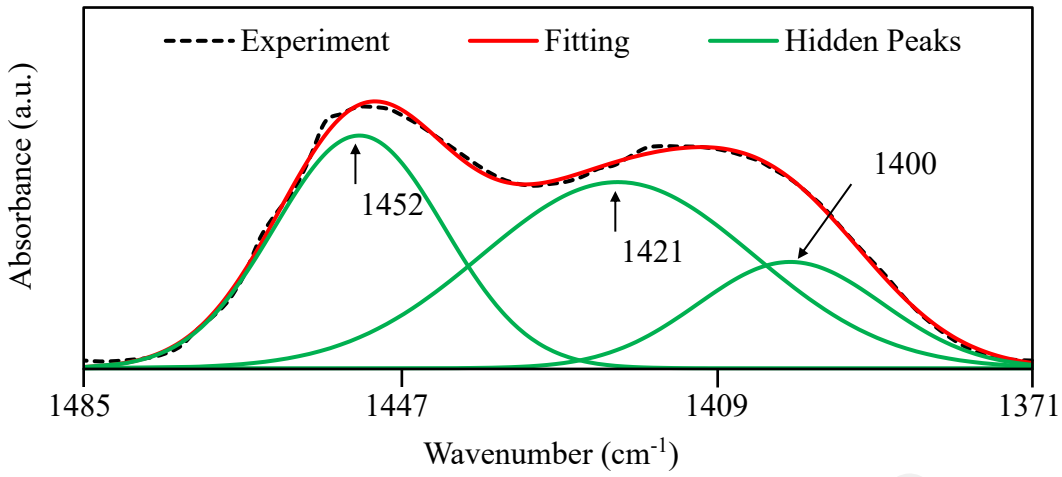

Figure 4.4: Deconvolution of FTIR region of 1371 to 1485 cm^{-1}.

From the literature review, it is possible for the alkali metal cation Na^+ of Na_2S to form a strong interaction with -$CONH_2$ and/or COO^- of PAAm-PAA. This is because carbonyl stretching (C=O bond) is found in both -$CONH_2$ and COO^-. In this way, Na^+ can interact with C=O either extending from an amide group or carboxylate group to form possible complex sites. Both functional groups are characteristic peaks in PAAm-PAA and could show a strong bond with Na_2S. Figure 4.5 depicts the infrared spectrum of PAAm-PAA-Na_2S GPE added with (a) 0 wt.% (W0) to (h) 35 wt.% (W7) PAAm-PAA in the region from 550 to 4000 cm^{-1}.

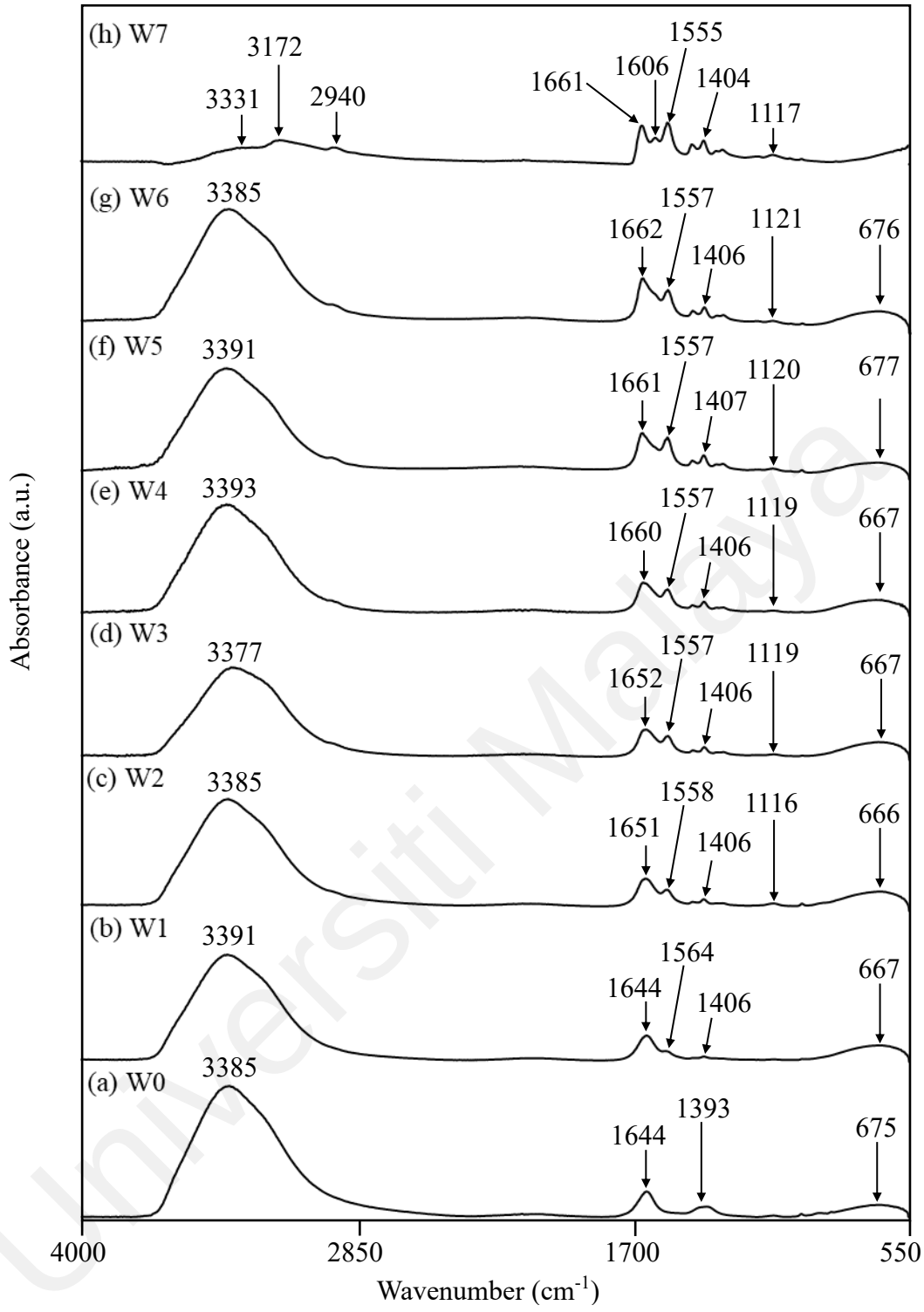

Figure 4.5: Infrared spectra of PAAm-PAA-Na_2S GPE added with (a) 0 wt.% (W0), (b) 5 wt.% (W1), (c) 10 wt.% (W2), (d) 15 wt.% (W3), (e) 20 wt.% (W4), (f) 25 wt.% (W5), (g) 30 wt.% (W6) and (h) 35 wt.% (W7) PAAm-PAA in the region between 550 and 4000 cm^{-1}.

Table 4.3: Assignment of IR spectra for PAAm-PAA-Na_2S GPE.

Assignment	Wavenumber (cm^{-1})							
	W0	**W1**	**W2**	**W3**	**W4**	**W5**	**W6**	**W7**
O-H stretching	3385	3391	3385	3377	3393	3391	3385	3331
Symmetric NH_2	-	-	-	-	-	-	-	3172
CH_2 stretching	-	-		-		-		2940
$CONH_2$ stretching	-	-	1651	1652	1660	1661	1662	1661
O-H bending	1644	1644	-	-	-	-	-	-
NH_2 bending	-	-	-	-	-	-	-	1606
Asymmetric COO^-	-	1564	1558	1557	1557	1557	1557	1555
Symmetric COO^-/ C-N stretching	-	1406	1406	1406	1406	1407	1406	1404
S=O stretching	1393	-	-	-	-	-	-	-
N-H rocking	-	-	1116	1119	1119	1120	1121	1117
Asymmetric SO_4^{2-} bending	675	667	666	667	667	677	676	-

In the spectrum of addition of 5 wt.% of PAAm-PAA (W1), the O-H bands are observed at 3391 cm^{-1} (O-H stretching) and 1644 cm^{-1} (O-H bending), upshifted from 3385 cm^{-1} and no shift from 1644 cm^{-1} of polysulfide electrolyte (W0), respectively. The v_4 SO_4^{2-} (asymmetric bending) of W1 is observed at 667 cm^{-1}, down-shifted from 675 cm^{-1} of W0. In addition, a shoulder peak at 1564 cm^{-1} (asymmetric COO^- stretching) and a new peak at 1406 cm^{-1} (symmetric COO^- stretching and/or C-N stretching), upshifted from 1558 cm^{-1} and down-shifted from 1411 cm^{-1} of PAAm-PAA (see Table 4.2), respectively, have been observed.

As the content of PAAm-PAA increases to 10 wt.% (W2), it is expected that more characteristic peaks from PAAm-PAA will be observed. This can be demonstrated by observing another new peak appears at 1116 cm^{-1} shifted from 1123 cm^{-1} (N-H rocking) of PAAm-PAA. In addition, by observing the change in peak shape and intensity, the peak at 1651 cm^{-1} in W2 is attributed to the overlapping of C=O of $CONH_2$ stretching of PAAm-PAA (shifted from 1654 cm^{-1}, refer to Figure 4.3) and O-H bending of water (shifted from 1644 cm^{-1}, refer to Figure 4.1). Similar finding was reported by Deng and

his coworkers (2006) that the overlap of the C=O stretching of amide and the O-H bending of water was detected in the region of 1651 to 1654 cm^{-1}. Figure 4.6 shows the deconvolution of hidden peaks in the region of 1591 to 1720 cm^{-1} of sample W2. The peaks observed at 1626 cm^{-1} and 1660 cm^{-1} are attributed to O-H bending and C=O of $CONH_2$, respectively. The O-H bending is superimposed with the C=O of $CONH_2$ at 1652 cm^{-1}. Therefore, it can be inferred that there is an interaction between distilled water (solvent) and PAAm-PAA (polymer host).

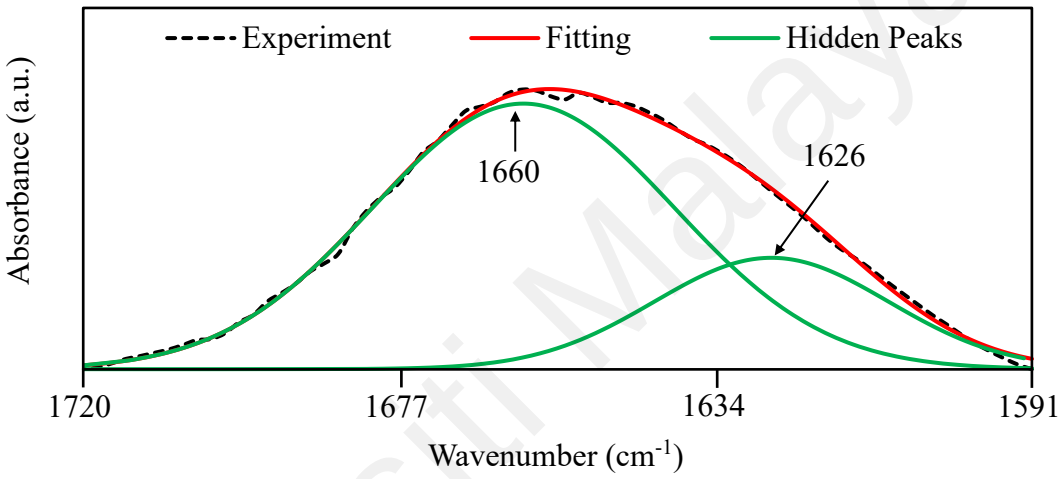

Figure 4.6: Deconvolution of FTIR region of 1591 to 1720 cm^{-1}.

On the other hand, the ν_4 SO_4^{2-} has upshifted from 667 cm^{-1} (W4, the GPE containing 20 wt.% of PAAm-PAA) to 677 cm^{-1} when 5 wt.% more of PAAm-PAA is added to the polysulfide electrolyte (W5). This indicates that Na_2S interacts with the copolymers. It is possible that the oxygen atom in the sulfate group interacts with the hydrogen atom and/or Na^+ cation from the PAAm-PAA.

At higher PAAm-PAA content (W7 or 35 wt.%), new peaks appear at 3172 cm^{-1} (NH_2 stretching), 2940 cm^{-1} (CH_2 stretching) and 1606 cm^{-1} (NH_2 bending) are down-shifted from 3194 cm^{-1}, maintain at 2940 cm^{-1} and down-shifted from 1610 cm^{-1} of PAAm-PAA, respectively. Besides, the O-H stretching of W7 is observed at 3331 cm^{-1}, down-shifted

from 3385 cm^{-1} of W0. All these changes indicate that there must be interaction between PAAm-PAA and distilled water, and between PAAm-PAA and Na_2S.

All the peaks have been summarized on a comparison table. Referring to Table 4.3, major shifting in the wavenumber of alcohol O-H, amide C=O of $CONH_2$, asymmetric COO^- stretching and v_4 SO_4^{2-} bands have been observed.

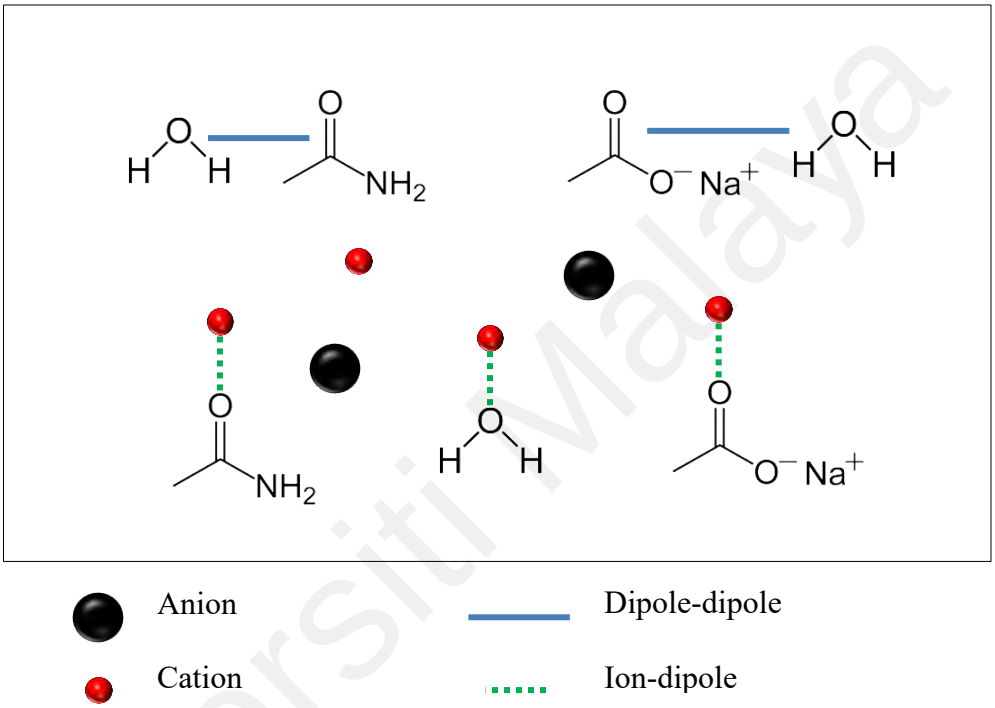

Figure 4.7: Schematic diagram of possible dipole-dipole and ion-dipole in system W.

In this system, the hydrogen atom in hydroxyl group of distilled water forms a dipole-dipole with oxygen atom in amide group of PAAm-PAA and oxygen atom in carboxylate group of PAAm-PAA. Meanwhile, Na^+ cation of Na_2S may form an ion-dipole with oxygen atom in amide group and/or carboxylate group of PAAm-PAA, as shown in Figure 4.7. This can be proven by the shift in the wavenumber of amide C=O of $CONH_2$ and asymmetric COO^- stretching bands (see Table 4.3). In addition, Na^+ cation of Na_2S could also forms an ion-dipole with oxygen atom in hydroxyl group of distilled water. This can be shown by the shift in the wavenumber of O-H band (refer to Figure 4.1). It

can be inferred that when the copolymer content increases, more interactions occur between copolymers and water molecules, and between copolymers and Na^+ cations.

In this work, the goal is to produce a GPE with high mechanical strength and dimensional stability at outdoor ambient temperature that can be easily cast into any profile for the design of solar cell devices. A simple test (i.e. recording the duration it takes for the GPE to reach the bottom by inverting the GPE container) has been performed to study the reverse flow rate of the GPE. Figure 4.8 shows the gelatinization of GPE using PAAm-PAA in system W. The texture of GPE changes from liquid to gel. The viscosity of GPE increased with the increase of PAAm-PAA content.

Figure 4.8: Texture of W0 (from left) to W7 GPE.

Table 4.4: Texture and duration of reverse flow of system W.

GPE	Texture	Duration of reverse flow (s)
W0	Liquid	< 1
W1	Liquid	< 1
W2	Liquid	≈ 1
W3	Quasi-solid	≈ 4
W4	Quasi-solid	≈ 22
W5	Quasi-solid	≈ 47
W6	Quasi-solid	> 150
W7	Solid	> 150

Table 4.4 lists the texture and reflow durations for system W. The duration it takes for the GPE to reach the bottom of the container is recorded in seconds. GPEs containing 10

wt.% or less PAAm-PAA (W0 to W2) require less than and/or equal to 1 s to reach the bottom of the container. Quasi-solid textures start at W3 and take 4 s to reach the bottom of the container. At higher PAAm-PAA content (W6 or 30 wt.%), the time to reach the bottom of the container exceeded 150 s. In the case of the W7, the GPE did not even start to flow in reverse after 150 s. The purpose of this experiment is to optimize GPE with slow but steady flow rates. Undoubtedly, the hasty electrolyte flow assists the rapid diffusion of charge carriers to produce efficient solar cells, however, the hasty electrolyte flow also means that the electrolyte is likely to leak, volatilize and fluctuate all the time, especially in outdoor environment at ambient temperature.

Quasi-solids are intermediates between liquids and solids. As the quasi-solid electrolyte becomes more liquid (i.e. GPE with 15 wt.% or less PAAm-PAA, W0 to W3), it inherits the hasty electrolyte flow, but may leak, volatilize and fluctuate. On the other hand, it inherits slow electrolyte flow but may have lower ionic conductivity when moving towards the solid state. The electrical properties of GPE are a vital element influencing device performance, hence GPEs containing 30 wt.% (W6) or more PAAm-PAA are not considered for further experiments. Besides, despite the electrical properties, dimensional stability at ambient temperature is also considered a consideration for good device performance. Among the W4 and W5 GPEs, W5 has been chosen as the optimized composition due to its slower electrolyte flow rate and better dimensional stability at moderate temperatures.

4.3 X System – Gel Polymer Electrolytes with Various Molarity of Salt

In the previous system W, the polysulfide electrolyte was prepared with a fixed molar salt content (4 M Na_2S and 1 M S). The optimized ratio of Na_2S aqueous solution and PAAm-PAA was finally determined to be 75:25 (W5, optimized GPE in system W). Therefore, in this system, a fixed amount of PAAm-PAA was used, while various molar

concentrations of Na_2S from 2 M to 6 M were added. It must be noted that in system X, the W5 GPE is designated as the X3 GPE. The Na_2S:S content is always fixed at 4:1 according to the literature (Baharun et al., 2020; Karageorgopoulos et al., 2012). Figure 4.9 shows the infrared spectrum of PAAm-PAA-Na_2S GPE added with (a) 2 M (X1) to (e) 6 M (X5) Na_2S in the region between 550 and 4000 cm^{-1}.

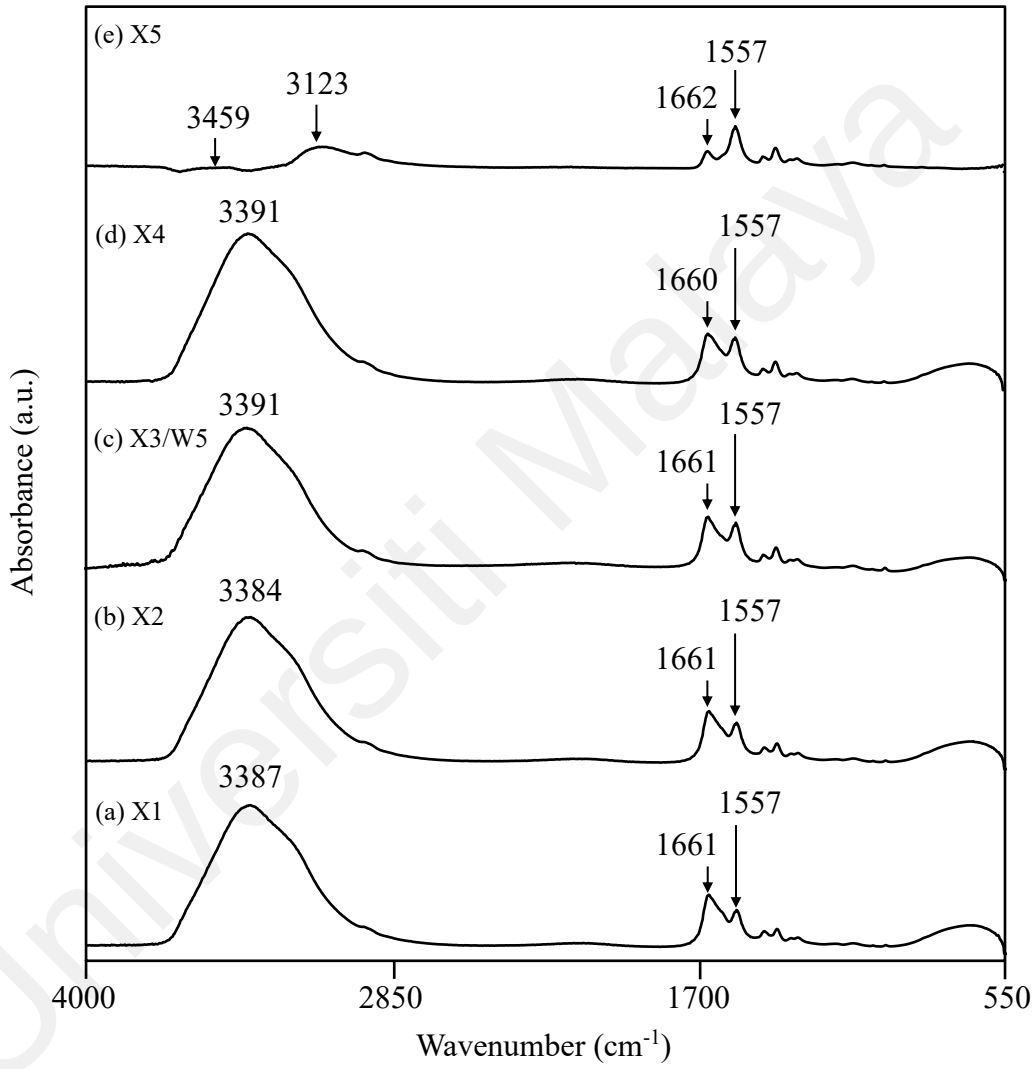

Figure 4.9: Infrared spectra of PAAm-PAA-Na_2S GPE added with (a) 2 M (X1), (b) 3 M (X2), (c) 4 M (X3/W5), (d) 5 M (X4) and (e) 6 M (X5) Na_2S in the region between 550 and 4000 cm^{-1}.

As for the GPE containing 1 M Na_2S (X1), the O-H stretching was observed at 3387 cm^{-1}, C=O of $CONH_2$ and/or O-H bending at 1661 cm^{-1}, and asymmetric COO^- stretching was found at 1557 cm^{-1}. No minimal change in peak position was observed, except for

O-H stretching which upshifted from 3384 cm^{-1} to 3391 cm^{-1} when 4 M more of Na_2S was added to PAAm-PAA-Na_2S GPE. This suggests that Na_2S interacts with water. At higher Na_2S content (X5 or 6 M), the O-H band is examined at 3459 cm^{-1}, blue shift from 3387 cm^{-1} of X1 with a reduction in the peak intensity. In addition, the band observed at 3123 cm^{-1} is attributed to symmetric NH_2 stretching of PAAm-PAA, down-shifted from 3194 cm^{-1} of PAAm-PAA.

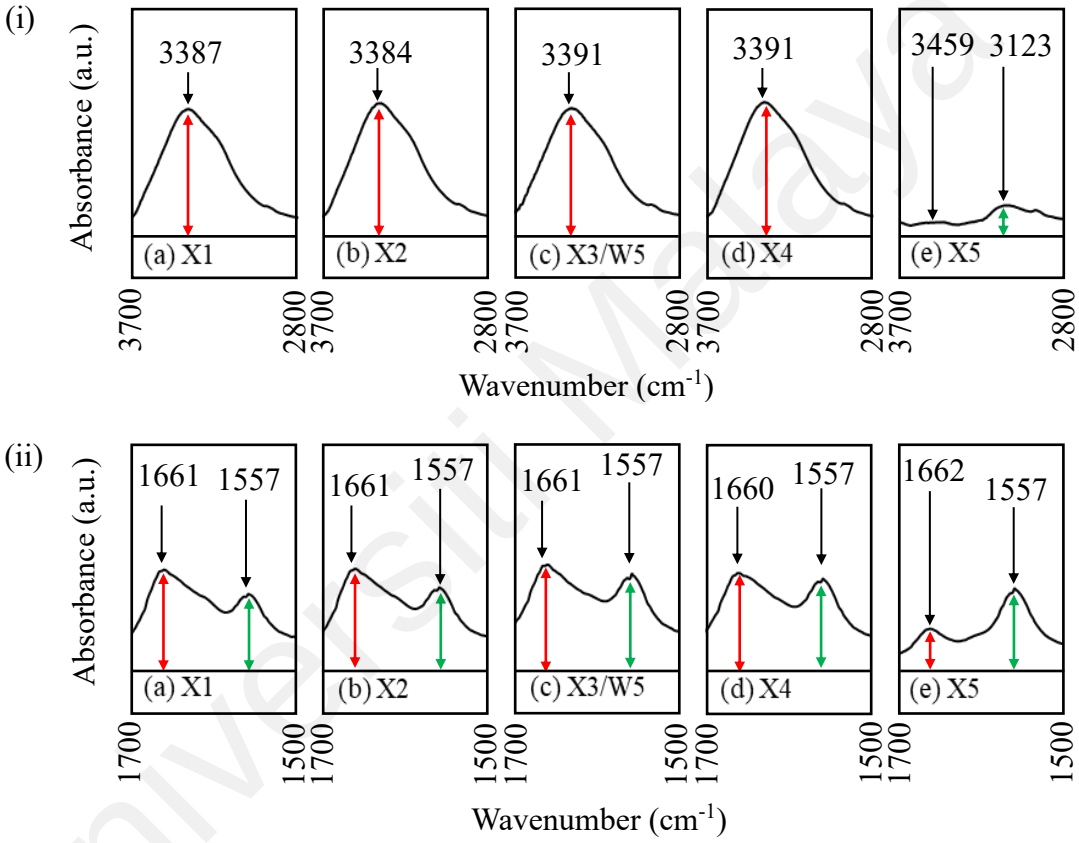

Figure 4.10: Magnified infrared spectra of PAAm-PAA-Na_2S GPE in the regions of (i) 2800 to 3700 cm^{-1} and (ii) 1500 to 1700 cm^{-1}.

In addition to the peak shifts, the peak intensities of the alcohol O-H, amide -$CONH_2$ and carboxylate COO^- bands were further discussed by observing the magnified infrared spectrum of system X in the region of (i) 2800 to 3700 cm^{-1} and (ii) 1500 to 1700 cm^{-1}, respectively, as shown in Figure 4.10. From the graph, a baseline (black line) is used to compare the peak intensities of alcohol, amide, carboxylate and sulfate groups. All graphs are plotted in absorbance units on the same scale. In Figure 4.10 (i), the peak intensity of

O-H stretching does not change significantly until after 5 M Na_2S or X4. Even if the O-H band position is blue-shifted, the band intensity decreases. Furthermore, the symmetric stretching peak of NH_2 appears at 3123 cm^{-1}. This indicates that the higher the molar concentration of Na_2S, the stronger the interaction between Na^+ cation and amine group of PAAm-PAA, thereby weakening the interaction between Na^+ cation and water.

It can be observed that the peak position of C=O of $CONH_2$ and/or O-H bending and asymmetric COO^- stretching do not change significantly, but the peak intensity decreases with the addition of Na_2S, which can be observed by comparing the height of the red and green arrow lines from each peak to the baseline in Figure 4.10 (ii). This suggests that copolymers interact with Na^+ cations.

4.4 Y System – Gel Polymer Electrolytes with Single Additive

EC is an organic compound and also known as cyclic carbonate (Gnanasambandam & Proctor, 2000; Lewis et al., 1994; Pazos et al., 2014). It was chosen as an additive to lubricate the coordination between PAAm-PAA and Na_2S because it can affect inter-chain and intra-chain arrangement in the PAAm-PAA-Na_2S GPE. PAAm-PAA contains $CONH_2$ and COO^- groups (Bashir et al., 2017; Jing et al., 2019; Nesrinne & Djamel, 2017), where EC also contains a carbonyl (C=O) group (Woo et al., 2013), which makes both PAAm-PAA and EC form complexes with sulfide salts. Figure 4.11 depicts the infrared spectrum of pure EC in the region of 550 to 1900 cm^{-1}. The chemical formula of EC is $C_3H_4O_3$, given as an inset in Figure 4.11. EC contain possible stretching modes such as C=O stretching, CH_2 stretching and ring stretching.

Refer to Figure 4.11, the C=O bands of EC are observed at 1797 cm^{-1} (C=O stretching), 1771 cm^{-1} (C=O stretching) and 715 cm^{-1} (C=O bending). Meanwhile, the CH_2 bands of EC are observed at 1553 cm^{-1} (CH_2 scissoring), 1484 cm^{-1} (CH_2 bending), 1473 cm^{-1} (CH_2 bending), 1392 cm^{-1} (CH_2 wagging), 1230 cm^{-1} (CH_2 twisting) and 1218 cm^{-1} (CH_2

twisting). In addition, the ring bands of EC are observed at 1160 cm^{-1} (ring stretching), 1069 cm^{-1} (ring breathing), 892 cm^{-1} (ring breathing) and 773 cm^{-1} (ring stretching), while the skeletal stretching of EC is observed at 971 cm^{-1}. Table 4.5 lists the peaks and assignments belonging to pure EC obtained from Figure 4.11.

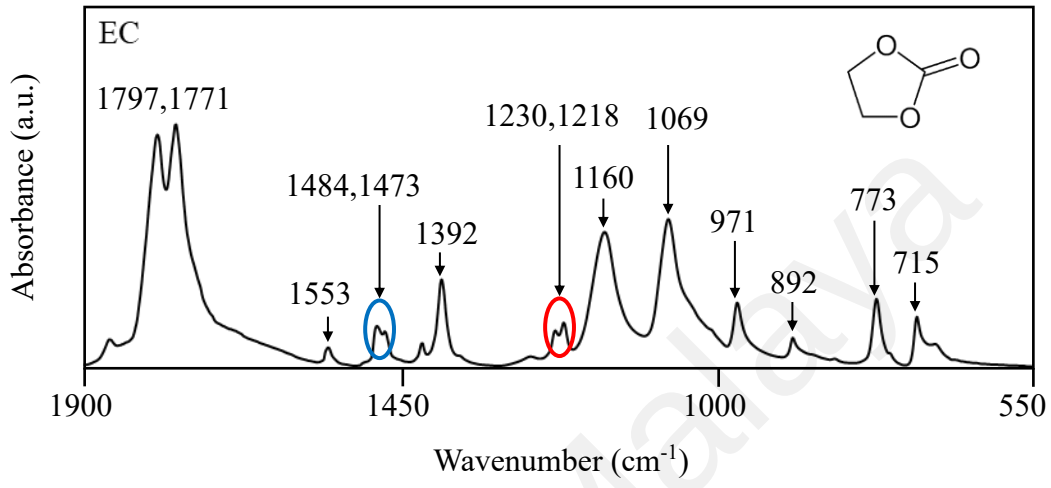

Figure 4.11: Infrared spectra of EC in the region between 550 and 1900 cm^{-1}.

Table 4.5: Assignment of IR spectra for EC.

Wavenumber (cm^{-1})	Assignment	Reference
1797, 1771	C=O stretching	(Kadir et al., 2011; Osman & Arof, 2003; Woo & Arof, 2016)
1553	CH_2 scissoring	(Masia et al., 2004; Woo & Arof, 2016)
1484, 1473	CH_2 bending	(Osman & Arof, 2003; Woo & Arof, 2016)
1392	CH_2 wagging	(Brennan et al., 2017; Osman & Arof, 2003; Woo & Arof, 2016)
1230,1218	CH_2 twisting	(Brennan et al., 2017; Masia et al., 2004; Woo & Arof, 2016)
1160	Ring stretching	(Brennan et al., 2017; Woo & Arof, 2016)
1069	Ring breathing	(Brennan et al., 2017; Osman & Arof, 2003; Woo & Arof, 2016)
971	Skeletal stretching	(Osman & Arof, 2003; Woo & Arof, 2016)
892	Ring breathing	(Osman & Arof, 2003; Woo & Arof, 2016)
773	Ring stretching	(Woo & Arof, 2016)
715	C=O bending	(Woo & Arof, 2016)

From the literature review, EC exhibits strong molecular interaction (dipole-dipole interaction) through its carbonyl group. When EC was added, the overall electronegativity of the carbonyl group in PAAm-PAA-Na_2S-EC GPE is estimated to undergo a change. This can be attributed to the fact that oxygen atoms are more electronegative than covalently bonded carbon atoms. Oxygen atoms attract more electrons related to the bond than carbon atoms, thus causing partial negative charges on the oxygen atoms and partial positive charges on the carbon atoms, as shown in Figure 4.12. EC has part of the positive carbon atoms from the carbonyl group, it will attract the part of the negative oxygen atoms from the carbonyl group of PAAm-PAA, thereby causing molecular interaction (Woo & Arof, 2016; Xu, 2020).

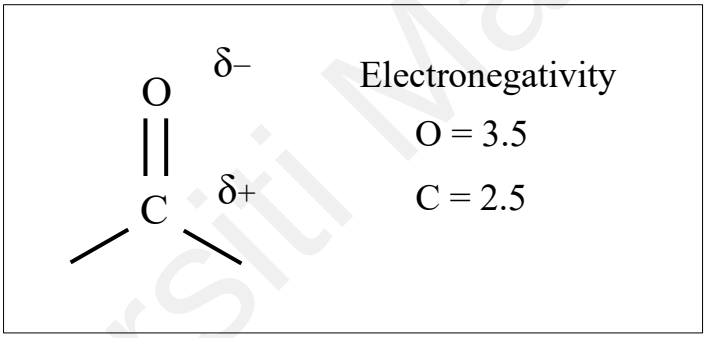

Figure 4.12: Symbols δ− and δ+ indicate the polarity of the C=O bond.

In system Y, samples were prepared by adding various wt.% of EC to the previously optimized Na_2S-PAAm-PAA GPE. The optimized GPE in system X is X3 (also known as W5), which exhibits the highest ionic conductivity (will be discussed in Chapter 5). The optimized GPE without EC is designated as X3/W5. Figure 4.13 depicts the infrared spectrum of PAAm-PAA-Na_2S GPE with addition of (a) 0 wt.% (X3/W5) to (e) 0.8 wt.% (Y4) of EC in the region of 550 to 4000 cm^{-1}. In the spectrum of X3/W5 (PAAm-PAA-Na_2S GPE), the peaks observed at 3391 cm^{-1}, 1661 cm^{-1}, 1557 cm^{-1}, 1407 cm^{-1}, 1120 cm^{-1}, 998 cm^{-1} and 677 cm^{-1} are attributed to O-H stretching, C=O of $CONH_2$ and/or O-H

bending, asymmetric COO^- stretching, symmetric COO^- stretching and/or C-N stretching, N-H rocking, v_1 SO_4^{2-} and v_4 SO_4^{2-}, respectively, as aforementioned.

No difference or minimal change in peak position was observed, let alone a new peak from EC in the Y1 sample (0.2 wt.% EC), except for v_4 SO_4^{2-} which down-shifted from 677 cm^{-1} to 667 cm^{-1} when 0.2 wt.% more of EC was added to PAAm-PAA-Na_2S GPE, as shown in Figure 4.13. This suggests that Na_2S interacts with EC. Moreover, when more than 0.2 wt.% of EC was added to the PAAm-PAA-Na_2S GPE, the O-H stretching upshifted from 3391 cm^{-1} to 3397 cm^{-1}, as shown in Figure 4.13 (c). Referring to Figure 4.12, it can be inferred that the positive carbon atom on the carbonyl group of EC attracts the negative oxygen atom of water from its alcohol group, so the molecular interaction between EC and water occurs through dipole-dipole and results in the shift of the wavenumber.

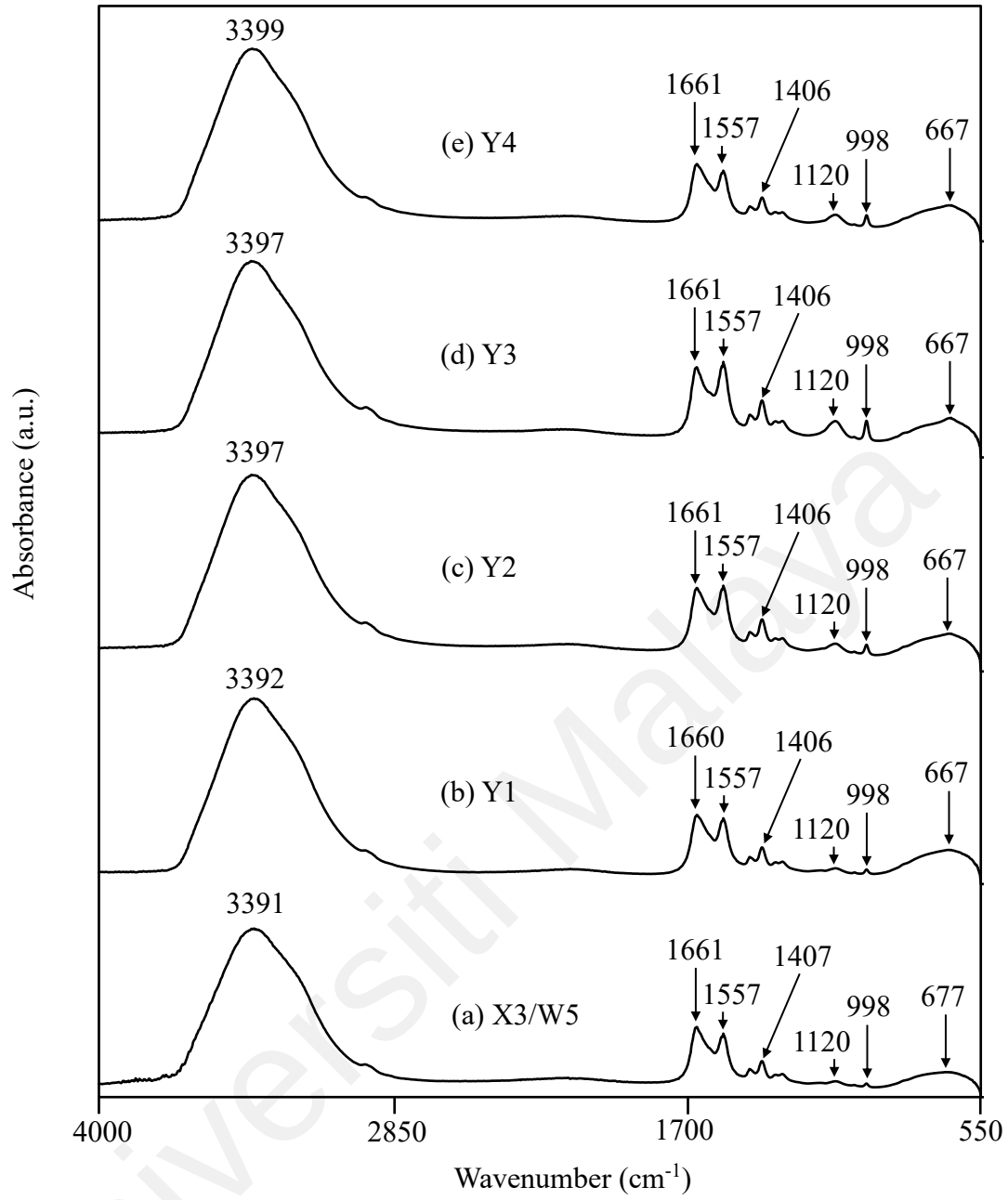

Figure 4.13: Infrared spectra of PAAm-PAA-Na_2S GPE added with (a) 0 wt.% (X3/W5), (b) 0.2 wt.% (Y1), (c) 0.4 wt.% (Y2), (d) 0.6 wt.% (Y3) and (e) 0.8 wt.% (Y4) EC in the region between 550 and 4000 cm^{-1}.

Although no changes were observed in other wavenumbers, the intensities of the amide, carboxylate and sulfate bands appeared to increase with the addition of EC. When the peak intensity increases, it can be deduced that the number of functional groups associated with molecular bonds increases, which suggests that EC interacts with PAAm-PAA through dipole-dipole bonds. The change in band intensity will be further discussed

by observing the magnified infrared spectrum of system Y in the region of 900 to 1700 cm^{-1}.

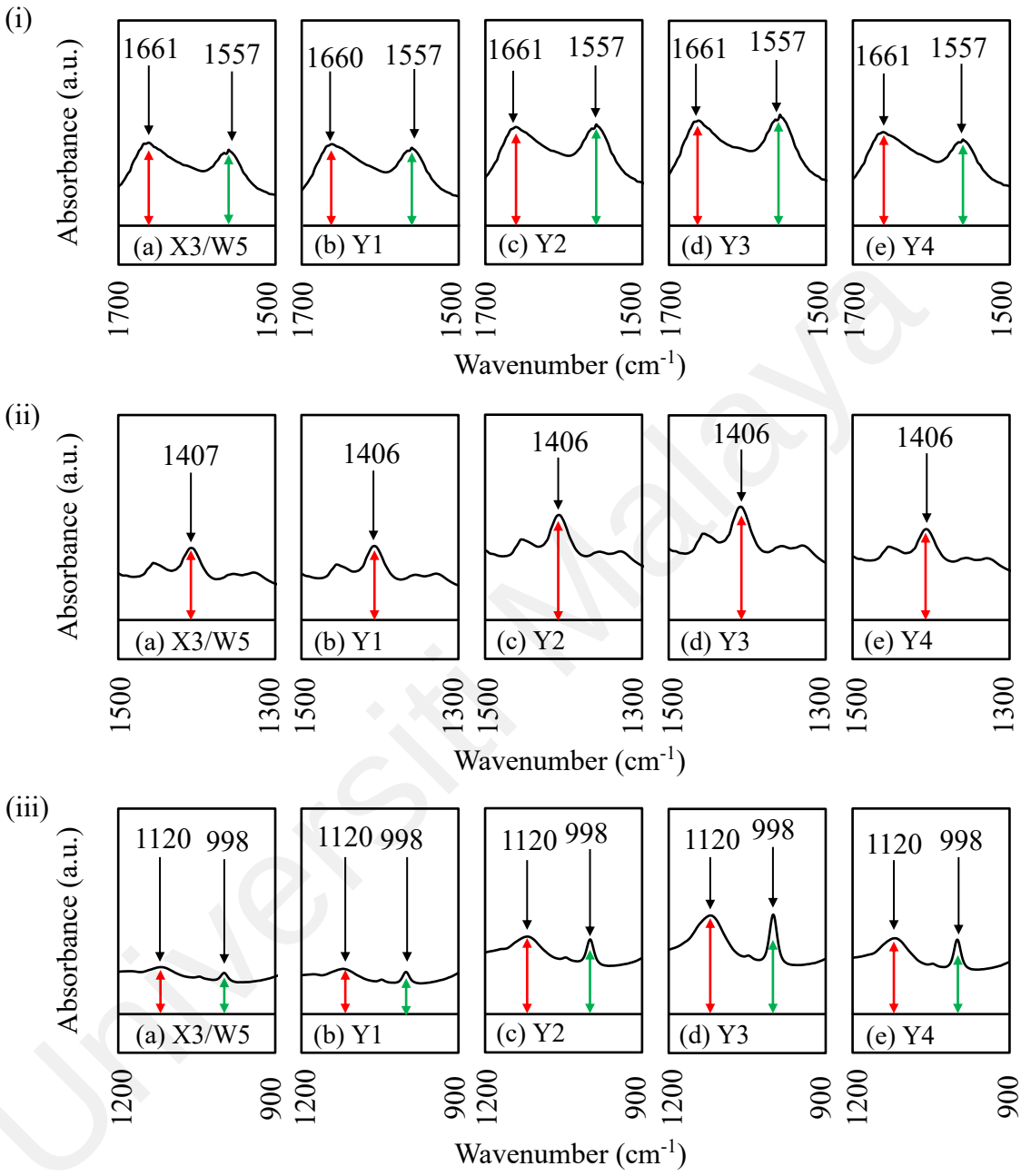

Figure 4.14: Magnified infrared spectra of PAAm-PAA-Na_2S-EC GPE in the regions of (i) 1500 to 1700 cm^{-1}, (ii) 1300 to 1500 cm^{-1} and (iii) 900 to 1200 cm^{-1}.

The magnified infrared spectrum of PAAm-PAA-Na_2S-EC GPE in the (i) 1500 to 1700 cm^{-1}, (ii) 1300 to 1500 cm^{-1} and (iii) 900 to 1200 cm^{-1} regions are shown in Figure 4.14. The same scale of absorbance units of all peaks is used to compare the peak intensity between PAAm-PAA-Na_2S-EC system. Refer to Figure 4.14 (i), (ii) and (iii), in the

spectrum of X3/W5 (PAAm-PAA-Na_2S GPE), the peaks observed at 1661 cm^{-1}, 1557 cm^{-1}, 1407 cm^{-1}, 1120 cm^{-1} and 998 cm^{-1} are attributed to C=O of $CONH_2$ and/or O-H bending, asymmetric COO^- stretching, symmetric COO^- stretching and/or C-N stretching, N-H rocking and v_1 SO_4^{2-}, respectively. As mentioned earlier, the peak position did not change significantly, but the peak intensity gradually increased with increasing EC mass loading, which can be seen by comparing the height of the red and green arrow lines from each peak to the baseline in Figure 4.14.

The change in peak intensity proves the complexation between EC and PAAm-PAA via formation of dipole-dipole interaction. This indicates that EC interacts with the oxygen atom of PAAm-PAA from its amide and carboxylate groups as well as the nitrogen atom on the amide group. On the other hand, by observing the band intensity of 998 cm^{-1} in Figure 4.14 (iii), it can be deduced that EC also forms ion-dipoles interaction with Na^+ cations in Na_2S. The maximum peak height and area for all peaks are mainly observed in the samples from 0.4 (Y2) to 0.6 wt.% (Y3) of EC in Figure 4.14, indicating that the highest number of functional groups associated with molecular bonds is found in the 0.4 to 0.6 wt.% EC samples. Other than the wavenumber shift in v_4 SO_4^{2-} (see Figure 4.13 (b)), its band intensity also increased, as shown in Figure 4.15 (i). This further proves that there is a strong interaction occurs between EC and Na^+ cations as the intensity of the characteristic peaks increases. Similar to the v_4 SO_4^{2-} band, there are also wavenumber shifts and band intensity changes in the O-H stretching, as shown in Figure 4.13 (c) and Figure 4.15 (ii), respectively. These findings suggest that the highest ionic conductivity obtained in 0.4 wt.% EC or Y2 sample (will be discussed in Chapter 5) in this work is due to the strong interaction between EC and PAAm-PAA, water and sulfide salt.

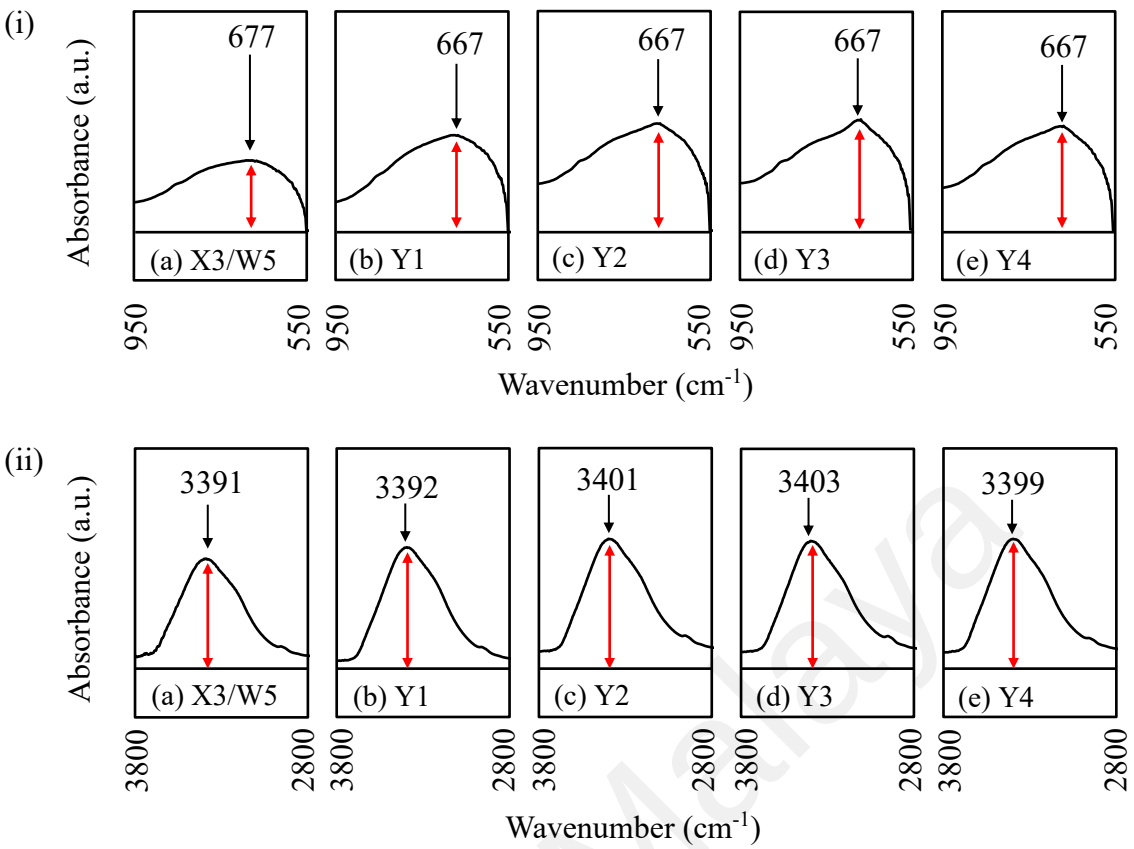

Figure 4.15: Magnified infrared spectra of PAAm-PAA-Na_2S-EC GPE in the regions of (i) 550 to 950 cm^{-1} and (ii) 2800 to 3800 cm^{-1}.

In view of conductivity mechanism of polymer-based electrolyte, the new dipole-dipole interaction between EC and PAAm-PAA, dipole-dipole between EC and water, and ion-dipole between EC and Na^+ cations of Na_2S may facilitate better Na^+ mobility to move around. EC provides additional hopping sites for Na^+, thus reduces the effective distance of Na^+ hoping from one site to another site. Various intermolecular interactions may occur between the carbonyl group of EC and the carboxylate COO^- group of PAAm-PAA, such as dipole-dipole, hydrogen bond and electrostatic interaction (Nesrinne & Djamel, 2017). Additional complexation site can be formed by EC with either C=O of $CONH_2$, COO^-, C-N or N-H bands from PAAm-PAA. By observing the change in band intensity, it can be inferred that EC is more like to form complexes with the oxygen atoms from $CONH_2$ and COO^- as well as nitrogen atoms from NH_2. When an electric field was applied, the cations will move from one complex site to another to constitute electric

current. The extra coordination positions formed by EC with either oxygen atoms from $CONH_2$ or oxygen atoms from COO^- or nitrogen atoms from NH_2 act as new stop for cations to locate before or after moving to another complex site.

When EC is added to the PAAm-PAA-Na_2S GPE, the distance of ion hoping from one site to another site become shorten. This shortcut accelerates the polarization and results in high ionic conductivity, which will be discussed further in the next chapter. It can be deduced that the addition of EC has improved the susceptibility of PAAm-PAA-Na_2S GPE to the applied electric field. In addition, other than (i) oxygen atom from water molecule and (ii) oxygen atom from amide and carboxylate groups in PAAm-PAA, the carbonyl C=O in EC also act as an additional choice for the cations to form coordination site with. As can be observed from the Figure 4.14 and Figure 4.15, the alternation of SO_4^{2-} band intensity at 998 cm^{-1} and 677 cm^{-1} suggests that there must be molecular interaction between EC and Na_2S. The redshift of the v_4 SO_4^{2-} band, from 677 cm^{-1} of X3/W5 to 667 cm^{-1} of Y1, also proves the interaction between EC and Na_2S. Therefore, the EC-Na^+ complex should be formed in system Y (PAAm-PAA-Na_2S-EC GPE). This shows that EC acts as a strong competitor to PAAm-PAA for the coordination bond with Na^+ cations of sulfide salt (Woo & Arof, 2016; Woo et al., 2013).

4.5 Z System – Gel Polymer Electrolytes with Double Additives

KCl, a metal halide salt, is widely used in polysulfide electrolytes to enhance the plasticization and diffusion properties of GPE. It was chosen as an additive to enhance the overall performance of QDSSCs because it can easily diffuse into the MO layer and accelerate the charge transfer kinetics of QDSSCs (Jiang et al., 2016; Ren et al., 2015; Seo et al., 2013; Sun et al., 2018; Yu et al., 2017). According to literature review (Han et al., 2016; Peters & Noble, 2019), K^+ and Cl^- ions are attracted by OH groups to form dative bonds. KCl is readily soluble in water and causes perturbation in water. This is

because KCl can change the arrangement of water molecules through stronger and better aligned hydrogen bonds in aqueous solutions.

Similar to system Y, the interaction between additive and GPE was investigated by adding various wt.% additive to the most conductive sample of the previous system in system Z. Y2 is the most conductive sample in system Y (will be discussed in Chapter 5) and is referred to as PAAm-PAA-Na_2S-EC GPE or GPE without KCl in system Z. Figure 4.16 depicts the infrared spectrum of (a) KCl and PAAm-PAA-Na_2S-EC GPE with the addition of 0 wt.% (Y2) to 0.8 wt.% (Z4) of KCl in the region of 550 to 4000 cm^{-1}. The inset demonstrates the chemical structure of KCl, indicating that vibrational bands should not be detected in the KCl spectrum. For Y2 (GPE without KCl), the peaks observed at 3401 cm^{-1}, 1661 cm^{-1}, 1557 cm^{-1}, 1406 cm^{-1}, 1120 cm^{-1}, 998 cm^{-1} and 667 cm^{-1} are attributed to O-H stretching, C=O of $CONH_2$ and/or O-H bending, asymmetric COO^- stretching, symmetric COO^- stretching and/or C-N stretching, N-H rocking, v_1 SO_4^{2-} and v_4 SO_4^{2-}, respectively, as aforesaid.

After KCl addition, the O-H stretching down-shifted from 3401 cm^{-1} to 3391 cm^{-1}, the wavenumbers in the 900 to 3000 cm^{-1} infrared spectral region remain unchanged, and the v_4 SO_4^{2-} upshifted from 667 cm^{-1} to 677 cm^{-1}, as shown in Figure 4.16 (c). This suggests that KCl interacts with water. Furthermore, when more than 0.2 wt.% of KCl was added to the sample, the O-H stretching upshifted from 3391 cm^{-1} to 3399 cm^{-1}, as shown in Figure 4.16 (d). When the vibration band upshifts, it can be deduced that molecular vibration and bonding require more energy than the current bond. A higher infrared frequency will result in a stiffer bond in the alcohol group of water; thus, a stronger bond is demonstrated in the ion-dipole interaction between KCl and water. Besides, the v_4 SO_4^{2-} that down-shifted from 677 cm^{-1} to 667 cm^{-1} when 0.6 wt.% of KCl was added to the

sample (Z3), as shown in Figure 4.16 (e), indicating that K^+ cations were also attracted by the oxygen atoms in sulfate group to form dative bonds.

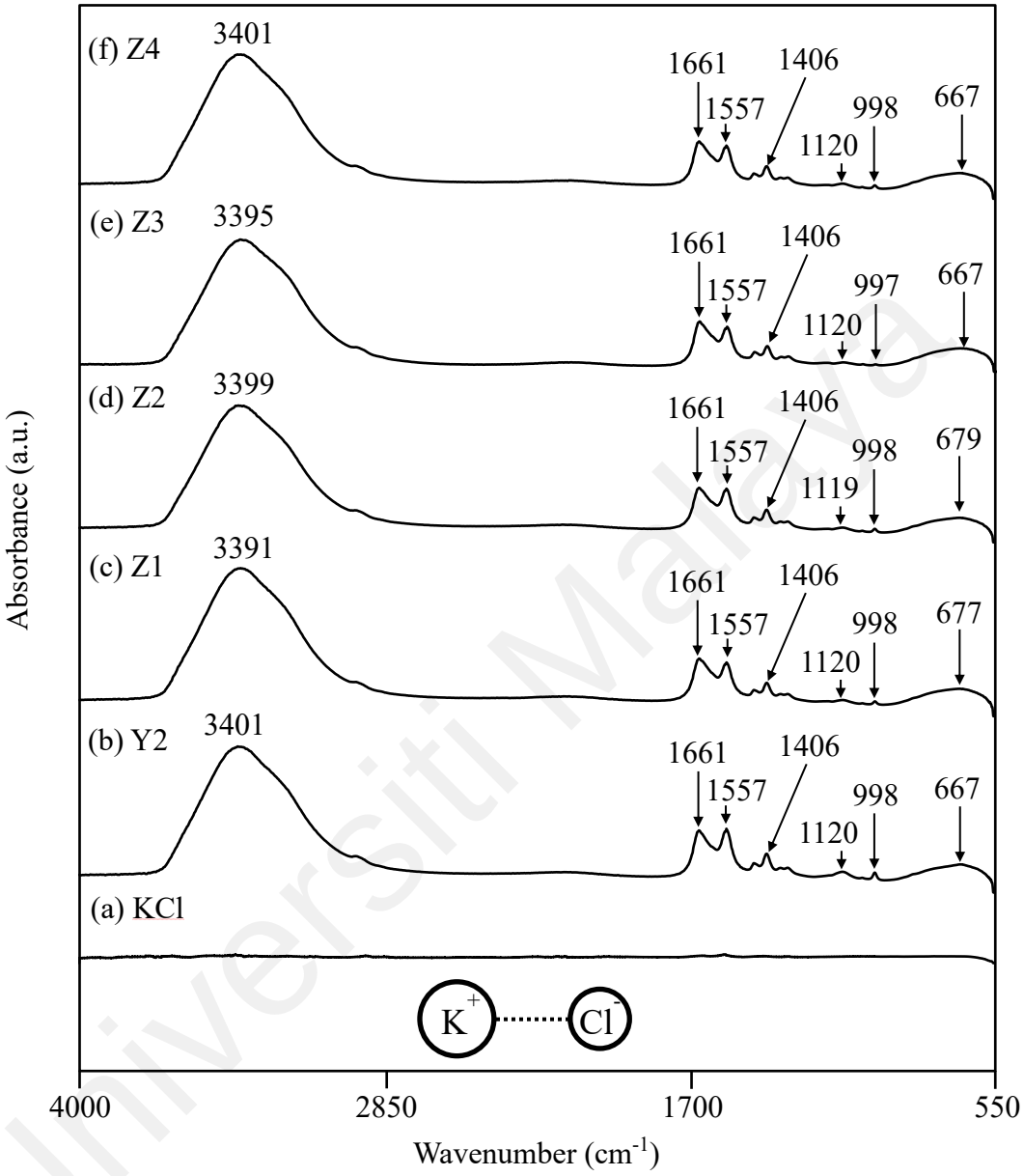

Figure 4.16: Infrared spectra of (a) KCl and PAAm-PAA-Na_2S-EC GPE added with (b) 0 wt.% (Y2), (c) 0.2 wt.% (Z1), (d) 0.4 wt.% (Z2), (e) 0.6 wt.% (Z3) and (f) 0.8 wt.% (Z4) KCl in the region between 550 and 4000 cm^{-1}.

As discussed earlier, the wavenumber shift and band intensity change of the v_4 SO_4^{2-} band, as shown in Figure 4.13 (b) and Figure 4.15 (i), respectively, proving a strong interaction between EC and Na^+ cations. In other words, the wavenumber shift and reduced band intensity of the v_4 SO_4^{2-} band, as shown in Figure 4.17, suggest that KCl

may weaken the interaction between EC and Na^+ cations. The red dashed line represents the peak height of the v_4 SO_4^{2-} band in sample Y2 (GPE without KCl). It serves as a reference guide for v_4 SO_4^{2-} peak heights in other samples. The intensity of the peaks was found to decrease with the addition of KCl, especially for sample Z3 (0.6 wt.% KCl). The K^+ cation, as a strong competitor of the Na^+ cation, may form a dative bond with EC, resulting in a shift in the peak position and reduced peak intensity of the v_4 SO_4^{2-} band.

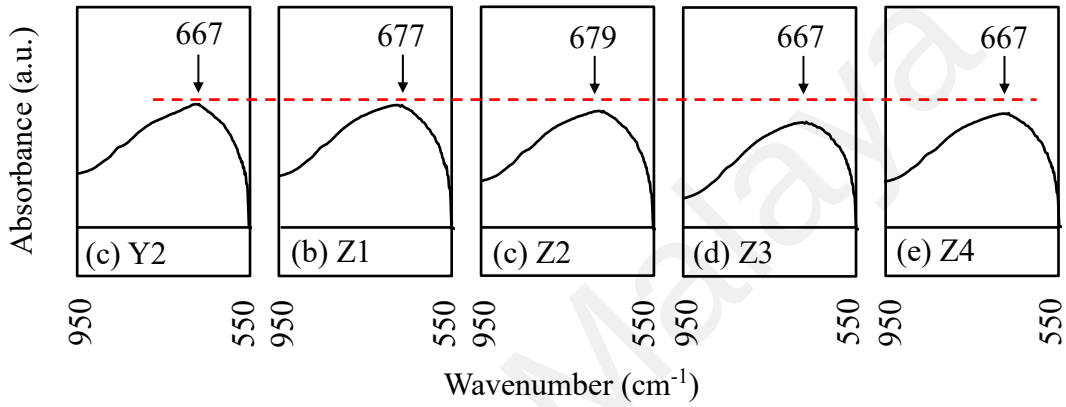

Figure 4.17: Magnified infrared spectra of PAAm-PAA-Na_2S-EC-KCl GPE in the region of 550 to 950 cm^{-1}.

The interaction between KCl and PAAm-PAA can be determined by observing the changes of peak intensities for amide and carboxylate bands in the magnified infrared spectrum of system Z in the regions of (i) 1500 to 1700 cm^{-1}, (ii) 1300 to 1500 cm^{-1} and (iii) 900 to 1200 cm^{-1} in Figure 4.18. After adding KCl, the peak intensity at 900~1700 cm^{-1} gradually decreased, especially for sample Z3 (0.6 wt.% KCl). This suggests that KCl interacts with PAAm-PAA by forming an ion-dipole. In addition to the oxygen atoms extending from the water alcohol group or the EC carbonyl group, K^+ cations are also attracted by the oxygen atoms in the PAAm-PAA amide or carboxylate groups, forming possible complexation sites. These characteristic peaks in water, EC or PAAm-PAA can show strong bonds with KCl.

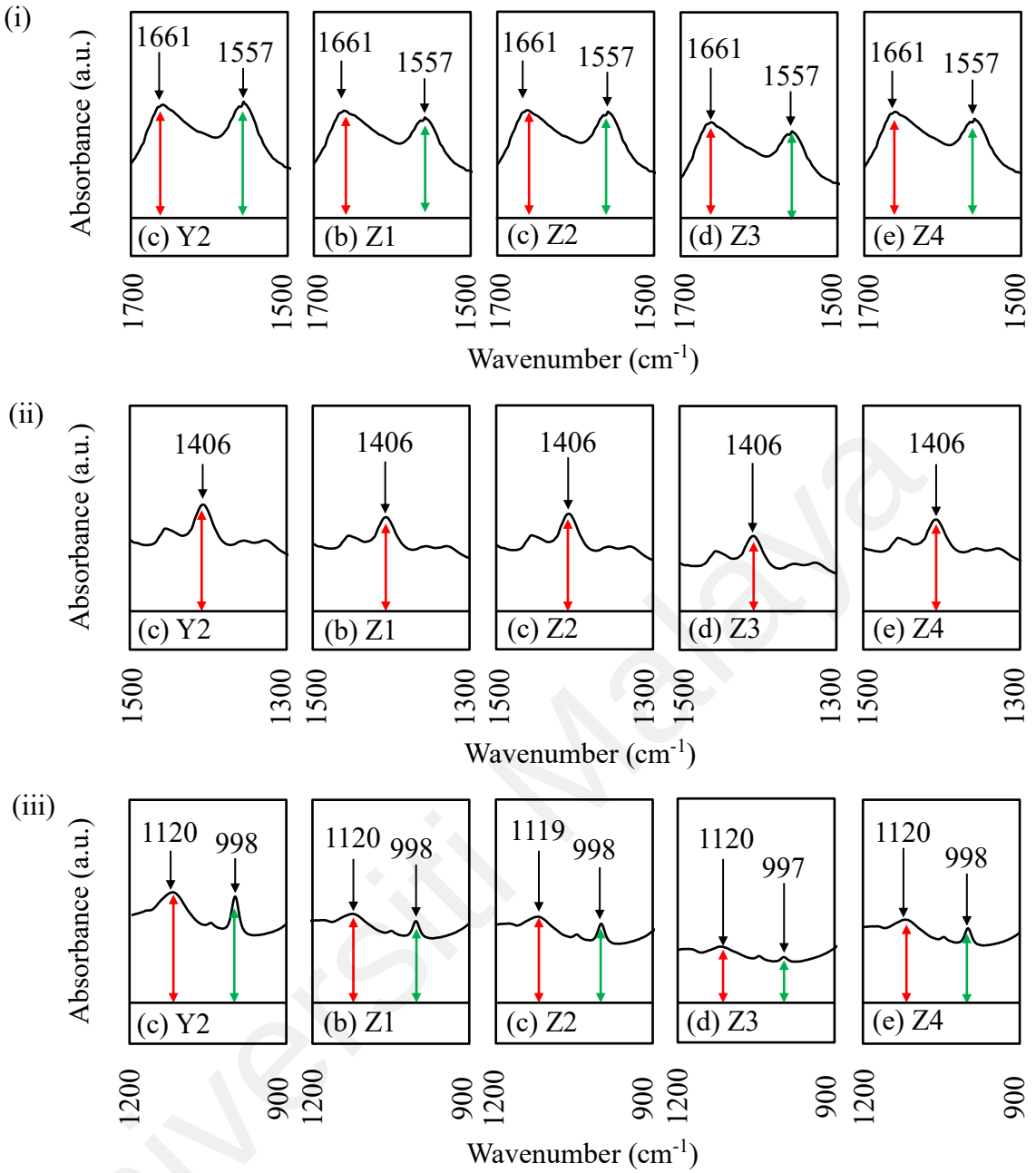

Figure 4.18: Magnified infrared spectra of PAAm-PAA-Na_2S-EC-KCl GPE in the regions of (i) 1500 to 1700 cm^{-1}, (ii) 1300 to 1500 cm^{-1} and (iii) 900 to 1200 cm^{-1}.

In system Z, possible dipole-dipoles consist of (i) PAAm-PAA and water, (ii) PAAm-PAA and EC and (iii) EC and water; ionic-dipoles consist of (i) Na^+ cation and water, (ii) Na^+ cation and PAAm-PAA, (iii) Na^+ cation and EC, (iv) K^+ cation and water, (v) K^+ cation and PAAm-PAA and (vi) K^+ cation and EC, as shown in Figure 4.19. When K^+ cations try to displace Na^+ cations to coordinate with PAAm-PAA or water or EC, the current generated by Na^+ cations will be interrupted. With increasing KCl content, more

K^+ cations appeared. It is advantageous for K^+ cations to compete with Na^+ cations to form dative bonds with PAAm-PAA or water or EC. As a result, Na^+ cations may recombine with S^- anions to form neutral ion pairs and reduce the ionic conductivity of GPE. However, when the K^+ cation moves in the direction of the applied electric field, it also constitutes a current. Therefore, it can contribute to the ionic conductivity of GPE. The electrical characteristics of GPE will be discussed further in Chapter 5.

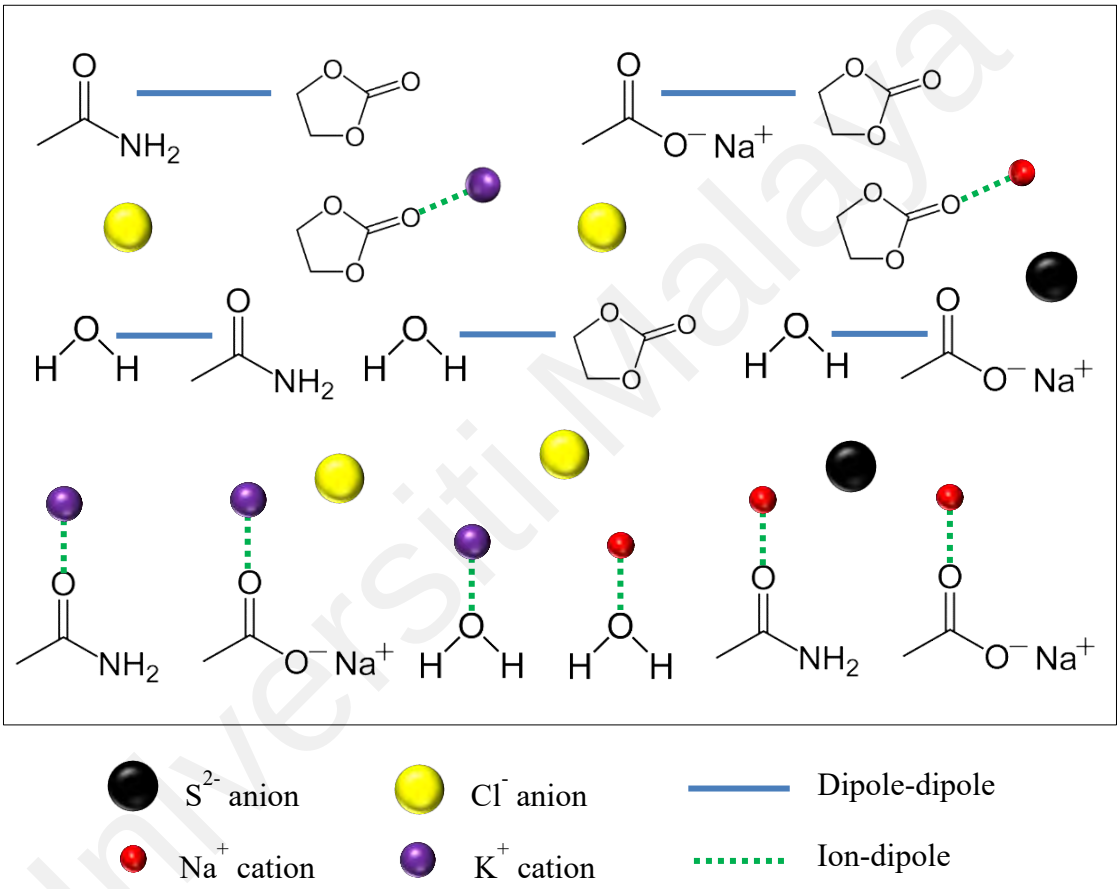

Figure 4.19: Schematic diagram of possible dipole-dipole and ion-dipole in system Z.

4.6 Summary

For polysulfide electrolyte, the molecular interaction between water and Na_2S is demonstrated by the emergence of new peaks at 1393 cm^{-1}, 998 cm^{-1} and 675 cm^{-1} when Na_2S was added to water. These new peaks are attributed to the S=O stretching, v_1 SO_4^{2-} and v_4 SO_4^{2-} of $Na_2S \cdot nH_2O$, respectively. In the case of PAAm-PAA-Na_2S GPE, the

molecular interaction between PAAm-PAA, Na_2S and water is through the occurrence of PAAm-PAA characteristic peaks, such as C=O of $CONH_2$, asymmetric COO^- stretching, symmetric COO^- stretching and/or C-N stretching and N-H rocking, when PAAm-PAA was added to liquid polysulfide electrolyte, and their respective wavenumbers change with increasing PAAm-PAA content. Upon addition of 5 wt.% PAAm-PAA (W1), the O-H stretching upshifted from 3385 cm^{-1} to 3391 cm^{-1}, where v_4 SO_4^{2-} down-shifted from 675 cm^{-1} to 667 cm^{-1}, indicating PAAm-PAA interacts with water and Na_2S, respectively. As the content of PAAm-PAA increases, more characteristic peaks of PAAm-PAA appear and wavenumbers shift, indicating Na^+ cations form dative bonds with the copolymers. Oxygen atom in the hydroxyl group of water and oxygen atom in the amide and/or carboxylate groups of PAAm-PAA are the choices for Na^+ cations to form ionic dipoles.

The molecular interaction between EC and PAAm-PAA-Na_2S GPE was determined by adding various wt.% of EC to the optimized PAAm-PAA-Na_2S GPE, which is designated as X3/W5. In X3/W5 spectrum, the peaks observed at 3391 cm^{-1}, 1661 cm^{-1}, 1557 cm^{-1}, 1407 cm^{-1}, 1120 cm^{-1}, 998 cm^{-1} and 677 cm^{-1} are attributed to O-H stretching, C=O of $CONH_2$ and/or O-H bending, asymmetric COO^- stretching, symmetric COO^- stretching and/or C-N stretching, N-H rocking, v_1 SO_4^{2-} and v_4 SO_4^{2-}, respectively. No difference or minimal change in peak position was observed in the EC-added GPE, let alone a new peak from EC. However, the interaction of EC with Na_2S and water can be explained by the wavenumber shift in the v_4 SO_4^{2-} (down-shifted from 677 cm^{-1} to 667 cm^{-1}) and O-H stretching (upshifted from 3391 cm^{-1} to 3397 cm^{-1}) bands, respectively. Although the peak position of C=O of $CONH_2$ and/or O-H bending, asymmetric COO^- stretching, symmetric COO^- stretching and/or C-N stretching and N-H rocking did not change significantly, but the peak intensity gradually increased with increasing EC mass

loading, indicating a dipole-dipole between EC and PAAm-PAA. The infrared studies of GPE based on PAAm-PAA-Na_2S-EC-KCl system were also examined.

In a nutshell, IR spectra has shown the possible dipole-dipole interactions between (i) PAAm-PAA and water, (ii) PAAm-PAA and EC and (iii) EC and water. On the other hand, ion-dipoles interactions may occur between (i) Na^+ cation and water, (ii) Na^+ cation and PAAm-PAA, (iii) Na^+ cation and EC, (iv) K^+ cation and water, (v) K^+ cation and PAAm-PAA and (vi) K^+ cation and EC. The changes in the shape, position and intensity of the vibration band observed from each system become evidence of molecular interaction.

CHAPTER 5: ELECTRICAL AND TRANSPORT PROPERTIES OF GEL POLYMER ELECTROLYTE

5.1 Introduction

The ionic conductivity and ion transport characteristics of the electrolyte can be examined by electrochemical impedance spectroscopy (EIS). This experiment generates complex impedance diagrams for impedance analysis: (i) ionic conductivity, (ii) dielectric properties, and (iii) temperature dependence of ionic conductivity. The ionic conductivity, dielectric and transport properties of all four GPE systems will be discussed in this chapter.

5.2 W System – Gel Polymer Electrolytes with Various Wt.% of Polymer Host

In system W, the amount of PAAm-PAA added to the liquid polysulfide is 0 to 35 wt.%, with an interval of 5 wt.%.

5.2.1 Room Temperature Ionic Conductivity

In general, the complex impedance diagram for polymer electrolyte may appear in three modes, such as a tilted spike, a depressed semicircle and a tilted spike or a depressed semicircle. An appropriate equivalent circuit fitting model will be used to fit the complex impedance diagram according to its mode. The complex impedance diagram shows the bulk resistance (R_b) and other parameters of the electronic components when the fitting is completed. Then, the room temperature ionic conductivity (σ) can be calculated using Equation 3.2, as expressed in Section 3.3.2. Figure 5.1 depicts the Nyquist plot of liquid polysulfide electrolyte doped with various wt.% of PAAm-PAA (W system) at room temperature.

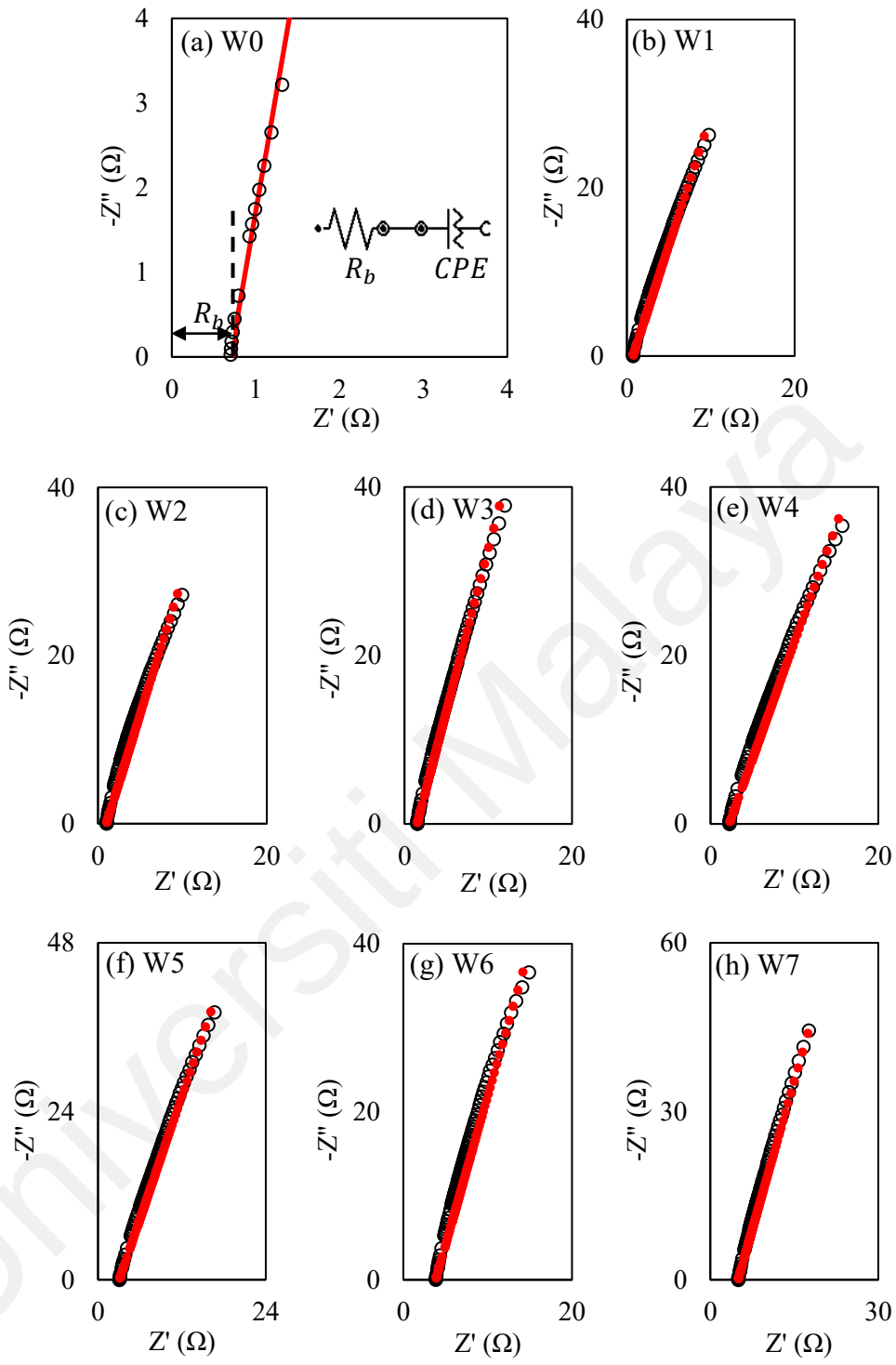

Figure 5.1: Nyquist plot (o) for liquid polysulfide electrolyte added with (a) 0 wt.% (W0), (b) 5 wt.% (W1), (c) 10 wt.% (W2), (d) 15 wt.% (W3), (e) 20 wt.% (W4), (f) 25 wt.% (W5), (g) 30 wt.% (W6) and (h) 35 wt.% (W7) PAAm-PAA and their corresponding fitting (●) at room temperature.

As can be seen from the figure, the Nyquist plot presents the shape of a tilted spike, and the tilted spike intercepts at the Z'. The relationship between the negative imaginary impedance (-Z'') and the real impedance (Z') is shown by the Nyquist plot. The tilted spike mode implies that the electrode polarization is dominant. The equivalent circuit fitting model is best represented by a resistor (R) connected in series with a constant phase element (CPE), as shown in the inset in Figure 5.1 (a). The value of R_b is obtained at the Z' intercept. CPE is a component that measures imperfect dielectrics. The complex impedance of CPE is given by Equation 5.1:

$$Z_{CPE} = \frac{1}{k(j\omega)^N} \tag{5.1}$$

where j is the imaginary number $\sqrt{(-1)}$, ω is the angular frequency, k is the CPE constant, and N is the inclination degree of the tilted spike relative to the Z' axis. The value of N is between 0 and 1. CPE is defined as pure resistance when $N = 0$, Warburg when $N = 0.5$, and pure capacitance when $N = 1$. The vertical spike represents a perfect capacitor. Therefore, the tilted spike or CPE is called an imperfect capacitor. The k value is obtained by fitting the Nyquist plot of the corresponding frequency by trial and error. The fitting point should be approximate to the experimental data. Table 5.1 lists the R_b, k and N values of system W. It can be seen from the table that as the content of PAAm-PAA increases, R_b increases.

Table 5.1: R_b, k and N values of system W.

GPE	R_b (Ω)	k (10^{-4} $F^{-1}s^{1-N}$)	N (10^{-1})
W0	0.68 ± 0.04	1.40 ± 0.08	8.08 ± 0.22
W1	0.77 ± 0.03	1.45 ± 0.15	8.06 ± 0.13
W2	1.06 ± 0.02	1.44 ± 0.13	8.17 ± 0.16
W3	1.61 ± 0.03	1.65 ± 0.04	8.04 ± 0.20
W4	2.25 ± 0.08	1.49 ± 0.09	7.76 ± 0.07
W5	2.91 ± 0.14	1.32 ± 0.11	8.04 ± 0.09
W6	3.73 ± 0.24	1.30 ± 0.07	8.08 ± 0.14
W7	4.98 ± 0.07	1.11 ± 0.03	8.13 ± 0.14

Based on Equation 3.2, if the values of R_b, t and A are known, the ionic conductivity can be calculated. Given that the thickness, t of the coin cell is 0.32 cm and the surface area, A of the coin cell is 2.1538 cm^2, the room temperature ionic conductivity of system W is obtained, as shown in Figure 5.2. The ionic conductivity of the liquid polysulfide electrolyte (W0) obtained in Figure 5.2 is (22.02 ± 1.34) × 10^{-2} S·cm^{-1}. When adding 5 wt.% PAAm-PAA (W1), the ionic conductivity of GPE decreases to (19.25 ± 0.73) × 10^{-2} S·cm^{-1}. As the content of PAAm-PAA increases, the ionic conductivity continues to decrease. It can be deduced that PAAm-PAA is not a conductive polymer and will significantly reduce the ionic conductivity of W GPEs. In addition, the viscosity of the polymer host will also affect the ionic conductivity of W GPEs, because it will affect the ion motion in system W (Son & Wang, 2020). As discussed in the previous chapter, W5 was selected as the optimized composition due to its preferable fluid flow rate and good dimensional stability at room temperature. The ionic conductivity of W5 is (5.11 ± 0.24) × 10^{-2} S·cm^{-1}.

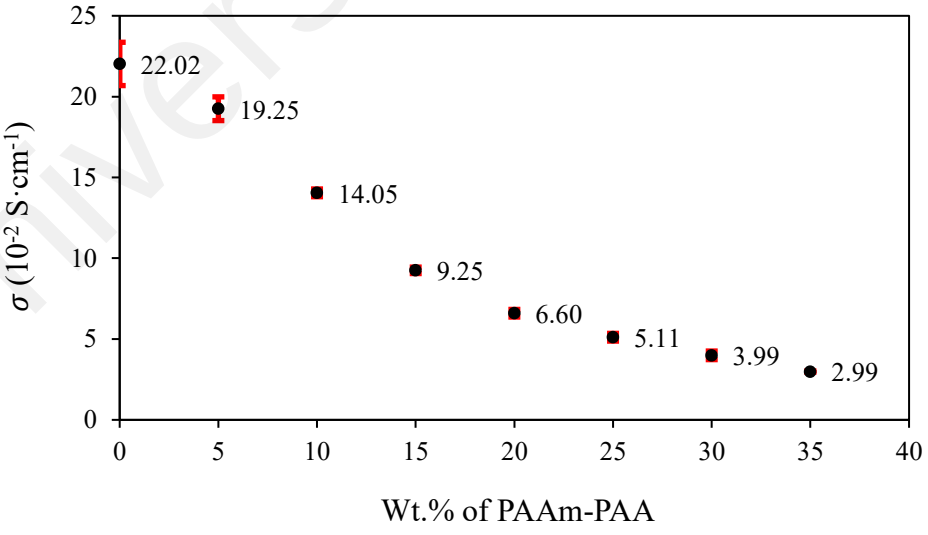

Figure 5.2: Room temperature ionic conductivity of system W.

5.2.2 Dielectric and Transport Properties

The dielectric properties of the electrolyte determine its ion transport properties and relaxation mechanism. The effect of the PAAm-PAA wt.% on the dielectric properties of polysulfide electrolyte was studied. The frequency dependence of the dielectric constant has been carried out for system W. The dielectric constant (ε') represents the charge stored in the GPE. It can be calculated by the following equation (Buraidah et al., 2009):

$$\varepsilon' = \frac{Z_i}{\omega C_0 (Z_r^2 + Z_i^2)} \tag{5.2}$$

where $C_0 = \varepsilon_0 A/t$ and $\omega = 2\pi f$. ε_0 is the permittivity of free space, Z_i and Z_r are the imaginary and real parts of the complex permittivity, respectively, and f is the frequency (Buraidah et al., 2009). Therefore, the ion transport characteristics of the GPE will be studied: (i) ionic mobility (μ) and (ii) charge carrier density (n). The values of μ and n can be calculated using equations (5.3) and (5.4) respectively (Arof et al., 2014a).

$$\mu = \frac{e[(k^{-1}\varepsilon_0\varepsilon_r A)^2]\tau^{-1}}{k_b T} \tag{5.3}$$

$$n = \frac{\sigma}{\mu e} \tag{5.4}$$

where ε_0 is vacuum permittivity (8.854×10^{-14} F·cm^{-1}), ε_r is dielectric constant, A is the electrolyte/electrode contact area, τ is the $1/\omega$ value taken at the frequency corresponding to the minimum value of the imaginary impedance, k_b is the Boltzmann constant (1.38×10^{-23}) and e is the electron charge (1.602×10^{-19} C).

Figure 5.3 depicts the PAAm-PAA wt.% dependence of ε' of system W at the following selected frequencies: 5 kHz, 7 kHz, 10 kHz, 20 kHz and 30 kHz. In Figure 5.3, the trend of ε' values decrease upon incorporation of PAAm-PAA at vary frequencies. It can be deduced that as the amount of PAAm-PAA increases, ε' decreases, and the

variation of ε' with PAAm-PAA content seems to follow the variation of ionic conductivity with PAAm-PAA content (see Figure 5.2). According to the literature, when the wt.% of PAAm-PAA added increases, the viscosity of GPE increases and hinders ion movement (Arya et al., 2018; Woo et al., 2013). Therefore, the permittivity depends on ion movement and polarization (Aziz et al., 2017).

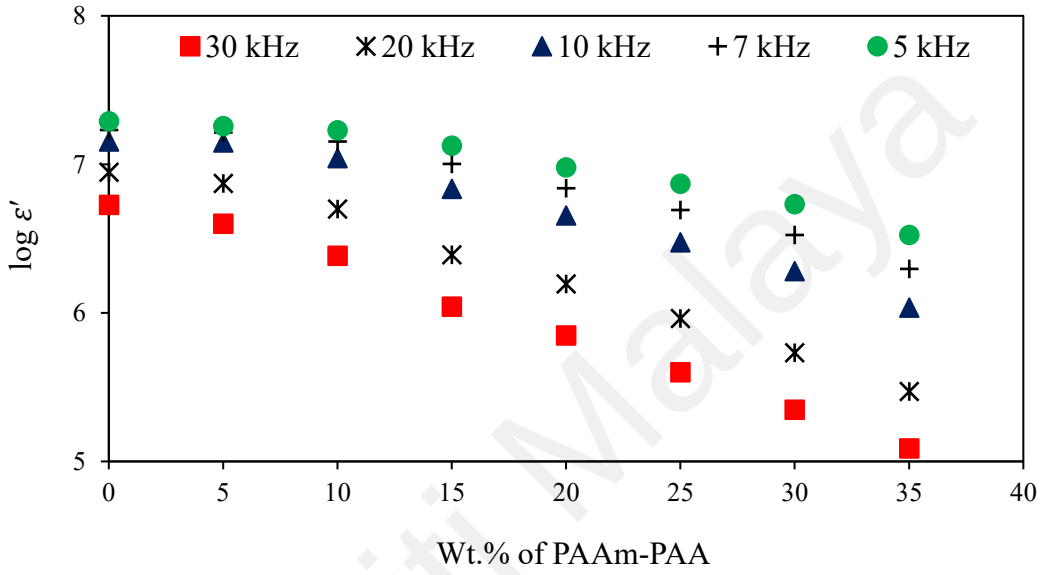

Figure 5.3: PAAm-PAA wt.% dependence of ε' of system W at selected frequencies.

Table 5.2 lists the calculated ε' value of system W at different frequencies. As the frequency decreases, ε' increases due to the electrode polarization effect. For instance, the ε' of W0 increases from $(5.33 \pm 0.32) \times 10^6$ of 30 kHz to $(19.45 \pm 2.24) \times 10^6$ of 5 kHz. Electrode polarization or hetero-charge layer mostly happens in the low frequency region. At low frequencies, the periodic reversal of the applied electric field is slow, so along the direction of the applied electric field, the dipole molecules have enough time to orient themselves, therefore the trapped ions gather near the electrode-electrolyte interface and generate a different charge layer. At high frequencies, due to fast periodic reversal of the applied electric field, the dipole orientation unable to catch up, thus it is unlikely that excessive ion diffusion of polarization will occur (Ali et al., 2013; Arya et al., 2018; Hafiza et al., 2014; Rani et al., 2018; Serghei et al., 2009; Woo et al., 2013).

Table 5.2: ε' value of system W at selected frequencies.

GPE	30 kHz	20 kHz	10 kHz	7 kHz	5 kHz
	ε' (10^6)	ε' (10^6)	ε' (10^6)	ε' (10^6)	ε' (10^6)
W0	5.33 ± 0.32	8.84 ± 0.49	14.20 ± 2.03	17.00 ± 1.67	19.45 ± 2.24
W1	3.97 ± 0.37	7.41 ± 0.32	13.98 ± 1.03	16.36 ± 2.78	18.05 ± 3.29
W2	2.42 ± 0.18	4.98 ± 0.28	11.00 ± 0.28	14.19 ± 0.40	16.91 ± 0.77
W3	1.10 ± 0.13	2.45 ± 0.24	6.84 ± 0.38	10.05 ± 0.33	13.31 ± 0.38
W4	0.70 ± 0.05	1.56 ± 0.11	4.53 ± 0.32	6.89 ± 0.44	9.52 ± 0.53
W5	0.40 ± 0.06	0.92 ± 0.11	2.98 ± 0.20	4.93 ± 0.27	7.40 ± 0.44
W6	0.22 ± 0.02	0.54 ± 0.05	1.90 ± 0.18	3.34 ± 0.30	5.37 ± 0.42
W7	0.12 ± 0.02	0.30 ± 0.04	1.08 ± 0.14	1.98 ± 0.23	3.34 ± 0.32

Based on Equation 5.3 and 5.4, if the values of k, ε_0, ε_r, A, τ, e, k_b, T and σ are known, then the values of μ and n can be calculated. In Figure 5.4 (a), the μ and n values of system W are calculated at a frequency of 30 kHz. It is observed that with the addition of PAAm-PAA, μ decreases, which obeys the variation of ionic conductivity with the content of PAAm-PAA.

At low frequency (5 kHz), μ increases at 5 wt.% PAAm-PAA (W1) and then decreases with increasing PAAm-PAA content, as depicted in Figure 5.4 (b). In addition, n gradually decreased upon incorporation of PAAm-PAA and then increased after adding 15 wt.% PAAm-PAA (W3). Clearly, different trends in μ and n are observed at different frequencies, which are due to polarization. According to Equation 5.3, the calculated μ depends on the value of ε'. Due to electrode polarization, when the frequency decreases, ε' is likely to increase to one decimal place, so the value of μ also increase as expected. It can be deduced that polarization will not only lead to high ε', but also μ. Since μ is inversely proportional to n according to Equation 5.4, the polarization will reduce the value of n at low frequencies.

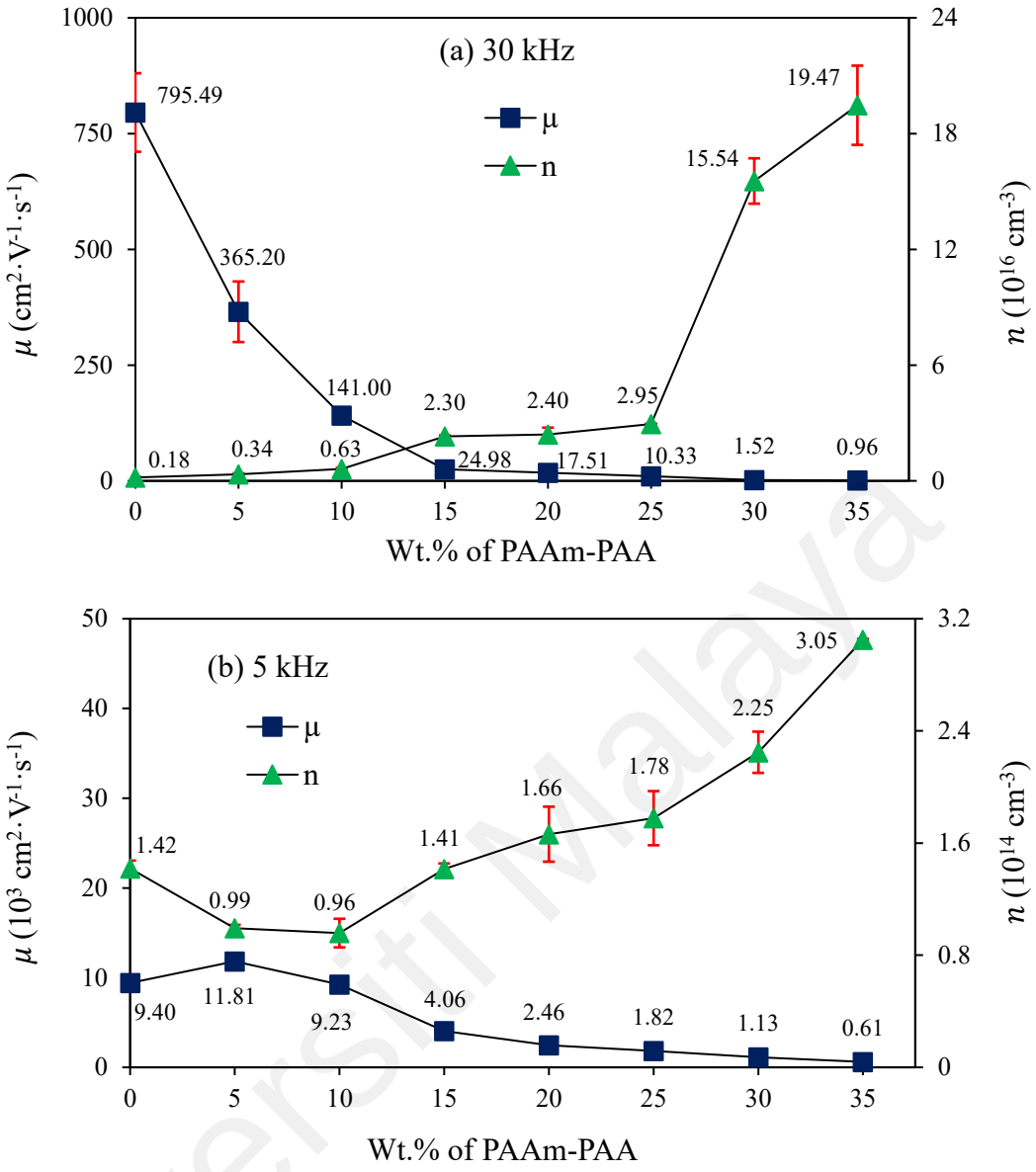

Figure 5.4: Variation of μ and n of system W at (a) 30 kHz and (b) 5 kHz.

The ionic conductivity depends on μ and n, which can be described by Equation 5.4. Since there is an inverse relationship between μ and n, a trend of n increasing after the addition of PAAm-PAA is observed. It can be concluded that μ and n are two influential factors that determine the ionic conductivity of GPE. n is the charge carrier density (also known as the number of charge carriers per unit volume). Charge carriers or free ions include free cations and free anions. μ is the ionic mobility, that is, the speed at which free ions move in the medium under the action of an external electric field.

As discussed in the previous chapter, when the copolymer content increases, more interactions occur between the copolymer and Na^+ cations. Therefore, the number of dissociated S^{2-} anion increases and n increases, as shown in Figure 5.5. In Figure 5.5 (a), there are ion pairs (Na_2S), free ions (red atoms are Na^+ cations and black atoms are S^{2-} anions) and water (H_2O) in the electrolyte system, indicating an electrolyte system without addition of polymer (W0). A dative bond (green dashed line) is occurred between the Na^+ cation and water. The free ions are dissociated by water. Note that the n in W0 is only $(0.18 \pm 0.02) \times 10^{16}$ cm^{-3} at a frequency of 30 kHz. After adding PAAm-PAA, amide ($-CONH_2$) and carboxylate (-COONa) groups appeared in the electrolyte system, as schematized in Figure 5.5 (b) and Figure 4.5. The copolymer can form a complex with water (the blue line is a dipole-dipole bond) and a dative bond with Na^+ cations. It is believed that the ion pairs are dissociated by the copolymer. Therefore, at W7 in Figure 5.4 (a), n increases to the highest value of $(19.47 \pm 2.05) \times 10^{16}$ cm^{-3}.

It is known that the higher the number of free ions, the higher the electrolyte ionic conductivity. However, in system W, although the addition of the copolymer can dissociate more free ions and increase n, μ decreases drastically and dominates the ionic conductivity of GPE. According to the literature, as the copolymer content increases, the significant decrease in μ is in response to the polymer segment mobility (Arya et al., 2018; Kim & Oh, 2000). Since the copolymer segment restricts the movement of free ions, μ decreases and the ionic conductivity decreases. It can be seen from the figure that after the copolymer is added, the space for ion movement is limited. The more copolymer is added, the fewer the space for ion movement. The crowded medium causes the ions to move slowly to conduct current when an electric field is applied. Therefore, despite the larger volume of free ions, they move slowly and result in a smaller μ. This has been demonstrated in the discussion in the previous chapter that adding more copolymers will

increase the viscosity of the GPE and eventually solidify (i.e., a solid texture was observed in W7). This hinders the movement of ions and reduces ionic conductivity.

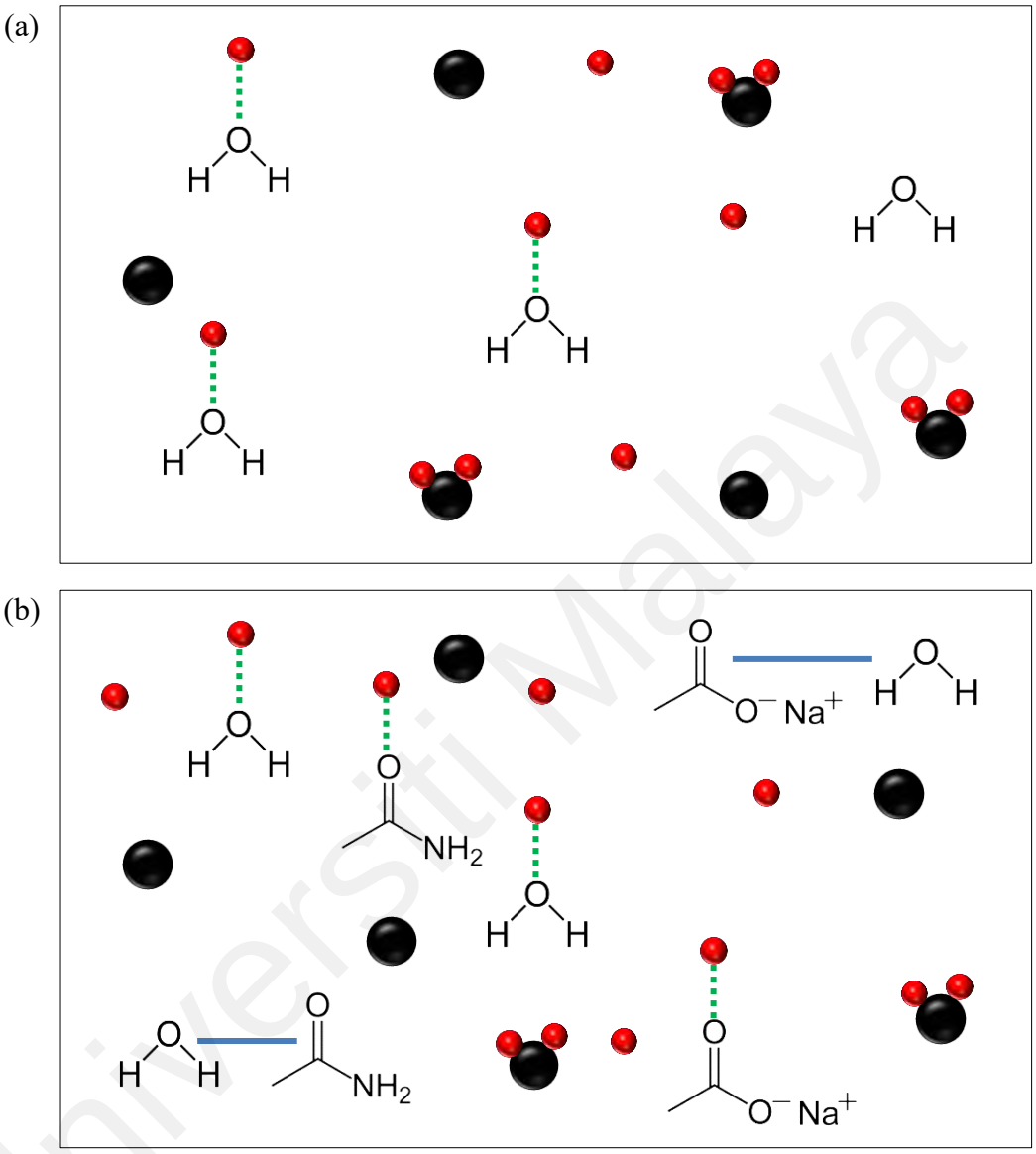

Figure 5.5: Ion mobility in the electrolyte system of (a) without polymer and (b) with the addition of PAAm-PAA.

In addition to copolymer segment, the μ of Na^+ cations may be affected by different coordination sites of Na^+ cations, such as Na^+-water complex, Na^+-PAAm-PAA complex and PAAm-PAA-Na^+-water complex. This is because different types of cation coordination can produce different cation mobility. The vehicular motion of small molecule solvated cations (solvent coordination) is always faster than the chain dynamics of copolymers and cationic coordination (polymer coordination). In W0, Na^+ cations are

completely coordinated by water molecules (solvent), so the μ value of W0 is higher than other W GPEs. The more Na^+ cations coordinated purely by PAAm-PAA, the slower the μ of Na^+ cations (Ford et al., 2020). It can be deduced that the decrease in ionic conductivity is due to the decrease in μ.

5.2.3 Temperature Dependence of Ionic Conductivity

The electrolyte system is characterized by EIS from room temperature to 100 ℃ to analyze temperature-dependent ionic conductivity. The reading is taken every 5 ℃ increment. In the ionic conductivity-temperature relationship, the variation of σ with temperature determines which model to be applied. The model can be an Arrhenius or Vogel-Fulcher-Tammann (VFT) relationship. The calculation method of activation energy (E_A) varies by the model. E_A is the minimum energy acquired by the ion jumping from one to another donor site while moving. The ion hopping leads to charge conduction.

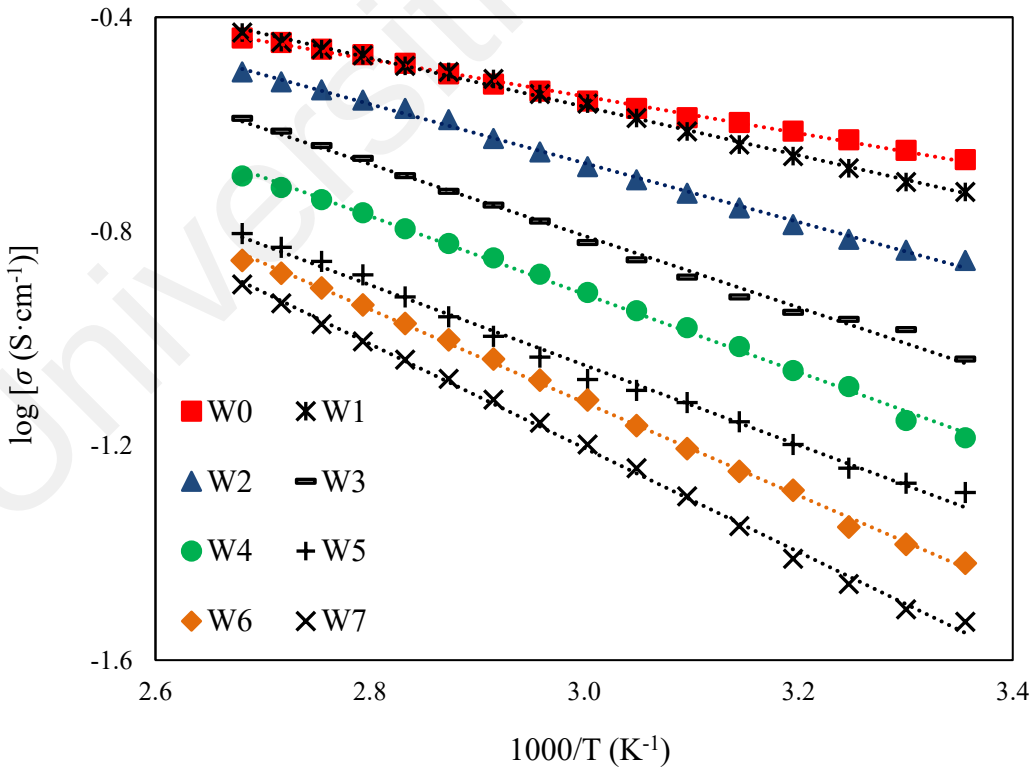

Figure 5.6: Temperature dependence of ionic conductivity of system W.

Figure 5.6 depicts the temperature dependence of the ionic conductivity of system W. The relationship between log σ and 1000/T can be examined by the graph. These two variables have a negative linear relationship and an inverse relationship. When the temperature (1000/T) increases, the ionic conductivity (log σ) decreases. The coefficient of determination (R^2) of all W GPEs is close to 0.99, indicating that the temperature dependence of the ionic conductivity of the W system obeys to the Arrhenius rule. By obeying the Arrhenius rule, E_A can be calculated from the Equation 5.5:

$$\sigma = \sigma_0 \exp\left[\frac{-E_A}{k_b T}\right] \tag{5.5}$$

where σ_0 is a pre-exponential factor and T is the temperature (K). Therefore, the value of E_A can be obtained by deriving Equation 5.5:

$$E_A = -\frac{k_b \, x \, m \, x \, 1000}{0.4343} \tag{5.6}$$

Table 5.3 lists the gradient (m), E_A and R^2 values of system W.

Table 5.3: Gradient (m), E_A and R^2 values of system W.

GPE	m (10^{-2} K)	E_A (10^{-1} eV)	R^2
W0	-34.39	0.68	0.996
W1	-45.44	0.90	0.996
W2	-55.03	1.09	0.997
W3	-66.89	1.33	0.994
W4	-72.78	1.44	0.998
W5	-74.74	1.48	0.994
W6	-86.86	1.72	0.998
W7	-97.07	1.93	0.998

When ions jump from one position to another with the assistance of temperature, they obey the Arrhenius rule. It can be seen from Table 5.3 that as PAAm-PAA wt.% increases, the gradient obtained in Figure 5.6 increases, and the calculated E_A also increases. This implies the trend of E_A increases as the ionic conductivity of GPE decreases, as depicted

in Figure 5.7. E_A is inversely proportional to ionic conductivity. In addition, more copolymer content helps to increase the viscosity of GPE (see Figure 4.5). It has been revealed that the viscosity of GPE increases and solidifies beyond 30 wt.% PAAm-PAA (W6, see Table 4.4). When the GPE tends to a solid state, the dissociated ions will not be able to move freely, thus reducing the ionic conductivity of the GPE. It can be deduced that highly conductive GPE (W0) has higher free ion mobility, so it requires lower energy (E_A) for ion hopping (Ahmed & Abdullah, 2020b; Buraidah et al., 2009). This can be proven by the decrease in μ from (795.49 ± 84.90) $cm^2 \cdot V^{-1} \cdot s^{-1}$ of W0 to (0.96 ± 0.11) $cm^2 \cdot V^{-1} \cdot s^{-1}$ of W7 at a frequency of 30 kHz.

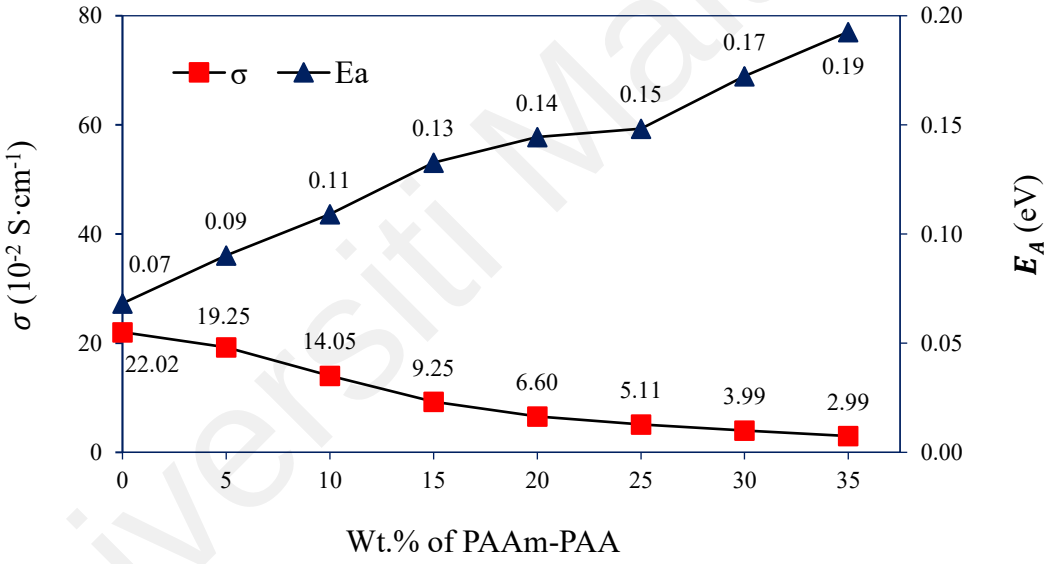

Figure 5.7: Variation of room temperature ionic conductivity and activation energy dependence in system W.

5.3 X System – Gel Polymer Electrolytes with Various Molarity of Salt

In system X, the optimized ratio of PAAm-PAA to polysulfide electrolyte is fixed at 25:75 (see W5, optimized GPE in system W). For the optimized composition W5 (also called X3 in this system), the molarity of Na_2S in the polysulfide electrolyte varies from 2 M to 6 M with an interval of 1 M. The content of Na_2S:S is fixed at 4:1.

5.3.1 Room Temperature Ionic Conductivity

In system X, the shape of the Nyquist plot appears as tilted spike, as shown in Figure 5.8. The tilted spike is fitted using the equivalent circuit, where R_b is connected in series with CPE. The fitting points (●) are similar to the experimental data. Table 5.4 lists the R_b, k and N values of system X. Refer to Table 5.4, as the molarity of Na_2S increases, R_b decreases. Beyond 4 M Na_2S (X3/W5), R_b starts to increase. According to Equation 3.2, R_b is inversely proportional to ionic conductivity. When R_b starts to increase, the ionic conductivity drops.

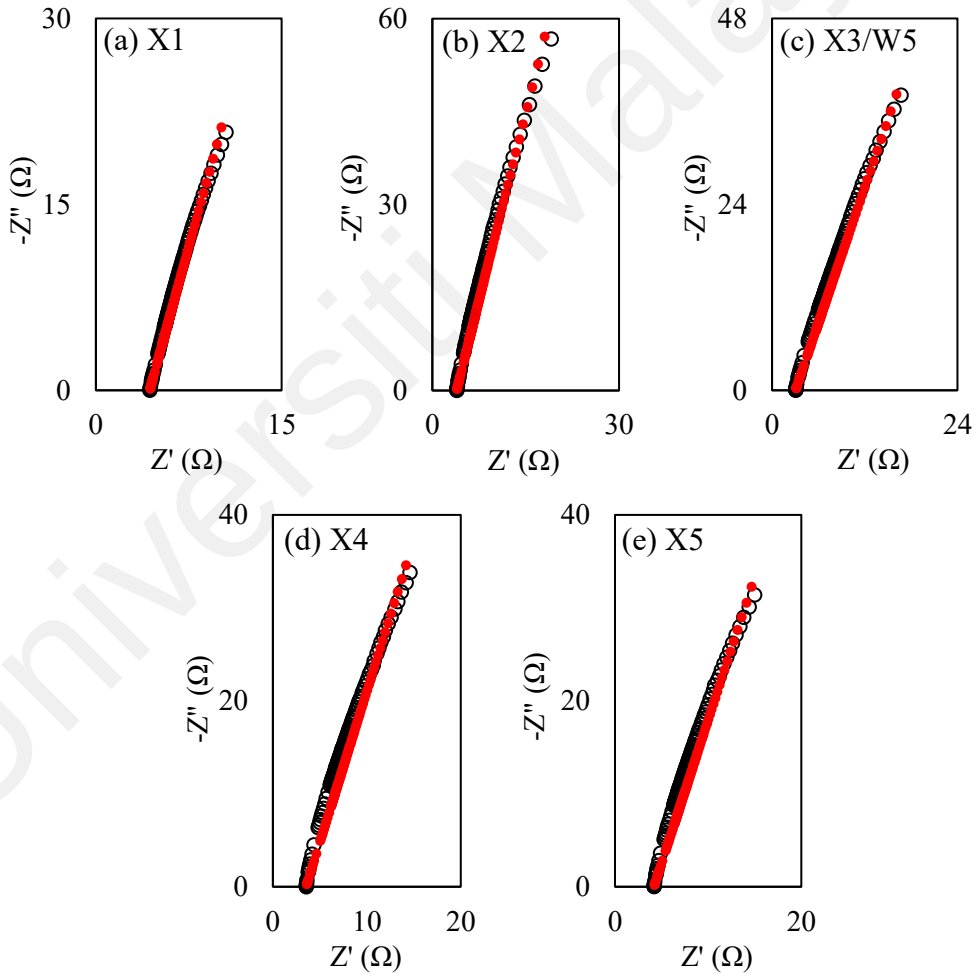

Figure 5.8: Nyquist plot (○) for PAAm-PAA aqueous solution added with (a) 2 M (X1), (b) 3 M (X2), (c) 4 M (X3/W5), (d) 5 M (X4) and (e) 6 M (X5) Na_2S and their corresponding fitting (●) at room temperature.

Table 5.4: R_b, k and N values of system X.

GPE	R_b (Ω)	k (10^{-4} $F^{-1}s^{1-N}$)	N (10^{-1})
X1	4.26 ± 0.07	1.37 ± 0.12	8.09 ± 0.22
X2	3.90 ± 0.03	1.29 ± 0.06	7.97 ± 0.28
X3/W5	2.91 ± 0.14	1.32 ± 0.11	8.04 ± 0.09
X4	3.70 ± 0.08	1.26 ± 0.12	8.04 ± 0.19
X5	4.13 ± 0.08	1.24 ± 0.09	8.07 ± 0.08

The room temperature ionic conductivity of system X is calculated using Equation 3.2, as depicted in Figure 5.9. The highest ionic conductivity is observed at (5.11 ± 0.24) × 10^{-2} S·cm^{-1} of X3/W5. Although the molar concentration of Na_2S increases, the ionic conductivity of X4 decreases from (5.11 ± 0.24) × 10^{-2} S·cm^{-1} to (4.01 ± 0.09) × 10^{-2} S·cm^{-1}. This can be attributed to ion aggregation. When the amount of Na_2S exceeds the limit, the distance between ions becomes shorter and the ions collide to form aggregates. When ion aggregation occurs, free ions move slowly in the medium while conducting current, thereby decreasing the ionic conductivity (Ahmed & Abdullah, 2020b; Aziz et al., 2014; Noor et al., 2011; Noor et al., 2014). The GPE with the highest ionic conductivity will be selected as the optimized GPE for the next system.

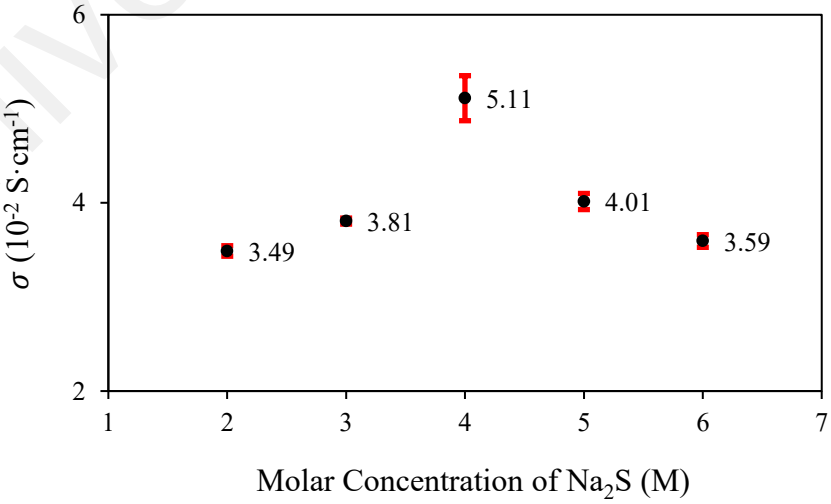

Figure 5.9: Room temperature ionic conductivity of system X.

5.3.2 Dielectric and Transport Properties

In Figure 5.10, the trend of ε' increases as the molar concentration of Na_2S increases. After adding 5 M Na_2S, ε' began to decrease. This trend applies to all frequencies. It can be deduced that in system X, the variation of ε' with Na_2S molar concentration follows the variation of ionic conductivity. Due to electrode polarization, the calculated value of ε' increases as the frequency decreases. For instance, the ε' of X1 in Table 5.5 has increased from $(0.14 \pm 0.05) \times 10^6$ at 30 kHz to $(4.05 \pm 0.71) \times 10^6$ at 5 kHz.

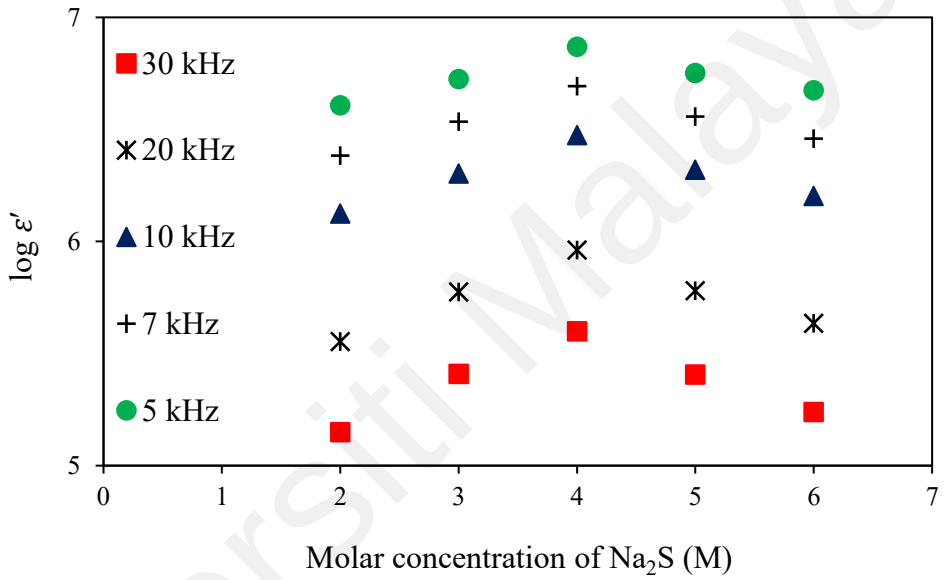

Figure 5.10: Na_2S molar concentration dependence of ε' of system X at selected frequencies.

Table 5.5: ε' value of system X at selected frequencies.

GPE	30 kHz	20 kHz	10 kHz	7 kHz	5 kHz
	ε' (10^6)	ε' (10^6)	ε' (10^6)	ε' (10^6)	ε' (10^6)
X1	0.14 ± 0.05	0.36 ± 0.10	1.33 ± 0.32	2.42 ± 0.50	4.05 ± 0.71
X2	0.26 ± 0.05	0.60 ± 0.09	2.01 ± 0.22	3.42 ± 0.28	5.31 ± 0.29
X3/W5	0.40 ± 0.06	0.92 ± 0.11	2.98 ± 0.20	4.93 ± 0.27	7.40 ± 0.44
X4	0.26 ± 0.06	0.60 ± 0.13	2.09 ± 0.35	3.61 ± 0.48	5.65 ± 0.51
X5	0.17 ± 0.02	0.43 ± 0.04	1.60 ± 0.12	2.88 ± 0.20	4.73 ± 0.30

Based on Equation 5.3 and 5.4, the calculated values of μ and n for system X at selected frequencies (30 kHz and 5 kHz) are shown in Figure 5.11. The variation of μ

with Na_2S molar concentration is similar to the variation of ionic conductivity. This has been observed at all frequencies. In Figure 5.11 (a), n decreases when 3 M Na_2S (X2) is added, and then increases after 4 M Na_2S (X3/W5). It was observed that the highest n was obtained by 2 M Na_2S (X1), which was $(33.34 \pm 0.30) \times 10^{16}$ cm^{-3}, and then reduced to $(10.43 \pm 0.52) \times 10^{16}$ cm^{-3} (X2). The lowest n is observed at X3/W5, which is $(2.95 \pm 0.00) \times 10^{16}$ cm^{-3}. After that, as the molar concentration of Na_2S increases, n gradually increases. At the low frequency of 5 kHz in Figure 5.11 (b), n also decreases when higher molar concentration of Na_2S is added up to 4 M (X3/W5). However, the variation of n with Na_2S molar concentration is not obvious as compared to 30 kHz.

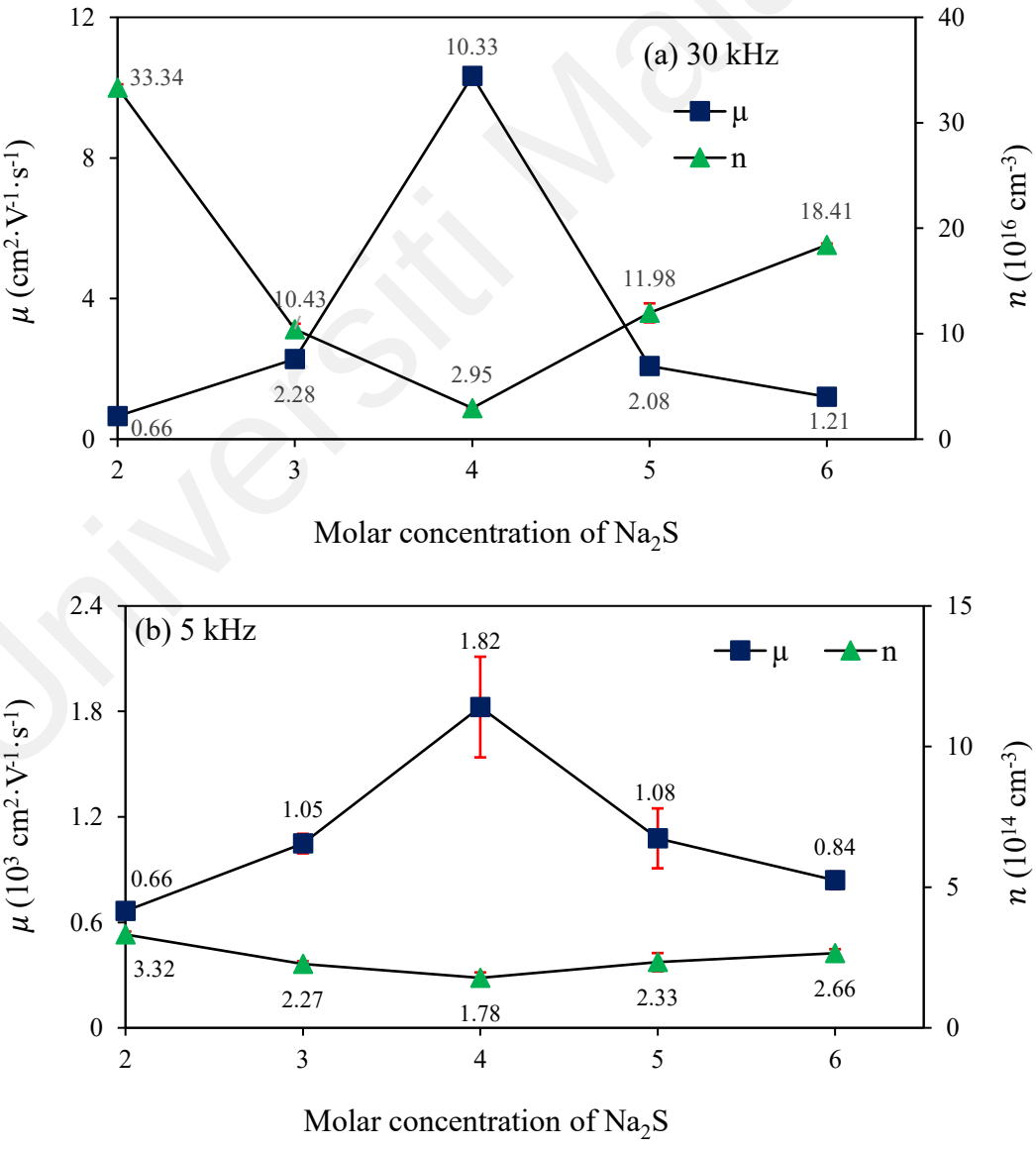

Figure 5.11: Variation of μ and n of system X at (a) 30 kHz and (b) 5 kHz.

It is reported that the ionic conductivity of the electrolyte is significantly affected by ionic mobility. At high concentrations, the ionic mobility will be affected by ion aggregation. Therefore, the study of electrolyte ionic conductivity should always start with dilute electrolytes (Bruce & Vincent, 1993). In system X, we first examine the ionic conductivity of the sample at a relatively low salt concentration, which is 2 M Na_2S (X1). It can be considered that X1 is the most dilute GPE, in which the Na_2S salt is completely dissociated into independent ions (the red atoms are Na^+ cations, and the black atoms are S^{2-} anions), as schematized in Figure 5.12 (a). This explains the highest n obtained by X1 at all frequencies. However, due to the low ionic mobility, X1 exhibits low ionic conductivity.

According to the literature, when a higher molar concentration of salt is added, n usually increases. Interestingly, when the molar concentration of Na_2S increases to 3 M (X2) and 4 M (X3/W5), n decreases. The decrease in n at higher salt concentrations can be attributed to ion re-association or the inability of the polymer matrix in the electrolyte system to effectively dissociate the salt. When the dissolution of salt in the gel polymer matrix is slow, the ions will recombine, and the salt will recrystallize in the gel polymer matrix (Ahmed & Abdullah, 2020a; Bruce & Vincent, 1993). In this fashion, despite the presence of free ions, there is also ion associates in the electrolyte system. Ion associates include ion pairs, triatomic groups, and higher-order associates. It can be considered that in the X2 GPE system, the ion re-association rate is faster than the ion dissociation rate, so although there are free cations (red atoms) and free anions (black atoms), there are also ion pairs (a single black atom bonded by two red atoms) and ion associates (blue atoms), as schematized in Figure 5.12 (b). This is advantageous for the μ of the electrolyte system, because when free ions recombine to form ion pairs, it free up the complexing sites. Figure 5.12 (b) shows the hopping of Na^+ cation from the occupied complex site to the empty site before moving to another position (see the direction of the black arrow). The

complexing sites could serve as a temporary parking lot, which saves the energy required for the movement of free ions in the medium to conduct current and increases μ.

As Na_2S molar concentration increases up to 5 M (X4), the distance between ions becomes shorter, below the critical distance, which promotes the formation of ion aggregates (green atoms), as schematized in Figure 5.12 (c). The critical distance (Å) between ions can be determined, such as between Na^+ and S^{2-} ions, between Na^+ and Na^+ ions, and between S^{2-} and S^{2-} ions. One of the methods is called site-site radial distribution function (RDF). When the relative distance between ions gets closer and lower than their critical distance, ion aggregates form (Choi & Cho, 2014; Molinari et al., 2018). In addition, the permittivity decreases at X4. In addition, when the permittivity of the electrolyte system is low, the degree of association increases as the salt concentration increases (Son & Wang, 2020; Voropaeva et al., 2020). This creates a large potential energy between the ions in contact, hence promoting ion association. Ion association may also occur between free ions and neutral ion pairs to form ion aggregates (Bruce & Vincent, 1993). Ion aggregates include positively charged ion aggregates, negatively charged ion aggregates, sodium aggregates, and sulfur aggregates (Kleinjan et al., 2005; Moon & Lim, 2020). The formation of ion aggregates may contribute to the increase in n after 4 M Na_2S (X3/W5).

Due to the high salt concentration, the congestion of neutral ion pairs, free ions, and ion aggregates is likely to occur in the medium. Ion aggregates are undesirable because they lower the μ of the electrolyte system. The mass of the ion aggregate is the sum of all attached ions; therefore, the movement speed of the ion aggregate is slower than that of a single free ion. It can be seen from the figure that the ion aggregates (green atoms) may block the passage of Na^+ cations (red atoms) when the electric field is applied and reduce the μ of Na^+ cations (see the black arrow direction).

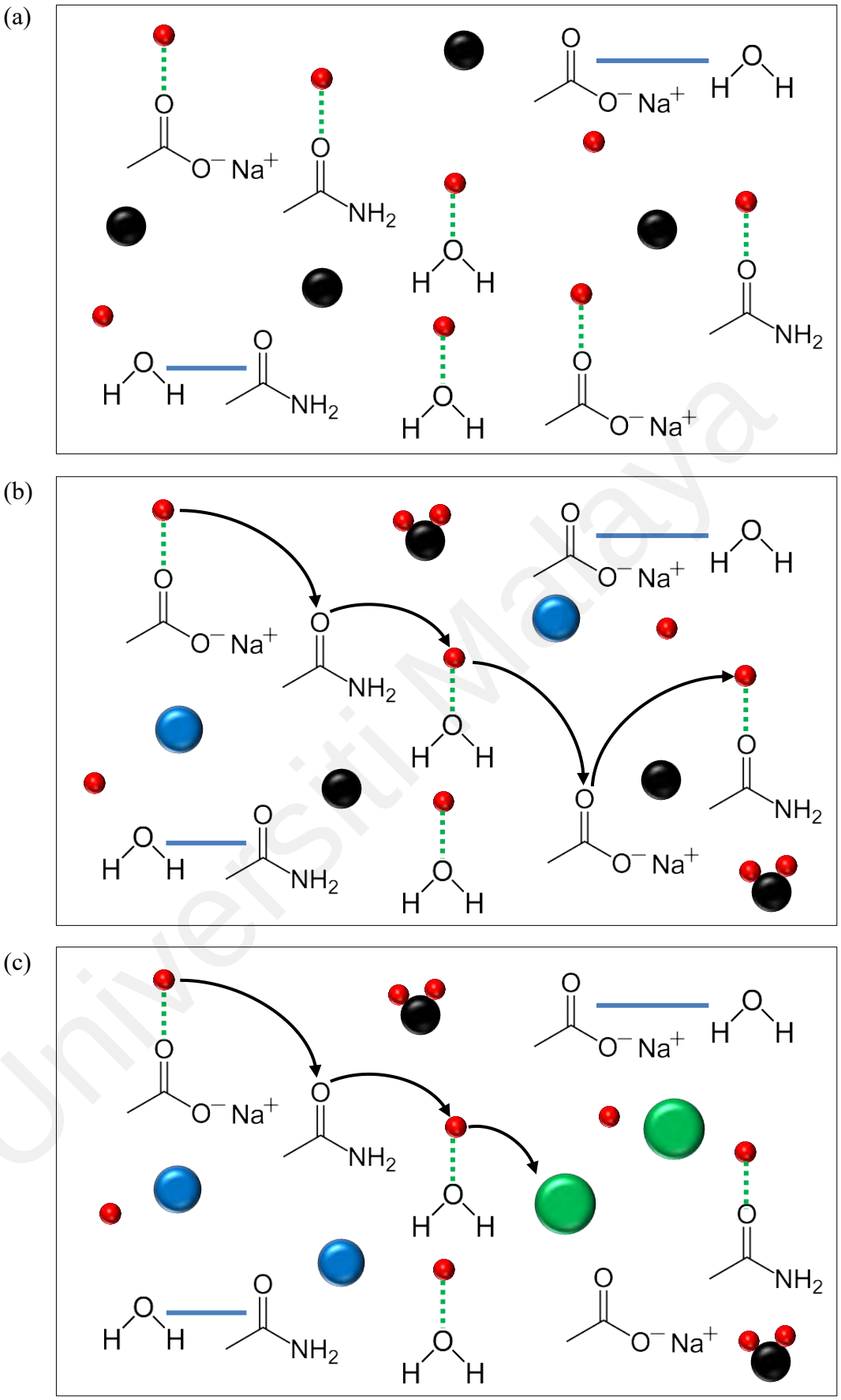

Figure 5.12: Ion mobility in the electrolyte system of (a) X1, (b) X2 and (c) X4.

In addition, the cation mobility is affected by the coordination environment of cation (Molinari et al., 2018; Rosenwinkel et al., 2020). The more Na^+ cations coordinated by the S^{2-} anion, the lower its mobility. It is known that ionic conductivity depends on μ and n. Despite the increase of n due to high salt concentration, when μ decreases drastically, the ionic conductivity of X4 decreases. Therefore, it can be deduced that μ dominates the ionic conductivity of GPE in system X.

5.3.3 Temperature Dependence of Ionic Conductivity

In Figure 5.13, a negative linear relationship is observed, and R^2 is in the range of 0.98 to 1.00. This indicates that the Arrhenius rule also applies to the temperature dependence of the ionic conductivity of system X. It can be seen from the figure that the slopes of all X GPEs are almost the same.

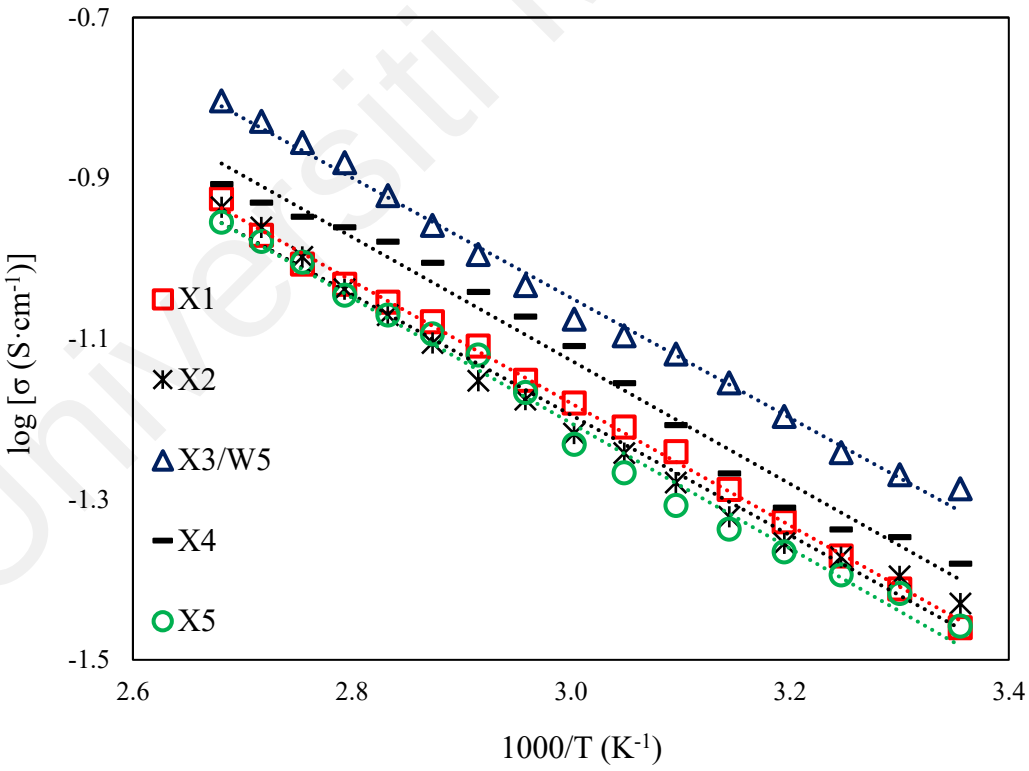

Figure 5.13: Temperature dependence of ionic conductivity of system X.

Referring to Table 5.6, as the molar concentration of Na_2S increases, the slope change obtained from Figure 5.13 is negligible. The calculated E_A is in the range of 0.15 to 0.16

eV. Although the lowest E_A (0.148 eV) of the highest ionic conductivity X3/W5 GPE was found, the overall result does not convincingly imply that E_A increases as the ionic conductivity of GPE decreases, because this slope change is negligible. This is expected because the addition of Na_2S:S only brings about a weight percentage difference of 1.0 to 1.5 wt.% (see Table 3.3). Moreover, in the context of quasi-solid electrolyte, E_A depends on the nature of the solvent heteroatom rather than the salt concentration. In the ion transport mechanism of quasi-solid electrolytes, the functional groups in the solvent influence the dipole reorientation (a single activation process of ion transport) (Arof et al., 2014b; Bandara et al., 2013; Dissanayake et al., 2012). Therefore, the calculated E_A is almost the same in system X, regardless of the Na_2S molar concentration.

Table 5.6: Gradient (m), E_A and R^2 values of system X.

GPE	m (10^{-2} K)	E_A (10^{-1} eV)	R^2
X1	76.12	1.51	0.998
X2	74.89	1.49	0.988
X3/W5	74.74	1.48	0.994
X4	76.84	1.52	0.984
X5	78.04	1.55	0.990

5.4 Y System – Gel Polymer Electrolytes with Single Additive

In system Y, EC is added as an additive to improve the electrical properties of GPE. The ionic conductivity and dielectric properties of the optimized GPE (X3/W5) will be examined by adding various wt.% of EC, ranging from 0 to 0.8 wt.%.

5.4.1 Room Temperature Ionic Conductivity

Figure 5.14 depicts the Nyquist plot of PAAm-PAA-Na_2S GPE doped with various wt.% of EC (Y system) at room temperature. After adding EC, the shape of the Nyquist plot remains as a tilted spike, and the value of R_b can be obtained at the Z' intercept. Table 5.7 lists the parameters of CPE obtained by fitting Nyquist experimental data. Trial and

error technique is used to fit the Nyquist experimental data of the corresponding frequency.

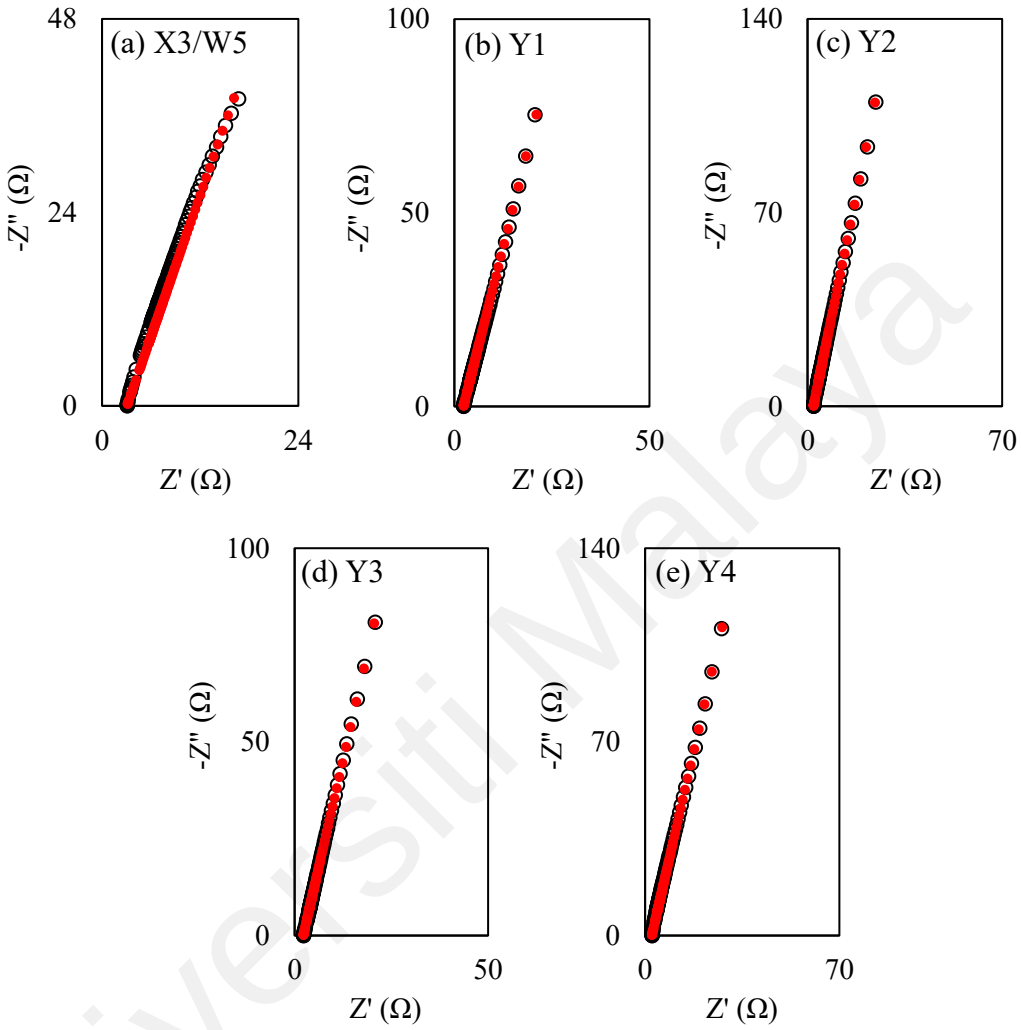

Figure 5.14: Nyquist plot (○) for PAAm-PAA-Na_2S GPE added with (a) 0 wt.% (X3/W5), (b) 0.2 wt.% (Y1), (c) 0.4 wt.% (Y2), (d) 0.6 wt.% (Y3) and (e) 0.8 wt.% (Y4) EC and their corresponding fitting (●) at room temperature.

Table 5.7: R_b, k and N values of system Y.

GPE	R_b (Ω)	k (10^{-5} $F^{-1}s^{1-N}$)	N (10^{-1})
X3/W5	2.91 ± 0.14	13.23 ± 1.12	8.04 ± 0.09
Y1	2.38 ± 0.02	5.34 ± 0.65	8.70 ± 0.28
Y2	2.15 ± 0.01	6.88 ± 0.34	8.65 ± 0.08
Y3	2.32 ± 0.03	6.78 ± 0.74	8.64 ± 0.06
Y4	2.39 ± 0.05	6.38 ± 0.11	8.54 ± 0.06

According to the literature (Noor et al., 2014; Woo et al., 2013), EC was added to create more coordination sites in the electrolyte system, which makes it easier for ions to jump to constitute electric currents. This shortcut promotes fast ion movement and results in lower energy required by ions to move (see Figure 5.15). As discussed in the previous chapter, interaction occur between EC and Na^+ cations in PAAm-PAA-Na_2S-EC GPE. The EC-Na^+ complex is formed in system Y. Figure 5.15 (a) shows the interaction between PAAm-PAA (amide -$CONH_2$ group and carboxylate COO^-Na^+ group) and Na^+ cations (red atom) in X3/W5 (GPE without EC). After adding EC, EC-Na^+ complexes occurred between PAAm-PAA-Na^+ complexes, as illustrated in Figure 5.15 (b).

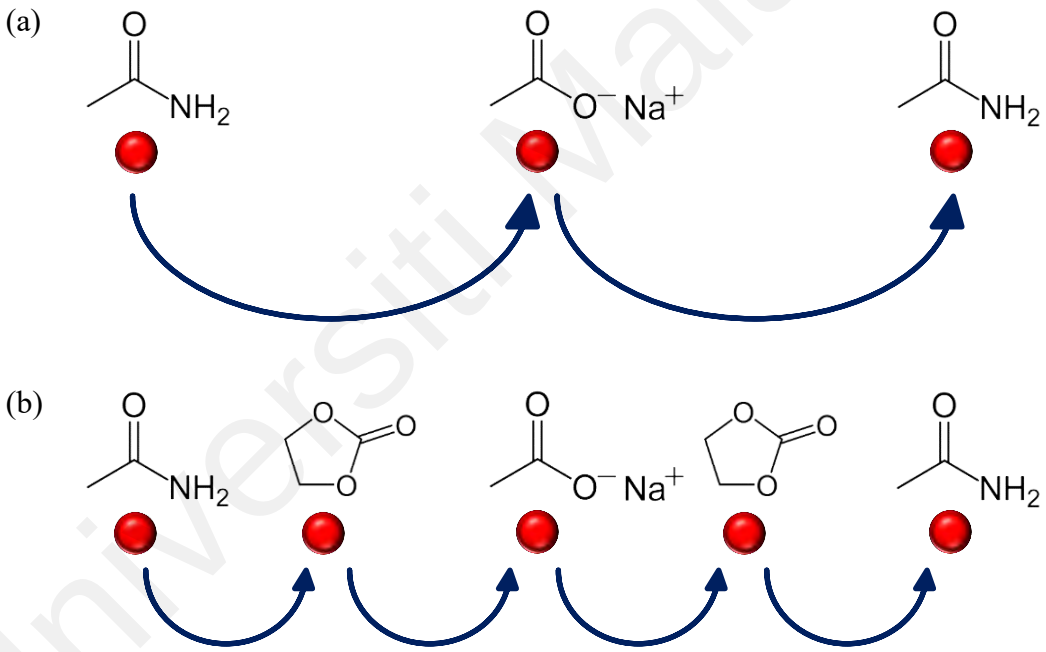

Figure 5.15: Coordination sites in system Y of (a) without EC and (b) with EC.

It can be observed that the distance of ion jumping (see blue arrow) becomes shorter because the shortcut is created by EC-Na^+ complex. This shortcut accelerates the ionic conductivity of the GPE. Therefore, upon incorporation of EC, the ionic conductivity of Y GPEs increase (see Figure 5.16). The ionic conductivity of Y2 (0.4 wt.% EC) demonstrates the highest ionic conductivity at $(6.92 \pm 0.02) \times 10^{-2}$ $S \cdot cm^{-1}$. It can be

observed that the ionic conductivity of the optimized X3/W5 GPE in system X has increased by 35%. Overall, the ionic conductivity of Y GPEs are similar.

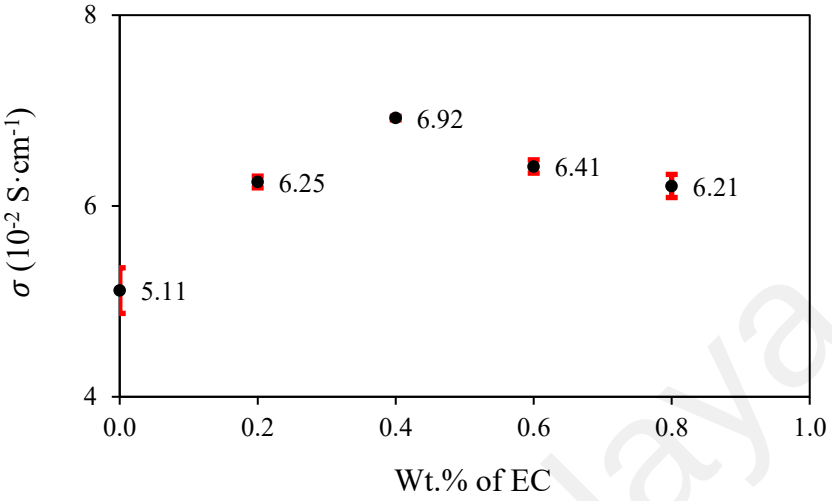

Figure 5.16: Room temperature ionic conductivity of system Y.

5.4.2 Dielectric and Transport Properties

Figure 5.17 shows the variation of ε' upon incorporation of EC at vary frequencies. The ε' values are listed in Table 5.8. As other system, the calculated values of ε' are increase with a decrease in frequency due to the electrode polarization. Electrode polarization is proportional to material permittivity. From Table 5.8, the ε' values are similar for all Y GPEs at 30 kHz and 20 kHz. A significant increment upon addition of EC (Y1 and Y2) can be observed at 10 kHz, 7 kHz and 5 kHz. Beyond 0.4 wt.% EC (Y2), the ε' values drop and become constant (Y3 and Y4). Overall, the variation of ε' with EC content has follow the variation of ionic conductivity with EC content as the highest ionic conductivity Y2 still has the highest ε' value at vary frequencies. In addition, it has been observed that the ε' for all Y GPEs especially at low frequencies are higher than X3/W5 (GPE without EC). This can be deduced that addition of EC increases the value of ε' as it has high dielectric constant (89.8) (Woo et al., 2013).

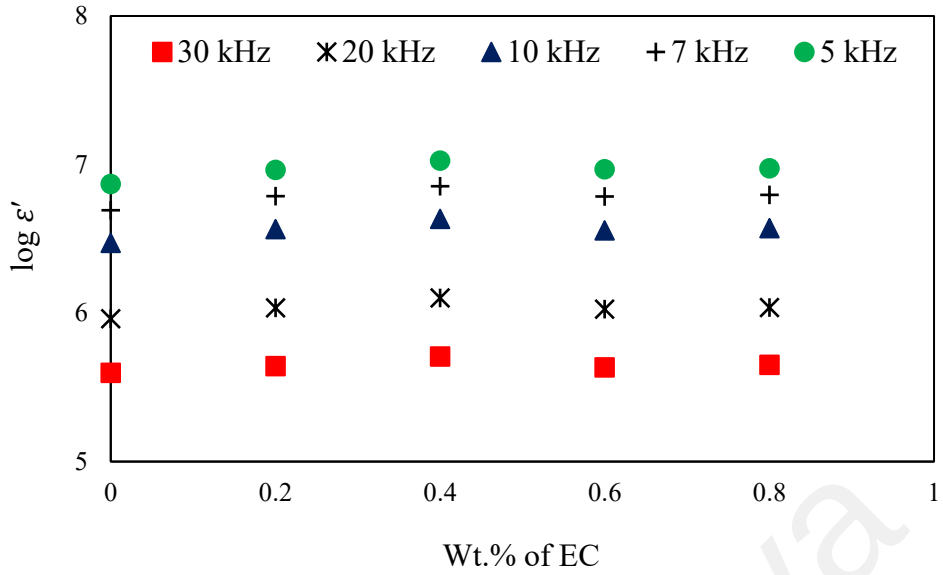

Figure 5.17: EC wt.% dependence of ε' of system Y at selected frequencies.

Table 5.8: ε' value of system Y at selected frequencies.

GPE	30 kHz	20 kHz	10 kHz	7 kHz	5 kHz
	ε' (10^6)	ε' (10^6)	ε' (10^6)	ε' (10^6)	ε' (10^6)
X3/W5	0.40 ± 0.06	0.92 ± 0.11	2.98 ± 0.20	4.93 ± 0.27	7.40 ± 0.44
Y1	0.44 ± 0.09	1.09 ± 0.18	3.68 ± 0.46	6.14 ± 0.60	9.23 ± 0.62
Y2	0.51 ± 0.04	1.27 ± 0.05	4.31 ± 0.10	7.17 ± 0.08	10.64 ± 0.07
Y3	0.43 ± 0.05	1.06 ± 0.11	3.61 ± 0.29	6.11 ± 0.36	9.31 ± 0.34
Y4	0.45 ± 0.02	1.09 ± 0.02	3.73 ± 0.01	6.28 ± 0.02	9.47 ± 0.08

Figure 5.18 depicts the variation of μ and n of system Y at 30 kHz and 5 kHz. A similar trend of the EC wt.% dependence of μ and n are observed for both frequencies. It can be observed that the mobility of charge carriers in Y GPEs is higher than the X3/W5 (GPE without EC). This observation supports the role play of EC in creating additional complexing sites in the electrolyte system. These vacancies act as additional parking lots before free ions jump to another, thus reducing the distance of ion jumping and increasing μ (Noor et al., 2014; Woo et al., 2013). In Figure 5.18 (a), after adding EC, μ is significantly increased from (10.33 ± 0.18) $cm^2 \cdot V^{-1} \cdot s^{-1}$ of X3/W5 to (42.89 ± 3.67) $cm^2 \cdot V^{-1} \cdot s^{-1}$ of Y1, and then gradually decreased with the increase of EC content.

As discussed in the previous chapter, by observing the changes in the intensity of the $CONH_2$ and COONa groups, it is proved that EC interacts with PAAm-PAA. Therefore, the decrease in μ may be due to the interaction between EC and PAAm-PAA. When EC forms a complex with PAAm-PAA, a new EC-PAAm-PAA complex site is formed. It can be considered that as the content of EC increases, the number of EC-PAAm-PAA coordination sites increases. Since different cation coordination produces different cation mobility, the μ of Na^+ cations coordinated purely by EC is different from the μ of Na^+ cations coordinated by EC-PAAm-PAA. Likewise, the μ of Na^+ cations coordinated purely by PAAm-PAA is also different from the μ of Na^+ cations coordinated by EC-PAAm-PAA (Ford et al., 2020). Therefore, it can be deduced that the decrease in μ may be due to the formation of EC-PAAm-PAA complex site. Due to inverse relationship between μ and n, μ decreases and n increases. It can be deduced that the increase in μ dominates the increase in the ionic conductivity of Y GPEs.

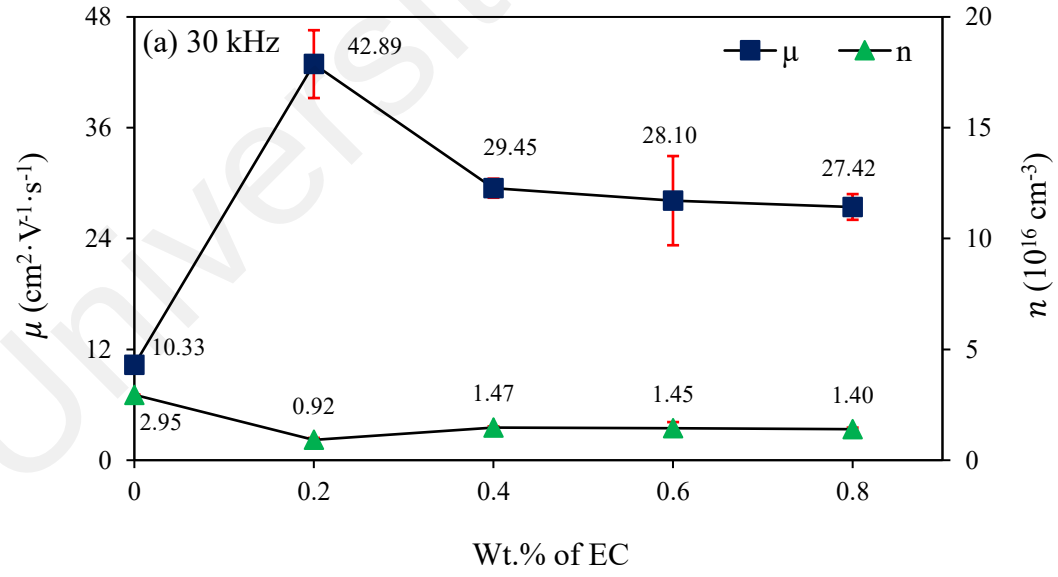

Figure 5.18: Variation of μ and n of system Y at (a) 30 kHz and (b) 5 kHz.

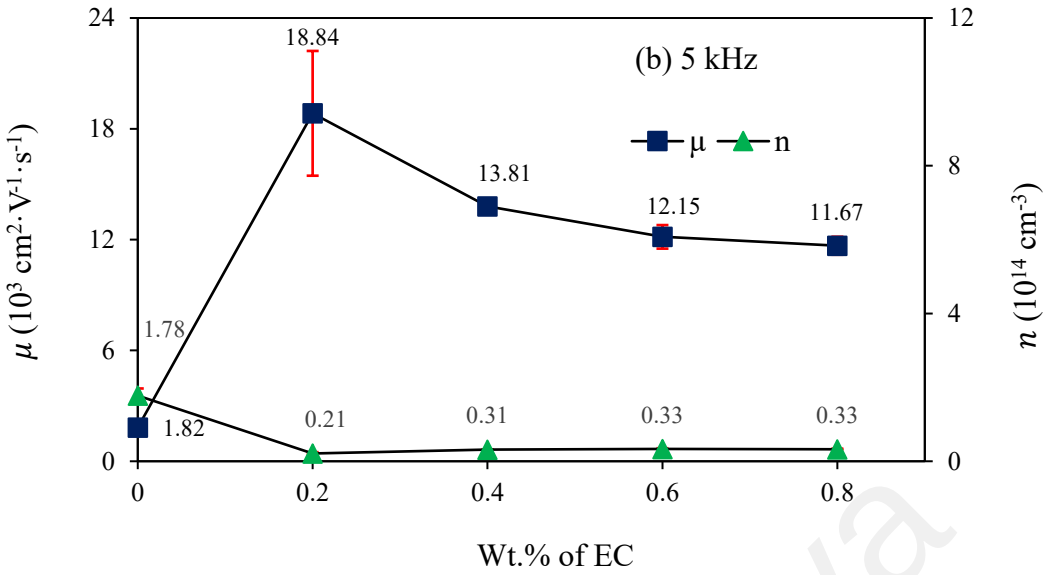

Figure 5.18, continued.

5.4.3 Temperature Dependence of Ionic Conductivity

Figure 5.19 depicts the temperature dependence of the ionic conductivity of system Y. After adding EC, the slope of log σ versus 1000/T changed. The inclination angle of Y1 (from the x-axis) is smaller than the inclination angle of X3/W5. According to Equation 5.6, when m decreases, E_A decreases. The slope depends on the angle of inclination. When the inclination angle increases, the slope becomes more sloping and m increases. This shows that adding EC to GPE will affect the E_A of GPE. Table 5.9 summarizes the gradient (m), E_A and R^2 values of system Y. Upon incorporation of EC, the value of E_A gradually decreases. Y2 has the lowest E_A because it is reported as the most conductive GPE in the Y system. It has been observed that the R^2 of Y2 is 0.987, which is due to the two points being out of range at higher temperatures (see blue triangle). This is because the ionic conductivity of Y2 increases drastically when assisted by temperature. This indicates that the higher the temperature, the faster the ion movement, and the higher the ionic conductivity of GPE.

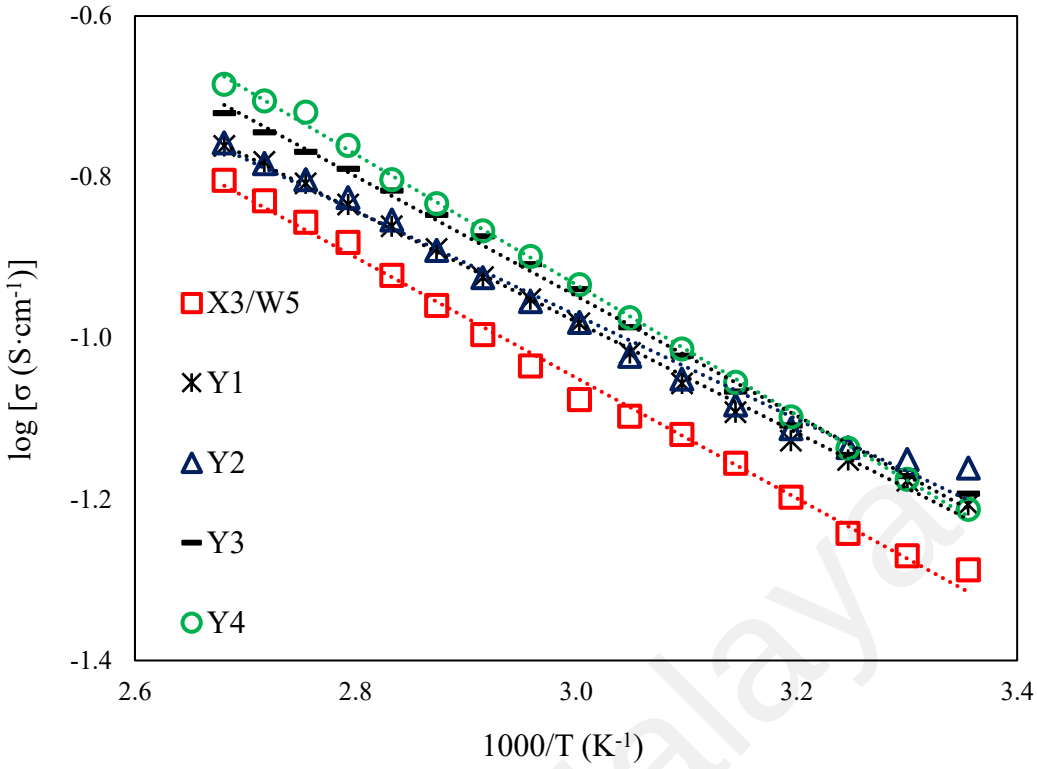

Figure 5.19: Temperature dependence of ionic conductivity of system Y.

Table 5.9: Gradient (m), E_A and R^2 values of system Y.

GPE	m (10^{-2} K)	E_A (10^{-1} eV)	R^2
X3/W5	-74.74	1.48	0.994
Y1	-68.83	1.37	0.997
Y2	-64.60	1.28	0.987
Y3	-74.31	1.47	0.996
Y4	-80.92	1.61	0.999

Figure 5.20 shows that E_A is inversely proportional to ionic conductivity. When the ionic conductivity increases, the E_A of Y GPEs decreases. As mentioned earlier, EC was added to create more coordination sites for ion hopping, therefore make it easier for ions to hop from one location to another. It can be deduced that adding EC to GPE minimize the energy required for ions jumping.

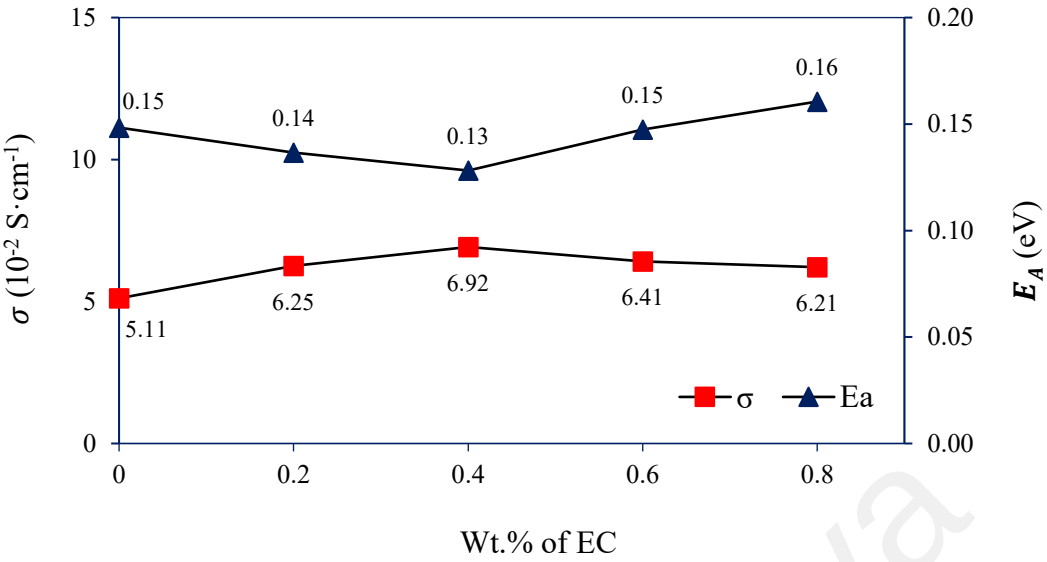

Figure 5.20: Variation of room temperature ionic conductivity and activation energy dependence in system Y.

5.5 Z System – Gel Polymer Electrolytes with Double Additives

In system Y, Y2 is the optimized GPE because it has the highest ionic conductivity. Various wt.% of KCl are added to the optimized GPE to prepare the Z GPEs.

5.5.1 Room Temperature Ionic Conductivity

The Nyquist plot of PAAm-PAA-Na_2S-EC-KCl GPE (Z system) is drawn and fitted through trial and error to obtain R_b and CPE parameters (see Figure 5.21), which are listed in Table 5.10. The shape of the Nyquist plot of Z GPE is still a tilted spike. Referring to Table 5.10, Z1 exhibits the highest R_b at (2.67 ± 0.02) Ω, and gradually decreases with the increase of KCl content. Z3 (0.6 wt.% KCl) has the lowest R_b, which is (2.10 ± 0.02) Ω.

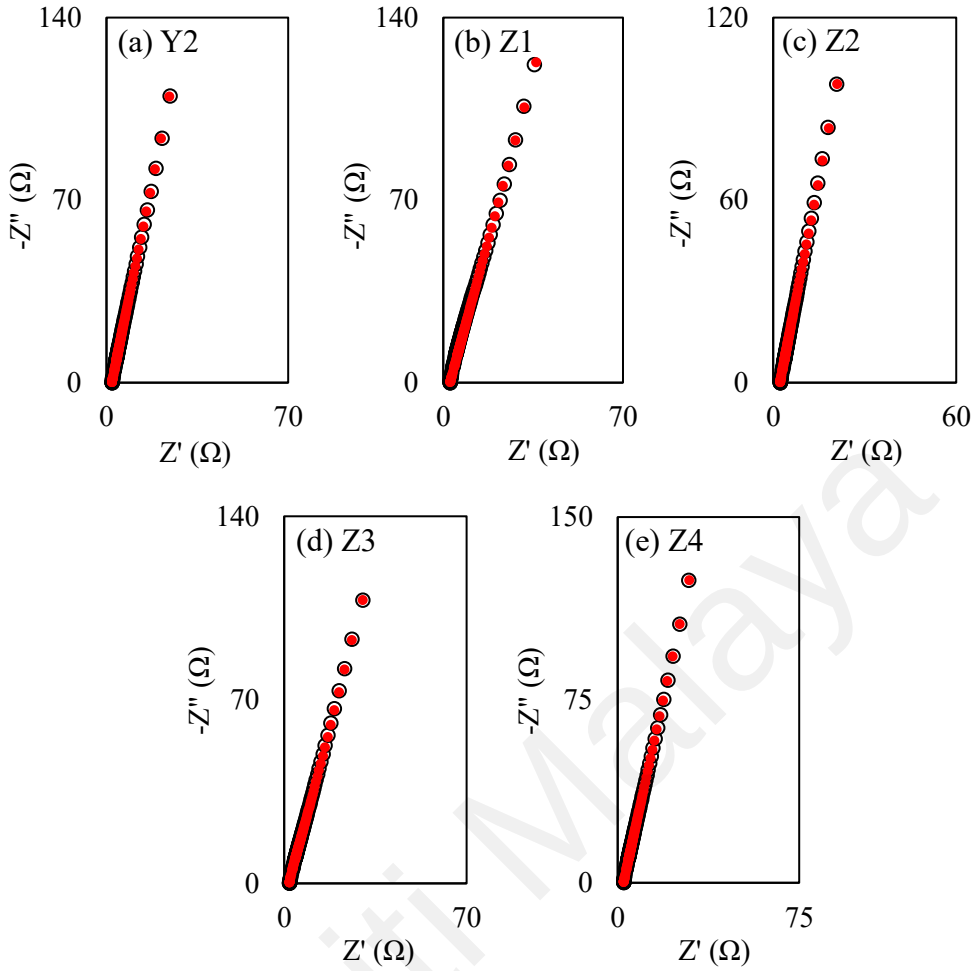

Figure 5.21: Nyquist plot (○) for PAAm-PAA-Na_2S-EC GPE added with (a) 0 wt.% (Y2), (b) 0.2 wt.% (Z1), (c) 0.4 wt.% (Z2), (d) 0.6 wt.% (Z3) and (e) 0.8 wt.% (Z4) KCl and their corresponding fitting (●) at room temperature.

Table 5.10: R_b, k and N values of system Z.

GPE	R_b (Ω)	k (10^{-4} $F^{-1}s^{1-N}$)	N (10^{-1})
Y2	2.15 ± 0.01	6.88 ± 0.34	8.65 ± 0.08
Z1	2.67 ± 0.02	6.04 ± 0.52	8.46 ± 0.14
Z2	2.26 ± 0.03	6.55 ± 0.28	8.73 ± 0.11
Z3	2.10 ± 0.02	7.05 ± 0.28	8.49 ± 0.12
Z4	2.42 ± 0.03	5.53 ± 0.03	8.64 ± 0.05

Since R_b is inversely proportional to the ionic conductivity, Z1 has the lowest ionic conductivity at (5.56 ± 0.04) × 10^{-2} S·cm^{-1}, and Z3 has the highest ionic conductivity at (7.08 ± 0.06) × 10^{-2} S·cm^{-1} (see Figure 5.22). A 2% increase in ionic conductivity from the ionic conductivity of Z3 to that of the optimized Y2 GPE has been observed.

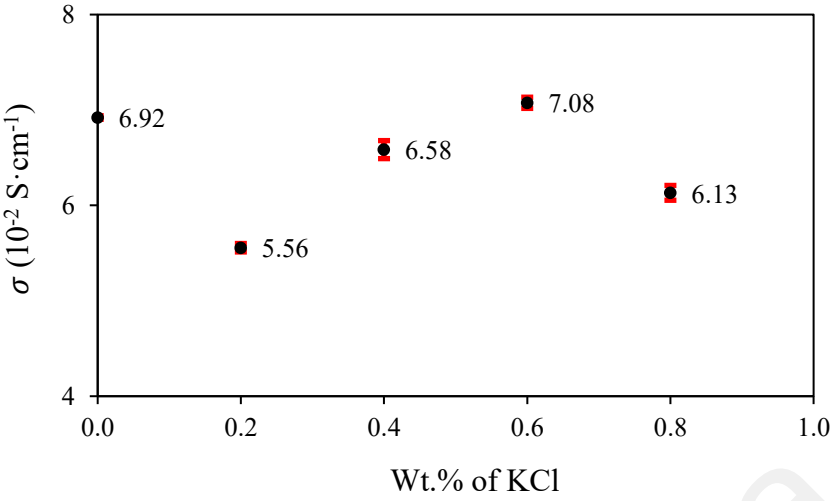

Figure 5.22: Room temperature ionic conductivity of system Z.

5.5.2 Dielectric and Transport Properties

Figure 5.23 shows the variation of ε' upon incorporation of KCl at vary frequencies. Table 5.11 lists the values of ε'. From Table 5.11, the ε' values are similar for all Z GPEs at 30 kHz. Significant changes are observed at 20 kHz, 10 kHz, 7 kHz and 5 kHz. Beyond 0.6 wt.% KCl (Z3), the ε' values drop (Z4). It can be deduced that the variation of ε' with KCl content has follow the variation of ionic conductivity with KCl content as the highest ionic conductivity Z3 has the highest ε' value at vary frequencies.

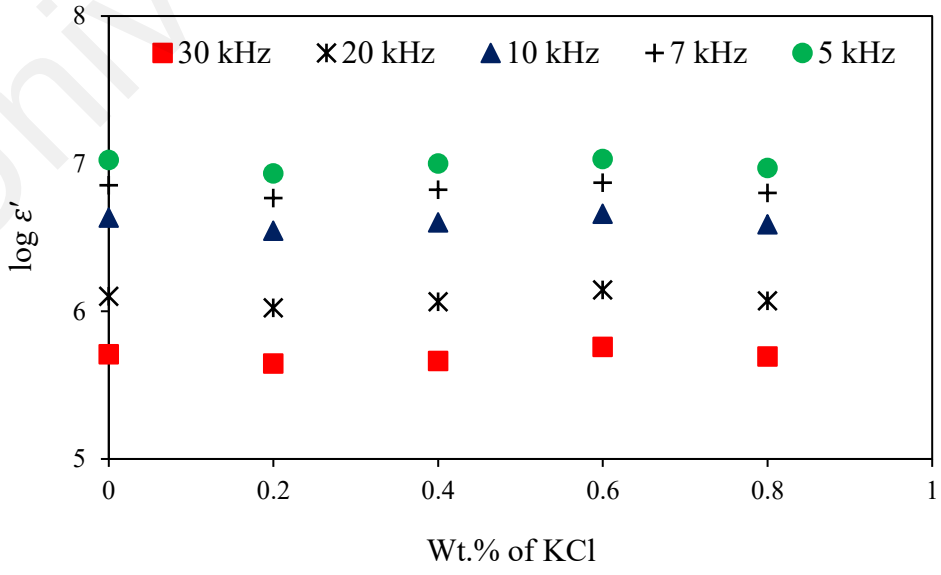

Figure 5.23: KCl wt.% dependence of ε' of system Z at selected frequencies.

Table 5.11: ε' value of system Z at selected frequencies.

GPE	30 kHz	20 kHz	10 kHz	7 kHz	5 kHz
	ε' (10^6)	ε' (10^6)	ε' (10^6)	ε' (10^6)	ε' (10^6)
Y2	0.51 ± 0.04	1.27 ± 0.05	4.31 ± 0.10	7.17 ± 0.08	10.64 ± 0.07
Z1	0.44 ± 0.02	1.06 ± 0.03	3.53 ± 0.06	5.85 ± 0.07	8.63 ± 0.08
Z2	0.46 ± 0.04	1.16 ± 0.09	4.01 ± 0.25	6.68 ± 0.33	10.03 ± 0.29
Z3	0.57 ± 0.07	1.40 ± 0.15	4.59 ± 0.35	7.43 ± 0.34	10.78 ± 0.26
Z4	0.50 ± 0.03	1.18 ± 0.06	3.89 ± 0.20	6.36 ± 0.22	9.37 ± 0.18

As discussed in the previous chapter, adding KCl may weaken the interaction of Na^+ cations in Z GPE with PAAm-PAA or EC or water. This is because KCl is a metal halide salt, which can also form coordination sites with PAAm-PAA or EC or water. Adding KCl to GPE provides multiple choices for PAAm-PAA, EC and water to form a complex. However, although KCl is a salt, it does not significantly increase the ionic conductivity of Y2 GPE but improve the μ of GPE (see Figure 5.24). Figure 5.24 shows the variation of μ and n with KCl content at 30 kHz and 5 kHz. It is observed that the variation of μ and n with KCl content does not follow the variation of ε' and ionic conductivity. In addition, the trends of μ and n with KCl content at 30 kHz are different from 5 kHz. At high frequency of 30 kHz, n decreases at 0.2 wt.% KCl (Z1) and increases at 0.4 wt.% KCl (Z2). After 0.4 wt.% KCl, n gradually decreases to $(0.71 \pm 0.00) \times 10^{16}$ cm^{-3}. At the low frequency of 5 kHz, the value of n constant and decreases after 0.6 wt.% KCl (Z3).

KCl is a salt containing K^+ cations and Cl^- anions. Therefore, it is expected that the addition of KCl will increase the n. However, this scenario did not apply to the Z GPEs in Figure 5.24. This may be attributed to the ion association. As discussed in system X, due to the low permittivity of the electrolyte system and the short critical distance between ions at high salt concentrations, the ion re-association rate is faster than the ion dissociation rate. The decrease of n will decrease the ionic conductivity of Z GPEs. It can be deduced that the decrease in ionic conductivity of Z GPEs is dominated by n, which is attributed to the fast ion re-association speed between ions.

In the case of μ, it increases as the amount of KCl increases except for 0.2 wt.% KCl (Z1) at 5 kHz as shown in Figure 5.24 (a) and (b). By observing the change trend of μ and n, the addition of KCl increased the mobility of free ions and reduced the number of free ions. According to the literature, of the Na^+ and K^+ cations, K^+ preferentially to transforms the polymer from the crystalline phase to the amorphous phase. It is reported that under the same salt concentration, the volume fraction of the amorphous phase in the K^+ containing system is higher (Zhang et al., 2003). It is well known that ions move faster in the amorphous phase. Therefore, the increase of μ in Z GPEs can be attributed to the existence of K^+. In this fashion, although the μ of Z GPEs increases as the amount of KCl increases, the ionic conductivity of Z GPEs are not improved due to decrease in n.

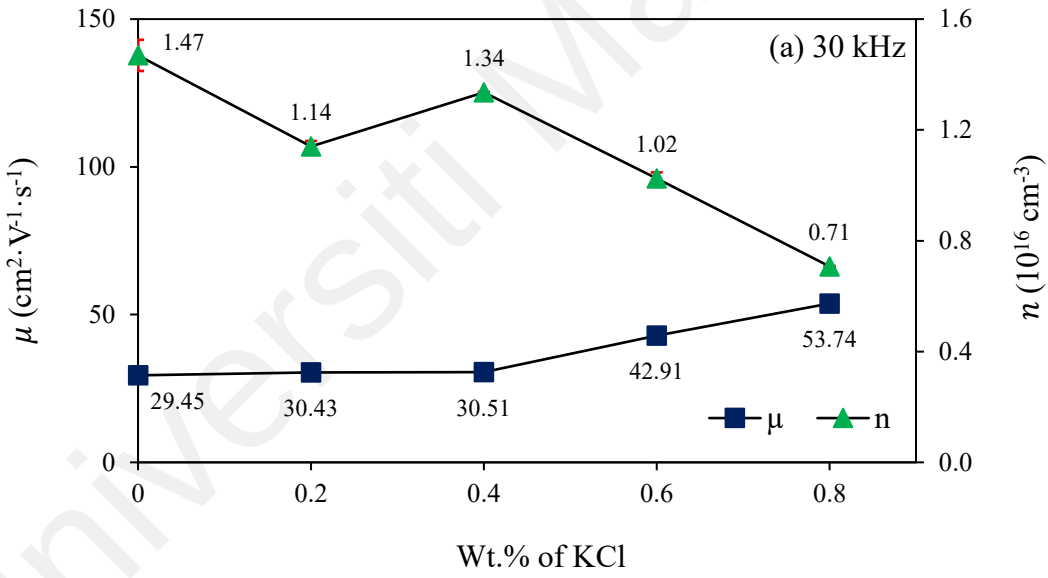

Figure 5.24: Variation of μ and n of system Z at (a) 30 kHz and (b) 5 kHz.

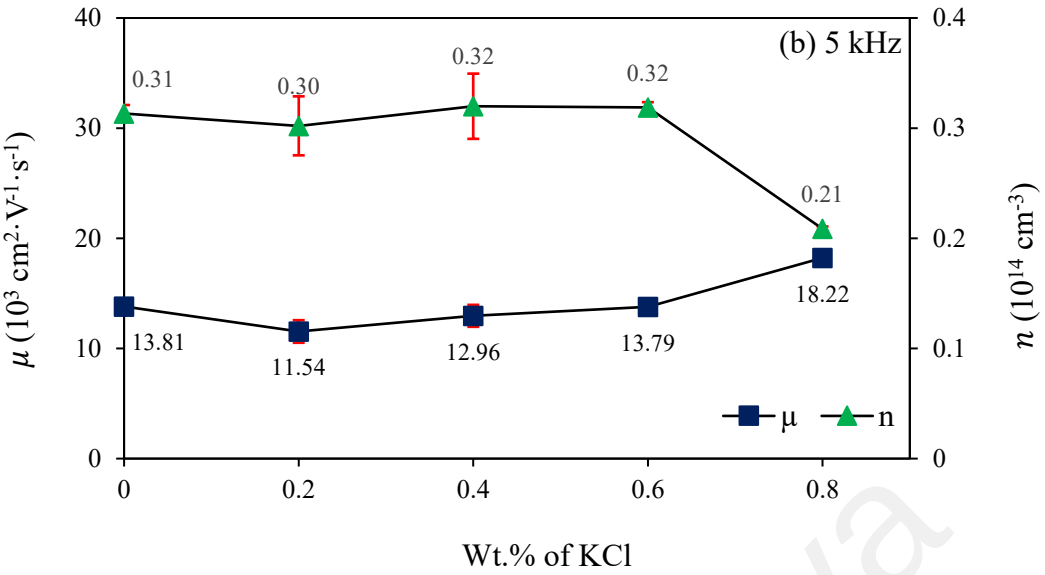

Figure 5.24, continued.

5.5.3 Temperature Dependence Ionic Conductivity

Figure 5.25 shows the temperature dependence ionic conductivity of the Z GPEs. The R^2 of all Z GPEs are nearly one. This observation verifies that the Arrhenius rule applies to the temperature dependence of the ionic conductivity of system Z. As mentioned in the system X, in GPE, E_A is not related to the salt concentration but depends on the heteroatoms in the solvent. Although KCl is a salt, it can be used as an additive to GPE. It forms coordination sites with PAAm-PAA or EC or water. In addition to the PAAm-PAA-Na^+ complex, EC-Na^+ complex and water-Na^+ complex from Y GPEs, adding KCl will produce another PAAm-PAA-K^+ complex, EC-K^+ complex and water-K^+ complex in Z GPEs. Table 5.12 lists the values of E_A for Z GPEs and its relationship with ionic conductivity is shown in Figure 5.26. According to Table 5.12 and Figure 5.26, E_A of Z GPEs are almost the same as the E_A of Y2 except for Z1. This is because the ionic conductivity of Z2, Z3 and Z4 are nearly the same as the Y2. Therefore, the lowest ionic conductivity value of Z1 exhibits the highest value of E_A.

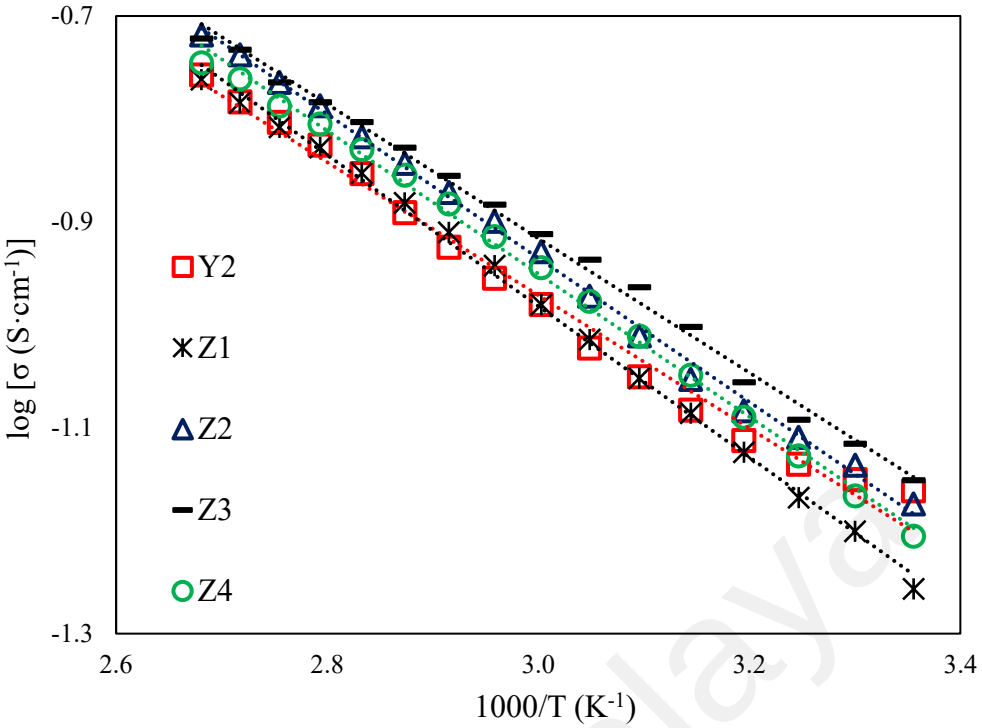

Figure 5.25: Temperature dependence of ionic conductivity of system Z.

Table 5.12: Gradient (m), E_A and R^2 values of system Z.

GPE	m (10^{-2} K)	E_A (10^{-1} eV)	R^2
Y2	-64.60	1.28	0.987
Z1	-73.37	1.46	0.998
Z2	-69.89	1.39	0.997
Z3	-65.22	1.29	0.996
Z4	-69.46	1.38	0.997

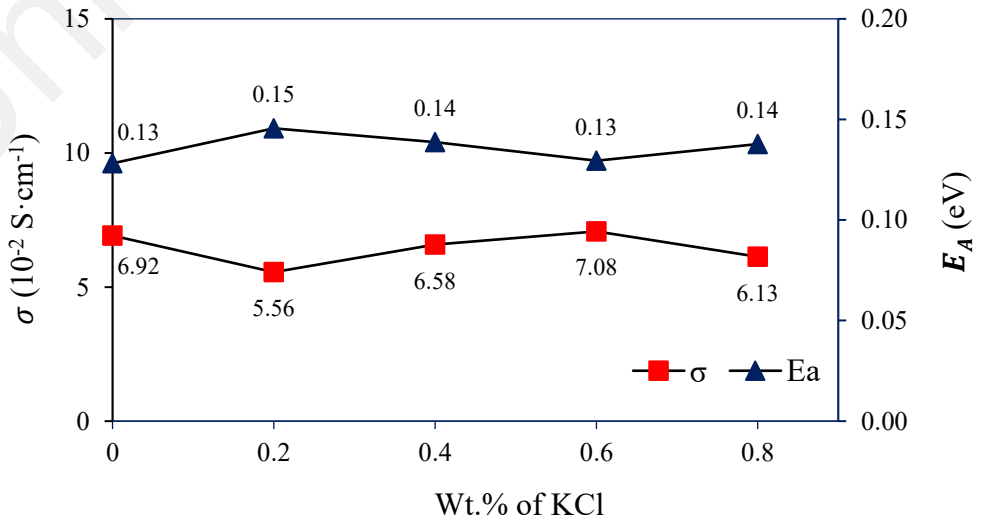

Figure 5.26: Variation of room temperature ionic conductivity and activation energy dependence in system Z.

5.6 Summary

In summary, the effects of Na_2S, EC and KCl on the electrical and transport property of PAAm-PAA based GPE have been studied through respective X, Y and Z systems. The findings in EIS are correlated to Chapter 4 structural properties. Figure 5.27 depicts the room temperature ionic conductivity of the optimized GPE for each system. Among PAAm-PAA-Na_2S GPE, the optimized X3/W5 exhibits the highest ionic conductivity, which is $(5.11 \pm 0.24) \times 10^{-2}$ S·cm^{-1}. After adding EC, Y2 exhibits the highest ionic conductivity, reaching $(6.92 \pm 0.02) \times 10^{-2}$ S·cm^{-1}, which is 35% higher than the optimized X3/W5. The optimized PAA-Na_2S-EC-KCl GPE is Z3, and the highest ionic conductivity is obtained at $(7.08 \pm 0.06) \times 10^{-2}$ S·cm^{-1}. As discussed in Chapter 4 structural properties, the interaction between water, PAAm-PAA, Na_2S, EC and KCl has been confirmed. Therefore, the increase in GPE ionic conductivity can be attributed to the addition of Na_2S, EC and KCl.

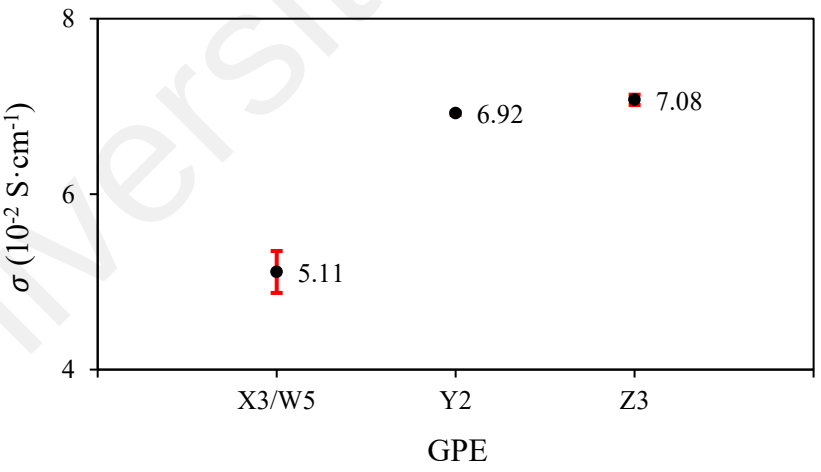

Figure 5.27: Room temperature ionic conductivity of different GPE compositions.

The change in ε' is consistent with the ionic conductivity of all the four GPE systems. In addition, the value of ε' increases as the frequency decreases due to electrode polarization. In Table 5.13, it can be observed that at vary frequencies, compared with X3/W5, the ε' value of Y2 is significantly improved, and the change between Y2 and Z3

is negligible. It can be deduced that the addition of EC has an impact on the ε' value of PAAm-PAA based GPE because of its high dielectric constant property.

Table 5.13: ε' value of different GPE compositions at selected frequencies.

GPE	30 kHz	20 kHz	10 kHz	7 kHz	5 kHz
	ε' (10^6)	ε' (10^6)	ε' (10^6)	ε' (10^6)	ε' (10^6)
X3/W5	0.40 ± 0.06	0.92 ± 0.11	2.98 ± 0.20	4.93 ± 0.27	7.40 ± 0.44
Y2	0.51 ± 0.04	1.27 ± 0.05	4.31 ± 0.10	7.17 ± 0.08	10.64 ± 0.07
Z3	0.57 ± 0.07	1.40 ± 0.15	4.59 ± 0.35	7.43 ± 0.34	10.78 ± 0.26

The ionic conductivity of GPE depends on μ and n. As discussed earlier, at selected frequency (30 kHz), the μ of the optimized X3/W5 is (10.33 ± 0.18) $cm^2 \cdot V^{-1} \cdot s^{-1}$. After adding EC, the μ of Y2 is (29.45 ± 1.03) $cm^2 \cdot V^{-1} \cdot s^{-1}$, which is 185% higher than the optimized X3/W5. The optimized PAA-Na_2S-EC-KCl GPE is Z3, and μ is obtained at (42.91 ± 0.92) $cm^2 \cdot V^{-1} \cdot s^{-1}$, which is 46% higher than the optimized Y2. The increase in μ is attributable to the role play of EC and KCl in the electrolyte system. EC promotes additional complexing sites which serve as additional parking lots before free ions jump to another, thus reducing the distance of ion jumping and increasing μ. It can be concluded that the ionic conductivity of PAAm-PAA based GPE is dominated by the ion motion in the electrolyte system.

The temperature dependence of ionic conductivity of all GPE systems obeys to the Arrhenius rule. Among all four GPE systems, the GPE with the highest ionic conductivity achieved the lowest E_A. It can be deduced that E_A increases as the ionic conductivity of GPE decreases. However, this trend is not implied in system X, because E_A is not related to the salt concentration but depends on the heteroatoms in the solvent. Other than that, it can be concluded that the higher the ionic conductivity, the lower the energy required for ion movement to conduct current.

CHAPTER 6: PHOTOVOLTAIC PERFORMANCE OF QUANTUM DOT-SENSITIZED SOLAR CELLS

6.1 Introduction

In this chapter, the optimized GPE from each system was used for QDSSC. Prior to this, as described in Chapter 3, the photoanode sensitized with TiO_2/CdS/ZnS and the CE catalyzed with Pt were fabricated in-house. The preparation of TiO_2/CdS/ZnS photoanode is divided into three steps, namely spin-coated TiO_2 compact layer, doctor blade TiO_2 mesoporous layer and SILAR synthesis of CdS/ZnS QD. The surface morphology, elemental analysis and structure of the TiO_2/CdS/ZnS photoanode were determined by FESEM, EDX and XRD. Furthermore, the influence of TiO_2 film thickness on the performance of QDSSC will be studied. The TiO_2 film thickness on the TiO_2/CdS/ZnS photoanode were controlled by two deposition methods, namely spin coating and doctor blade. The effect of GPEs and TiO_2 layers on the electrochemical performance of QDSSC will be discussed.

6.2 Characterization of TiO_2/CdS/ZnS Photoanode

FESEM, EDX and XRD are the characterization techniques used to ascertain the presence of all elements (TiO_2, CdS and ZnS) on the prepared photoanode. The photoanode is composed of three different materials: (i) TiO_2 layer, (ii) CdS sensitizer and (iii) ZnS passivation layer. The TiO_2 layer can be prepared by two deposition methods (spin coating and/or doctor blade), while the CdS/ZnS QD were synthesized by SILAR method. Figure 6.1 depicts the schematic diagram and image of the TiO_2/CdS/ZnS photoanode. It can be seen from the figure that the photoanode is dark yellow (see Figure 6.1 (b)). Since the formation of TiO_2 layer and ZnS QD are in white and the formation of CdS QD is bright yellow, the dark yellow indicates that TiO_2/CdS/ZnS QD has been synthesized on the surface of the photoanode (Kim et al., 2016a).

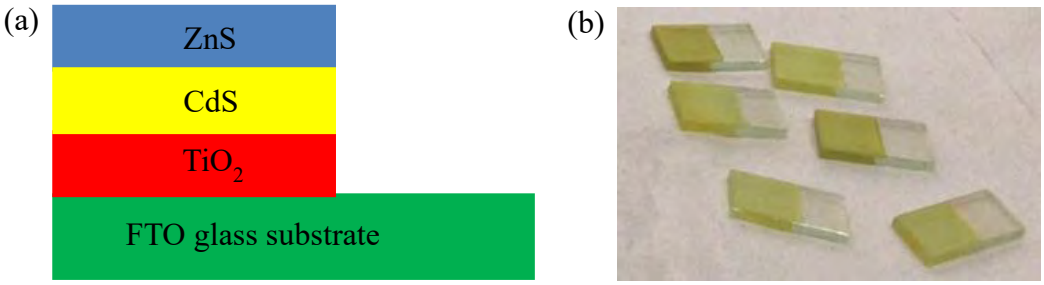

Figure 6.1: (a) Schematic diagram and (b) image of TiO_2/CdS/ZnS photoanode.

6.2.1 Field Emission Scanning Electron Microscopy (FESEM)

FEI Quanta 450 FEG FESEM has been used to examine the surface morphology of the TiO_2/CdS and TiO_2/CdS/ZnS photoanodes, as shown in Figure 6.2. FESEM images were captured at magnifications of 150,000 times under high vacuum system (scale bar = 500 nm).

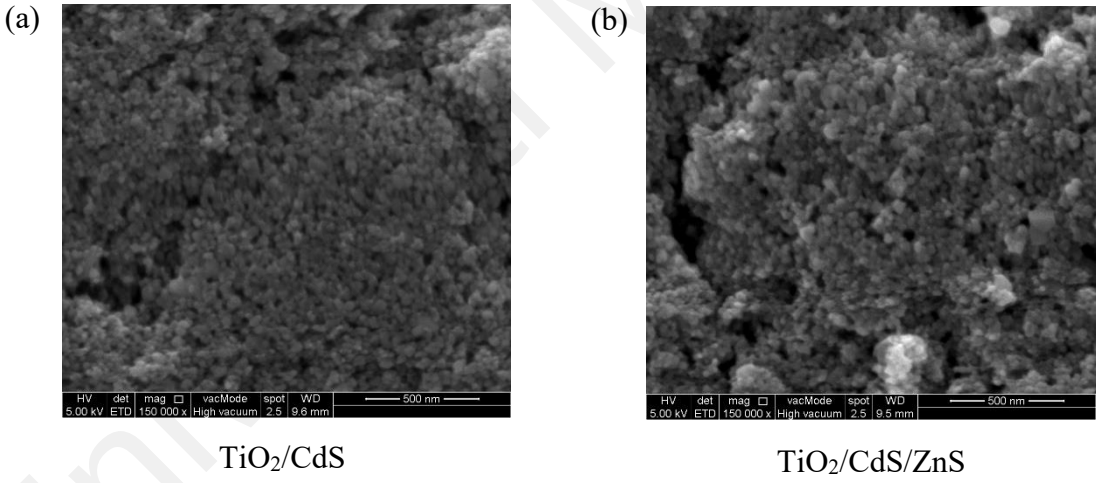

TiO_2/CdS TiO_2/CdS/ZnS

Figure 6.2: FESEM image of (a) TiO_2/CdS and (b) TiO_2/CdS/ZnS photoanodes.

It can be seen from Figure 6.2 (a) that the nanoparticles have a uniform distribution and equiaxed grain structure. The uniform distribution of nanoparticles on the prepared photoanode shows that CdS nanoparticles are well-dispersed on the surface of TiO_2 layer via facile SILAR technique. No obvious changes are observed when the ZnS layer were deposited on the TiO_2/CdS photoanode except for some nanoparticle aggregates and rough surface (see Figure 6.2 (b)). However, the FESEM image observation of TiO_2/CdS

and TiO_2/CdS/ZnS photoanode cannot convincingly confirm that TiO_2, CdS and ZnS nanoparticles are formed on the surface of the photoanode. Similar observations are also reported in the literature (Lee et al., 2016; Mingsukang et al., 2017b). Mingsukang and his coworkers claimed that the particle size of CdS was very small compared to that of the TiO_2, and thus, the nanoparticles observed in Figure 6.2 can only be considered as TiO_2 nanoparticles. Therefore, in order to ratify the prepared TiO_2/CdS/ZnS photoanode, other characterization techniques such as EDX and XRD, were performed to determine the constituent elements of the prepared photoanode. Table 6.1 summarizes the preparation of electrodes with different combinations of TiO_2 layers. The intention of this experiment is to examine the outcome of different TiO_2 layer combinations and their deposition methods on the surface of FTO glass substrate.

Table 6.1: Preparation of electrodes with different combinations of TiO_2 layer.

Electrode	TiO_2 powder		Deposition method	
	First layer	Second layer	First layer	Second layer
A1	P90	-	Spin coating	-
A2	P90	-	Doctor blade	-
B1	P25	-	Doctor blade	-
B2	P90	P25	Doctor blade	Doctor blade
B3	P90	P25	Spin coating	Doctor blade

The surface morphology of electrodes with different combinations of TiO_2 layer has been examined by Carl Zeiss AURIGA FESEM, as shown in Figure 6.3. It is obvious that the surface morphology of the electrodes in system A is significantly different from that of system B. In system A, a dense microstructure without porosity is observed. In addition, the TiO_2 nanoparticles that have been prepared via doctor blade technique have a uniform distribution structure as can be seen in Fig. 6.3 (b) as compared to the spin-coated nanoparticles (Fig. 6.3 (a)). This shows that the doctor blade method is conducive to the uniform deposition of TiO_2 layer on FTO glass substrate. Referring to Fig. 6.3 (c),

the microstructure of electrode B1 is highly porous. The particle shape of granular TiO_2 nanoparticles has also observed in system B. Apparently, the surface morphology of B2 (Fig. 6.3 (d)) and B3 (Fig. 6.3 (e)) is rougher than B1. Since they have two layers (P25 on top of P90), their microstructures are similar to B1 which is highly porous rather than dense microstructure.

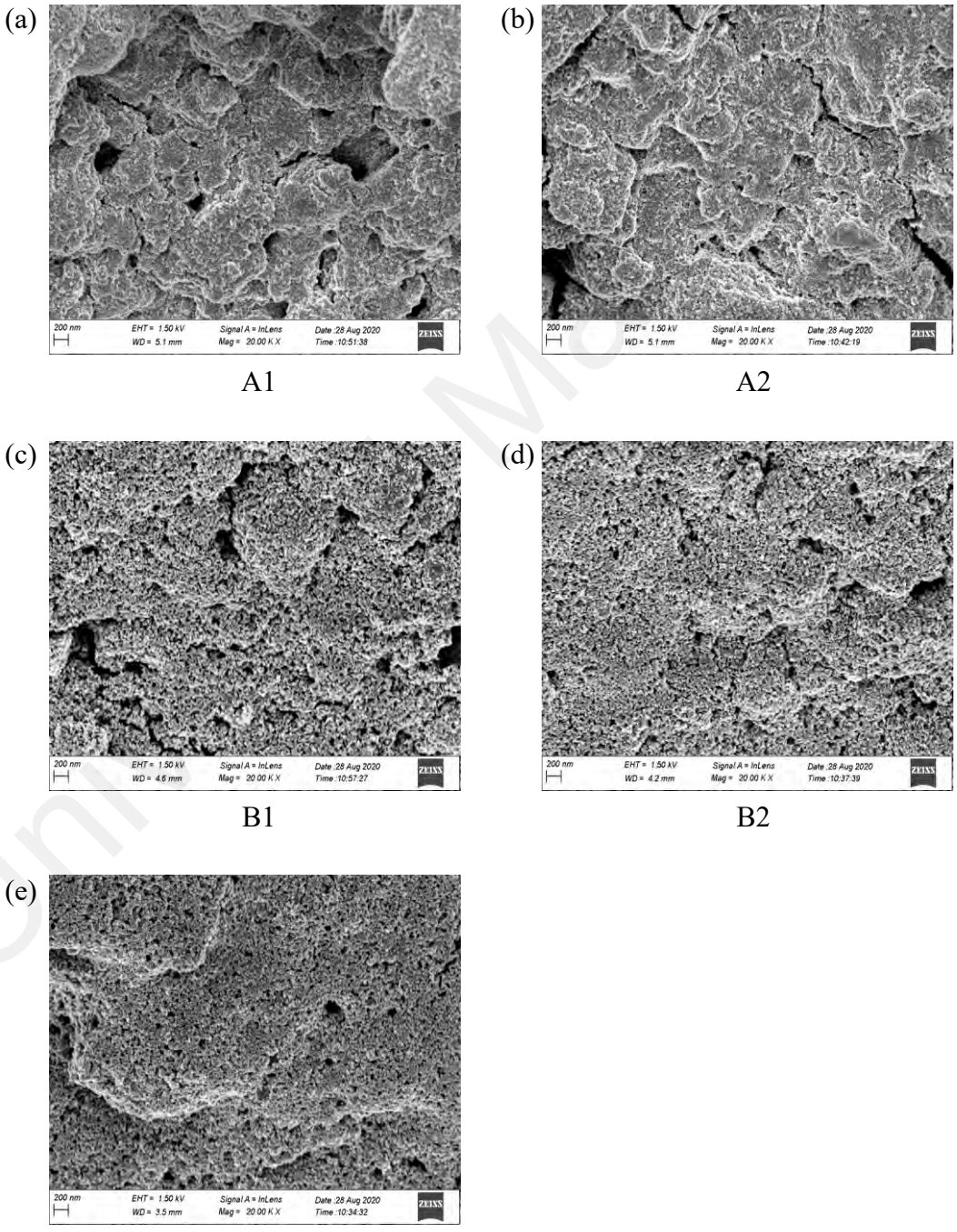

Figure 6.3: FESEM image of electrode (a) A1, (b) A2, (c) B1, (d) B2 and (e) B3.

In addition, the side view of the FESEM images of B2 and B3 was captured at magnifications of 1000 times with a scale of 10 μm to reveal the thickness of each TiO_2 film of the B2 and B3 electrodes, as shown in Figure 6.4. It can be seen from the figure that the thickness of the first layer in B2 is (10.51 ± 0.35) μm, and the thickness of the second layer is (21.24 ± 0.53) μm. In B3, the thickness of the first and second layers is (0.70 ± 0.01) μm and (30.70 ± 0.58) μm, respectively. Therefore, the total thickness of B2 is (31.75 ± 0.64) μm and the total thickness of B3 is (31.40 ± 0.58) μm. It is evident that the thickness of the TiO_2 layer prepared by the spin coating method and the doctor blade method is significantly different.

As described in Chapter 3, for the spin coating method, the speed of the spin coater is set to 2350 rpm, and the FTO glass has been rotated for 1 min to coat the glass with a uniformly distributed TiO_2 layer. Its thickness is (0.70 ± 0.01) μm (Fig. 6.4 (b)). In the doctor blade method, a glass rod is used to roll the TiO_2 paste on the FTO glass to produce a uniformly distributed TiO_2 layer on the surface. Prior to this, the thickness of the TiO_2 layer can be controlled by attaching Scotch tape (thickness 60 μm) on the edge of the FTO glass. The contrast between the thickness of the Scotch tape and the thickness of the TiO_2 layer ((10.51 ± 0.35) μm) is because the solvent used in the TiO_2 paste eventually gets evaporated and leave a residue of TiO_2 powder. Therefore, the thickness of the TiO_2 layer will be less than 60 μm. For the B2 electrode, the thickness of the first and second TiO_2 layers are different although same preparation method (doctor blade technique) has been employed. This is due to the particle size difference of P90 and P25 TiO_2. The second layer (P25 TiO_2) is thicker than P90 TiO_2 layer due to its large particle size (21 nm). Hence, it can be inferred that the thickness of the TiO_2 layer is affected by the particle size of the TiO_2. Meanwhile, a doctor blade method was used to prepare the second layers of B2 and B3 electrodes, and the Scotch tape of same thickness was used. In this case, the total thickness of B2 is almost the same as the total thickness of B3. Since

the thickness of the first layer in B2 is thicker and the space left for the second layer in B2 is smaller as compared to B3, and therefore, the thickness of the second layer in B2 is lesser than that of B3.

(a)

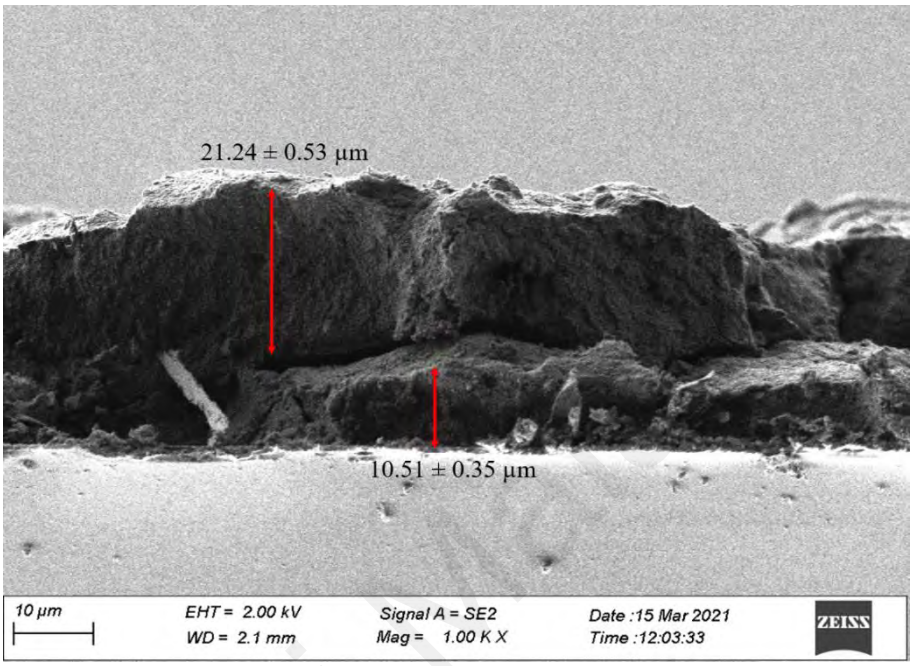

(b)

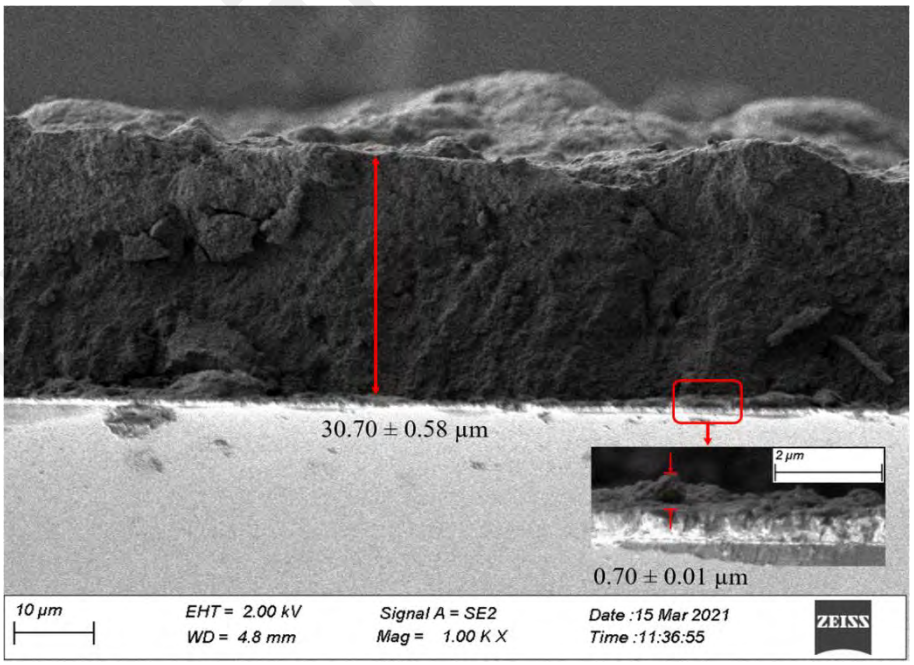

Figure 6.4: Side view of (a) B2 and (b) B3 electrodes.

6.2.2 Energy Dispersive X-Ray Spectroscopy (EDX)

The FESEM image of TiO_2/CdS and TiO_2/CdS/ZnS photoanodes was line-scanned for EDX analysis. Figure 6.5 shows the EDX spectrum of (a) TiO_2/CdS and (b) TiO_2/CdS/ZnS photoanodes. The observation of Ti, O, Cd and S elements in Figure 6.5 (a) indicates that TiO_2 and CdS nanoparticles were formed on the surface of prepared TiO_2/CdS photoanode via SILAR method. New elements such as Zn and Na in Figure 6.5 (b) indicates that ZnS nanoparticle was also successfully sensitized via SILAR method. The trace of Na was identified, which is attributed to the Na_2S methanol solution used in the SILAR method.

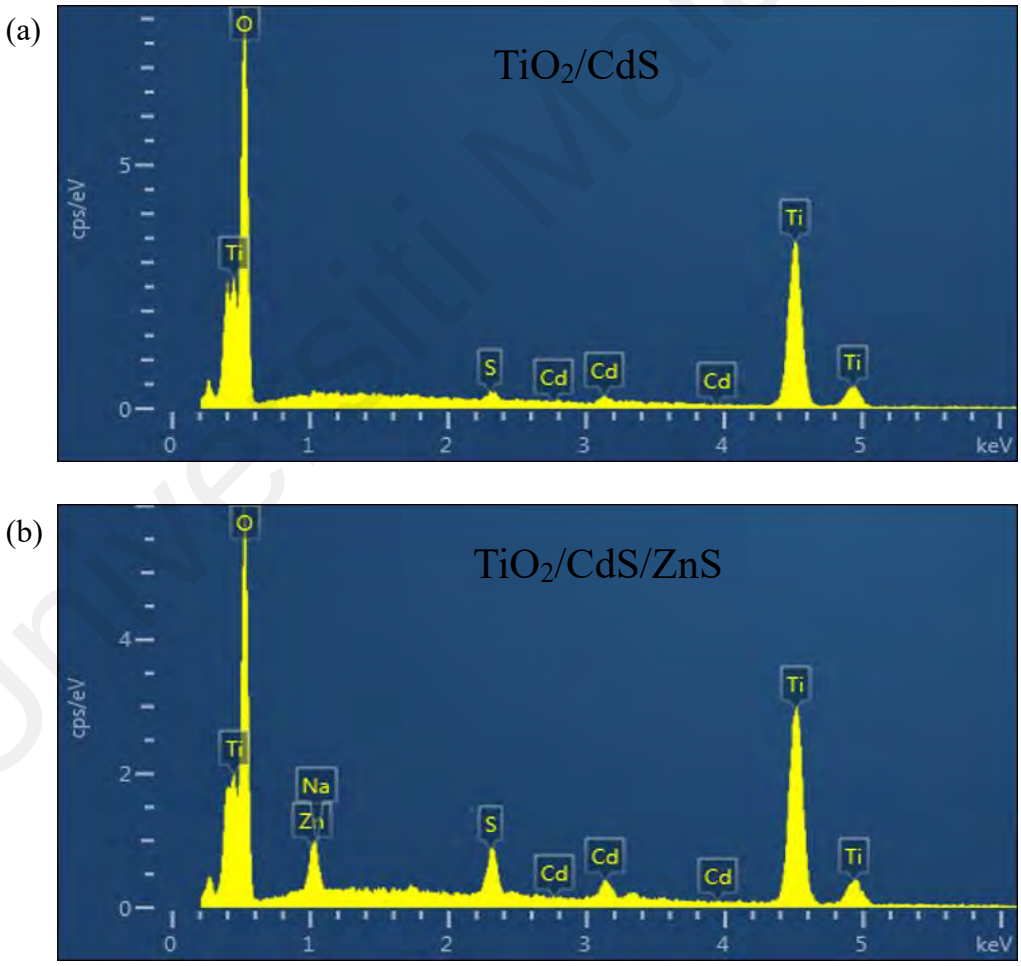

Figure 6.5: EDX spectrum of (a) TiO_2/CdS and (b) TiO_2/CdS/ZnS photoanodes.

According to the line sum spectrum in Figure 6.5, each element has a different weight percentage. Table 6.2 summarizes the atomic mass, weight percentage and composition

stoichiometric number of each element in the prepared TiO_2/CdS and TiO_2/CdS/ZnS photoanodes. It can be seen from the table that majority of the composition is contributed by Ti and O. In addition, it is observed that the wt.% of Zn is lower than the wt.% of Cd because only two SILAR cycles are used to synthesize ZnS, whereas five SILAR cycles are used to synthesize CdS. The stoichiometric number of each element can be calculated by dividing the wt.% of the element by its atomic mass.

Table 6.2: Atomic mass, weight percentage and composition stoichiometric number of each element in the TiO_2/CdS and TiO_2/CdS/ZnS photoanodes.

Element	Atomic mass (u)	TiO_2/CdS		TiO_2/CdS/ZnS	
		Wt.%	Stoichiometric number	Wt.%	Stoichiometric number
Ti	47.86	55.3	1.16	54.3	1.13
O	15.99	42.1	2.63	34.3	2.15
Cd	112.41	2.0	0.02	4.6	0.04
S	32.06	0.6	0.02	2.7	0.08
Zn	65.38	-	-	3.5	0.05
Na	22.98	-	-	0.6	0.03

According to the stoichiometric number, the synthesized TiO_2 was in the range of $TiO_{1.90}$ to $TiO_{2.27}$, and CdS was successfully synthesized. When the CdS photoanode was passivated with ZnS QD, CdS/$Zn_{1.25}$S QD was successfully synthesized. The observed stoichiometric ratios of TiO_2, CdS and ZnS are consistent with the expected stoichiometric ratios in Table 6.3.

Table 6.3: Elemental compositions of TiO_2/CdS and TiO_2/CdS/ZnS photoanodes.

Photoanodes	Expected stoichiometric ratio			Observed stoichiometric ratio		
	Ti: O	Cd: S	Zn: S	Ti: O	Cd: S	Zn: S
TiO_2/CdS	0.5	1	-	0.44	1	-
TiO_2/CdS/ZnS	0.5	1	1	0.53	1	1.25

6.2.3 X-Ray Diffraction (XRD)

Figure 6.6 shows the X-ray diffraction pattern of TiO_2/CdS/ZnS photoanode. All the crystalline peaks are identified as belonging to four groups. The peaks marked with star are ascribed to the FTO glass substrate and those peaks marked with triangle are associated with the reflection of tetragonal structure of anatase TiO_2. Meanwhile, the peaks marked with square are attributed to the cubic structure of hawleyite CdS and those marked with circle are corresponded to the hexagonal phase of ZnS.

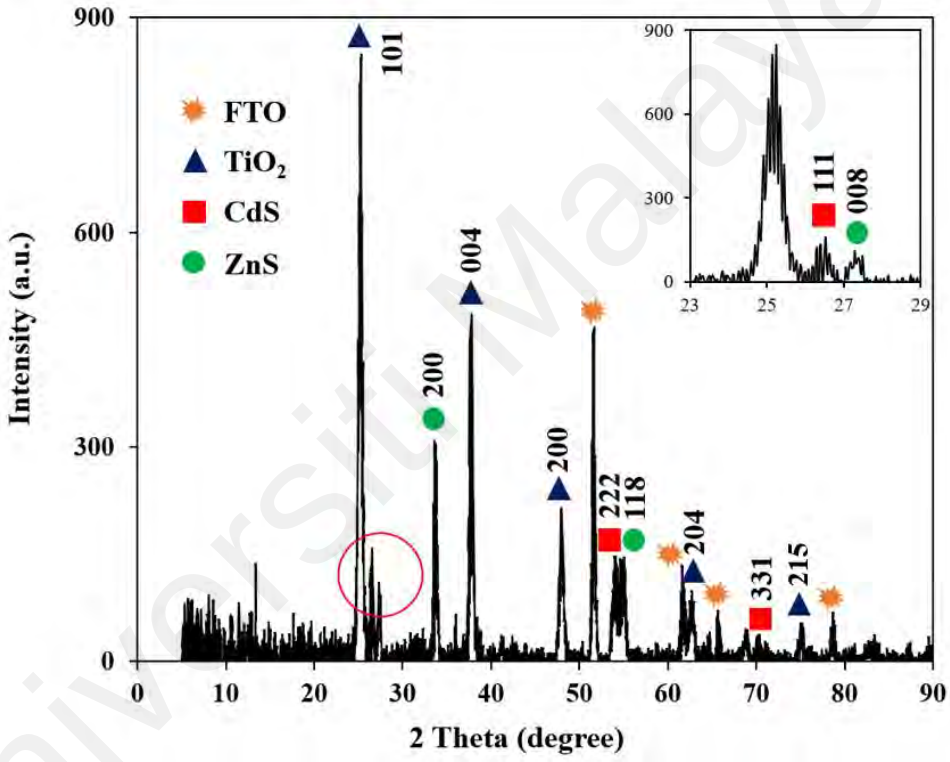

Figure 6.6: X-ray diffraction pattern of TiO_2/CdS/ZnS photoanode. The inset shows the enlarged XRD pattern at 2θ = 23° to 29°.

The crystalline peaks of TiO_2 which are observed at 2θ = 25.24º, 37.67º, 47.90º, 62.71º and 75.12º correspond to the hkℓ planes of (101), (004), (200), (204) and (215), respectively. Similar observations have been reported in the literature (Alavi et al., 2020; Banerjee et al., 2019; Lee et al., 2016; Mahalingam et al., 2022; Shaban et al., 2017). As P90 and P25 were used for the prepared TiO_2/CdS/ZnS photoanode, hence the crystal planes of TiO_2 tetragonal anatase structure are identified as expected. In addition, three

significant peaks of CdS are clearly shown at angles 2θ = 26.56º, 55.01º and 70.20º, corresponding to the hkℓ planes of (111), (222) and (331) (Alavi et al., 2020; Kim et al., 2016a; Lee et al., 2016; Lee et al., 2017; Wang & Zhang, 2014). The XRD pattern of ZnS exhibit sharp peaks at 2θ = 27.28º, 33.71º and 55.01º, corresponding to the hkℓ planes of (008), (200) and (118) (Kassim et al., 2010; Lee et al., 2017; Vashistha et al., 2015; Wang & Zhang, 2014). From the results, this indicates that the prepared photoanode comprised of TiO_2 layer, CdS QD sensitizer and ZnS passivation layer. The diffraction peaks of element TiO_2, CdS and ZnS are summarized in Table 6.4.

Table 6.4: Diffraction peaks of element TiO_2, CdS and ZnS.

Element	hkℓ plane	Position, 2θ (°)	d-spacing (Å)	Reference code
TiO_2	101	25.24	3.53	98-015-4602
TiO_2	004	37.67	2.39	98-015-4602
TiO_2	200	47.90	1.90	98-015-4602
TiO_2	204	62.71	1.48	98-015-4602
TiO_2	301	75.12	1.26	98-015-4602
CdS	111	26.56	3.36	98-002-9278
CdS	222	55.01	1.67	98-002-9278
CdS	331	70.20	1.34	98-002-9278
ZnS	008	27.28	3.27	98-001-5477
ZnS	200	33.71	2.66	98-001-5477
ZnS	118	55.01	1.67	98-001-5477

6.3 Photocurrent Density-Voltage (*J-V*) Performance

Photocurrent density-voltage (*J-V*) characterization was performed to determine the photovoltaic performance of QDSSCs. Upon light illumination, the solar cells generate photocurrent density, J (affected by light intensity and absorption, and charge transportation) and photovoltage, V (change in Fermi level between semiconductor photoanode and electrolyte species) (Hwang & Yong, 2015). As a result, the *J-V* curves have been obtained and the output of J_{sc} and V_{oc} were used to calculate FF and η (Chen et al., 2013a; Fukui et al., 2009).

6.3.1 QDSSC with Different GPE Compositions

In this system, three different GPE compositions were used for quasi-solid QDSSC. As discussed in the previous chapters, all three GPEs are GPEs based on PAAm-PAA. X3/W5 is a GPE composed of PAAm-PAA and polysulfide electrolyte, Y2 is a single additive (EC) PAAm-PAA-Na_2S GPE, and Z3 is a dual additives (EC and KCl) PAAm-PAA-Na_2S GPE. This experiment aims to explore the effect of adding EC and KCl to GPE on the photovoltaic performance of QDSSC. The *J-V* characterization of QDSSC with three different GPEs are shown in Figure 6.7.

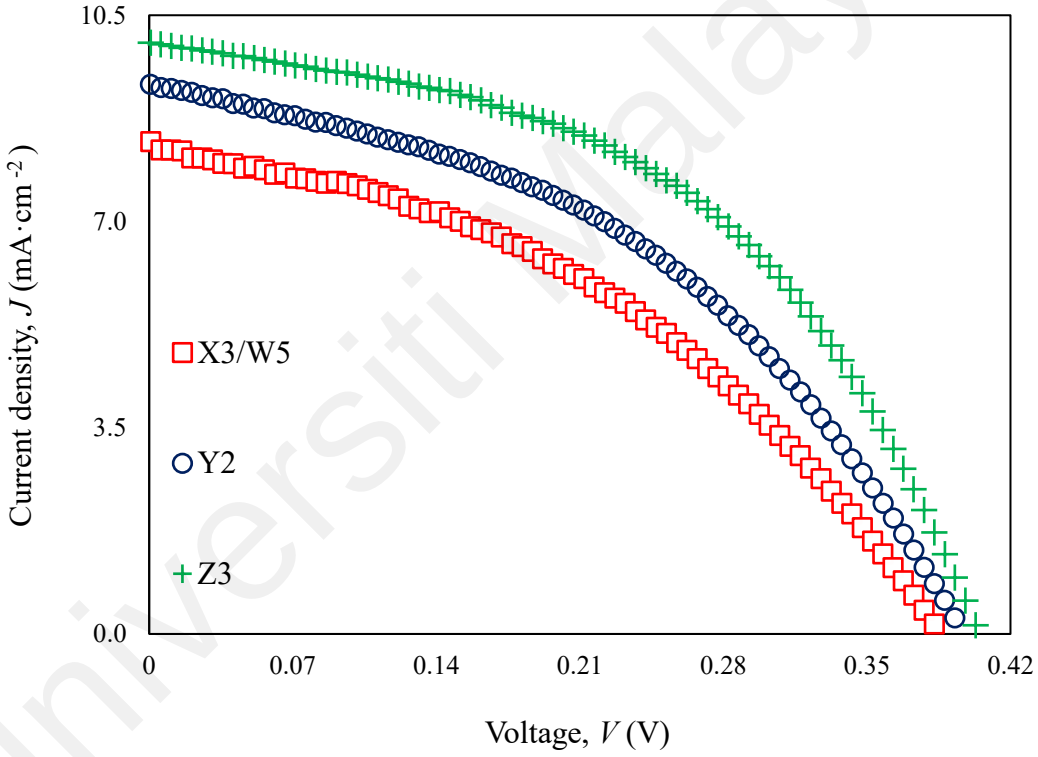

Figure 6.7: *J-V* curve of the quasi-solid QDSSCs.

It can be observed from the figure that the output of J_{sc} shows an upward trend from X3/W5 to Z3. The highest J_{sc} of QDSSC having Z3 electrolyte has been observed. This increase is credited to the ionic conductivity of the GPE used in the quasi-solid QDSSC. As discussed in Chapter 5, Z3 has higher ionic conductivity and mobility than X3/W5 and Y2, so charge carriers move faster in Z3, which led to faster reduction and oxidation rate in GPE, resulting higher J_{sc} (Jin et al., 2018; Kelly & Meyer, 2001; Longo & De

Paoli, 2003). Besides, other justifications for the increase in J_{sc} are the penetration of additional small-sized cations (K^+) into the mesoporous TiO_2 layer (Teo et al., 2018) and the low resistivity of the electrolyte due to the addition of KCl (Ganjian et al., 2017). According to Teo et al. (2018), the Fermi level of TiO_2 and the CB edge will be positively shifted due to the cation intercalation on TiO_2 surface, thereby strong electronic coupling will occur between TiO_2 and CdS, and hence, J_{sc} will increase. However, the downward shift of the Fermi level of TiO_2 usually results in lower V_{oc}. But in this work, there are negligible changes in V_{oc} in all GPE compositions as observed in Figure 6.7 and Table 6.5. Therefore, the higher J_{sc} value obtained for QDSSC using Z3 GPE as compared to other GPEs may be due to the fast transport speed of electrons in TiO_2 arising from the formation of ambipolar K^+-e^- (Wu et al., 2008).

In the *J-V* curve, J_{sc} is the y-axis intercept, and V_{oc} is x-axis intercept. According to Equation 3.3 and 3.4 in Section 3.6.4, these two parameters are used to calculate the FF and η. Table 6.5 summarizes the photovoltaic performance parameters obtained from the multiple quasi-solid QDSSCs. It has been observed that the η of X3/W5 is (1.40 ± 0.06)%, the η of Y2 is (1.50 ± 0.13)%, and Z3 produces the best η which is (1.80 ± 0.15)%. By observing the average value and standard deviation of η in Table 6.5, the Z3 QDSSC shows higher η than X3/W5 and Y2 QDSSCs with the confidence level of 68% and 95%, respectively. Therefore, it can be concluded that adding KCl to GPE based on PAAm-PAA can increase the photovoltaic performance of QDSSC by 29%.

Table 6.5: Photovoltaic performance parameters of the quasi-solid QDSSCs.

GPE	J_{sc} (mA·cm^{-2})	V_{oc} (V)	FF	η (%)
X3/W5	8.91 ± 0.85	0.37 ± 0.01	0.43 ± 0.03	1.40 ± 0.06
Y2	9.44 ± 0.68	0.38 ± 0.03	0.43 ± 0.03	1.50 ± 0.13
Z3	10.01 ± 0.98	0.38 ± 0.01	0.47 ± 0.02	1.80 ± 0.15

According to the literature, KCl is the most studied additive in polysulfide electrolyte because it is compatible with various types of solutions and comprehensively improves QDSSC performance (see Chapter 2). Potassium halides with excellent plasticization and diffusion properties can easily diffuse into the QD layer and create a good interface contact between the nanopores photoanode and the electrolyte, therefore the crystallinity and light absorption of QDSSC will be improved (Gupta & Rhee, 2013; Wang et al., 2018a). In addition, it is reported that KCl can activate the redox reaction of S^{2-}/S_n^{2-} ions, which helps to improve the performance of QDSSC (Seo et al., 2013). It is believed that KCl affects the charge transfer kinetics in QDSSC. The faster S^{2-}/S_n^{2-} moves, the higher the QD regeneration, and more electrons accumulate on the photoanode, thus η increases (Rasal et al., 2021). Therefore, Section 6.4 will further explore the effect of KCl on the impedance characteristics of QDSSC by discussing the working principle of charge transfer in the QDSSC.

6.3.2 QDSSC with Different TiO_2 Layers

In addition to the effect of different GPE compositions, the effect of different TiO_2 layer combinations on the photovoltaic performance of QDSSCs was also investigated. According to the literature review (Bandara et al., 2013; Choi et al., 2012; Krašovec et al., 2009; Seo et al., 2011), the TiO_2 layer plays multi roles in the working mechanism of QDSSC. It can be a barrier between the FTO glass substrate and GPE, or it can be a loading platform for QD. Other than TiO_2 layer combination, the thickness of the TiO_2 layer, which was controlled by spin coating and doctor blade methods, may also affect the photovoltaic performance of QDSSC. The effect of different TiO_2 layer combinations and TiO_2 layer thickness on the photovoltaic performance of QDSSCs can be examined from the *J-V* curves, as shown in Figure 6.8. For this study, the most conductive GPE (Z3 GPE) has been used as the electrolyte. The photoanode has been divided into two systems (A and B) as listed in Table 6.1. From Figure 6.8, it is evident that the A1 QDSSC has

the lowest J_{sc} value, while the J_{sc} of B1 and B2 QDSSCs are the highest. In the case of V_{oc}, B2 is the lowest whereas B3/Z3 cell has the highest value. The photovoltaic parameters for all QDSSCs are tabulated in Table 6.6.

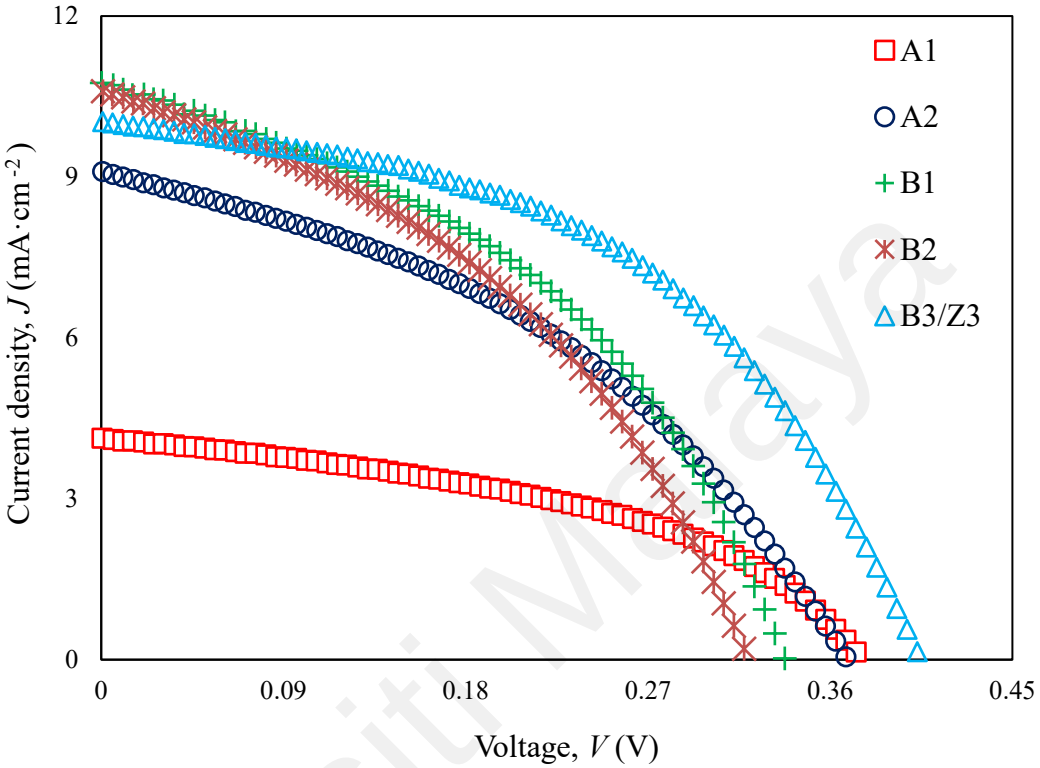

Figure 6.8: *J-V* curves of the QDSSCs using different TiO_2/CdS/ZnS photoanodes.

Table 6.6: Photovoltaic performance parameters of the QDSSCs using different TiO_2/CdS/ZnS photoanodes.

Photoanode	J_{sc} (mA·cm^{-2})	V_{oc} (V)	*FF*	η (%)
A1	4.29 ± 0.59	0.36 ± 0.01	0.45 ± 0.02	0.70 ± 0.11
A2	9.43 ± 0.56	0.36 ± 0.01	0.41 ± 0.01	1.40 ± 0.10
B1	10.55 ± 0.71	0.34 ± 0.02	0.42 ± 0.01	1.52 ± 0.19
B2	10.72 ± 0.17	0.32 ± 0.01	0.41 ± 0.01	1.40 ± 0.04
B3/Z3	10.01 ± 0.98	0.38 ± 0.01	0.47 ± 0.02	1.80 ± 0.15

As can be observed in Table 6.6, QDSSC with A1 photoanode has the lowest η i.e. (0.70 ± 0.11)% which can be attributed to its lowest J_{sc} value at (4.29 ± 0.59) mA·cm^{-2}. In the case of A2, J_{sc} is obtained at (9.43 ± 0.56) mA·cm^{-2}, which resulted in a η of (1.40 ± 0.10)%. It can be noted that J_{sc} and η of A2 cell have increased by ~100% as compared

to A1 QDSSC. In the system A, both photoanodes are composed of a single layer of P90 TiO_2 but were prepared by different deposition methods. Figure 6.9 shows the images of A1 and A2 electrodes after sintering at 450 °C. It can be observed that the A1 electrode has light transmittance, while the A2 electrode does not transmit light. Since the formation of the TiO_2 layer is white colour, therefore the TiO_2 layer will become opaque as it thickens. The P90 TiO_2 layer prepared by the doctor blade method (A2 electrode) is thicker than that prepared by the spin coating method (A1 electrode). This is in agreement with the FESEM results (thickness observed from the side view of the FESEM image in Figure 6.4).

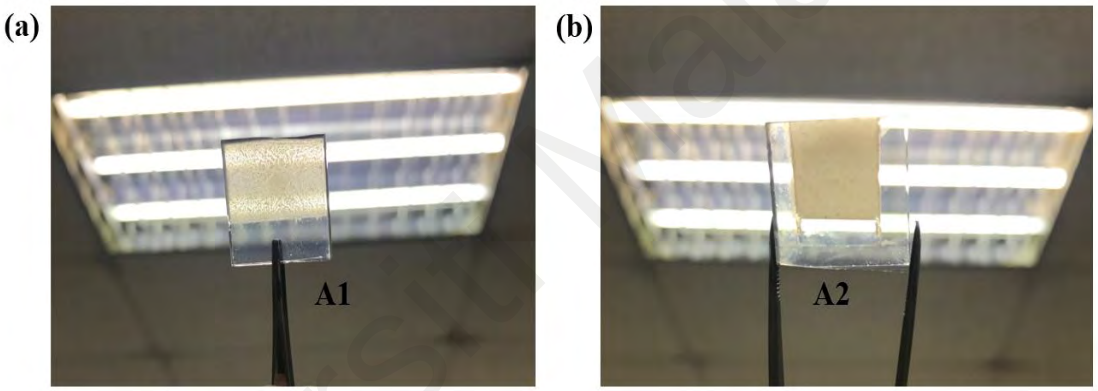

Figure 6.9: Photographs of (a) A1 and (b) A2 electrodes after sintered at 450 °C.

According to literature review (Ayele et al., 2013; Choi et al., 2012; Jun et al., 2013b), the performance of QDSSCs is affected by the thickness of the TiO_2 layer on the photoanode. When the thickness of TiO_2 layer increases, more CdS QDs are loaded on its surface and thus increase the light absorption ability. However, if the thickness of the TiO_2 layer exceeds the optimal value, η will then decrease. This is because more trap states will be found in the thicker layer, which can effectively block the path of electrons from the TiO_2 layer to the FTO glass substrate (Choi et al., 2012).

As a comparison, B1 cell which has mesoporous P25 TiO_2 layer exhibits better performance in terms of η and J_{sc} than system A. The mesoporous structure provides a

larger surface area for the CdS QD loading. It is claimed that the presence of a mesoporous layer in the photoanode can increase light absorption and subsequently increasing η (Arof et al., 2014b; Bandara et al., 2013; Khan et al., 2010). This is due to the characteristics of P25 TiO_2 having high surface area and volume with large pore size which can create extra reactive sites on the surface of the photoanode and thus promote the photocatalytic reaction in QDSSC (Khan et al., 2010; Krašovec et al., 2009; Li et al., 2014). In addition, the increase in J_{sc} can also be attributed to the easy penetration of the Na^+ and K^+ cations of the Z3 GPE to the mesoporous P25 TiO_2 layer as compared to the compact P90 TiO_2 layer, as aforementioned (Barea et al., 2010; Duan et al., 2015b; Xu et al., 2012).

It is noticeable from system A that the efficiency of A2 is higher than that of A1. Therefore, a combination of A2 and B1 was prepared and designated as B2 to obtain a double-layer TiO_2 coating of the photoanode in order to enhance the photovoltaic performance of QDSSC. As mentioned earlier, P90 TiO_2 is introduced as a barrier between the FTO glass substrate and GPE to suppress electron recombination at the FTO/electrolyte interface and improve interfacial adhesion (Choi et al., 2012; Seo et al., 2011). Meanwhile, P25 TiO_2 is introduced as a mesoporous layer between the FTO glass substrate and the QD sensitizer to allow QD to be loaded onto the photoanode surface (Aziz et al., 2015; Baharun et al., 2020; Bandara et al., 2013; Choi et al., 2012; Lee et al., 2006; Teo et al., 2018) and increase the η of QDSSC as if it was to combine with the compact layer (P90 TiO_2) of the photoanode (Choi et al., 2012; Seo et al., 2011; Wu et al., 2014). However, the η of B2 is only (1.40 ± 0.04)%, which is almost the same as A2 or slightly lower than B1. From Table 6.6, it is noted that J_{sc}, V_{oc} and FF values of B1 and B2 are nearly constant. Therefore, the combination of A2 and B1 (i.e. B2) does not improve the photovoltaic performance of QDSSC.

Conversely, B3 in which A1 and B1 were combined has been prepared according to the literature (Aziz et al., 2015; Baharun et al., 2020; Bandara et al., 2013; Choi et al., 2012; Lee et al., 2006; Teo et al., 2018). B3 was also designated as Z3 in the previous experiment. By observing the average value and standard deviation of η in Table 6.6, the B3/Z3 QDSSC produces higher η than B1 and B2 QDSSCs with the confidence level of 68% and 95%, respectively. Therefore, it can be concluded that combining A1 and B1 can increase the photovoltaic performance of QDSSC by 18%. Similar to B2, B3/Z3 photoanode is also composed of a double-layer TiO_2 coating, but the η of B3/Z3 ((1.80 ± 0.15)%) is higher than that of B2 ((1.40 ± 0.04)%). Since their J_{sc} values are nearly constant, the high η is attributed to the increase of V_{oc} ((0.38 ± 0.01) V) and FF (0.47 ± 0.02) in B3/Z3. The increase of V_{oc} is related to the negative movement of the TiO_2 CB position (Zhang et al., 2014a). The high V_{oc} and FF in B3/Z3 are attributable to the spin coated P90 TiO_2 compact layer.

According to Equation 3.4, FF is the ratio of the maximum output power to the product of J_{sc} and V_{oc} (Trukhanov et al., 2015). According to the literature review (Kim et al., 2009; Liu et al., 2018; Qi & Wang, 2013; Servaites et al., 2010; Xue et al., 2004), FF measures the quality of the fabricated solar cells. Two important parameters which are shunt resistance (R_{sh}) and series resistance (R_s) contribute to the FF as shown in Figure 6.10. R_{sh} (also known as parallel resistance) is the current loss and charge recombination of the device, which is affected by impurities, morphology and thickness of the semiconductor layer, defect trap sites, etc. (Kim et al., 2009; Liu et al., 2018; Qi & Wang, 2013); while R_s is the total resistance of the device, including electrode resistance, contact resistance of each interface, etc. (Kim et al., 2009; Servaites et al., 2010; Xue et al., 2004).

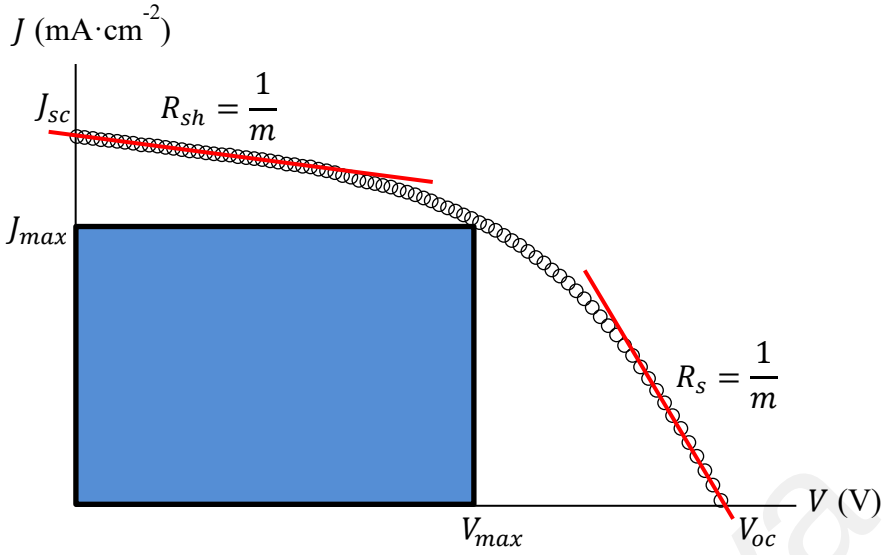

Figure 6.10: Calculation of R_{sh} and R_s.

Table 6.7 shows the R_{sh} and R_s of the QDSSCs obtained using different TiO_2/CdS/ZnS photoanodes. It is evident that A1 QDSSC has the highest values of R_{sh} and R_s among the cells. Compared with cell having B2 photoanode, B3/Z3 cell shows a higher R_{sh} value, which is attributed to the spin coated P90 TiO_2 compact layer. In the case of R_s, system B shows a lower R_s than system A which is attributed to the P25 TiO_2 mesoporous layer.

Table 6.7: Fill factor parameters of the QDSSCs using different TiO_2/CdS/ZnS photoanodes.

Photoanode	R_{sh} (10^{-1} Ω)	R_s (10^{-2} Ω)	FF
A1	2.20 ± 0.34	2.72 ± 0.54	0.45 ± 0.02
A2	0.87 ± 0.09	1.73 ± 0.21	0.41 ± 0.01
B1	0.73 ± 0.07	1.31 ± 0.09	0.42 ± 0.01
B2	0.66 ± 0.07	1.46 ± 0.22	0.41 ± 0.01
B3/Z3	1.31 ± 0.27	1.41 ± 0.12	0.47 ± 0.02

According to the literature (Kim et al., 2009; Qi & Wang, 2013), the thickness of semiconductor layer affects the R_{sh}. Kim and his coworkers reported that when the thickness of semiconductor layer increases, the J_{sc} increases but R_{sh} decreases (Kim et al., 2009). This is attributed to the longer distance travel by electrons to reach the CE.

When the transit time increases, the electron recombination may occur (Kim et al., 2009; Qi & Wang, 2013). In this work, it can be observed that A2 cell has a smaller R_{sh} than the A1 cell. It can then be deduced that the thickness of doctor blade P90 TiO_2 compact layer ((10.51 ± 0.35) μm) exceeds the optimal thickness for a dense/compact layer, hence A2 and B2 cells have lower FF values as compared to A1 and B3/Z3 cells. In addition, R_{sh} depends on the quantity of defect trap sites. The sites include bulk traps and surface traps (Zhang et al., 2014a). When QD has an optimal interface with photoanode, it will result in low defect trap sites and R_{sh} increases (Liu et al., 2018). A high R_{sh} indicates that a good interfacial morphology is fabricated and thus effectively prevent current leakage and surface recombination leading to the increase in FF (Qi & Wang, 2013). It is obvious that the increase of FF is one of the main reasons for the improved η of B3/Z3 QDSSC. On the other hand, low mobility of electrons results in a high value of R_s (Qi & Wang, 2013; Servaites et al., 2010; Tress et al., 2011). By observing the trend of R_s in Table 6.7, the charge carriers move faster in P25 TiO_2 than that in P90 TiO_2. The high FF value in B3/Z3 QDSSC is attributed to its high R_{sh} value. The lowest η exhibited by A1 cell can be said to be due to high R_s value.

6.4 Electrochemical Impedance Spectroscopy (EIS)

The photovoltaic performance of QDSSC involves the efficiency of electron separation, collection and regeneration, which is reflected in the output of J_{sc} and η. High-performance solar cells require efficient charge transfer. The interfacial resistance and charge transfer between the electrolyte and electrodes can be examined by electrochemical impedance spectroscopy (under illumination) (Adachi et al., 2011). As a result, a Nyquist plot will be obtained and reveal the output of charge transfer resistance at the photoanode/electrolyte interface and the CE/electrolyte interface (Kumari et al., 2016; Liu et al., 2022). In general, the Nyquist plot of a solar cell composed of three semicircles. The first semicircle is in the high frequency region, the second semicircle is

in the middle frequency region, and the third semicircle is in the extremely low frequency region. Figure 6.11 depicts an example of the Nyquist plot obtained from QDSSC. In the Nyquist plot, -Z'' is drawn against Z'. The experimental data is fitted with an equivalent circuit (red line), which consists of a resistor (R) connected in series with two parallel combinations of R and CPE, as shown in the inset in Figure 6.11. From the figure, R_Ω is the ohmic resistance of the QDSSC. In descending order of frequency, the first semicircle is related to the charge transfer resistance at the CE/electrolyte interface (R_{PT}), and the second semicircle links to the charge transfer resistance at the photoanode/electrolyte interface (R_{CT}).

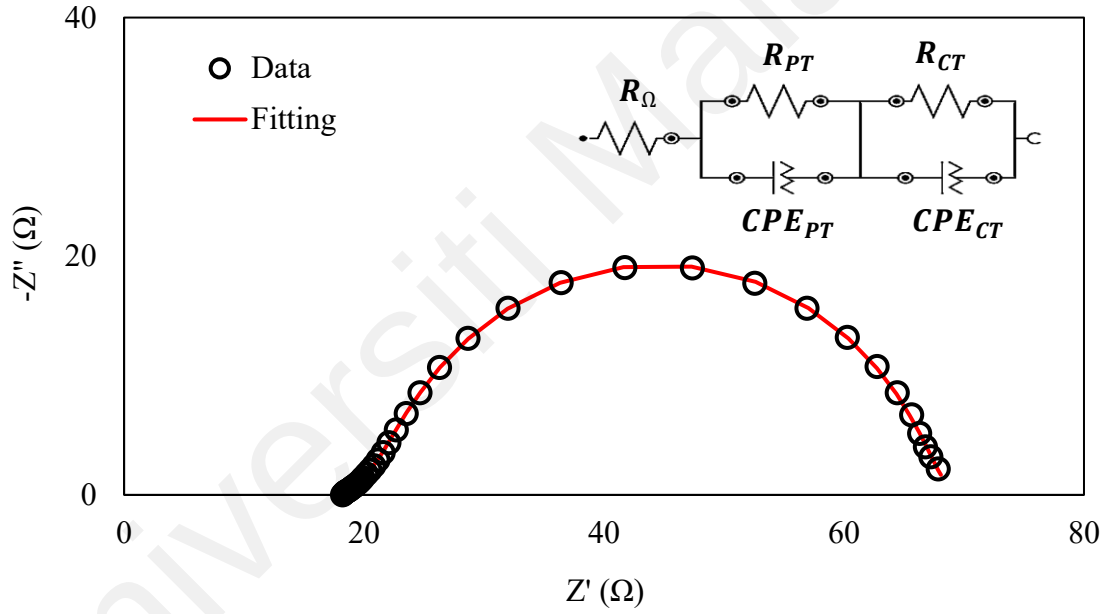

Figure 6.11: Nyquist plot obtained from QDSSC.

Figure 6.12 exemplifies each component involved in the charge transfer mechanism in a QDSSC. To further explain the charge transfer mechanism in QDSSCs, different types of charge transfer are outlined (see red and blue arrows): (I) electron injection from CdS to the TiO_2 layer, (II) electron diffusion from the TiO_2 layer to the FTO glass substrate, (III) regeneration of QDs, (IV) reduction of S_n^{2-} to S^{2-}, (V) recombination of electrons with oxidized QDs, (VI) reverse reaction of electrons from TiO_2 CB with S_n^{2-}, and (VII) reverse reaction of FTO electrons with S_n^{2-}. The movement of the blue arrows represents

possible recombination and reverse reactions that may occur before the electrons are successfully transferred to the external circuit, generate a load, and enter the CE in the QDSSC.

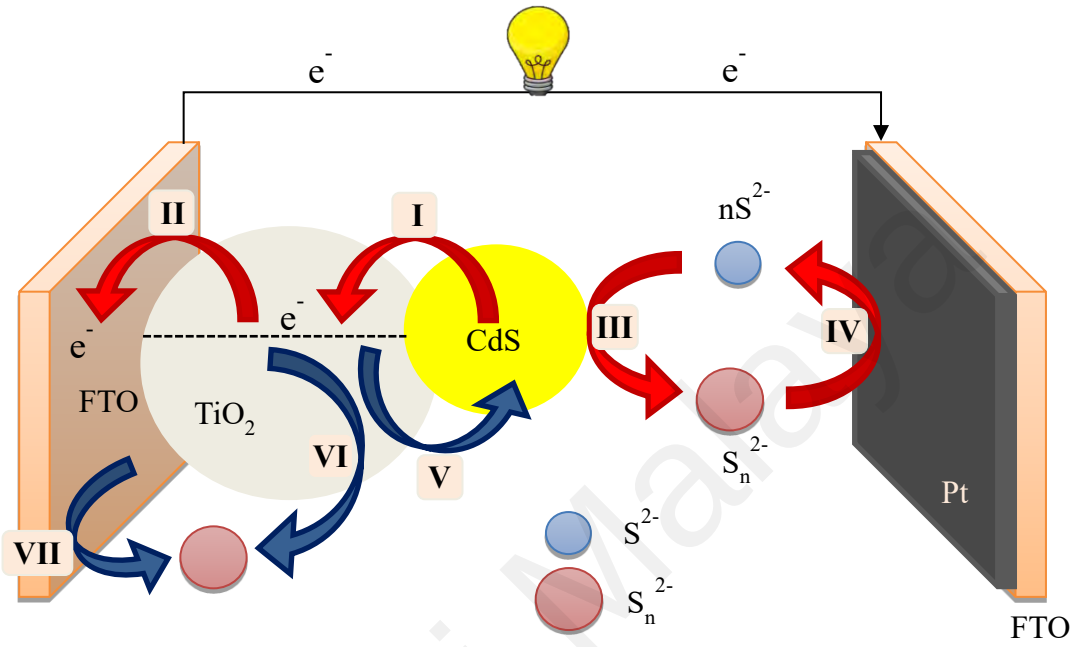

Figure 6.12: Schematic diagram of charge transfer mechanism involved in QDSSC.

6.4.1 QDSSC with Different GPE Compositions

Figure 6.13 and Table 6.8 show the Nyquist plots and electrochemical performance parameter of the quasi-solid QDSSCs. From the figure, all the Nyquist plots consist of two semicircles. Similar observations have also been studied in the literature (Baharun et al., 2020; Mingsukang et al., 2017b). They reported that this model is best represented by an equivalent circuit where R is connected in series with two parallel combinations R and CPE (see the inset of Figure 6.11). In Table 6.8, the R_{PT} value (first semicircle) is in the range of 10 Ω, and the R_{CT} value (second semicircle) is in the range of 35 to 45 Ω. QDSSC with Z3 GPE has the lowest charge transfer resistance at the CE/electrolyte interface (R_{PT}) and the photoanode/electrolyte interface (R_{CT}). This supports the findings in the previous section 6.3.1 that the optimal η for QDSSC with Z3 GPE is (1.80 ± 0.15)%. The lower the R_{PT}, the faster the reduction rate from S_n^{2-} to S^{2-} and the regeneration of QDs,

thereby increasing η. Meanwhile, the lower the R_{CT}, the faster the electrons can be injected into the TiO_2 layer and transferred to the external circuit and CE.

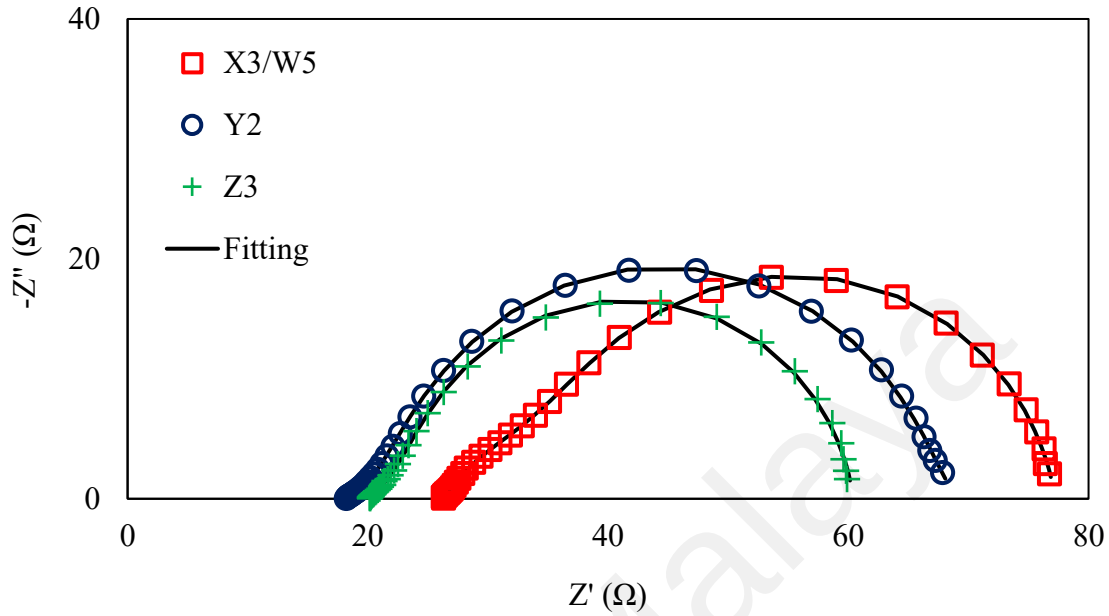

Figure 6.13: Nyquist plot of the quasi-solid QDSSCs.

Table 6.8: Electrochemical performance of the quasi-solid QDSSCs.

GPE	R_{Ω} (Ω)	R_{PT} (Ω)	R_{CT} (Ω)
X3/W5	26.43 ± 3.22	9.94 ± 1.09	45.04 ± 4.57
Y2	16.92 ± 1.67	9.23 ± 1.71	38.01 ± 2.57
Z3	21.48 ± 1.79	3.74 ± 0.71	35.33 ± 5.55

Figure 6.14 shows the proposed reaction of S_n^{2-} to S^{2-} at the CE/electrolyte interface. CE is a collector of electrons from an external circuit. After the electrons reach the CE through the external circuit, they will be transferred to S_n^{2-} in the electrolyte, become S^{2-}, and then continue to diffuse to the photoanode. S^{2-} is oxidized back to S_n^{2-} to regenerate QDs. The speed of the redox reaction can be attributed to the ionic mobility of the electrolyte. In a fast redox reaction, electrons are transferred faster to the redox couple. Seo and his coworkers reported that the addition of KCl activates redox reactions and expedites the movement of electrons in QDSSCs (Seo et al., 2013). In this work, it can be observed that the R_{PT} value of QDSSC with Z3 GPE has drastically decreased from

(9.23 ± 1.71) Ω to (3.74 ± 0.71) Ω, which can be attributed to the addition of KCl to the GPE. From this, it can be inferred that the addition of KCl accelerates the reduction rate of S_n^{2-} to S^{2-}, reduces the charge transfer resistance at the CE/electrolyte interface, and hastens the electron movement in the QDSSC, hence Z3 cell has lower R_{PT} value as compared to X3/W5 and Y2 cells. This is in agreement with the ion mobility (μ) results (μ that calculated at 30 kHz in Figure 5.24).

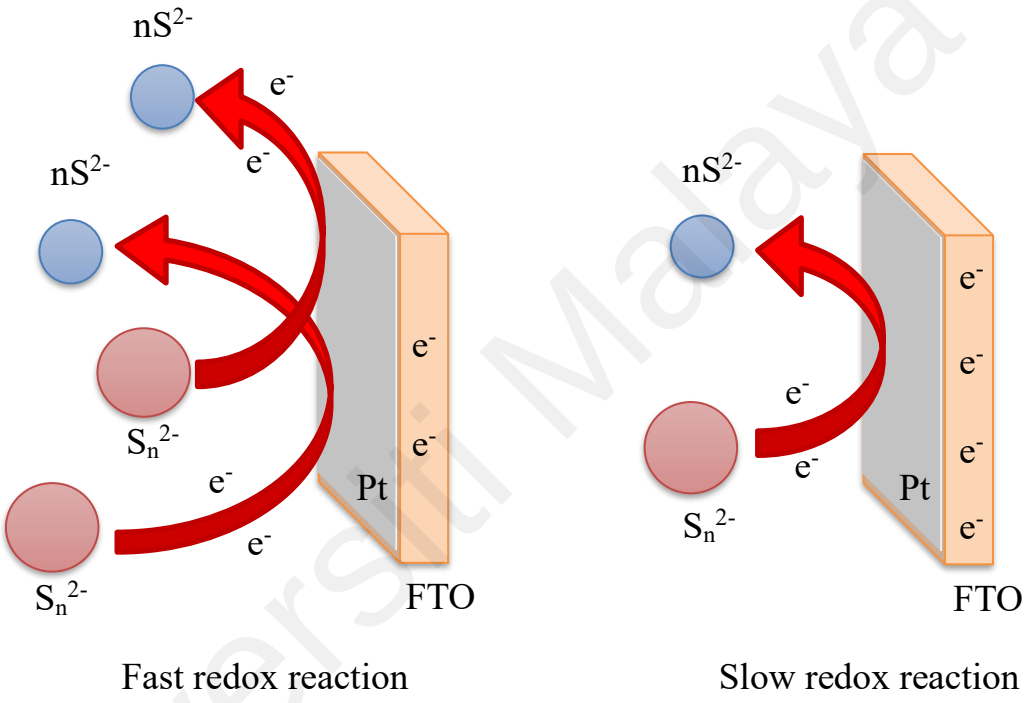

Figure 6.14: Redox reaction of S_n^{2-} to S^{2-} at CE/electrolyte interface.

6.4.2 QDSSC with Different TiO_2 Layers

Figure 6.15 and Table 6.9 show the Nyquist plots and electrochemical performance parameters of QDSSCs fabricated with different TiO_2/CdS/ZnS photoanodes. All Nyquist plots consist of two semicircles, as aforementioned. In this work, the first semicircle is insignificant to observe due to the extreme low resistance of R_{PT} compared to R_{CT}. Comparison among the cells shows A1 cell has the highest R_{CT} value while B3/Z3 cell has the lowest. This indicates that the thickness and types of TiO_2 layer influence the charge transfer kinetics in QDSSCs. The R_Ω values for all types of photoanodes are in the

range of 15 to 22 Ω. In addition, the output of R_{PT} is between (1.31 ± 0.40) Ω and (3.74 ± 0.71) Ω.

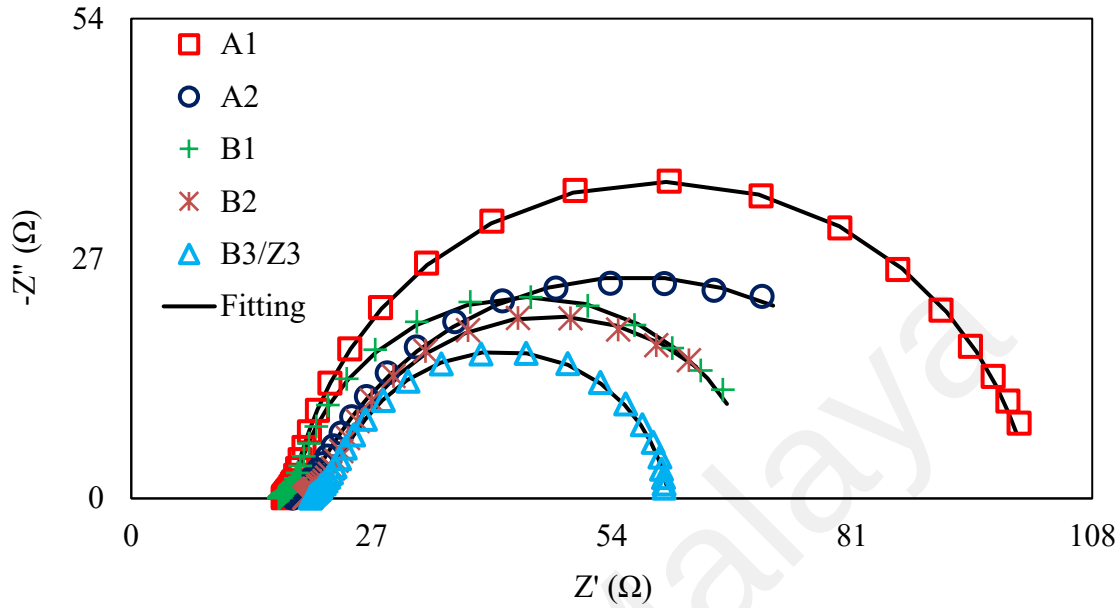

Figure 6.15: Nyquist plots of the QDSSCs using different TiO_2/CdS/ZnS photoanodes.

Table 6.9: Electrochemical performance parameters of the QDSSCs using different TiO_2/CdS/ZnS photoanodes.

Photoanode	R_{CT} (Ω)
A1	78.35 ± 6.86
A2	69.16 ± 6.28
B1	56.22 ± 4.92
B2	47.08 ± 4.21
B3/Z3	35.33 ± 5.55

As evident from Table 6.9, B3/Z3 cell possesses the lowest R_{CT} value which indicates that electrons diffuse rapidly into the TiO_2 layer (better charge carrier transfer at the interface) (Liu et al., 2022). Other photoanodes show higher R_{CT}, especially A1 having TiO_2 film thickness of (0.70 ± 0.01) µm, which has the highest R_{CT} at (78.35 ± 6.86) Ω. Higher charge transfer resistance means lower recombination resistance (Dissanayake et al., 2020) and shorter electron lifetime, which will lead to lower charge collection and photocurrent generation in QDSSC (Theint et al., 2020). This supports the findings of A1

which has a minimum J_{sc} of (4.29 ± 0.59) mA·cm^{-2} (see Table 6.6). When the thickness of the TiO_2 layer increases, the adsorption capacity of the QD will increase. The R_{CT} of B2 with a film thickness of (31.75 ± 0.64) µm is (47.08 ± 4.21) Ω, while the R_{CT} of B3/Z3 with a film thickness of (31.40 ± 0.58) µm is (35.33 ± 5.55) Ω. The difference in R_{CT} is attributed to the difference in P90 TiO_2 film thickness. Only the optimal compact TiO_2 film thickness can efficiently reduce electron recombination rate (Rhee & Kwon, 2011). It can be deduced that the film thickness ((10.51 ± 0.35) µm) of the P90 compact layer in B2 has exceeded the optimal value, which creates resistance to the movement of electrons from the TiO_2 layer to the FTO glass substrate. Subsequently, this may contribute to the recombination of electrons with oxidized QD and the reverse reaction of electrons from TiO_2 CB with S_n^{2-} in GPE.

6.5 Summary

CdS/ZnS QDSSCs were fabricated in-house through the SILAR method. CdS QD was synthesized from 0.1 M Cd^{2+} precursor solution and 0.1 M S^{2-} precursor solution, each with 5 dipping cycles and 1 min dipping time, while ZnS QD was synthesized from 0.1 M Zn^{2+} precursor solution and 0.1 M S^{2-} precursor solution, each with 2 dipping cycles and 1 min dipping time. Three GPE compositions were used in the quasi-solid CdS/ZnS QDSSC. The η of the optimized quasi-solid CdS/ZnS QDSSC is (1.80 ± 0.15)%. It was observed that after adding KCl to GPE, R_{PT} decreased from (9.23 ± 1.71) Ω to (3.74 ± 0.71) Ω. The effect of fast redox reaction leads to an increase in η. In addition, different types of TiO_2 layers and their film thicknesses have an impact on the electrochemical performance of QDSSC. The increase in the thickness of the TiO_2 layer increases the number of electron injection because it allows great amount of CdS QDs to be loaded onto its surface. Conversely, if the film thickness exceeds the optimal value, η will decrease because electrons are prohibited from diffusing through the TiO_2 layer to the FTO glass substrate. In addition, FF decreases when the carriers have to travel over

longer distance. Therefore, it can be concluded that FF and η are affected by the thickness of the TiO_2 layer. The introduction of the double-layer TiO_2 coating can prevent recombination of electrons. The double-layer TiO_2 coating has a low R_{CT}. Lower R_{CT} means higher recombination resistance and longer electron lifetime, thereby increasing charge collection and photocurrent generation in QDSSC. The R_{CT} of the optimized CdS/ZnS QDSSC with double-layer TiO_2 coating is (35.33 ± 5.55) Ω.

CHAPTER 7: CONCLUSIONS AND SUGGESTIONS FOR FUTURE WORK

7.1 Conclusions

This thesis focuses on the optimization of Na_2S salt and dual additives (EC and KCl) in GPE to improve QDSSC performance. GPE consists of a polymer host, salt solution and additives. Each component can be optimized for high ionic conductivity GPE and high performance QDSSC. GPE is prepared through stepwise parameter optimization. The results of the optimization work are introduced and discussed in two chapters (Chapter 4 to 5). FTIR characterization confirmed the success of PAAm-PAA-Na_2S-EC-KCl GPE. FTIR spectra verified the preparation of PAAm-PAA-Na_2S-EC-KCl GPE by the presence of characteristic peaks at 3395 cm^{-1}, 1661 cm^{-1}, 1557 cm^{-1}, 1406 cm^{-1}, 1120 cm^{-1}, 997 cm^{-1} and 667 cm^{-1} corresponding to the O-H stretching, C=O of $CONH_2$, ν_{as} COO^-, ν_s COO^- and/or C-N stretching, C-C skeletal and/or N-H rocking, ν_1 SO_4^{2-} and ν_4 SO_4^{2-}, respectively. In PAAm-PAA-Na_2S-EC-KCl GPE, there are molecular interactions between PAAm-PAA and distilled water, between PAAm-PAA and EC, and between EC and distilled water, and the ion-dipole is in (i) Na^+ cation and distilled water, (ii) Na^+ cation and PAAm-PAA, (iii) Na^+ cation and EC, (iv) K^+ cation and distilled water, (v) K^+ cation and PAAm-PAA and (vi) K^+ cation and EC. Various molar concentrations of Na_2S aqueous solutions have been introduced into PAAm-PAA based GPE, ranging from 2 M to 6 M Na_2S. GPE composed of PAAm-PAA : Na_2S aqueous solution : S in wt.% ratio of 25 : 73.2 : 1.8 obtains the best ionic conductivity at 51.13 $mS \cdot cm^{-1}$ and shows a η of 1.40% in QDSSC. As to enhance the ionic conductivity of GPE, various weight percentages (0.2 to 0.8 wt.%) of EC have been introduced into GPE. EC with high dielectric properties marginally increases the ionic conductivity and ionic mobility of GPE. GPE composed of PAAm-PAA: Na_2S aqueous solution: S: EC in wt.% ratio of 24.9: 72.9: 1.8: 0.4 shows the highest ionic conductivity of 69.21 $mS \cdot cm^{-1}$ and the η of QDSSC at 1.50%. The dielectric constant and ion mobility of PAAm-PAA-Na_2S-EC GPE

are marginally increased from (7.40×10^6) to (1.06×10^7) and from 10.33 $cm^2 \cdot V^{-1} \cdot s^{-1}$ to 29.45 $cm^2 \cdot V^{-1} \cdot s^{-1}$, respectively. The smaller cation K^+ was introduced into GPE to increase the reduction rate from S_n^{2-} to S^{2-} and penetrate into the TiO_2 layer to improve the performance of QDSSC. Various weight percentages of KCl have been introduced into GPE, ranging from 0.2 wt.% to 0.8 wt.% KCl. The GPE with PAAm-PAA : Na_2S aqueous solution : S : EC : KCl in wt.% ratio of 24.7 : 72.5 : 1.8 : 0.4 : 0.6 obtains the highest ionic conductivity of 70.75 $mS \cdot cm^{-1}$ and shows the best performance in QDSSC with η of 1.80%.

The different deposition methods and film thickness of the TiO_2 layer also affect the QDSSC performance. The best charge transfer mechanism was obtained by B3/Z3. The charge transfer resistance at the photoanode/electrolyte interface was 35.33 Ω. The success of TiO_2/CdS/ZnS photoanode was confirmed by EDX and XRD techniques. The EDX diagram verified the fabrication of TiO_2/CdS/ZnS photoanode by the presence of elements of Ti, O, Cd, Zn and S corresponds to 54.3 wt.%, 34.3 wt.%, 4.6 wt.%, 3.5 wt.% and 2.7 wt.%, respectively; and XRD ascertained that the photoanode used was composed of TiO_2, CdS and ZnS by the presence of hkℓ plane at 101, 004, 200, 204, 301, 111, 222, 331, 008 and 118 corresponds to TiO_2, CdS and ZnS, respectively.

7.2 Suggestions for Future Work

Although the optimization of the GPE and TiO_2 layers on the photoanode reported and discussed in this thesis has been completed, there are still other factors that need to be improved in order to produce high-performance QDSSC. Further work should be carried out to improve the performance of GPE in QDSSC, and to study the effect of TiO_2 film thickness on QDSSC performance.

1. To optimize the viscosity of GPE using rheology technique.

2. Conduct stability experiments to study the lifespan of liquid QDSSC and quasi-solid QDSSC.
3. To optimize the thickness of the TiO_2 layer using spin coating parameters for the enhancement of QDSSC performance.

REFERENCES

Adachi, M., Noda, K., Tanino, R., Adachi, J., Tsuchiya, K., Mori, Y., & Uchida, F. (2011). Comparison of electrochemical impedance spectroscopy between illumination and dark conditions. *Chemistry Letters, 40*(8), 890-892.

Ahmed, H. T., & Abdullah, O. G. (2020a). Impedance and ionic transport properties of proton-conducting electrolytes based on polyethylene oxide/methylcellulose blend polymers. *Journal of Science: Advanced Materials and Devices, 5*(1), 125-133.

Ahmed, H. T., & Abdullah, O. G. (2020b). Structural and ionic conductivity characterization of PEO: MC-NH_4I proton-conducting polymer blend electrolytes based films. *Results in Physics, 16*, 102861-102872.

Akinoglu, B. G., Tuncel, B., & Badescu, V. (2021). Beyond 3rd generation solar cells and the full spectrum project. Recent advances and new emerging solar cells. *Sustainable Energy Technologies and Assessments, 46*, Article#101287.

Alavi, M., Rahimi, R., Maleki, Z., & Hosseini-Kharat, M. (2020). Improvement of power conversion efficiency of quantum dot-sensitized solar cells by doping of manganese into a ZnS passivation layer and cosensitization of zinc-porphyrin on a modified graphene oxide/nitrogen-doped TiO_2 photoanode. *ACS omega, 5*(19), 11024-11034.

Ali, T. M., Padmanathan, N., & Selladurai, S. (2013). Structural, conductivity, and dielectric characterization of PEO–PEG blend composite polymer electrolyte dispersed with TiO_2 nanoparticles. *Ionics, 19*(8), 1115-1123.

Arof, A., Amirudin, S., Yusof, S., & Noor, I. (2014a). A method based on impedance spectroscopy to determine transport properties of polymer electrolytes. *Physical Chemistry Chemical Physics, 16*(5), 1856-1867.

Arof, A., Jun, H., Sim, L., Kufian, M., & Sahraoui, B. (2013). Gel polymer electrolyte based on LiBOB and PAN for the application in dye-sensitized solar cells. *Optical Materials, 36*(1), 135-139.

Arof, A. K., Aziz, M. F., Noor, M. M., Careem, M. A., Bandara, L. R. A. K., Thotawatthage, C. A., ... Dissanayake, M. A. K. L. (2014b). Efficiency enhancement by mixed cation effect in dye-sensitized solar cells with a PVdF based gel polymer electrolyte. *International Journal of Hydrogen Energy, 39*(6), 2929-2935.

Arya, A., Sadiq, M., & Sharma, A. (2018). Effect of variation of different nanofillers on structural, electrical, dielectric, and transport properties of blend polymer nanocomposites. *Ionics, 24*(8), 2295-2319.

Ayele, D. W., Su, W. N., & Hwang, B. J. (2013). A Low-Cost Polytetrafluoroethylene-Framed TiO_2 Electrode Decorated with Oleic Acid-Capped CdSe Quantum Dots for Solar Cell. *Journal of Energy, 2013*, 1-9.

Aziz, M. F., Buraidah, M. H., Careem, M. A., & Arof, A. K. (2015). PVA based gel polymer electrolytes with mixed iodide salts (K^+I^- and $Bu_4N^+I^-$) for dye-sensitized solar cell application. *Electrochimica Acta, 182*, 217-223.

Aziz, M. F., Noor, I. M., Sahraoui, B., & Arof, A. K. (2014). Dye-sensitized solar cells with PVA–KI–EC–PC gel electrolytes. *Optical Quantum Electronics, 46*(1), 133-141.

Aziz, S. B., Abdullah, O. G., Hussein, S. A., & Ahmed, H. M. (2017). Effect of PVA blending on structural and ion transport properties of CS: AgNt-based polymer electrolyte membrane. *Polymers, 9*(11), 622-638.

Aziz, S. B., Woo, H. J., Kadir, M. F. Z., & Ahmed, H. M. (2018). A conceptual review on polymer electrolytes and ion transport models. *Journal of Science: Advanced Materials and Devices, 3*, 1-17.

Babar, F., Mehmood, U., Asghar, H., Mehdi, M. H., Khan, A. U. H., Khalid, H., ... Fatima, Z. (2020). Nanostructured photoanode materials and their deposition methods for efficient and economical third generation dye-sensitized solar cells: A comprehensive review. *Renewable and Sustainable Energy Reviews, 129*, Article#109919.

Bagher, A. M. (2016). Solar cell quantum dots. *American Journal of Renewable and Sustainable Energy, 2*(1), 1-5.

Baharun, N. N. S., Mingsukang, M. A., Buraidah, M. H., Woo, H. J., Teo, L. P., & Arof, A. K. (2020). Development of solid polymer electrolytes based on sodium-carboxymethylcellulose (NaCMC)-polysulphide for quantum dot-sensitized solar cells (QDSSCs). *Ionics, 26*(3), 1365-1378.

Bai, Y., Mora-Sero, I., De Angelis, F., Bisquert, J., & Wang, P. (2014). Titanium dioxide nanomaterials for photovoltaic applications. *Chemical Reviews, 114*(19), 10095-10130.

Bandara, T. M. W. J., Jayasundara, W. J. M. J. S. R., Dissanayake, M. A. K. L., Furlani, M., Albinsson, I., & Mellander, B. E. (2013). Effect of cation size on the performance of dye sensitized nanocrystalline TiO_2 solar cells based on quasi-solid state PAN electrolytes containing quaternary ammonium iodides. *Electrochimica Acta, 109*, 609-616.

Banerjee, S., Zangiabadi, A., Mahdavi-Shakib, A., Husremovic, S., Frederick, B. G., Barmak, K., ... Billinge, S. J. L. (2019). Quantitative Structural Characterization of Catalytically Active TiO_2 Nanoparticles. *ACS Applied Nano Materials, 2*(10), 6268-6276.

Bang, J. H., & Kamat, P. V. (2010). Solar cells by design: photoelectrochemistry of TiO_2 nanorod arrays decorated with CdSe. *Advanced Functional Materials, 20*(12), 1970-1976.

Barea, E. M., Shalom, M., Giménez, S., Hod, I., Mora-Seró, I., Zaban, A., & Bisquert, J. (2010). Design of injection and recombination in quantum dot sensitized solar cells. *Journal of the American Chemical Society, 132*(19), 6834-6839.

Bashir, S., Teo, Y. Y., Naeem, S., Ramesh, S., & Ramesh, K. (2017). pH responsive N-succinyl chitosan/poly(acrylamide-co-acrylic acid) hydrogels and in vitro release of 5-fluorouracil. *Plos One, 12*(7), 0179250-0179273.

Ben Mabrouk, K., Kauffmann, T. H., Aroui, H., & Fontana, M. D. (2013). Raman study of cation effect on sulfate vibration modes in solid state and in aqueous solutions. *Journal of Raman Spectroscopy, 44*(11), 1603-1608.

Brennan, M. D., Breedon, M., Best, A. S., Morishita, T., & Spencer, M. J. S. (2017). Surface Reactions of Ethylene Carbonate and Propylene Carbonate on the Li (001) Surface. *Electrochimica Acta, 243*, 320-330.

Bruce, P. G., & Vincent, C. (1993). Polymer electrolytes. *Journal of the Chemical Society, Faraday Transactions, 89*(17), 3187-3203.

Bulakhe, R., Shinde, N., Thorat, R., Nikam, S., & Lokhande, C. (2013). Deposition of copper iodide thin films by chemical bath deposition (CBD) and successive ionic layer adsorption and reaction (SILAR) methods. *Current Applied Physics, 13*(8), 1661-1667.

Buraidah, M., Shah, S., Teo, L., Chowdhury, F. I., Careem, M., Albinsson, I., ... Arof, A. (2017). High efficient dye sensitized solar cells using phthaloylchitosan based gel polymer electrolytes. *Electrochimica Acta, 245*, 846-853.

Buraidah, M. H., Teo, L. P., Majid, S. R., & Arof, A. K. (2009). Ionic conductivity by correlated barrier hopping in NH_4I doped chitosan solid electrolyte. *Physica B: Condensed Matter, 404*(8-11), 1373-1379.

Califano, M., Zunger, A., & Franceschetti, A. (2004). Efficient inverse Auger recombination at threshold in CdSe nanocrystals. *Nano Letters, 4*(3), 525-531.

Chae, S. Y., Hwang, Y. J., & Joo, O.-S. (2014). Role of HA additive in quantum dot solar cell with $Co[(bpy)_3]^{2+/3+}$ based electrolyte. *RSC Advances, 4*(51), 26907-26911.

Chang, C. H., & Lee, Y. L. (2007). Chemical bath deposition of CdS quantum dots onto mesoscopic TiO_2 films for application in quantum-dot-sensitized solar cells. *Applied Physics Letters, 91*(5), 053503-053505.

Chang, J., Oshima, T., Hachiya, S., Sato, K., Toyoda, T., Katayama, K., ... Shen, Q. (2015). Uncovering the charge transfer and recombination mechanism in ZnS-coated PbS quantum dot sensitized solar cells. *Solar Energy, 122*, 307-313.

Chasan, D. E., & Norwitz, G. (1969). *Infrared determination of inorganic sulfates and carbonates by the pellet technique*: FRANKFORD ARSENAL PHILADELPHIA PA.

Chebrolu, V. T., & Kim, H. J. (2019). Recent progress in quantum dot sensitized solar cells: an inclusive review of photoanode, sensitizer, electrolyte, and the counter electrode. *Journal of Materials Chemistry C, 7*(17), 4911-4933.

Chen, G., Seo, J., Yang, C., & Prasad, P. N. (2013a). Nanochemistry and nanomaterials for photovoltaics. *Chemical Society Reviews, 42*(21), 8304-8338.

Chen, H. Y., Lin, L., Yu, X. Y., Qiu, K. Q., Lü, X. Y., Kuang, D. B., & Su, C. Y. (2013b). Dextran based highly conductive hydrogel polysulfide electrolyte for efficient quasi-solid-state quantum dot-sensitized solar cells. *Electrochimica Acta, 92*, 117-123.

Chen, J., Lei, W., & Deng, W. Q. (2011). Reduced charge recombination in a co-sensitized quantum dot solar cell with two different sizes of CdSe quantum dot. *Nanoscale, 3*(2), 674-677.

Chen, X. C., Sacci, R. L., Osti, N. C., Tyagi, M., Wang, Y., Palmer, M. J., & Dudney, N. J. (2019). Study of segmental dynamics and ion transport in polymer–ceramic composite electrolytes by quasi-elastic neutron scattering. *Molecular Systems Design & Engineering, 4*, 379-385.

Cheng, X., Pan, J., Zhao, Y., Liao, M., & Peng, H. (2018). Gel polymer electrolytes for electrochemical energy storage. *Advanced Energy Materials, 8*(7), 1702184-1702199.

Chiem, L. T., Huynh, L., Ralston, J., & Beattie, D. A. (2006). An in situ ATR–FTIR study of polyacrylamide adsorption at the talc surface. *Journal of Colloid and Interface Science, 297*(1), 54-61.

Choi, H., Nahm, C., Kim, J., Moon, J., Nam, S., Jung, D. R., & Park, B. (2012). The effect of $TiCl_4$-treated TiO_2 compact layer on the performance of dye-sensitized solar cell. *Current Applied Physics, 12*(3), 737-741.

Choi, J., & Cho, M. (2014). Ion aggregation in high salt solutions. II. Spectral graph analysis of water hydrogen-bonding network and ion aggregate structures. *The Journal of Chemical Physics, 141*(15), 154502-154514.

ChuláKim, J., BokáLee, Y., HoonáHong, J., InáLee, J., WookáYang, J., InáLee, W., & HwiáHur, N. (2006). Enhanced photocatalytic activity in composites of TiO_2 nanotubes and CdS nanoparticles. *Chemical Communications*(48), 5024-5026.

Chung, N. T. K., Nguyen, P. T., Tung, H. T., & Phuc, D. H. (2021). Quantum dot sensitized solar cell: photoanodes, counter electrodes, and electrolytes. *Molecules, 26*(9), Article#2638.

Cook, T. R., Dogutan, D. K., Reece, S. Y., Surendranath, Y., Teets, T. S., & Nocera, D. G. (2010). Solar energy supply and storage for the legacy and nonlegacy worlds. *Chemical Reviews, 110*(11), 6474-6502.

Deng, Y., Dixon, J. B., White, G. N., Loeppert, R. H., & Juo, A. S. R. (2006). Bonding between polyacrylamide and smectite. *Colloids and Surfaces A: Physicochemical and Engineering Aspects, 281*(1-3), 82-91.

Diguna, L. J., Shen, Q., Kobayashi, J., & Toyoda, T. (2007). High efficiency of CdSe quantum-dot-sensitized TiO_2 inverse opal solar cells. *Applied Physics Letters, 91*(2), 023116-023118.

Dissanayake, M., Thotawatthage, C., Senadeera, G., Bandara, T., Jayasundera, W., & Mellander, B. E. (2012). Efficiency enhancement by mixed cation effect in dye-

sensitized solar cells with PAN based gel polymer electrolyte. *Journal of Photochemistry and Photobiology A: Chemistry, 246*, 29-35.

Dissanayake, M. A. K. L., Jaseetharan, T., Senadeera, G. K. R., & Thotawatthage, C. A. (2018). A novel, PbS: Hg quantum dot-sensitized, highly efficient solar cell structure with triple layered TiO_2 photoanode. *Electrochimica Acta, 269*, 172-179.

Dissanayake, M. A. K. L., Liyanage, T., Jaseetharan, T., Senadeera, G. K. R., & Dassanayake, B. S. (2020). Effect of PbS quantum dot-doped polysulfide nanofiber gel polymer electrolyte on efficiency enhancement in CdS quantum dot-sensitized TiO_2 solar cells. *Electrochimica Acta, 347*, Article#136311.

Doyen, L., & Frech, R. (1996). Structure and vibrational dynamics of sodium sulfate/sodium chromate solid solutions. *The Journal of chemical physics, 104*(20), 7847-7853.

Du, J., Du, Z., Hu, J.-S., Pan, Z., Shen, Q., Sun, J., ... Zhong, X. (2016a). Zn–Cu–In–Se quantum dot solar cells with a certified power conversion efficiency of 11.6%. *Journal of the American Chemical Society, 138*(12), 4201-4209.

Du, J., Du, Z., Hu, J. S., Pan, Z., Shen, Q., Sun, J., ... Wan, L. J. (2016b). Zn–Cu–In–Se quantum dot solar cells with a certified power conversion efficiency of 11.6%. *Journal of the American Chemical Society, 138*(12), 4201-4209.

Du, J., Meng, X., Zhao, K., Li, Y., & Zhong, X. (2015). Performance enhancement of quantum dot sensitized solar cells by adding electrolyte additives. *Journal of Materials Chemistry A, 3*(33), 17091-17097.

Du, Z., Pan, Z., Fabregat-Santiago, F., Zhao, K., Long, D., Zhang, H., ... Bisquert, J. (2016c). Carbon counter-electrode-based quantum-dot-sensitized solar cells with certified efficiency exceeding 11%. *The Journal of Physical Chemistry Letters, 7*(16), 3103-3111.

Duan, J., Tang, Q., Li, R., He, B., Yu, L., & Yang, P. (2015a). Multifunctional graphene incorporated polyacrylamide conducting gel electrolytes for efficient quasi-solid-state quantum dot-sensitized solar cells. *Journal of Power Sources, 284*, 369-376.

Duan, J., Zhang, H., Tang, Q., He, B., & Yu, L. (2015b). Recent advances in critical materials for quantum dot-sensitized solar cells: a review. *Journal of Materials Chemistry A, 3*(34), 17497-17510.

Duan, Y., Tang, Q., Liu, J., He, B., & Yu, L. (2014). Transparent metal selenide alloy counter electrodes for high-efficiency bifacial dye-sensitized solar cells. *Angewandte Chemie International Edition, 53*(52), 14569-14574.

Ellingson, R. J., Beard, M. C., Johnson, J. C., Yu, P., Micic, O. I., Nozik, A. J., ... Efros, A. L. (2005). Highly efficient multiple exciton generation in colloidal PbSe and PbS quantum dots. *Nano Letters, 5*(5), 865-871.

Estrada, D., Echeverry, L., Ramirez, A., & Gutierrez, L. (2020). Molybdenite flotation in the presence of a polyacrylamide of low anionicity subjected to different conditions of mechanical shearing. *Minerals, 10*(10), Article#895.

Evangelista, R. M., Makuta, S., Yonezu, S., Andrews, J., & Tachibana, Y. (2016). Semiconductor quantum dot sensitized solar cells based on ferricyanide/ferrocyanide redox electrolyte reaching an open circuit photovoltage of 0.8 V. *ACS Applied Materials & Interfaces, 8*(22), 13957-13965.

Feng, W., Li, Y., Du, J., Wang, W., & Zhong, X. (2016a). Highly efficient and stable quasi-solid-state quantum dot-sensitized solar cells based on a superabsorbent polyelectrolyte. *Journal of Materials Chemistry A, 4*(4), 1461-1468.

Feng, W., Zhao, L., Du, J., Li, Y., & Zhong, X. (2016b). Quasi-solid-state quantum dot sensitized solar cells with power conversion efficiency over 9% and high stability. *Journal of Materials Chemistry A, 4*(38), 14849-14856.

Ford, H. O., Park, B., Jiang, J., Seidler, M. E., & Schaefer, J. L. (2020). Enhanced Li^+ conduction within single-ion conducting polymer gel electrolytes via reduced cation–polymer interaction. *ACS Materials Letters, 2*(3), 272-279.

Fukui, A., Fuke, N., Komiya, R., Koide, N., Yamanaka, R., Katayama, H., & Han, L. (2009). Dye-sensitized photovoltaic module with conversion efficiency of 8.4%. *Applied Physics Express, 2*(8), 082202-082204.

Ganjian, M., Kolahdouz, M., Aletayeb, A., Norouzi, M., Ebrahimi, P., Pourjafari, S., & Mousavi, M. S. S. (2017). ZnS shell-like CdS quantum dot-sensitized solar cell grown by SILAR approach; effect of electrolyte, counter electrode, and shell thickness. *Vacuum, 146*, 548-553.

Gnanasambandam, R., & Proctor, A. (2000). Determination of pectin degree of esterification by diffuse reflectance Fourier transform infrared spectroscopy. *Food Chemistry, 68*(3), 327-332.

Golodnitsky, D., Strauss, E., Peled, E., & Greenbaum, S. (2015). On order and disorder in polymer electrolytes. *Journal of The Electrochemical Society, 162*(14), A2551-A2566.

González-Pedro, V., Xu, X., Mora-Sero, I., & Bisquert, J. (2010). Modeling high-efficiency quantum dot sensitized solar cells. *ACS Nano, 4*(10), 5783-5790.

Gopi, C. V., Venkata-Haritha, M., Seo, H., Singh, S., Kim, S. K., Shiratani, M., & Kim, H. J. (2016). Improving the performance of quantum dot sensitized solar cells through CdNiS quantum dots with reduced recombination and enhanced electron lifetime. *Dalton Transactions, 45*(20), 8447-8457.

Green, M. A. (2019). Photovoltaic technology and visions for the future. *Progress in Energy, 1*(1), Article#013001.

Guo, Y., Zhou, X., Tang, Q., Bao, H., Wang, G., & Sáha, P. (2016). A self-healable and easily recyclable supramolecular hydrogel electrolyte for flexible supercapacitors. *Journal of Materials Chemistry A, 4*(22), 8769-8776.

Gupta, R. K., & Rhee, H. W. (2013). Plasticizing effect of K^+ ions and succinonitrile on electrical conductivity of [poly (ethylene oxide)–succinonitrile]/KI–I_2 redox-

couple solid polymer electrolyte. *The Journal of Physical Chemistry B, 117*(24), 7465-7471.

Hafiza, M., Bashirah, A., Bakar, N., & Isa, M. (2014). Electrical properties of carboxyl methylcellulose/chitosan dual-blend green polymer doped with ammonium bromide. *International Journal of Polymer Analysis Characterization, 19*(2), 151-158.

Han, C.-Y., Kim, H.-S., & Yang, H. (2020). Quantum Dots and Applications. *Materials, 13*(4), 897-899.

Han, X., Peng, Y., & Ma, Z. (2016). Effect of magnetic field on optical features of water and KCl solutions. *Optik, 127*(16), 6371-6376.

Haring, A. J., Pomatto, M. E., Thornton, M. R., & Morris, A. J. (2014). $Mn^{II/III}$ complexes as promising redox mediators in quantum-dot-sensitized solar cells. *ACS Applied Materials & Interfaces, 6*(17), 15061-15067.

Hassan, M. F., & Yusof, S. Z. M. (2014). Poly(acrylamide-co-acrylic acid)-zinc acetate polymer electrolytes: studies based on structural and morphology and electrical spectroscopy. *Microscopy Research, 2*(2), 30-38.

Hodes, G. (2008). Comparison of dye-and semiconductor-sensitized porous nanocrystalline liquid junction solar cells. *The Journal of Physical Chemistry C, 112*(46), 17778-17787.

Huang, F., Hou, J., Zhang, Q., Wang, Y., Massé, R. C., Peng, S., ... Cao, G. (2016). Doubling the power conversion efficiency in CdS/CdSe quantum dot sensitized solar cells with a ZnSe passivation layer. *Nano Energy, 26*, 114-122.

Huo, Z., Tao, L., Wang, S., Wei, J., Zhu, J., Dong, W., ... Dai, S. (2015). A novel polysulfide hydrogel electrolyte based on low molecular mass organogelator for quasi-solid-state quantum dot-sensitized solar cells. *Journal of Power Sources, 284*, 582-587.

Hwang, I., & Yong, K. (2015). Counter electrodes for quantum-dot-sensitized solar cells. *ChemElectroChem, 2*(5), 634-653.

Ileperuma, O. A. (2013). Gel polymer electrolytes for dye sensitised solar cells: a review. *Materials Technology, 28*(1-2), 65-70.

Iwakura, C., Nohara, S., Furukawa, N., & Inoue, H. (2002). The possible use of polymer gel electrolytes in nickel/metal hydride battery. *Solid State Ionics, 148*(3-4), 487-492.

Jasim, K. E. (2015). Quantum dots solar cells. *Solar Cells-New Approaches and Reviews*, 303-331.

Jia, J., Mu, L., Lin, Y., & Zhou, X. (2018). Rutile versus anatase for quantum dot sensitized solar cell. *Electrochimica acta, 266*, 103-109.

Jiang, G., Pan, Z., Ren, Z., Du, J., Yang, C., Wang, W., & Zhong, X. (2016). Poly(vinyl pyrrolidone): a superior and general additive in polysulfide electrolytes for high efficiency quantum dot sensitized solar cells. *Journal of Materials Chemistry A, 4*(29), 11416-11421.

Jiao, S., Du, J., Du, Z., Long, D., Jiang, W., Pan, Z., ... Zhong, X. (2017). Nitrogen-doped mesoporous carbons as counter electrodes in quantum dot sensitized solar cells with a conversion efficiency exceeding 12%. *The journal of physical chemistry letters, 8*(3), 559-564.

Jin, X., You, L., Chen, Z., & Li, Q. (2018). High-efficiency platinum-free quasi-solid-state dye-sensitized solar cells from polyaniline (polypyrrole)-carbon nanotube complex tailored conducting gel electrolytes and counter electrodes. *Electrochimica acta, 260*, 905-911.

Jing, Z., Xu, A., Liang, Y. Q., Zhang, Z., Yu, C., Hong, P., & Li, Y. (2019). Biodegradable poly(acrylic acid-co-acrylamide)/poly(vinyl alcohol) double network hydrogels with tunable mechanics and high self-healing performance. *Polymers, 11*(6), 952-969.

John, T., & Tony, W. (2017). Renewable Energy Resources Second Edition. In: Taylor & Francis.

Jones, L. H., & McLaren, E. (1954). Infrared spectra of CH_3COONa and CD_3COONa and assignments of vibrational frequencies. *The Journal of chemical physics, 22*(11), 1796-1800.

Jun, H., Careem, M., & Arof, A. (2013a). A suitable polysulfide electrolyte for CdSe quantum dot-sensitized solar cells. *International Journal of Photoenergy, 2013*(942139), 1-10.

Jun, H. K., Careem, M. A., & Arof, A. K. (2013b). Quantum dot-sensitized solar cells—perspective and recent developments: a review of Cd chalcogenide quantum dots as sensitizers. *Renewable and Sustainable Energy Reviews, 22*, 148-167.

Jun, H. K., Careem, M. A., & Arof, A. K. (2014). Fabrication, characterization, and optimization of CdS and CdSe quantum dot-sensitized solar cells with quantum dots prepared by successive ionic layer adsorption and reaction. *International Journal of Photoenergy, 2014*(939423), 1-14.

Kadir, M. F. Z., Aspanut, Z., Majid, S. R., & Arof, A. K. (2011). FTIR studies of plasticized poly (vinyl alcohol)–chitosan blend doped with NH_4NO_3 polymer electrolyte membrane. *Spectrochimica Acta Part A: Molecular and Biomolecular Spectroscopy, 78*(3), 1068-1074.

Kamat, P. V. (2012). Boosting the efficiency of quantum dot sensitized solar cells through modulation of interfacial charge transfer. *Accounts of chemical research, 45*(11), 1906-1915.

Kannan, N., & Vakeesan, D. (2016). Solar energy for future world: - A review. *Renewable and Sustainable Energy Reviews, 62*, 1092-1105.

Karageorgopoulos, D., Stathatos, E., & Vitoratos, E. (2012). Thin ZnO nanocrystalline films for efficient quasi-solid state electrolyte quantum dot sensitized solar cells. *Journal of Power Sources, 219*, 9-15.

Kassim, A., Nagalingam, S., Min, H. S., & Karrim, N. (2010). XRD and AFM studies of ZnS thin films produced by electrodeposition method. *Arabian Journal of Chemistry, 3*(4), 243-249.

Kebede, Z., & Lindquist, S.-E. (1998). The obstructed diffusion of the I_3^- ion in mesoscopic TiO_2 membranes. *Solar Energy Materials and Solar Cells, 51*(3-4), 291-303.

Kelly, C. A., Farzad, F., Thompson, D. W., Stipkala, J. M., & Meyer, G. J. (1999). Cation-controlled interfacial charge injection in sensitized nanocrystalline TiO_2. *Langmuir, 15*(20), 7047-7054.

Kelly, C. A., & Meyer, G. J. (2001). Excited state processes at sensitized nanocrystalline thin film semiconductor interfaces. *Coordination Chemistry Reviews, 211*(1), 295-315.

Kessinger, M. C., Langlois, R., Roof, J., Shaikh, S. M., Tanko, J. M., & Morris, A. J. (2018). Improving the Efficiency of the $Mn^{2+/3+}$ Couple in Quantum Dot Solar Cells: The Role of Spin Crossover. *The Journal of Physical Chemistry C, 122*, 14135−14149.

Khan, M. A., Akhtar, M. S., & Yang, O. B. (2010). Synthesis, characterization and application of sol–gel derived mesoporous TiO_2 nanoparticles for dye-sensitized solar cells. *Solar Energy, 84*(12), 2195-2201.

Khodam, F., Amani-Ghadim, A. R., & Aber, S. (2019). Preparation of CdS quantum dot sensitized solar cell based on ZnTi-layered double hydroxide photoanode to enhance photovoltaic properties. *Solar Energy, 181*, 325-332.

Kim, C. S., & Oh, S. M. (2000). Importance of donor number in determining solvating ability of polymers and transport properties in gel-type polymer electrolytes. *Electrochimica Acta, 45*(13), 2101-2109.

Kim, D. H., Park, M. A., Kim, S. E., Kim, J. H., Ahn, K. S., & Kang, M. S. (2017). Tough hydrogel electrolytes doped with polysulfide redox couples for quantum-dot-sensitized solar cells. *Chemistry Letters, 47*(1), 51-54.

Kim, H., Hwang, I., & Yong, K. (2014). Highly durable and efficient quantum dot-sensitized solar cells based on oligomer gel electrolytes. *ACS Applied Materials & Interfaces, 6*(14), 11245-11253.

Kim, H. J., Kim, J. H., Durga, I. K., Punnoose, D., Kundakarla, N., Reddy, A. E., & Rao, S. S. (2016a). Densely packed zinc sulfide nanoparticles on TiO_2 for hindering electron recombination in dye-sensitized solar cells. *New Journal of Chemistry, 40*(11), 9176-9186.

Kim, J.-Y., Yang, J., Yu, J. H., Baek, W., Lee, C.-H., Son, H. J., ... Ko, M. J. (2015). Highly efficient Copper–Indium–Selenide quantum dot solar cells: suppression of

carrier recombination by controlled ZnS overlayers. *ACS Nano, 9*(11), 11286-11295.

Kim, M. S., Kim, B. G., & Kim, J. (2009). Effective variables to control the fill factor of organic photovoltaic cells. *ACS Applied Materials & Interfaces, 1*(6), 1264-1269.

Kim, T.-Y., Song, D., Barea, E. M., Lee, J. H., Kim, Y. R., Cho, W., ... Kang, Y. S. (2016b). Origin of high open-circuit voltage in solid state dye-sensitized solar cells employing polymer electrolyte. *Nano Energy, 28*, 455-461.

Kinoshita, S. C., Kotato, M., Sakata, Y., Ue, M., Watanabe, Y., Morimoto, H., & Tobishima, S. I. (2008). Effects of cyclic carbonates as additives to γ-butyrolactone electrolytes for rechargeable lithium cells. *Journal of Power Sources, 183*(2), 755-760.

Kleinjan, W. E., de Keizer, A., & Janssen, A. J. (2005). Equilibrium of the reaction between dissolved sodium sulfide and biologically produced sulfur. *Colloids Surfaces B: Biointerfaces, 43*(3-4), 228-237.

Kong, X., Zhang, L., Liu, B., Gao, H., Zhang, Y., Yan, H., & Song, X. (2019). Graphene/Si Schottky solar cells: a review of recent advances and prospects. *RSC Advances, 9*(2), 863-877.

Kouhnavard, M., Ikeda, S., Ludin, N. A., Khairudin, N. B. A., Ghaffari, B. V., Mat-Teridi, M. A., ... Sopian, K. (2014). A review of semiconductor materials as sensitizers for quantum dot-sensitized solar cells. *Renewable and Sustainable Energy Reviews, 37*, 397-407.

Krašovec, U. O., Berginc, M., Hočevar, M., & Topič, M. (2009). Unique TiO_2 paste for high efficiency dye-sensitized solar cells. *Solar Energy Materials and Solar Cells, 93*(3), 379-381.

Kumar, S., Demappa, T., & Sannappa, J. (2022). Influence of KI salt concentration on the hydroxypropyl methylcellulose films: optical study. *Optical Materials, 129*, Article#112474.

Kumaran, V. S., Ng, H. M., Ramesh, S., Ramesh, K., Vengadaesvaran, B., & Numan, A. (2018). The conductivity and dielectric studies of solid polymer electrolytes based on poly(acrylamide-co-acrylic acid) doped with sodium iodide. *Ionics, 24*(7), 1947-1953.

Kumari, J. M. K. W., Sanjeevadharshini, N., Dissanayake, M. A. K. L., Senadeera, G. K. R., & Thotawatthage, C. A. (2016). The effect of TiO_2 photoanode film thickness on photovoltaic properties of dye-sensitized solar cells. *Ceylon Journal of Science, 45*(1), 33-41.

Kurc, B. (2014). Precipitated silica as filler for polymer electrolyte based on poly (acrylonitrile)/sulfolane. *Journal of Solid State Electrochemistry, 18*(7), 2035-2046.

Lane, M. D. (2007). Mid-infrared emission spectroscopy of sulfate and sulfate-bearing minerals. *American Mineralogist, 92*(1), 1-18.

Lee, H. J., Chen, P., Moon, S. J., Sauvage, F., Sivula, K., Bessho, T., ... Seok, S. I. (2009). Regenerative PbS and CdS quantum dot sensitized solar cells with a cobalt complex as hole mediator. *Langmuir, 25*(13), 7602-7608.

Lee, H. J., Yum, J. H., Leventis, H. C., Zakeeruddin, S. M., Haque, S. A., Chen, P., ... Nazeeruddin, M. K. (2008a). CdSe quantum dot-sensitized solar cells exceeding efficiency 1% at full-sun intensity. *The Journal of Physical Chemistry C, 112*(30), 11600-11608.

Lee, K. M., Suryanarayanan, V., & Ho, K. C. (2006). The influence of surface morphology of TiO_2 coating on the performance of dye-sensitized solar cells. *Solar Energy Materials and Solar Cells, 90*(15), 2398-2404.

Lee, Y. L., Huang, B. M., & Chien, H. T. (2008b). Highly efficient CdSe-sensitized TiO_2 photoelectrode for quantum-dot-sensitized solar cell applications. *Chemistry of Materials, 20*(22), 6903-6905.

Lee, Y. C., Buraidah, M. H., & Woo, H. J. (2020). Poly(acrylamide-co-acrylic acid) gel polymer electrolyte incorporating with water-soluble sodium sulfide salt for quasi-solid-state quantum dot-sensitized solar cell. *High Performance Polymers, 32*(2), 183-191.

Lee, Y. L., & Chang, C. H. (2008). Efficient polysulfide electrolyte for CdS quantum dot-sensitized solar cells. *Journal of Power Sources, 185*(1), 584-588.

Lee, Y. L., & Lo, Y. S. (2009). Highly efficient quantum-dot-sensitized solar cell based on co-sensitization of CdS/CdSe. *Advanced Functional Materials, 19*(4), 604-609.

Lee, Y. S., Gopi, C. V., Venkata-Haritha, M., & Kim, H. J. (2016). Recombination control in high-performance quantum dot-sensitized solar cells with a novel TiO_2/ZnS/CdS/ZnS heterostructure. *Dalton Transactions, 45*(32), 12914-12923.

Lee, Y. S., Gopi, C. V. V. M., Reddy, A. E., Nagaraju, C., & Kim, H. J. (2017). High performance of TiO_2/CdS quantum dot sensitized solar cells with a Cu–ZnS passivation layer. *New Journal of Chemistry, 41*(5), 1914-1917.

Lewis, R. N., McElhaney, R. N., Pohle, W., & Mantsch, H. H. (1994). Components of the carbonyl stretching band in the infrared spectra of hydrated 1,2-diacylglycerolipid bilayers: a reevaluation. *Biophysical Journal, 67*(6), 2367-2375.

Li, B., Wang, L., Kang, B., Wang, P., & Qiu, Y. (2006). Review of recent progress in solid-state dye-sensitized solar cells. *Solar Energy Materials and Solar Cells, 90*(5), 549-573.

Li, L., Liu, L., Qing, Y., Zhang, Z., Yan, N., Wu, Y., & Tian, C. (2018). Stretchable alkaline poly(acrylic acid) electrolyte with high ionic conductivity enhanced by cellulose nanofibrils. *Electrochimica Acta, 270*, 302-309.

Li, L., Yang, X., Gao, J., Tian, H., Zhao, J., Hagfeldt, A., & Sun, L. (2011). Highly efficient CdS quantum dot-sensitized solar cells based on a modified polysulfide electrolyte. *Journal of the American Chemical Society, 133*(22), 8458-8460.

Li, W., Wu, Z., Wang, J., Elzatahry, A. A., & Zhao, D. (2014). A perspective on mesoporous TiO_2 materials. *Chemistry of Materials, 26*(1), 287-298.

Liao, Y., Zhang, J., Liu, W., Que, W., Yin, X., Zhang, D., ... Zhang, H. (2015). Enhancing the efficiency of CdS quantum dot-sensitized solar cells via electrolyte engineering. *Nano Energy, 11*, 88-95.

Liu, Y., Chen, K., Peng, Z., & Chen, W. (2018). Flexible Quantum Dot Sensitized Solar Cells. In *Flexible Energy Conversion Storage Devices* (pp. 339-382).

Liu, Y., Hagfeldt, A., Xiao, X.-R., & Lindquist, S. E. (1998). Investigation of influence of redox species on the interfacial energetics of a dye-sensitized nanoporous TiO_2 solar cell. *Solar Energy Materials and Solar Cells, 55*(3), 267-281.

Liu, Y., Wang, Z., Li, L., Gao, S., Zheng, D., Yu, X., ... Yang, W. (2022). Highly efficient quantum-dot-sensitized solar cells with composite semiconductor of ZnO nanorod and oxide inverse opal in photoanode. *Electrochimica Acta, 412*, Article#140145.

Longo, C., & De Paoli, M. A. (2003). Dye-sensitized solar cells: a successful combination of materials. *Journal of the Brazilian Chemical Society, 14*(6), 898-901.

Lu, X., & Mi, Y. (2005). Characterization of the interfacial interaction between polyacrylamide and silicon substrate by Fourier transform infrared spectroscopy. *Macromolecules, 38*(3), 839-843.

Luceño-Sánchez, J. A., Díez-Pascual, A. M., & Peña Capilla, R. (2019). Materials for photovoltaics: State of art and recent developments. *International Journal of Molecular Sciences, 20*(4), Article#976.

Luo, T., Vohs, J. M., & Gorte, R. J. (2002). An examination of sulfur poisoning on Pd/Ceria catalysts. *Journal of Catalysis, 210*, 397–404.

M.H., S., & Al-Jawad. (2017). Comparative study between CBD and SILAR methods for deposited TiO_2, CdS, and TiO_2/CdS core-shell structure. *Materials Science in Semiconductor Processing, 67*, 75-83.

Magalhães, A. S. G., Almeida Neto, M. P., Bezerra, M. N., Ricardo, N. M., & Feitosa, J. (2012). Application of FTIR in the determination of acrylate content in poly (sodium acrylate-co-acrylamide) superabsorbent hydrogels. *Química Nova, 35*(7), 1464-1467.

Mahalingam, S., Manap, A., Lau, K. S., Omar, A., Chelvanathan, P., Chia, C. H., ... Rahim, N. A. (2022). Mixture deposition method for graphene quantum dots-based dye-sensitized solar cell. *Electrochimica Acta, 404*, Article#139732.

Malhotra, S., & Varshney, P. K. (2015). Effect of fillers on composite polymer electrolytes- a study. *International Journal of Applied Engineering Research, 10*(94), Article#2015.

Masia, M., Probst, M., & Rey, R. (2004). Ethylene carbonate−Li^+: A theoretical study of structural and vibrational properties in gas and liquid phases. *The Journal of Physical Chemistry B, 108*(6), 2016-2027.

Matsui, H., Okada, K., Kitamura, T., & Tanabe, N. (2009). Thermal stability of dye-sensitized solar cells with current collecting grid. *Solar Energy Materials and Solar Cells, 93*(6-7), 1110-1115.

Mekhilef, S., Safari, A., Mustaffa, W., Saidur, R., Omar, R., & Younis, M. (2012). Solar energy in Malaysia: current state and prospects. *Renewable and Sustainable Energy Reviews, 16*(1), 386-396.

Meyer, W. H. (1998). Polymer electrolytes for lithium-ion batteries. *Advanced materials, 10*(6), 439-448.

Mingsukang, M. A., Buraidah, M. H., & Careem, M. A. (2017a). Development of gel polymer electrolytes for application in quantum dot-sensitized solar cells. *Ionics, 23*(2), 347-355.

Mingsukang, M. A., Buraidah, M. H., Careem, M. A., Albinsson, I., Mellander, B. E., & Arof, A. K. (2017b). Investigation of counter electrode materials for gel polymer electrolyte based quantum dot sensitized solar cells. *Electrochimica Acta, 241*, 487-496.

Mojet, B. L., Ebbesen, S. D., & Lefferts, L. (2010). Light at the interface: the potential of attenuated total reflection infrared spectroscopy for understanding heterogeneous catalysis in water. *Chemical Society Reviews, 39*(12), 4643-4655.

Molinari, N., Mailoa, J. P., & Kozinsky, B. (2018). Effect of salt concentration on ion clustering and transport in polymer solid electrolytes: a molecular dynamics study of peo–litfsi. *Chemistry of Materials, 30*(18), 6298-6306.

Moon, D. J., & Lim, W. T. (2020). Synthesis and single-crystal structure of sodium sulfide cationic cluster in the sodalite cavity of zeolite Y (FAU, Si/Al= 1.56). *Journal of Porous Materials, 27*, 1233-1240.

Mora-Sero, I., Gimenez, S., Fabregat-Santiago, F., Gomez, R., Shen, Q., Toyoda, T., & Bisquert, J. (2009). Recombination in quantum dot sensitized solar cells. *Accounts of Chemical Research, 42*(11), 1848-1857.

Muthalif, M. P. A., Sunesh, C. D., & Choe, Y. (2019). Enhanced light absorption and charge recombination control in quantum dot sensitized solar cells using tin doped cadmium sulfide quantum dots. *Journal of Colloid and Interface Science, 534*, 291-300.

Nash, D. B. (1988). Infrared reflectance spectra of Na_2S with contaminant Na_2CO_3: Effects of adsorbed H_2O and CO_2 and relation to studies of Io. *Icarus, 74*(2), 365-368.

Natesan, B., Karan, N. K., Rivera, M. B., Aliev, F. M., & Katiyar, R. S. (2006). Segmental relaxation and ion transport in polymer electrolyte films by dielectric spectroscopy. *Journal of Non-Crystalline Solids, 352*(42-49), 5205-5209.

Nesrinne, S., & Djamel, A. (2017). Synthesis, characterization and rheological behavior of pH sensitive poly (acrylamide-co-acrylic acid) hydrogels. *Arabian Journal of Chemistry, 10*(4), 539-547.

Ngai, K. S., Ramesh, S., Ramesh, K., & Juan, J. C. (2016). A review of polymer electrolytes: fundamental, approaches and applications. *Ionics, 22*(8), 1259-1279.

Nogueira, A., Longo, C., & De Paoli, M. A. (2004). Polymers in dye sensitized solar cells: overview and perspectives. *Coordination Chemistry Reviews, 248*(13-14), 1455-1468.

Nogueira, A. F., De Paoli, M. A., Montanari, I., Monkhouse, R., Nelson, J., & Durrant, J. R. (2001). Electron transfer dynamics in dye sensitized nanocrystalline solar cells using a polymer electrolyte. *The Journal of Physical Chemistry B, 105*(31), 7517-7524.

Noor, M., Buraidah, M., Yusuf, S., Careem, M., Majid, S. R., & Arof, A. K. (2011). Performance of dye-sensitized solar cells with (PVDF-HFP)-KI-EC-PC electrolyte and different dye materials. *International Journal of Photoenergy, 2011*, 960487-960491.

Noor, M. M., Buraidah, M. H., Careem, M. A., Majid, S. R., & Arof, A. K. (2014). An optimized poly (vinylidene fluoride-hexafluoropropylene)–NaI gel polymer electrolyte and its application in natural dye sensitized solar cells. *Electrochimica Acta, 121*, 159-167.

Nyquist, R. A. (2001). Thiols, Sulfides and Disulfides, Alkanethiols, and Alkanedithiols (S− H Stretching). *Interpreting Infrared, Raman, and Nuclear Magnetic Resonance Spectra, 2*, 65-83.

Oskam, G., Bergeron, B. V., Meyer, G. J., & Searson, P. C. (2001). Pseudohalogens for dye-sensitized TiO_2 photoelectrochemical cells. *The Journal of Physical Chemistry B, 105*(29), 6867-6873.

Osman, Z., & Arof, A. K. (2003). FTIR studies of chitosan acetate based polymer electrolytes. *Electrochimica Acta, 48*(8), 993-999.

Pan, Z., Mora-Ser , I. n., Shen, Q., Zhang, H., Li, Y., Zhao, K., ... Bisquert, J. (2014). High-efficiency "green" quantum dot solar cells. *Journal of the American Chemical Society, 136*(25), 9203-9210.

Park, I. S., Li, W., & Manthiram, A. (2010). Fabrication of catalyst-coated membrane-electrode assemblies by doctor blade method and their performance in fuel cells. *Journal of Power Sources, 195*(20), 7078-7082.

Patil, K. R., Sathaye, S. D., Khollam, Y. B., Deshpande, S. B., Pawaskar, N. R., & Mandale, A. B. (2003). Preparation of TiO_2 thin films by modified spin-coating method using an aqueous precursor. *Materials Letters, 57*(12), 1775-1780.

Pazos, I. M., Ghosh, A., Tucker, M. J., & Gai, F. (2014). Ester carbonyl vibration as a sensitive probe of protein local electric field. *Angewandte Chemie International Edition, 53*(24), 6080-6084.

Peters, R. D., & Noble, S. D. (2019). Using near infrared measurements to evaluate NaCl and KCl in water. *Journal of Near Infrared Spectroscopy, 27*(2), 147-155.

Ping, Z. H., Nguyen, Q. T., Chen, S. M., Zhou, J. Q., & Ding, Y. D. (2001). States of water in different hydrophilic polymers—DSC and FTIR studies. *Polymer, 42*(20), 8461-8467.

Qi, B., & Wang, J. (2013). Fill factor in organic solar cells. *Physical Chemistry Chemical Physics, 15*(23), 8972-8982.

Radich, J. G., Dwyer, R., & Kamat, P. V. (2011). Cu_2S reduced graphene oxide composite for high-efficiency quantum dot solar cells. Overcoming the redox limitations of S_2^{-}/S_n^{2-} at the counter electrode. *The Journal of Physical Chemistry Letters, 2*(19), 2453-2460.

Raga, S. R., Barea, E. M., & Fabregat-Santiago, F. (2012). Analysis of the origin of open circuit voltage in dye solar cells. *The Journal of Physical Chemistry Letters, 3*(12), 1629-1634.

Rani, M. S. A., Ahmad, A., & Mohamed, N. S. (2018). A comprehensive investigation on electrical characterization and ionic transport properties of cellulose derivative from kenaf fibre-based biopolymer electrolytes. *Polymer Bulletin, 75*(11), 5061-5074.

Raphael, E., Jara, D. H., & Schiavon, M. A. (2017). Optimizing photovoltaic performance in $CuInS_2$ and CdS quantum dot-sensitized solar cells by using an agar-based gel polymer electrolyte. *RSC Advances, 7*(11), 6492-6500.

Rasal, A. S., Korupalli, C., Getachew, G., Chou, T. H., Lee, T. Y., Ghule, A. V., & Chang, J. Y. (2021). Towards green, efficient and stable quantum-dot-sensitized solar cells through nature-inspired biopolymer modified electrolyte. *Electrochimica Acta, 391*, Article#138972.

Ren, F., Li, S., & He, C. (2015). Electrolyte for quantum dot-sensitized solar cells assessed with cyclic voltammetry. *Science China Materials, 58*(6), 490-495.

Rhee, S. W., & Kwon, W. (2011). Key technological elements in dye-sensitized solar cells (DSC). *Korean Journal of Chemical Engineering, 28*(7), 1481-1494.

Roelands, M., Cuypers, R., Kruit, K. D., Oversloot, H., de Jong, A. J., Duvalois, W., ... Hoegaerts, C. (2015). Preparation & characterization of sodium sulfide hydrates for application in thermochemical storage systems. *Energy Procedia, 70*(0), 257-266.

Rosenwinkel, M. P., Andersson, R., Mindemark, J., & Sch nhoff, M. (2020). Coordination effects in polymer electrolytes: fast Li^+ transport by weak ion binding. *The Journal of Physical Chemistry C, 124*(43), 23588-23596.

Rosiles-Perez, C., Cerdán-Pasarán, A., Sidhik, S., Esparza, D., López-Luke, T., & De la Rosa, E. (2018). Improved performance of CdS quantum dot sensitized solar cell by solvent modified SILAR approach. *Solar Energy, 174*, 240-247.

Rudolph, W. W., Fischer, D., & Irmer, G. (2014). Vibrational spectroscopic studies and DFT calculations on $NaCH_3CO_2$(aq) and CH_3COOH(aq). *Dalton Transactions, 43*(8), 3174-3185.

Rühle, S., Shalom, M., & Zaban, A. (2010). Quantum-dot-sensitized solar cells. *ChemPhysChem, 11*(11), 2290-2304.

Sahu, A., Garg, A., & Dixit, A. (2020). A review on quantum dot sensitized solar cells: Past, present and future towards carrier multiplication with a possibility for higher efficiency. *Solar Energy, 203*, 210-239.

Sato, K., Ono, K., Izuishi, T., Kuwahara, S., Katayama, K., Toyoda, T., ... Shen, Q. (2016). The effect of CdS on the charge separation and recombination dynamics in PbS/CdS double-layered quantum dot sensitized solar cells. *Chemical Physics, 478*, 159-163.

Schaller, R. D., Agranovich, V. M., & Klimov, V. I. (2005). High-efficiency carrier multiplication through direct photogeneration of multi-excitons via virtual single-exciton states. *Nature Physics, 1*(3), 189-194.

Schaller, R. D., & Klimov, V. I. (2004). High efficiency carrier multiplication in PbSe nanocrystals: implications for solar energy conversion. *Physical Review Letters, 92*(18), 186601-186604.

Sekhar, M. C., Santhosh, K., Praveen Kumar, J., Mondal, N., Soumya, S., & Samanta, A. (2014). CdTe quantum dots in ionic liquid: stability and hole scavenging in the presence of a sulfide salt. *The Journal of Physical Chemistry C, 118*(32), 18481-18487.

Seo, H., Son, M. K., Kim, J. K., Shin, I., Prabakar, K., & Kim, H. J. (2011). Method for fabricating the compact layer in dye-sensitized solar cells by titanium sputter deposition and acid-treatments. *Solar Energy Materials and Solar Cells, 95*(1), 340-343.

Seo, H., Wang, Y., Uchida, G., Kamataki, K., Itagaki, N., Koga, K., & Shiratani, M. (2013). Analysis on the effect of polysulfide electrolyte composition for higher performance of Si quantum dot-sensitized solar cells. *Electrochimica Acta, 95*, 43-47.

Sequeira, C., & Santos, D. (2010). *Polymer electrolytes: fundamentals and applications*. Woodhead Publishing Limited: Elsevier.

Serghei, A., Tress, M., Sangoro, J., & Kremer, F. (2009). Electrode polarization and charge transport at solid interfaces. *Physical Review B, 80*(18), 184301-184305.

Servaites, J. D., Yeganeh, S., Marks, T. J., & Ratner, M. A. (2010). Efficiency enhancement in organic photovoltaic cells: consequences of optimizing series resistance. *Advanced Functional Materials, 20*(1), 97-104.

Shaban, M., Poostforooshan, J., & Weber, A. P. (2017). Surface-initiated polymerization on unmodified inorganic semiconductor nanoparticles via surfactant-free aerosol-

based synthesis toward core–shell nanohybrids with a tunable shell thickness. *Journal of Materials Chemistry A, 5*(35), 18651-18663.

Shalom, M., Dor, S., Ruhle, S., Grinis, L., & Zaban, A. (2009a). Core/CdS quantum dot/shell mesoporous solar cells with improved stability and efficiency using an amorphous TiO_2 coating. *The Journal of Physical Chemistry C, 113*(9), 3895-3898.

Shalom, M., Hod, I., Tachan, Z., Buhbut, S., Tirosh, S., & Zaban, A. (2011). Quantum dot based anode and cathode for high voltage tandem photo-electrochemical solar cell. *Energy & Environmental Science, 4*(5), 1874-1878.

Shalom, M., Ruhle, S., Hod, I., Yahav, S., & Zaban, A. (2009b). Energy level alignment in CdS quantum dot sensitized solar cells using molecular dipoles. *Journal of the American Chemical Society, 131*(29), 9876-9877.

Sharma, K., Sharma, V., & Sharma, S. (2018). Dye-sensitized solar cells: fundamentals and current status. *Nanoscale Research Letters, 13*(1), 1-46.

Shen, Q., Kobayashi, J., Diguna, L. J., & Toyoda, T. (2008). Effect of ZnS coating on the photovoltaic properties of CdSe quantum dot-sensitized solar cells. *Journal of Applied Physics, 103*(8), 084304-084308.

Shockley, W., & Queisser, H. J. (1961). Detailed balance limit of efficiency of p‐n junction solar cells. *Journal of Applied Physics, 32*(3), 510-519.

Sima, C., Grigoriu, C., & Antohe, S. (2010). Comparison of the dye-sensitized solar cells performances based on transparent conductive ITO and FTO. *Thin Solid Films, 519*(2), 595-597.

Singh, S., Khan, Z. H., Khan, M. B., Kumar, P., & Kumar, P. (2022). Quantum dots-sensitized solar cells: a review on strategic developments. *Bulletin of Materials Science, 45*(2), 1-13.

Siriwardane, R. V., & Woodruff, S. (1997). In situ Fourier transform infrared characterization of sulfur species resulting from the reaction of water vapor and oxygen with zinc sulfide. *Industrial Engineering Chemistry Research, 36*(12), 5277-5281.

Smestad, G. P., Spiekermann, S., Kowalik, J., Grant, C. D., Schwartzberg, A. M., Zhang, J., ... Moons, E. (2003). A technique to compare polythiophene solid-state dye sensitized TiO_2 solar cells to liquid junction devices. *Solar Energy Materials and Solar Cells, 76*(1), 85-105.

Sogabe, T., Shen, Q., & Yamaguchi, K. (2016). Recent progress on quantum dot solar cells: a review. *Journal of Photonics for Energy, 6*(4), 040901-040927.

Son, C. Y., & Wang, Z. G. (2020). Ion transport in small-molecule and polymer electrolytes. *The Journal of chemical physics, 153*(10), 100903-100921.

Song, H., Rao, H., & Zhong, X. (2018). Recent advances in electrolytes for quantum dot-sensitized solar cells. *Journal of Materials Chemistry A, 6*(12), 4895-4911.

Su'ait, M. S., Rahman, M. Y. A., & Ahmad, A. (2015). Review on polymer electrolyte in dye-sensitized solar cells (DSSCs). *Solar Energy, 115*, 452-470.

Sun, J. K., Jiang, Y., Zhong, X., Hu, J. S., & Wan, L. J. (2017). Three-dimensional nanostructured electrodes for efficient quantum-dot-sensitized solar cells. *Nano Energy, 32*, 130-156.

Sun, Y., Jiang, G., Zhou, M., Pan, Z., & Zhong, X. (2018). Origin of the effects of PEG additives in electrolytes on the performance of quantum dot sensitized solar cells. *RSC Advances, 8*(52), 29958-29966.

Swapna, V. P., Abhisha, V. S., & Stephen, R. (2020). Polymer/polyhedral oligomeric silsesquioxane nanocomposite membranes for pervaporation. In *Polymer nanocomposite membranes for pervaporation* (pp. 201-229): Elsevier.

Tachibana, Y., Umekita, K., Otsuka, Y., & Kuwabata, S. (2008). Performance improvement of CdS quantum dots sensitized TiO_2 solar cells by introducing a dense TiO_2 blocking layer. *Journal of Physics D: Applied Physics, 41*(10), 102002-102006.

Tan, A. L., Khoo, L. J., Alias, S. S., & Mohamad, A. A. (2012). ZnO nanoparticles and poly(acrylic) acid-based polymer gel electrolyte for photo electrochemical cell. *Journal of Sol-Gel Science And Technology, 64*(1), 184-192.

Tang, Z., Wu, J., Liu, Q., Zheng, M., Tang, Q., Lan, Z., & Lin, J. (2012). Preparation of poly(acrylic acid)/gelatin/polyaniline gel-electrolyte and its application in quasi-solid-state dye-sensitized solar cells. *Journal of Power Sources, 203*, 282-287.

Teo, L. P., Tiong, T. S., Buraidah, M. H., & Arof, A. K. (2018). Effect of lithium iodide on the performance of dye sensitized solar cells (DSSC) using poly(ethylene oxide)(PEO)/poly (vinyl alcohol)(PVA) based gel polymer electrolytes. *Optical Materials, 85*, 531-537.

Theint, M. M., Maung, H. E., Aung, S. H., Lwin, N. W., & Oo, T. Z. (2020). Effect of photoanode modification on charge transport, recombination and efficiency of dye sensitized solar cells using synthetic organic dyes. *Journal of Materials Science and Engineering A, 10*(1-2), 30-36.

Tress, W., Petrich, A., Hummert, M., Hein, M., Leo, K., & Riede, M. (2011). Imbalanced mobilities causing S-shaped IV curves in planar heterojunction organic solar cells. *Applied Physics Letters, 98*(6), 063301-063303.

Trukhanov, V. A., Bruevich, V. V., & Paraschuk, D. Y. (2015). Fill factor in organic solar cells can exceed the Shockley-Queisser limit. *Scientific Reports, 5*(1), 1-10.

Tubtimtae, A., Lee, M. W., & Wang, G. J. (2011). Ag_2Se quantum-dot sensitized solar cells for full solar spectrum light harvesting. *Journal of Power Sources, 196*(15), 6603-6608.

Tyagi, J., Gupta, H., & Purohit, L. (2020). Cascade Structured ZnO/TiO_2/CdS quantum dot sensitized solar cell. *Solid State Sciences, 102*, 106176-106181.

Vashistha, I. B., Sharma, M. C., Sharma, R., & Sharma, S. K. (2015). *Effect of dopent on the structural and optical properties of ZnS thin film as a buffer layer in solar cell application.* Paper presented at the AIP Conference Proceedings.

Veamatahau, A., Jiang, B., Seifert, T., Makuta, S., Latham, K., Kanehara, M., ... Tachibana, Y. (2015). Origin of surface trap states in CdS quantum dots: relationship between size dependent photoluminescence and sulfur vacancy trap states. *Physical Chemistry Chemical Physics, 17*(4), 2850-2858.

Veerathangam, K., Pandian, M. S., & Ramasamy, P. (2018). Size-dependent photovoltaic performance of cadmium sulfide (CdS) quantum dots for solar cell applications. *Journal of Alloys and Compounds, 735*, 202-208.

Voropaeva, D. Y., Novikova, S. A., & Yaroslavtsev, A. B. (2020). Polymer electrolytes for metal-ion batteries. *Russian Chemical Reviews, 89*(10), 1132-1155.

Wang, P., Wang, J., Zhang, X., Wang, H., Cui, X., Yuan, S., ... Zheng, L. (2018a). Boosting the performance of perovskite solar cells through a novel active passivation method. *Journal of Materials Chemistry A, 6*(32), 15853-15858.

Wang, S., Zhang, Q. X., Xu, Y. Z., Li, D. M., Luo, Y. H., & Meng, Q. B. (2013). Single-step in-situ preparation of thin film electrolyte for quasi-solid state quantum dot-sensitized solar cells. *Journal of Power Sources, 224*, 152-157.

Wang, X., Feng, W., Wang, W., Wang, W., Zhao, L., & Li, Y. (2018b). Sodium carboxymethyl starch-based highly conductive gel electrolyte for quasi-solid-state quantum dot-sensitized solar cells. *Research on Chemical Intermediates, 44*(2), 1161-1172.

Wang, Y. F., & Zhang, W. (2014). Chemical depositing of CdS/ZnS composition nanostructure modified TiO_2 thin film. *Chalcogenide Letters, 11*(8), 389-395.

Wei, H., Wang, G., Shi, J., Wu, H., Luo, Y., Li, D., & Meng, Q. (2016). Fumed SiO_2 modified electrolytes for quantum dot sensitized solar cells with efficiency exceeding 11% and better stability. *Journal of Materials Chemistry A, 4*(37), 14194-14203.

Woo, H. J., & Arof, A. K. (2016). Vibrational studies of flexible solid polymer electrolyte based on PCL–EC incorporated with proton conducting NH_4SCN. *Spectrochimica Acta Part A: Molecular and Biomolecular Spectroscopy, 161*, 44-51.

Woo, H. J., Majid, S. R., & Arof, A. K. (2013). Effect of ethylene carbonate on proton conducting polymer electrolyte based on poly (ε-caprolactone)(PCL). *Solid State Ionics, 252*, 102-108.

Wu, J., Lan, Z., Hao, S., Li, P., Lin, J., Huang, M., ... Huang, Y. (2008). Progress on the electrolytes for dye-sensitized solar cells. *Pure and Applied Chemistry, 80*(11), 2241-2258.

Wu, M., Lin, X., Wang, Y., & Ma, T. (2015). Counter electrode materials combined with redox couples in dye-and quantum dot-sensitized solar cells. *Journal of Materials Chemistry A, 3*(39), 19638-19656.

Wu, Y., Yang, X., Chen, H., Zhang, K., Qin, C., Liu, J., ... Han, L. (2014). Highly compact TiO_2 layer for efficient hole-blocking in perovskite solar cells. *Applied physics express, 7*(5), Article#052301.

Xu, J., Yang, X., Yang, Q. D., Wong, T. L., Lee, S. T., Zhang, W. J., & Lee, C. S. (2012). Arrays of CdSe sensitized ZnO/ZnSe nanocables for efficient solar cells with high open-circuit voltage. *Journal of Materials Chemistry, 22*(26), 13374-13379.

Xu, Y. (2020). *Multifunctional Soft Materials: Design, Development and Applications.* Arizona State University,

Xue, J., Uchida, S., Rand, B. P., & Forrest, S. R. (2004). 4.2% efficient organic photovoltaic cells with low series resistances. *Applied Physics Letters, 84*(16), 3013-3015.

Yang, Q., Yang, W., Duan, J., & Yang, P. (2018). A series of conducting gel electrolytes for quasi-solid-state quantum dot-sensitized solar cells with boosted electron transfer processes. *Journal of Energy Chemistry, 27*(2), 335-341.

Ye, M., Gao, X., Hong, X., Liu, Q., He, C., Liu, X., & Lin, C. (2017). Recent advances in quantum dot-sensitized solar cells: insights into photoanodes, sensitizers, electrolytes and counter electrodes. *Sustainable Energy & Fuels, 1*(6), 1217-1231.

Yu, J., Wang, W., Pan, Z., Du, J., Ren, Z., Xue, W., & Zhong, X. (2017). Quantum dot sensitized solar cells with efficiency over 12% based on tetraethyl orthosilicate additive in polysulfide electrolyte. *Journal of Materials Chemistry A, 5*(27), 14124-14133.

Yu, Z., Zhang, Q., Qin, D., Luo, Y., Li, D., Shen, Q., ... Meng, Q. (2010). Highly efficient quasi-solid-state quantum-dot-sensitized solar cell based on hydrogel electrolytes. *Electrochemistry Communications, 12*(12), 1776-1779.

Zhang, H., Xuan, X., Wang, J., & Wang, H. (2003). FT-IR investigations of ion association in PEO–MSCN (M= Na, K) polymer electrolytes. *Solid State Ionics, 164*(1-2), 73-79.

Zhang, J., Feng, J., Hong, Y., Zhu, Y., & Han, L. (2014a). Effect of different trap states on the electron transport of photoanodes in dye sensitized solar cells. *Journal of Power Sources, 257*, 264-271.

Zhang, Q., Guo, X., Huang, X., Huang, S., Li, D., Luo, Y., ... Meng, Q. (2011). Highly efficient CdS/CdSe-sensitized solar cells controlled by the structural properties of compact porous TiO_2 photoelectrodes. *Physical Chemistry Chemical Physics, 13*(10), 4659-4667.

Zhang, X., Yang, H., Xiong, H. M., Li, F. Y., & Xia, Y. Y. (2006). A quasi-solid-state dye-sensitized solar cell based on the stable polymer-grafted nanoparticle composite electrolyte. *Journal of Power Sources, 160*(2), 1451-1455.

Zhang, Z., Zuo, C., Liu, Z., Yu, Y., Zuo, Y., & Song, Y. (2014b). All-solid-state Al–air batteries with polymer alkaline gel electrolyte. *Journal of Power Sources, 251*, 470-475.

Zhao, K., Pan, Z., & Zhong, X. (2016). Charge recombination control for high efficiency quantum dot sensitized solar cells. *The Journal of Physical Chemistry Letters, 7*(3), 406-417.

Zhao, L., Zhao, L., Xue, W., Fang, W., Wang, Y., & Li, Y. (2018). N-doped carbon@Cu nanocomposites as counter electrode catalysts in quantum dot-sensitized solar cells. *Solar Energy, 169*, 505-511.

Zhong, M., Liu, Y. T., & Xie, X. M. (2015). Self-healable, super tough graphene oxide–poly(acrylic acid) nanocomposite hydrogels facilitated by dual cross-linking effects through dynamic ionic interactions. *Journal of Materials Chemistry B, 3*(19), 4001-4008.